In situ characterization during the synthesis and reaction of ceria-based mesoporous catalysts for NH₃-selective catalytic reduction (SCR) applications

In situ-Charakterisierung während der Synthese und Reaktion von Cerdioxid-basierten mesoporösen Katalysatoren für NH₃-selektive katalytische Reduktion (SCR)-Anwendungen

**at the Department of Chemistry
of the Technischen Universität Darmstadt**

submitted in fulfilment of the requirement for the degree
Doctor rerum naturalium
(Dr. rer. nat.)

Doctoral Thesis
By

Jun Shen

First reviewer: Prof. Dr. Christian Hess
Second reviewer: Prof. Dr.-Ing. Bastian J. M. Etzold

Darmstadt 2022

In situ characterization during the synthesis and reaction of ceria-based mesoporous catalysts for NH$_3$-selective catalytic reduction (SCR) applications

In situ-Charakterisierung während der Synthese und Reaktion von Cerdioxid-basierten mesoporösen Katalysatoren für NH$_3$-selektive katalytische Reduktion (SCR)-Anwendungen

Submitted doctoral thesis by Jun Shen

First reviewer: Prof. Dr. Christian Hess

Second reviewer: Prof. Dr.-Ing. Bastian J. M. Etzold

Date of submission: **07. Nov. 2022**

Day of the oral examination: **19. Dec. 2022**

Darmstadt - D 17

Erklärungen

§8 Abs. 1 lit. c der Promotionsordnung der TU Darmstadt
Ich versichere hiermit, dass die elektronische Version meiner Dissertation mit der schriftlichen Version übereinstimmt und für die Durchführung des Promotionsverfahrens vorliegt.

§8 Abs. 1 lit. d der Promotionsordnung der TU Darmstadt
Ich versichere hiermit, dass zu einem vorherigen Zeitpunkt noch keine Promotion versucht wurde und zu keinem früheren Zeitpunkt an einer in- oder ausländischen Hochschule eingereicht wurde. In diesem Fall sind nähere Angaben über Zeitpunkt, Hochschule, Dissertationsthema und Ergebnis dieses Versuchs mitzuteilen.

§9 Abs. 1 der Promotionsordnung der TU Darmstadt
Ich versichere hiermit, dass die vorliegende Dissertation selbstständig und nur unter Verwendung der angegebenen Quellen verfasst wurde.
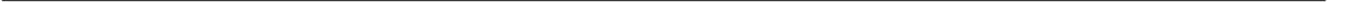
§9 Abs. 2 der Promotionsordnung der TU Darmstadt
Die Arbeit hat bisher noch nicht zu Prüfungszwecken gedient.

Darmstadt, den   07. Nov. 2022

Jun Shen

(Name und Unterschrift)

Abstract

Nitrogen oxides (NO_x) are major pollutants of the air environment, which are known as the major causes of haze, photochemical smog, acid rain, ozone depletion, and the greenhouse effect. Selective catalytic reduction using ammonia as a reductant (NH_3-SCR) is proved to be an effective method to remove nitrogen oxides ($DeNO_x$). Previous studies have reported that cerium-based oxide catalysts own the advantages of wide operating temperature windows and high catalytic activities in NH_3-SCR reactions. Mesoporous materials (e.g. SBA-15) are considered as a suitable support material for metal oxides, providing a high surface area and stabilization effect. Thus, this work addresses the synthesis of SBA-15 supported ceria-based catalysts and their application for the NH_3-SCR reaction.

First, the simplest system was considered by loading only ceria onto the mesoporous SBA-15 (CeO_2/SBA-15). In order to achieve a good dispersion of ceria on the inner surface, two kinds of samples were prepared by solid-state impregnation method following the "medium-synthesis" route (asSBA-CeO_2) and the "post-synthesis" route (tfSBA-CeO_2). Catalytic tests indicated that the $DeNO_x$ performance was enhanced by the assistance of template P123 in asSBA-CeO_2. *In situ* characterizations, which were performed to elucidate the effect of P123 during the synthesis process, revealed that the good dispersion effect of asSBA-15 supported ceria was due to the presence of template P123, playing a physical role to confine the growth of ceria and a chemical role in catalytically reducing the ceria simultaneously. After the synthesis, the catalysts were applied for the NH_3-SCR reaction and the mechanism was studied. *In situ* DRIFT spectra of CeO_2/SBA-15 were recorded to monitor the surface species changes as a function of feeding gas, time, and temperature. The results showed that two active species, $-NH_2$ and NO^-, were involved. In addition, the analysis of features at about 2100-2200 cm^{-1}, typically assigned to triple bonds, made it possible to deduce the formation of the side product N_2O by over-oxidation of NH_3. Moreover, the co-existence of the L-H and E-R routes for the NH_3-SCR reaction on CeO_2/SBA-15 was proved.

Considering the poor reactivity of bare CeO_2 for the NH_3-SCR reaction, a second metal oxide was added to form a MO_x-CeO_2 couple, which was expected to improve the catalytic performance due to the synergistic effect of M-O-Ce species. Firstly, a wide selection of secondary metal elements was employed to prepare SBA-CeCuO, SBA-CeMnO, SBA-CeNiO, SBA-CeMgO, and SBA-CeLaO, while SBA-CeO_2 served as a reference. The catalytic tests showed that the mixture with variable metals (Cu, Mn, Ni) resulted in enhanced $DeNO_x$ performance, while the mixture with permanent metals (Mg, La) exhibited a decreased performance. The observed behavior revealed that the redox ability rather than the acidity contributed to the NH_3-SCR reactivity. Based on the catalytic performance and due to its wide

application in various catalytic systems, the $CuO-CeO_2$ catalyst was selected for detailed analysis. Template-free SBA-15 and as-made SBA-15 were employed as support precursors to form $CuO-CeO_2$/SBA-15 and the synthesis process was monitored with *in situ* characterizations including Raman, DRIFT, and DR UV-Vis spectroscopy. The results specified the synthesis to follow two different routes, i.e. solid thermal decomposition for the template-free SBA-15 prepared sample and a hydrothermal route for the as-made SBA-15 prepared sample. The former route resulted in a mixed $CuO-CeO_2$ phase with strong redox ability, leading to a low optimal temperature window but poor N_2 selectivity, while the latter route led to separated CuO and CeO_2 phases with moderate redox properties, resulting in a high and broad working temperature window. These findings provided evidence for the presence of a more comprehensive research pattern, connecting catalyst synthesis, structure, property, and catalytic performance. Another bimetallic oxide catalyst, MnO_x-CeO_2 supported on SBA-15, was prepared due to its favorable $DeNO_x$ performance. *In situ* characterizations were applied to study the whole process from the catalyst synthesis to its application for the NH_3-SCR reaction. The results for the synthesis process revealed two different preparation routes when using a similar template strategy as for the CuO system. Based on *in situ* DRIFT spectra the mechanism of NH_3-SCR on MnO_x-CeO_2/SBA-15 was shown to follow mainly the E-R route and the quick regeneration of $-NH_2$ by strong redox properties contributed to the high reactivity.

Atomic layer deposition (ALD) was employed as another promising method to load active metal oxides onto mesoporous materials. Firstly, VO_x/TiO_2/SBA-15 catalysts were prepared by ALD to explore the feasibility of using mesoporous powder as a deposition substrate. The results showed that the prepared sample owns a high surface area as expected and the surface-loaded VO_x could be quantitatively controlled by the number of ALD cycles. Secondly, several atomic layers of SiO_2 were deposited on prepared CeO_2/SBA-15 to explore the activity of Ce-O-Si sites although SiO_2 itself is known as an inert support. Due to the sandwich structure of $SiO_2/CeO_2/SiO_2$ and the controllable amount of Ce-O-Si sites by ALD, Ce-O-Si was shown to be the active site for the NH_3-SCR reaction and the NO_x conversion was proportional to the SiO_2 coverage until full coverage of the surface. In addition, the SiO_2-covered sample showed a better SO_2 resistance than bare CeO_2/SBA-15. Besides, VO_x/CeO_2/SBA-15 was prepared by depositing VO_x on CeO_2/SBA-15 via the common ALD and a site-selective ALD (SSALD) method. This SSALD method is proposed here for the first time. As a crucial step it involves the pretreatment of the substrate with the target reaction gas (NH_3-SCR) before the ALD procedure. The results showed that the SSALD-coated sample exhibited a better DeNOx performance than the common ALD-coated sample. IR analysis of the catalyst surface revealed that the substrate pretreated with the SCR experimental gas showed the presence of NH_x and N_xO_y replacing hydroxyl groups. The NH_x species was inert to the vanadium precursor and retained the NH_3-active sites after coating, while the

N_xO_y species was desorbed and free water was transformed into -OH groups, resulting in more active VO_x species deposition.

During the study of the synthesis process by *in situ* characterizations, the synthesis reaction was realized to be important for determining the final catalyst structure and further the reactivity behavior in the target NH_3-SCR reaction. It is reasonable to hypothesize that there exists a correlation between the synthesis reaction and the target catalytic reaction. To test this hypothesis, CeO_2/SBA-15 samples were prepared by the SSI method and calcined in different gas atmospheres, from reductive NH_3 to oxidative O_2. Among the prepared samples, the sample calcined in the target reaction gas showed the best catalytic performance. Raman and DR UV-Vis spectra of the sample exposed to the target reaction gas revealed the presence of a moderate amount of oxygen vacancies, which is proposed to contribute to the high NO_x conversion due to the optimized adsorption of NH_3. In all, the correlation between synthesis reaction and target catalytic reaction is an interesting topic to be explored for other reactions, and *in situ* spectroscopy applied to both synthesis and reaction is a powerful tool to elucidate the underlying chemistry.

Zusammenfassung

Stickoxide (NO_x) gehören zu den Hauptschadstoffen der Luftumgebung, die als die Hauptursachen für Dunst, photochemischen Smog, sauren Regen, Ozonabbau und den Treibhauseffekt bekannt sind. Die selektive katalytische Reduktion mit Ammoniak als Reduktionsmittel (NH_3-SCR) hat sich als effektive Methode zur Entfernung von Stickoxiden ($DeNO_x$) erwiesen. Frühere Studien haben berichtet, dass oxidische Katalysatoren auf Basis von Cer einen weiten Bereich an Betriebstemperaturen ermöglichen und hohe katalytische Aktivitäten in NH_3-SCR-Reaktionen aufweisen. Mesoporöse Materialien (z.B. SBA-15) werden als gut geeignete Trägermaterialien für Metalloxide angesehen, um eine große spezifische Oberfläche bereitzustellen und stabilisierend zu wirken. Daher adressiert diese Arbeit die Synthese von Cerdioxid-basierten mesoporösen Katalysatoren unter Verwendung von SBA-15 als Trägermaterial sowie deren Anwendung in der NH_3-SCR-Reaktion.

Es wurde zunächst das einfachste System, bestehend aus Ceroxid auf mesoporösem SBA-15 (CeO_2/SBA-15), betrachtet. Um eine gute Dispersion von Cerdioxid auf der inneren Oberfläche der Poren zu erreichen, wurden zwei Arten von Proben durch Festkörperimprägnierung (SSI) hergestellt, und zwar basierend auf SBA-15 mit Templat (asSBA-CeO_2) und SBA-15 ohne Templat (tfSBA-CeO_2). Die katalytischen Tests zeigen, dass die DeNOx-Performanz durch die Gegenwart des Templats P123 im Falle von asSBA-CeO_2 verbessert wurde. Mit Hilfe von *in situ*-Charakterisierungen konnte die Wirkung von P123 während des Syntheseprozesses herausgearbeitet werden. So kann die gute Dispersion von asSBA-15-geträgertem Cerdioxid darauf zurückgeführt werden, dass das Templat P123 einerseits eine physikalische Rolle spielt, um das Wachstum von Cerdioxid zu begrenzen, andererseits eine chemische Rolle bei der gleichzeitig stattfindenden katalytischen Reduktion des Ceroxids. Mittels *in situ*-DRIFT-Spektroskopie wurden die Änderungen der Oberflächenspezies als Funktion des zugeführten Gases, der Zeit und der Temperatur analysiert, um mechanistische Einblicke zu erhalten. Die Ergebnisse zeigen, dass zwei aktive Spezies, $-NH_2$ und NO^-, an der NH_3-SCR-Reaktion über CeO_2/SBA-15-Katalysatoren beteiligt sind. Darüber hinaus ermöglicht es die Analyse der Banden innerhalb von 2100-2200 cm^{-1}, welche typischerweise Dreifachbindungen zugeordnet werden, die Bildung des Nebenprodukts N_2O durch Überoxidation von NH_3 abzuleiten. Darüber hinaus wird die Koexistenz der L-H- und E-R-Routen für die NH_3-SCR-Reaktion über CeO_2/SBA-15 nachgewiesen.

In Anbetracht der geringen Reaktivität von reinem CeO_2 in der NH_3-SCR-Reaktion wurde ein zweites Metalloxid hinzugefügt, um MO_x-CeO_2-Paare zu bilden, mit der Erwartung, dass die katalytische Leistung durch den synergistischen Effekt der M-O-Ce-Spezies verbessert wird. Zunächst wurde Cerdioxid mit einer breiten Auswahl an sekundären Metallelementen gemischt und SBA-CeCuO,

SBA-CeMnO, SBA-CeNiO, SBA-CeMgO und SBA-CeLaO hergestellt, wobei SBA-CeO$_2$ als Referenz diente. Die katalytischen Tests zeigten, dass die Mischung mit variablen Metallen (Cu, Mn, Ni) zu einer verbesserten DeNO$_x$-Performanz führte, während die Mischung mit permanenten Metallen (Mg, La) zu einer geringeren Leistung führte. Dieses Verhalten zeigt, dass die Redoxfähigkeit und nicht die Acidität zur NH$_3$-SCR-Reaktivität beiträgt. Auf Basis seiner katalytischen Performanz und aufgrund seiner breiten Anwendung in verschiedenen katalytischen Systemen wurde der CuO-CeO$_2$-Katalysator für eine detaillierte Analyse ausgewählt. Als Träger für die Synthese von CuO-CeO$_2$/SBA-15 wurde Templat-enhaltendes und templatfreies SBA verwendet und der Syntheseprozess von CuO-CeO$_2$/SBA-15 u.a. mittels *in situ*-Raman-, DRIFT- und DR-UV-Vis-Spektroskopie verfolgt. Die Ergebnisse zeigen, dass die Synthese je nach Träger unterschiedlich abläuft, und zwar einerseits über eine thermische Zersetzung (asSBA-15), andererseits über eine hydrothermale Zersetzung (tfSBA-15). Im ersten Fall wird eine gemischten CuO-CeO$_2$-Phase mit ausgeprägten Redoxeigenschaften erhalten, was die Reaktivität bei niedrigen Temperaturen begünstigt, aber eine geringe N$_2$-Selektivität mit sich bringt, während im zweiten Fall getrennte CuO- und CeO$_2$-Phasen mit gemäßigten Redoxeigenschaften entstehen, was einen breiten Arbeitsbereich und hohe Arbeitstemperaturen begünstigt. Die Ergebnisse weisen darauf hin, dass die Katalysatorsynthese, die Struktur und Eigenschaften des Katalysators und die katalytische Performanz miteinander verknüpft sind. Aufgrund seiner hervorragenden DeNO$_x$-Performanz wurde ein weiterer bimetallischer Oxidkatalysator, basierend auf MnO$_x$-CeO$_2$ auf SBA-15, hergestellt. Mittels *in situ*-Charakterisierung wurde der gesamte Prozess von der Katalysatorsynthese bis zur Anwendung in der NH$_3$-SCR-Reaktion untersucht. Die Ergebnisse für den Syntheseprozess zeigen wiederum verschiedene Herstellungswege bei Verwendung der zuvor beschriebenen Trägermaterialien (asSB-15, tfSBA-15). *In situ*-DRIFT-Spektren zeigen, dass der Mechanismus der NH$_3$-SCR-Reaktion über MnO$_x$-CeO$_2$/SBA-15 hauptsächlich der E-R-Route folgt und die schnelle Regeneration von -NH$_2$ durch die ausgeprägten Redox-Eigenschaften zu der hohen Reaktivität beiträgt.

Die Atomlagenabscheidung (ALD) wurde als weitere vielversprechende Methode eingesetzt, um aktive Metalloxide auf mesoporösen Materialien zu verankern. Zunächst wurden VO$_x$/TiO$_2$/SBA-15-Katalysatoren mittels ALD hergestellt, um die Anwendbarkeit von mesoporösem Pulver als Abscheidungssubstrat bei ALD-Prozessen zu untersuchen. Die Ergebnisse zeigen, dass die präparierte Probe wie erwartet eine große Oberfläche besitzt und die Beladung mit VO$_x$ durch die Anzahl der ALD-Zyklen kontrolliert werden kann. In einer weiteren Studie wurden mittels ALD SiO$_2$-Atomschichten auf hergestelltem CeO$_2$/SBA-15 kontrolliert abgeschieden, um die Aktivität der gebildeten Ce-O-Si-Spezies zu untersuchen. Aufgrund der Sandwich-Struktur von SiO$_2$/CeO$_2$/SiO$_2$ und der durch ALD kontrollierbaren Ce-O-Si-Konzentration konnte Ce-O-Si als aktives Zentrum für die NH$_3$-SCR-Reaktion identifiziert werden, basierend auf der Proportionalität zwischen der NO$_x$-Umwandlung und der

Bedeckung bis hin zur vollständigen Bedeckung der Oberfläche mit SiO_2. Darüber hinaus zeigte die SiO_2-beschichtete Probe eine bessere SO_2-Beständigkeit als reines CeO_2/SBA-15. In einer ALD-Studie zum Einfluß der Synthesebedingungen auf die Reaktivität, wurde $VO_x/CeO_2/SBA$-15 durch Abscheidung von VO_x auf CeO_2/SBA-15 einerseits über das übliche ALD-Verfahren, andererseits über ein ortsselektives ALD (SSALD)-Verfahren hergestellt. Dieses SSALD-Verfahren wird hier zum ersten Mal vorgeschlagen und enthält als wichtigen Schritt vor dem ALD-Verfahren die Vorbehandlung des Substrats mit dem Reaktionsgas der Zielreaktion (NH_3-SCR). Die Ergebnisse zeigen für die mit dem SSALD-Verfahren beschichtete Probe eine bessere DeNO$_x$-Performanz, welche mittels IR-Untersuchungen auf den Austausch von OH-Gruppen durch NH_x und N_xO_y während der Behandlung mit dem SCR-Reaktionsgas zurückgeführt werden kann. Dabei zeigte sich die NH_x-Spezies gegenüber dem Vanadium-ALD-Prekursor inert, so dass die NH_3-aktiven Zentren erhalten blieben, während die N_xO_y-Spezies unter Umwandlung von freiem Wasser in OH-Gruppen desorbiert wurde, was zu einer verstärkten Abscheidung der VO_x-Spezies führte.

Während der Untersuchung des Syntheseprozesses durch *in situ*-Charakterisierung zeigte sich die Bedeutung der Behandlung mit Reaktionsgas für die endgültige Katalysatorstruktur und die NH_3-SCR-Reaktivität. Um die vorgeschlagene Korrelation zwischen der Behandlung mit dem Reaktionsgas während der Synthese und der katalytischen Zielreaktion näher zu untersuchen, wurden CeO_2/SBA-15-Katalysatoren nach dem SSI-Verfahren hergestellt und in verschiedenen Gasatmosphären kalziniert, von reduktiven (NH_3) bis zu oxidativen (O_2) Bedingungen. Unter den hergestellten Proben zeigte die im Reaktionsgas kalzinierte Probe die beste katalytische Performanz. Raman- und DR-UV-Vis-Spektren zeigen für diese Probe die Gegenwart von Ceroxid mit einer gemäßigten Anzahl an Sauerstoffleerstellen, was zu der hohen NO$_x$-Umwandlung durch optimierte Adsorption von NH_3 beitragen könnte. Insgesamt stellt die Korrelation zwischen der Synthesereaktion und der katalytischen Zielreaktion ein interessantes Thema für zukünftige Untersuchungen an anderen Katalysatorsystemen dar, wobei die *in situ*-Spektroskopie ein leistungsfähiges Werkzeug für die Untersuchung der zugrundeliegenden chemischen Vorgänge darstellt.

Publications

High Surface Area VO$_x$/TiO$_2$/SBA-15 Model Catalysts for Ammonia SCR Prepared by Atomic Layer Deposition
J. Shen and C. Hess, *Catalysts*, 2020, 10, 1386.

Controlling the dispersion of ceria using nanoconfinement: application to CeO$_2$/SBA-15 catalysts for NH$_3$-SCR
J. Shen and C. Hess, *Mater. Adv.*, 2021, 2, 7400-7412.

Rational Design of Mesoporous CuO-CeO$_2$ Catalysts for NH$_3$-SCR Applications Guided by Multiple *In situ* Spectroscopies
J. Shen, S. Lauterbach and C. Hess, *ACS Appl. Mater. Interfaces*, 2022, 14, 43407-43420.

Other publication

Borate-driven ionic rectifiers based on sugar-bearing single nanochannels
V.M. Cayon, G. Laucirica, Y.T. Terrones, M.L. Cortex, G. Perez-Mitta, J. Shen, C. Hess, M.E. Molares, C. Trautmann, W.A. Marmissole, O. Azzaroni, *Nanoscale*, 2021, 13, 11232.

Posters

Ammonia selective catalytic reduction (SCR) on VO$_x$/TiO$_2$/SBA-15 model catalysts prepared by atomic layer deposition
J. Shen and C. Hess, Jahrestreffen Deutscher Katalytiker 2020 (Weimar).

Controlling the dispersion of ceria using nanoconfinement: application to CeO$_2$/SBA-15 catalysts for NH$_3$-SCR
J. Shen and C. Hess, Jahrestreffen Deutscher Katalytiker 2021 (Weimar)

Presentation

Rational Design of Mesoporous CuO-CeO$_2$ Catalysts for NH$_3$-SCR Applications Guided by Multiple *In situ* Spectroscopies
J. Shen and C. Hess, Jahrestreffen Deutscher Katalytiker 2022 (Weimar)

Acknowledgement

I would like to take this opportunity to thank all the people who contributed to the completion of this work.

First, I would like to give my special thanks to Prof. Dr. Christian Hess for the opportunity to work on this interesting topic. More importantly, his continuous encouragement supported me to reach my goal. Especially, as challenges like changing topics, repeated rejection of papers, prolonged time, and so on were encountered during the whole process. Without his trust, patience, and understanding, the work would not have become what it is today. From numerous formal or casual discussions and manuscript corrections, the doctoral thesis finally led to a happy end for me in which I developed much. I learned not only academic knowledge but also an earnest scientific attitude from Prof. Dr. Christian Hess, which will make effect on my future life and career.

Another special thanks goes to Claudia Jochem and Karl Kopp, who helped me a lot with office things and scientific things. As a foreign student, their help made my life and work easier after coming to Germany. What's more, because of their kind and friendly attitude they made me feel nice and fit into our group.

Thanks also goes to my colleagues, Marcel Heber, Anastasia Filtschew, Christian Schilling, Philip Ruff, Simone Rogg, Sebastian Berka, Mariusz Radtke, Marc Ziemba, Leon Schumacher, Jacob Weyel, Maximilian Pfeiffer, Xu Chen, and Jan Welzenbach. All of them were friendly and helped me more or less in daily life and research work. Especially, Philip Ruff is thanked for guiding me at the start of my project and introducing me into the lab work, thus building the foundation of my experimental work. Anastasia Filtschew is really appreciated for teaching me how to use spectrometers and kind time arrangements. In addition, I'd like to thank Simone Rogg for her beneficial academic discussion and for kindly encouraging me when I was upset about my results.

I'd like to thank Karl Kopp again for his XPS measurement and the technical support during the whole experimental period. Thank also goes to Prof. Dr. Barbara Albert and especially Dr. Kathrin Hofmann for the XRD measurements and the data analysis, to Dr. Stefan Lauterbach for the TEM measurements and the data analysis, as well as to Prof. Dr. Gerd Buntkowsky and especially Dr. Martin Brodrecht but also Till Wissel for the N_2 physisorption measurements.

Finally, I want to thank my family and friends for all the support, encouragement, and patience. Without your support, this thesis would not have been possible. Thank you all again.

Contents

Chemical formulae

$Ce(NO_3)_3 \cdot 6H_2O$	Cerium(III) nitrate hexahydrate
CeO_2	Cerium dioxide
C_xH_y	Hydrocarbons
CO_2	Carbon dioxide
CuO	Copper(II) oxide
Cu_2O	Copper(I) oxide
$Cu(NO_3)_3 \cdot 3H_2O$	Copper(II) nitrate trihydrate
H_2O	Water
$La(NO_3)_3 \cdot 6H_2O$	Lanthanum(III) nitrate hexahydrate
MgO	Magnesium oxide
$Mg(NO_3)_2 \cdot 6H_2O$	Magnesium nitrate hexahydrate
MnO_x	Manganese oxide
$Mn(NO_3)_2 \cdot 4H_2O$	Manganese(II) nitrate tetrahydrate
NH_3	Ammonia
$Ni(NO_3)_2 \cdot 6H_2O$	Nickel(II) nitrate hexahydrate
N_2O	Nitrous oxide
NO	Nitric oxide
NO_2	Nitrogen dioxide
NO_2^-	Nitrite
NO_3^-	Nitrate
SO_2	Sulfur dioxide
SO_4^-	Sulfate
$SiCl_4$	Tetrachlorosilane
TiO_2	Titanium oxide
$TiCl_4$	Titanium tetrachloride
V_2O_5	Vanadium(V) oxide
VO_x	Vanadium oxide
$VOCl_3$	Vanadium(V) oxychloride

General abbreviations

α	Absorption coefficient
γ	Grüneisen parameter
λ	Wavelength
ν	Frequency
d	Crystallite size
ALD	Atomic Layer Deposition
BET	Brunauer-Emmett-Teller
CIG	Catalytic Induced Growth
DRIFTS	Diffuse Reflectance Infrared Fourier Transform Spectroscopy
DR UV-Vis	Diffuse Reflectance Ultraviolet-Visible Spectroscopy
DeNO$_x$	Reduction of nitrogen oxides
EMSI	Electronic Metal-Support Interaction
F(R$_\infty$)	Kubelka-Munk function
FTIR	Fourier-Transform Infrared
FWHM	Full Width at Half Maximum
GHSV	Gas Hourly Space Velocity
G(R∞)	Function for correction of absorption effects
h	Planck constant
I$_0$	Raman laser intensity
HWHM	Half Width at Half Maximum
P123	Pluronic P123, Poly(ethylene glycol)-*block*-poly(propylene glycol)-*block*-poly(ethylene glycol)
SCR	Selective Catalytic Reduction
R$_\infty$	Reflectance of an infinitely thick sample
R	Reflectance
SBA-15	Santa Barbara Amorphous-15
SMSI	Strong Metal Support Interaction
SSALD	Site Selective Atomic Layer Deposition
SSI	Solid State Impregnation
TEM	Transmission Electron Microscopy
V$_O^{\cdot\cdot}$	Doubly positively charged oxygen vacancy
XPS	X-ray Photoelectron Spectroscopy
XRD	X-Ray Diffraction

1. Introduction and motivation

1.1. NO$_x$ pollution and emission control

NO$_x$ pollution is a major risk affecting both natural environments and our health.[1] From the environmental perspective, NO$_x$ emission will lead to acid rain, which further results in potential changes in soil and water quality. The effect can be significant including damage to the ecosystems and decreases in biodiversity. For health issues, NO$_x$ mainly affects respiratory conditions, causing airway inflammation at high levels. Long-term exposure can decrease lung function, increase the risk of respiratory infections, and increase the response to allergens. NO$_x$ also contributes to the formation of fine particles (PM) and ground-level ozone, both of which are associated with adverse health effects.[2]

Nitric oxide (NO) and nitrogen dioxide (NO$_2$) are collectively referred to as nitrogen oxides (NO$_x$), which are mainly produced and emitted by the combustion of fossil fuels, such as fuel vehicles (movable source) and coal-fired power plants (stationary source).[3] According to the European Union emission inventory report (1990-2019), the transport and energy industries shared 47 % and 34 % of the total NO$_x$ emission. Thus, it is important to reduce the NO$_x$ by controlling the NO$_x$ emission from the combustion of fossil fuels.[4]

The emission depends not only on the nitrogen content in the fuel but also on the combustion conditions. NO$_x$ is formed in the gas phase by three possible routes: (1) oxidation of nitrogen in the combustion air as "thermal NO$_x$", (2) oxidation of nitrogen in the fuel as "fuel NO$_x$", and (3) fast oxidation of nitrogen fixed by hydrocarbon fragments as "prompt NO$_x$".[5] The thermal NO$_x$ formation is sensitive to flame temperature and can be controlled by appropriately controlling peak temperature, while the fuel NO$_x$ depends on the availability of oxygen to react with the nitrogen. Thus, one strategy is to control the combustion process by adjusting the devolatilization of fuel-bound nitrogen, availability of oxygen, and flame temperature, which are denoted as primary control technologies as minimizing the initially produced NO$_x$ in the combustion zone.[6] In terms of such an idea, various techniques are developed such as low NO$_x$ burner (LNB), over fire air (OFA), dry low NO$_x$ (DLN), dilute injection, etc.[7] Another strategy is the use of secondary control technologies such as reducing the NO$_x$ in the exhausted gas from the combustion zone.[8] There are two main techniques for secondary controlling that are selective noncatalytic reduction (SNCR) and selective catalytic reduction (SCR).[9] Compared with the primary strategy, the second one provides a further decrease in NO$_x$ emission and does not affect the thermal output when adjusting the combustion conditions. In addition, for the comparison of SNCR and SCR, the non-catalytic reaction requires a higher reduction temperature and the treated gas shows a higher NO concentration than SCR treatment. At present, SCR with NH$_3$ is widely adopted for both

stationary and mobile sources to maintain the increasing request for NO_x removal ($DeNO_x$) by the latest regulations (Figure 1).[4] Even though, one can find that the practical emission consistently exceeds its limit for the same period (from EURO-III-2000 to EURO-VI-2014) in Europe, especially for the diesel source which owns typical low-temperature combustion conditions. Therefore, further improvement of $DeNO_x$ technology is of great importance regarding both scientific and industrial aspects.
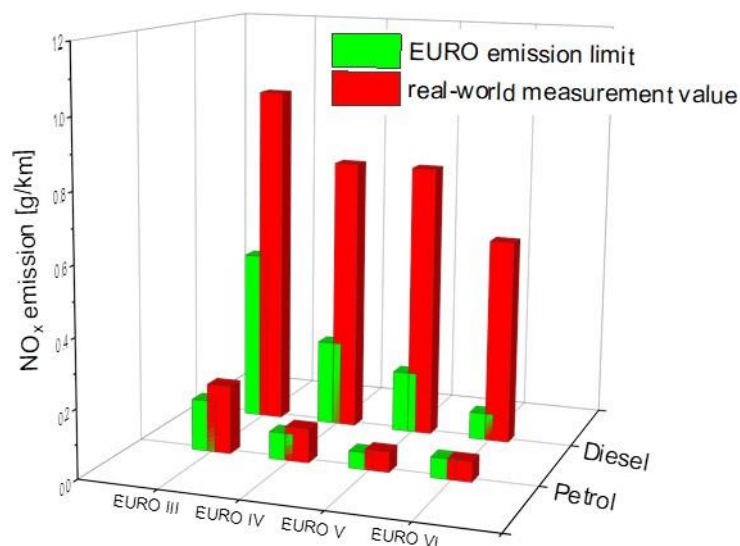

Figure 1. Comparison of NO_x emission standards for different Euro classes.

1.2. Role of characterization for the catalytic chemistry tetrahedron

The concept of materials science tetrahedron (MST) concisely depicts the inter-dependent relationships among the structure, property, performance, and processing of a material at the four vertices, which are achieved by the characterization sitting in the center of the material tetrahedron. Similar to its role in traditional materials science, catalysis research shares the same paradigm to encompass the scientific foundation and development of various catalysts and corresponding catalytic reactions, which is defined as catalytic chemistry tetrahedron (CCT).

As seen in Figure 2, the catalytic chemistry tetrahedron includes four corners as synthesis, structure, property, and performance, and one core inside as characterization. For an NH_3-SCR reaction on metal oxides, there have been a lot of publications about using various characterizations, including the typical ex-situ techniques (XPS, TEM, XRD, TP-R/D),[10] *in situ* DRIFT spectroscopy[11], and even transient Raman spectroscopy,[12] to explore the relationship amount the triangle side face "Structure-property-performance", which are denoted as reaction mechanism or structure-activity relationship.

However, the exploration of the corner "synthesis" is almost experiential because of lacking systemic investigations of the relationship between the synthesis process and the prepared catalysts. Putting aside the catalysts for NH_3-SCR reactions for the moment, using *in situ* characterizations to monitor the catalysts synthesis process and get insight into the mechanism of reactive component/structure formation has attracted more and more interest. Generally, *in situ* TEM and X-ray spectroscopy are widely adopted to explain the formation of nano metal particles. Wu et al. reported the *in situ* observation of Cu-Ni alloy nanoparticle formation by X-Ray Diffraction (XRD), X-Ray Absorption Spectroscopy (XAS), and Transmission Electron Microscopy (TEM).[13] Golks et al. presented detailed *in situ* surface X-ray scattering studies of homoepitaxial Cu electrodeposition on Cu(001) electrodes in electrolytes $Cu(ClO_4)_2$, revealing a pronounced mutual interaction of the Cl adlayer order and Cu growth behavior.[14] Phillion et al. researched the micropores formation of Al-Cu alloy by an X-ray tomography study, which was further developed by Weber et al. to understand the porous nickel alumina catalyst synthesis in 3D with X-ray ptychography.

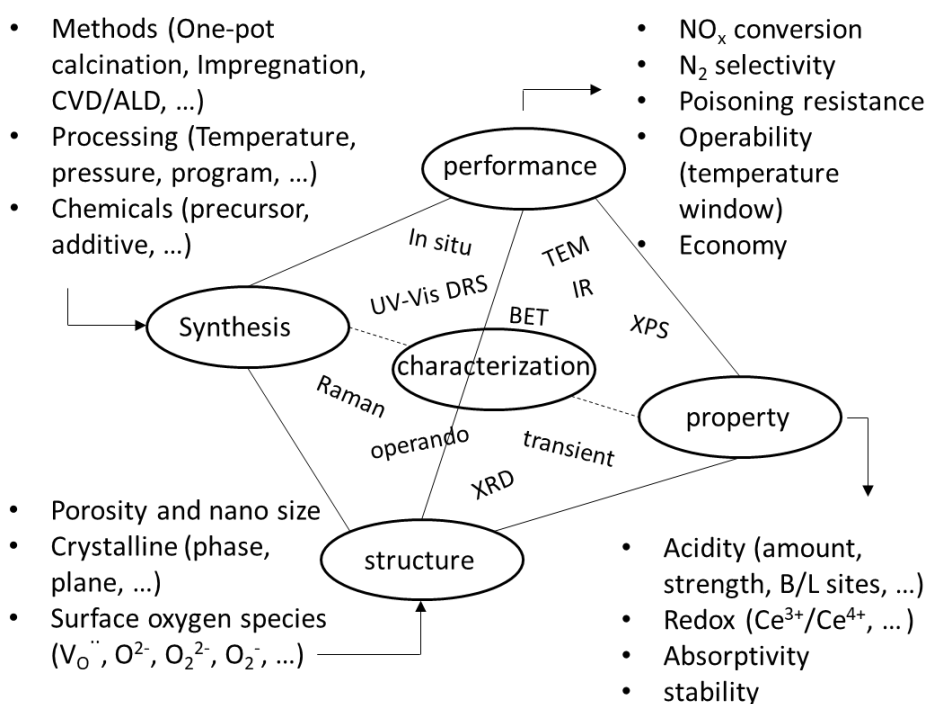Figure 2. The catalytic chemistry tetrahedron (for NH_3-SCR on metal oxide catalysts as an example).

So far *in situ* characterization has focused more on understanding the synthesis-structure relationship on the nanoscale by shape and phase identification. From a deeper level, the synthesis conditions directly affect the interactions among the original precursors and then reflect the evolution of

structures. Therefore, the description of the possible reaction during the process from metal precursors to their final oxides is important to understand the nucleation and growth of oxides. The orientation of growth and the defection structure is expected to be related to the interface reaction between transformed oxides and the precursors. There are lots of works on the reaction mechanism of mechanochemical synthesis by *in situ* Raman and NMR.[15, 16] Mechanistic understanding of mechanochemical reactions is sparse and has been acquired mostly by stepwise *ex situ* analysis.[16] Monitoring the course of mechanochemical transformations at the molecular level *in situ* and in real-time by Raman spectroscopy reveals the mechanochemical reactions to form coordination polymers and organic co-crystals, as well as the assessment of the reaction dynamics and course under different reaction conditions. On the other hand, *in situ* DRIFT spectroscopy is also a powerful tool to characterize the surface adsorbed species applying for the synthesis process by the atomic layer deposition (ALD) technique. For example, Du et al. used *in situ* DRIFT spectroscopy to monitor the growth of SiO_2 thin films by the ALD technique and discussed the catalytic effect of pyridine during the surface precursors reaction which achieved a low-temperature deposition window.[17]

In brief, for the catalytic system of NH_3-SCR, catalytic reaction mechanisms are widely researched by various characterizations to reveal the relationship between structure/property and the catalytic performance of prepared catalysts, while the synthesis process is rarely paid attention to, for example, by developing purposely designed routes to achieve expected active species instead of experiential try. Previous literature results have showed great promise in using *in situ* spectroscopy for material synthesis. Therefore, it is reasonable to consider the use of *in situ* spectroscopy to get insight into the NH_3-SCR catalyst synthesis mechanism and to achieve further control on the structure and catalytic performance.

1.3. Research outline

The present thesis addresses the catalytic chemistry tetrahedron of ceria-based catalysts applied to the NH_3-SCR reaction for NO abatement. For the choice of the catalyst, ceria is a present hot candidate, due to its unique redox properties, to replace the conventional vanadia-based catalyst attracting much research interest. As introduced above *in situ* spectroscopy has been applied to the material synthesis by mechanochemical and ALD methods; herein, solid-state impregnation (like the mechanochemical method) and ALD were adopted to prepare ceria-based catalysts. The *in situ* characterizations include Raman, DRIFT, and DR (diffuse reflectance) UV-Vis spectroscopy, applied to monitor the whole process, from catalysts synthesis to SCR reaction. Details are shown below (Figure 3).
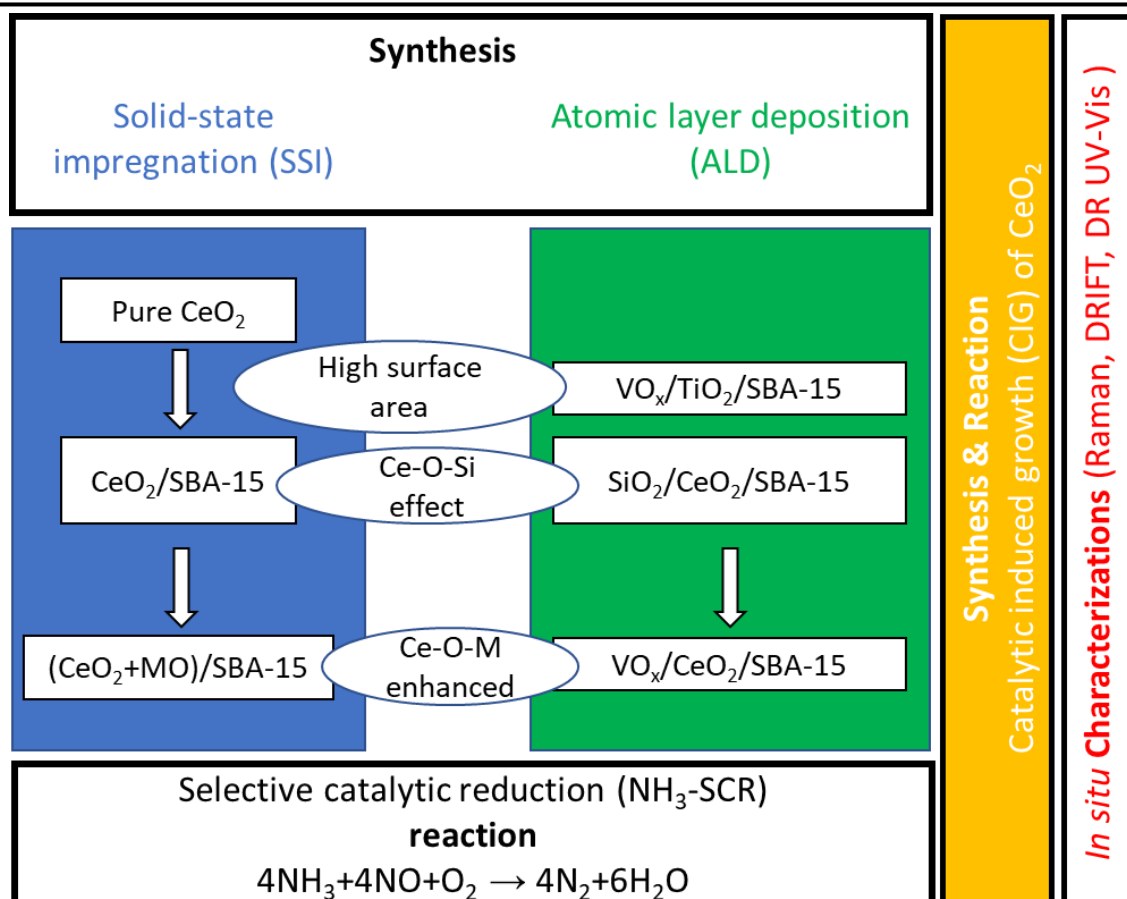
Figure 3. Schematic map of the research routes and the content of this thesis.

(1) Considering the low surface area of ceria, mesoporous SBA-15 was used as support to achieve a high surface area by dispersing the ceria on SBA-15. Various spectroscopies were performed for the synthesis process to get insight into the dispersion of ceria and the role of template P123. Then the prepared CeO_2/SBA-15 was applied for the NH_3-SCR to explore the reaction mechanism by *in situ* DRIFT spectroscopy. As a plugin, pure CeO_2 was prepared for NH_3-SCR application and *in situ* Raman spectroscopy was performed to investigate the role of surface oxygen species.

(2) Considering the rather poor catalytic performance of bare CeO_2 or CeO_2/SBA-15, at second metal component was added to achieve an enhanced NH_3-SCR reactivity. Firstly, $(CuO+CeO_2)$/SBA-15 was prepared for the possible SO_2-resistance of CuO and the synthesis process is investigated to make clear the loading mechanism of binary metal oxides on SBA-15 by SSI methods. Then (MnO_x+CeO_2)/SBA-15 was prepared to obtain sufficiently high $DeNO_x$ ability. At last, the reaction mechanism on (MnO_x+CeO_2)/SBA-15 was explored by *in situ* DRIFT spectroscopy.

(3) The ALD technique was adopted to prepare active oxides on porous SBA-15 obtaining a high surface area. In this case, the VO_x/TiO_2/SBA-15 was first prepared to explore the deposition of oxides on mesoporous supports. After that, CeO_2/SBA-15 (prepared by SSI methods) was adopted as the support and several atomic layers of SiO_2 were deposited yielding the "SiO_2/CeO_2/SiO_2" sandwich structure. The role of Ce-O-Si species on NH_3-SCR reactivity was studied by controllable adjustment. On the other hand, active VO_x was deposited on CeO_2/SBA-15 by the site-selective ALD (SSALD) method. In detail, the CeO_2/SBA-15 was pretreated in an experimental SCR atmosphere yielding various surface species and then the pretreated sample was coated with VO_x by ALD. DRIFT spectroscopy was adopted to depict the surface group changes of the pretreated and deposited samples.

(4) In the works above, the reaction during catalyst synthesis showed significant importance for the structure/property of prepared catalysts and further for the NH_3-SCR reactivity by both SSI and ALD techniques. In this case, the synthesis reaction was tried to be designed as the target SCR reaction, in other words, the metal oxide was formed (nucleation and growth) under the same atmosphere as the NH_3-SCR reaction, which was expected to own both high reactivity and stability. In detail, CeO_2/SBA-15 catalysts were prepared by calcination in various gas atmospheres, which was referred to as the catalytic induced growth (CIG) method. The prepared CeO_2/SBA-15 catalysts were further applied to the NH_3-SCR reaction and their catalytic performances are compared. At the end, the reason for the catalytic improvement was analyzed.

2. Background on the NH₃-SCR catalytic system

2.1. The NH₃-SCR technique

The technique of selective catalytic reduction of NO with NH_3 (NH_3-SCR) has been widely applied as an efficient post-combustion control to remove the NO_x gases.[18] The NH_3-SCR process, reducing toxic NO to harmless N_2 and H_2O, mainly contains the following reactions:[19]

$$4NO + 4NH_3 + O_2 \rightarrow 4N_2 + 6H_2O \qquad (1)$$

$$4NH_3 + 2NO + 2NO_2 \rightarrow 4N_2 + 6H_2O \qquad (2)$$
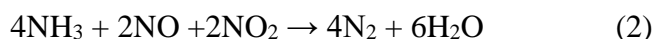
Reaction (1) is defined as a "Standard SCR" reaction, while reaction (2) is defined as a "Fast SCR" reaction as its reaction efficiency is at least 10 times faster than reaction (1) with the assistance of NO_2. Besides these, some undesirable side reactions also exist, such as:

$$4NH_3 + 7O_2 \rightarrow 4NO_2 + 6H_2O \qquad (3)$$

$$4NO + 4NH_3 + 3O_2 \rightarrow 4N_2O + 6H_2O \qquad (4)$$
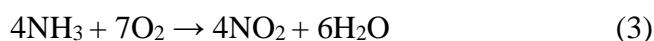
Due to the different reactivities of these reactions, the NO_x conversion and N_2 selectivity are used to evaluate the NH_3-SCR catalytic performance of a certain catalyst.

Catalysts for the NH_3-SCR reaction have been developed for decades, and as far as we know, the large amount of researched catalysts can be classified into three categories: noble metal catalysts, metal oxides catalysts, and zeolite catalysts.[19]

For noble metal catalysts, Pt, Pd, and Ag are used as active sites and supported on Al_2O_3, SiO_2, or TiO_2 to obtain typical catalysts in the early time.[20] The noble metal catalysts show good reactivity to react with NH_3 by H-abstraction. However, a too strong reductive results in the over-oxidation of NH_3, which wastes the NH_3 and decreases both the NO conversion and N_2 selectivity. Thus, the noble metal catalysts are only explored for H_2-SCR or CO-SCR reaction using H_2 or CO as the reductive agent. In addition, their processing cost is also quite high, which is not beneficial for large-scale applications, resulting in replacement by the following two types of catalysts.

Metal oxide catalysts mainly include oxides such as V_2O_5, TiO_2, CeO_2, MnO_2, CuO, and their composite oxides.[21, 22] On the basis of these active components, oxides promoters, and supports make additional effects. V_2O_5-WO_3(MoO_3)-TiO_2 is a present commercial catalyst applied in the treatment of coal-fire flue gas due its good reactivity and SO_2 resistance at 300-400 °C. However, there are several disadvantages for the commercial vanadia catalysts including the narrow operation temperature range at 300-400 °C, the toxicity of vanadia, low activity at low temperatures, and limited thermal stability at high temperatures, all of which limit the application of vanadia based catalysts.[22] To this end, CeO_2,

CuO, and MnO$_2$-based catalysts are focused on due to their high reactivity in a wide temperature window and environmentally friendly properties.

Zeolites are a class of aluminosilicates containing micropores (< 2 nm), which are described by the general formula M $^{n+}_{1/n}$ (AlO$_2$)$^-$ (SiO$_2$)$_x$·yH$_2$O (the M $^{n+}_{1/n}$ is either a metal ion or H$^+$) and which occur naturally but are also produced industrially on a large scale.[23] Since the first synthesis of ZSM-5 in the middle of the last century, different types of microporous molecular sieve catalysts rapidly caught attention of the research community,[24, 25] due to their unique pore structure and hydrothermal stability. According to the difference of skeleton structure and constituent elements, molecular sieves can be divided into many different types, such as Y-zeolite, ZSM series, and MFI. For NH$_3$-SCR application, the molecular sieve catalysts are mainly prepared by ion exchange with the metal elements, including Cu, Fe, Mn, Pd, Co, and Ce.[1] At present, Cu and Fe ions exchanged molecular sieve catalysts are being applied in practical engineering.[26] They show a high DeNO$_x$ performance and the active temperature range reaches usually as high as 600 °C, but the H$_2$O and SO$_2$ resistance of these catalysts needs to be further improved.[1]

2.2. Ceria-based catalyst for NH$_3$-SCR

As introduced above, commercial V$_2$O$_5$-WO$_3$(MoO$_3$)/TiO$_2$ is poisoned and not suitable for some special applications, for example, in low-temperature cement furnaces and diesel engines. Especially, Europe has discontinued the use of vanadium-based catalysts for these drawbacks.[27] Thus, many studies are focusing on searching for the gradual replacement of the V$_2$O$_5$-WO$_3$/TiO$_2$ catalyst by a non-vanadium catalyst.[27] Ceria is a promising catalytic material for NH$_3$-SCR due to its excellent redox properties,[28] high oxygen storage/release capacities,[29, 30] and good Ce^{3+}/Ce^{4+} transfer capacities (in Figure 4).[31]
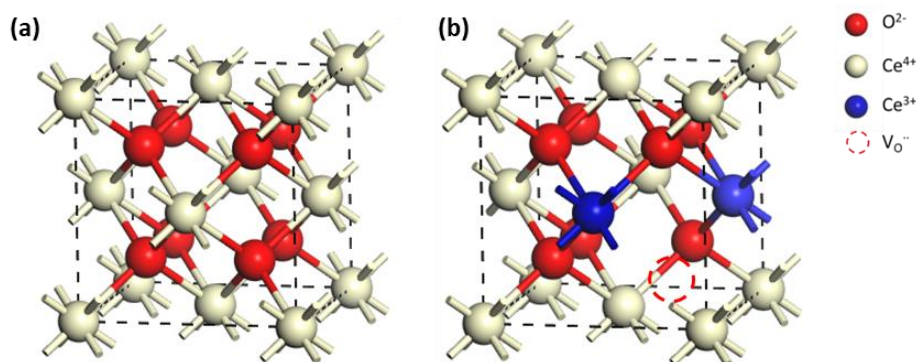

Figure 4. Cell structure of (a) the stoichiometric CeO$_2$, and (b) the non-stoichiometric CeO$_2$.

For NH$_3$-SCR applications, bare CeO$_2$ usually shows poor reactivity for NH$_3$-SCR. By choosing different cerium precursors for preparation, such as cerium sulfide,[32] and ceria nitride with pyrophosphoric,[33] the SCR activity was improved which was due to the increased acidity introduced by the acid ions. It implies that the poor SCR activity of pure CeO$_2$ was attributed to weak acidity. In the following text, ceria-based catalysts always mean the composite oxides including ceria as main components. According to the cerium sites or roles, they can be classified into three kinds, including usage as pure support/active component, for bulk doping, and for surface modification.[18]

When ceria is used as support for other active sites, it not only plays the role of dispersing active species but also enhances the activity through Ce-O-M interactions.[18] Fan et al. reported that CeO$_2$ as a dispersing auxiliary can inhibit the migration and aggregation of supported Cu-Mn oxides.[34] Xu et al. prepared MnO$_x$/CeO$_2$ and achieved superior catalytic performance for SCR of NO at low temperature which was attributed to the enhanced redox of active Mn ions by ceria.[35] Regarding the promotion of ceria, various catalysts were prepared by loading oxides from single metal oxide to bimetallic or even to trimetallic oxides systems.[36-38] In addition to the surface dispersed active species, the structure of ceria as a carrier constitutes another important factor that affects the final catalytic performance. The rapid development of materials science enables us to manufacture ceria with different structures. However, there are only few reports on exploring specially structured ceria as NH$_3$-SCR catalyst support. It should be noted that using bare ceria as the active component or support is helpful to study the structure-activity relationship of ceria-based catalysts in NH$_3$-SCR. However, from the perspective of activity improvement, the use of bare cerium dioxide as an active ingredient is not advocated. In the case of the introduction of foreign components, it is generally considered that sufficient contact between ceria and other components is required to obtain maximum activity. Taking this into account, the use of ceria as catalyst support does not seem to be advantageous.[37]

Compared with the supported catalysts by ceria, the ceria-based mixed oxides are dominated by mixtures of different metallic oxides, such as CeO$_2$-TiO$_2$, CeO$_2$-MnO$_x$, CeO$_2$-ZrO$_2$, CeO$_2$-CuO-TiO$_2$, etc. By mixing these oxides and aging at high temperatures, one obtains binary or multivariate solid solutions, spinel, perovskite oxides, or mixed oxides. In the composite oxide catalyst, one metal element can change the catalytic performance of another metal element, which is caused by the influence of electrons and structure. Li et al. studied the amorphous CeO$_2$-TiO$_2$ composite oxide SCR catalyst by means of XAFS and other characterization methods and determined the short-range ordered structure of Ce-O-Ti with atomic level interaction as the reaction active site of the catalyst.[39]

The third type of ceria-based catalyst is to load CeO$_2$ on other oxides supports. Oxides supports can be porous or nano-sized particles which could provide high surface areas, so that the loaded ceria can be

dispersed as smaller size crystals and form a separated active phase. The high surface area supports such as TiO_2, Al_2O_3, SiO_2, and carbon materials (active carbon and carbon nanotubes) are applied to ceria supporting low-temperature NH_3-SCR. Among them, SiO_2 was reported for its chemical inertia and availability. Especially, since the mesoporous SBA-15 was first introduced and synthesized at the end of the last century,[40] this kind of silicate support was widely used for the ceria loading and applied to the SCR reaction.[41] Based on this, adding other metal elements to form composite oxides on inert SBA-15 support is expected to further improve the catalytic activity.

2.3. Synthesis of SBA-15 and relevant mesoporous catalysts

Mesoporous materials have many excellent properties, such as high surface areas, large pore volumes, controllable pore sizes and shapes, and nanopores.[42] These features are particularly advantageous for applications in catalysis. Ordered mesoporous silica, M41S, was first reported in 1992. Afterwards, great progress has been made in morphology control, pore size adjustment, composition change, and application development.[43] In 1998, Zhao et al. proposed mesoporous (2-50 nm) SBA-15, and since then a large number of related support materials have been developed.[44] Compared with microporous material (< 2 nm), such as zeolite, the extended pore size of SBA-15 allows gas diffusion and mass transfer. Due to its large pore size (5-30 nm) and wall thickness (3.1-6.4 nm), its thermal and hydrothermal stability has been significantly improved, thus expanding the application range of mesoporous materials. Up to now, the research reports based on SBA-15 mesoporous materials have the highest number in the field of mesoporous materials.[45]
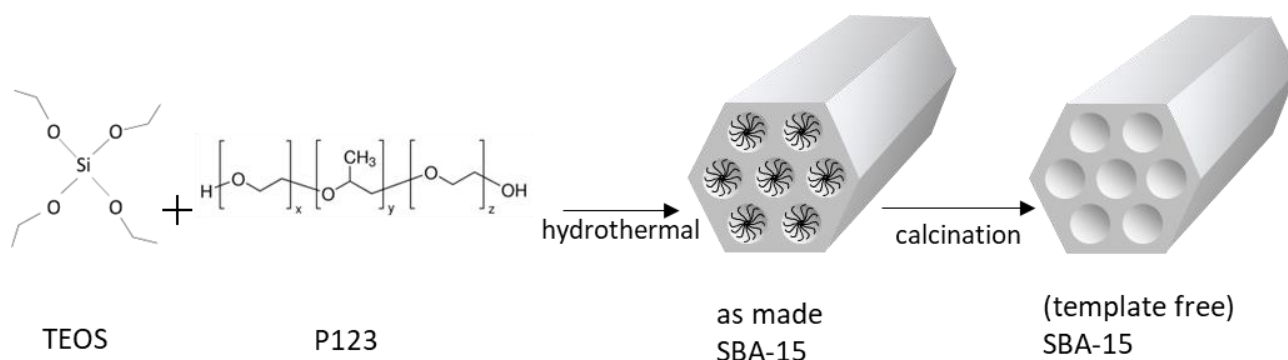

Figure 5. Synthesis of SBA-15 by the soft-templating method.

SBA-15 is synthesized in a cooperative self-assembly process with the use of a nonionic triblock copolymer consisting of ethylene oxide and propylene oxide units ($PEO_{20}POO_{70}PEO_{20}$) as template, also known as Pluronic P123, and tetraethoxysilane (TEOS) as silica source, which results in a 2-D array

with long 1-D channels. The propylene oxide unit forms the hydrophobic part while ethylene oxide units form the hydrophilic part, as shown in Figure 5.

Pure silica-based mesoporous materials have many limitations. Their catalytic activities for major reactions are quite low. And the low mechanical and hydrothermal stability of amorphous silica walls may cause problems in catalytic applications. Therefore, functionalization is needed to form metal anchored active sites. Generally, there are three strategies for the synthesis of active mesoporous catalysts.[45] The first strategy is noted as 'pre-synthesis' which is mixing the template P123 and silicon precursor TEOS as the solution phase and adding the active metal precursor into the solution followed by hydrothermal and calcination steps. The advantage of this method is that the metal element, as well as its oxides, are dispersed well on the support. But the doping of various valences of metal into the silicate framework breaks the ordered hexagonal array of pores structure, especially at high-temperature calcination, which leads to the loss of unique properties of SBA-15. The second strategy noted as 'post-synthesis' is preparing the SBA-15 first and then loading the active metal oxides on the SBA-15 by a mixture of SBA-15 with metal precursors in a solid state. In this method, the solvent-free technique is easy to operate, cheap, and environmentally friendly, which shows promising industrial application. However, this method is facing the dispersion problem of the competition between the immigrant of metal ions into the pore channels and the growth of metal oxides. Recently, a third strategy has been put forward as 'med-synthesis' which is like the post-synthesis process but replaces the SBA-15 by "as made SBA-15", thus the template P123 is not removed when mixing the SBA-15 support and active metal precursors. It is proved that the 'med-synthesis' owns both the advantages of the good dispersion of metal species and the ordered and stable mesoporous structures. The three strategies of loading active metal oxides on SBA-15 are schematically shown in Figure 6.
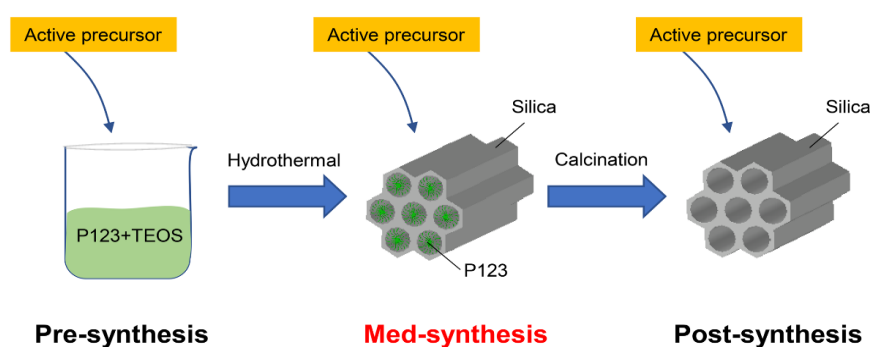

Figure 6. Synthesis approaches for mesoporous silicate materials (e.g. SBA-15) modified by the addition of an active component at different stages.

2.4. Reaction mechanism of NH$_3$-SCR

Getting insight into the reaction mechanism is helpful to guide the design of highly efficient SCR catalysts. In general, the NH$_3$-SCR mechanism contains two cycles: acid adsorption and redox reaction,[1, 18, 46, 47] as shown in Figure 7.
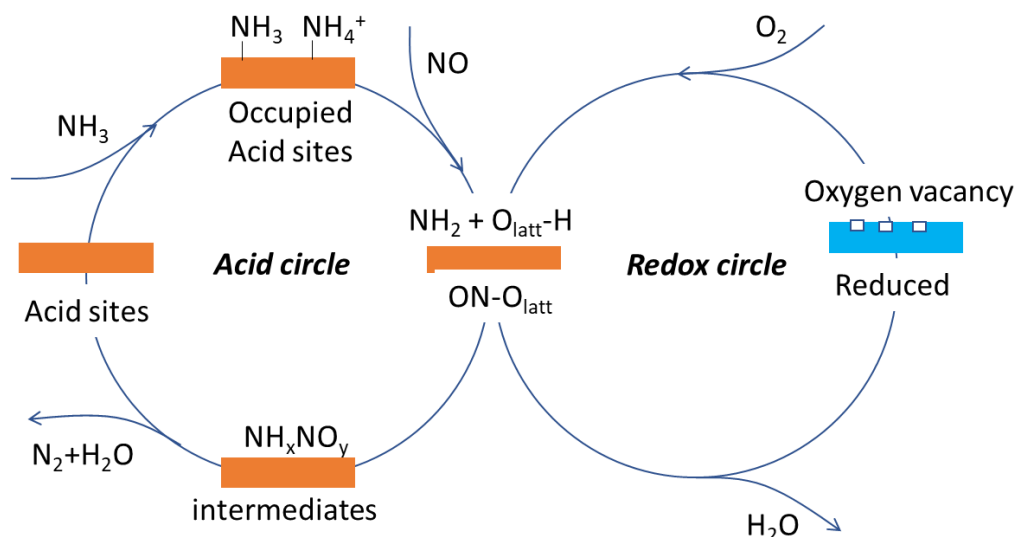
Figure 7. General NH$_3$-SCR reaction mechanism over metal oxide catalysts.

From a general point of view, the reaction mechanism involves three main points to be clarified. The first point refers to reaction route the SCR follows: a L-H (Langmuir-Hinshelwood) or an E-R (Eley-Rideal) mechanism? For the L-H route, the NH$_3$ is adsorbed on surface and reacts with adjunct adsorbed NO species, while for the E-R route, the adsorbed NH$_3$ reacts with gaseous NO. The second point refers the active sites for NH$_3$ adsorption: Lewis acid sites (L acid sites) or Bronsted acid sites (B acid sites)? No matter whether the reaction follows the E-R or L-H route, the initial step must be the adsorption of ammonia on the catalyst sites. Thus, it is important to make clear which sites are active for the effective adsorption of NH$_3$ that further reacts with adsorbed or gaseous NO molecules. The third point refers to the intermediate products which are related to the reaction route and NH$_3$ adsorption. However, based on the literature, the reaction mechanisms of NH$_3$-SCR remain controversial for diverse catalyst systems. Different catalyst systems have disparate redox and acidic capacities, which form various active intermediates that predominantly affect the pathway and reaction efficiency.

For the common VO$_x$ based catalysts, VO$_x$ is considered as the active site. Firstly, the sites for reactants adsorption (L vs B acid sites) have been a matter of debate. In brief, L acid sites were related to V=O and B acid sites to V-OH species. Earlier, Topsoe et al. had proposed B acid sites to be the

catalytically active sites as they detected a dominant amount of NH_4^+ adsorbed onto V-OH surface sites.[46, 48] On the other hand, Ramis et al. found NH_3 adsorbed on V=O sites to be thermally more stable than NH_4^+, implying that L acid sites were the dominant adsorption sites under reaction conditions [49], More recently, Marberger et al. supported the idea of Lewis acid sites being the active intermediate by observing a faster consumption of NH_3 adsorbed at L acid sites compared to NH_4^+ adsorbed at B acid sites.[50, 51] Zhu et al. objected to the standpoint of Lewis acid sites as active sites by concluding that minority L sites (V^{5+}=O) exhibited higher activity (TOF), while the more abundant B sites (V^{5+}-OH) dominated the overall reaction.[52] Thus, still no consensus has been reached regarding the role of L and B acid sites. Secondly, the redox reaction step has been related to the reactivity and connected to the VO_x surface structures. The use of *in situ* electron paramagnetic resonance (EPR) and X-ray absorption spectroscopy (XAS) under reaction conditions has revealed the reducing/re-oxidizing processes to be accompanied by changes of the vanadium valence and VO_x surface structure [53, 54]. Feng et al. reported VO_x with polymeric structure to be redox-active and provided an atomic view of the change of the VO_x structure with the redox state.[55, 56] Consistently, DFT results showed that formation of both oxidized and reduced VO_x, i.e., V^{5+} and V^{4+}, kept the vanadyl bond intact for isolated VO_x on TiO_2, as verified by *in situ* EPR data for VO_x/TiO_2 exposed to ammonia.[57] All these results have revealed that the redox reactivity of VO_x species is structure sensitive. Finally, the interaction between H_2O and surface VO_x sites was also explored. According to DFT calculations by Avdeev et al., adsorbed water changes the VO_x molecular configuration by spontaneous dissociation and formation of surface V-OH groups [58, 59]. Importantly, lattice oxygen of surface VO_x species was shown to originate from adsorbed water rather than gas-phase oxygen.[59] Oxygen-18 isotope labeling studies have revealed that both terminal V=O and bridging V-O-V bonds readily exchange oxygen with water vapor.[60]

In ceria-based catalysts, ceria can play different roles (active component, promotor, or supporter) depending on the state of ceria. Thus, the SCR reaction mechanism on ceria-containing catalysts is debatable and no consensus has been reached yet.

Bare ceria was proved to be the ideal catalyst to explore the role of cerium oxide acting as active component for the NH_3-SCR reaction. Guo et al. used different cerium precursors to prepare bare ceria catalysts by direct calcination at different temperatures and applied them for NH_3-SCR. It was reported that the performance of CeO_2 might be related to its surface area, redox ability, NH_3 adsorption capacity, amount of surface Ce^{3+}, and active oxygen.[61] Zhang et al. reported a simply pretreated bare CeO_2 by calcination in Argon atmosphere with increased surface oxygen vacancies showing enhanced SCR reactivity. Based on this result, it was concluded that oxygen vacancies accelerated the acidity and the redox cycle during the NH_3-SCR reaction, increasing the adsorption and promoting the activation of

NH_3 and NO, facilitating the restoration of Ce^{4+} from Ce^{3+} by adsorbed oxygen, and subsequently improving the NH_3-SCR catalytic performance.[62]

Considering the poor catalytic performance of bare CeO_2,[27] it is necessary to add additional active components to achieve synergistic effect. Therefore, there are new requirements for the research of the NH_3-SCR mechanism on composite oxide catalysts. WO_3-CeO_2-TiO_2 catalysts show high activity in a broad temperature range of 200-480 ^oC, which may be related to the synergistic effect between CeO_x and WO_x in the catalysts, including activation of oxygen and increase of both the Bronsted and Lewis acid sites.[63] It also found that the $Ce_{0.6}Zr_{0.4}O_2$ catalyst shows better NH_3-SCR activity and SO_2 resistance than the bare ceria due to the presence of more acid sites and reactions proceeding via the E-R mechanism.[64] $CeVO_4$ was prepared by adding ceria to V_2O_5/TiO_2, presenting stable Bronsted acid sites for NH_3 adsorption and moderate redox sites for NH_3 activation rather than polymeric VO_x for the V-based catalyst, which effectively suppressed the formation of N_2O and hence improved its high-temperature N_2 selectivity.[65] Even for inert elements, synergistic effects exist improving the NH_3-SCR reactivity or SO_2 resistance. An innovative CeO_2-SiO_2 mixed oxide catalyst was prepared with strong interaction between Ce and Si (Ce-O-Si) and the abundant surface hydroxyl groups.[66] The NH_3-SCR performance of CeO_2-SiO_2 was promoted by an enhanced Eley-Rideal (E-R) mechanism, by which gaseous NO could directly react with adsorbed NH_3. Thus, for composite oxide catalysts, it is important to make clear the mechanism and then provide a reaction mechanism-enhanced strategy to develop an environmentally friendly NH_3-SCR catalyst with superior SO_2 resistance.

2.5. Identification of IR vibrations related to the NH_3-SCR reaction

In order to find effective $DeNO_x$ catalyst, it is necessary to understand the mechanisms of the NH_3-SCR reaction in detail. A very powerful technique for this purpose is DRIFT spectroscopy, which provides direct information about the surface species during the reaction based on their vibrational signature. For the NH_3-SCR reaction, many different gas molecules and corresponding adsorbed species are involved, which makes it even more important to identify these species based on their IR signals.

Regarding the NH_3 gas, it is adsorbed on acid sites, including Lewis and Bronsted acid sites. The assignments of various IR bands resulting from to NH_3 - CeO_2 species are shown in Table 1. Generally, a band at above 3500 cm^{-1} is assigned to O-H stretching, whereas N-H stretch vibrations appear at about 3100-3400 cm^{-1}. Bending modes of NH_3 on L acid sites are located at about 1200 and 1600 cm^{-1}, while those for NH_4^+-B acid sites are located at about 1450 and 1650 cm^{-1}. The intermediate species NH_2 is characterized by a feature at about 1500-1550 cm^{-1}.

Table 1. Literature assignments of IR bands related to NH$_3$-ceria species.

Substrate	Wavenumber [cm^{-1}]						
	L-acid-site		B-acid site	NH$_2$	H$_2$O	OH	
CeO$_2$ cube	1289 1603		1407 1468 1775				[67]
Sulfated CeO$_2$	1273-1296 1678-1681		1435-1440 1485-1492				[67]
HSiW/CeO$_2$	1196, 1592		1420, 1663				[68]
Sulfated CeO$_2$			1431, 1323	1160	1628		[69]
CeO$_2$-MnO$_x$	1626, 1040-1200	3334	1692, 1642, 1458				[70]
VO$_x$/CeO$_2$	1127	3384, 3263, 3173	1436				[71]
CeO$_x$	1594, 1184						[72]
CeO$_2$/Ti-Zr-S	1251, 1685	3356, 3248, 3152	1438, 1665	1300, 1323		3674	[73]
Ce-Fe oxide	1181, 1361	3100-3400	1380, 1692	1559, 2348		3674	[74]
CeO$_2$-TiO$_2$	1591, 1299, 1148	3371, 3280	1461, 1421	1534, 1522, 1265		3680	[75]
CeO$_2$-TiO$_2$	1603		1670 1440	1550		3600-3740	[76]
CeZrO	1601, 1336, 1273	3346, 3271, 3404, 3276	1684, 1427, 1448	3107, 2700			[77]

Another important type of adsorbed species originates from the interaction between NO$_x$ and ceria-based catalysts. The differently structured NO$_x$ species, especially the NO$_3^-$ species, exhibit distinct activity. Table 2 summarizes literature assignments of surface NO$_x$ species resulting from the interaction of NO+O$_2$ with oxide catalysts. Generally, bands within 1500-1600 cm^{-1} are assigned to nitrate species. In detail, features in the 1500-1540 cm^{-1} range have been attributed to monodentate nitrate, those in the 1540-1580 cm^{-1} range to bidentate nitrate, and those in the 1580-1600 cm^{-1} range to bridging nitrate.

Table 2. Literature assignments of IR bands related to NO_x-ceria species.

	nitrate			nitrite	NO_2	
	monodentate	bidentate	bridging	monodentate		
CeO_2	1250, 1165, 1200, 1240, 1294		1597, 1552, 1545, 1589, 1563	1403, 1498, 1373, 1357, 1460, 1396	1615-1620	[67]
CeO_2-nanocube		1550, 1215	1255	1525		[78]
CeO_2-nanopolyhydrons		1347		1541, 1358		[78]
CeO_2	1547, 1356	1561, 1528, 1274, 1216	1600			[69]
CeO_2-MnO_x		1513				[70]
VO_x/CeO_2	1559	1577	1607		1636	[71]
CeO_x		1574		1253	1606	[72]
CeO_2/Ti-Zr-S	1286	1572, 1517	1211		1620	[73]
Ce-Fe oxide	1393	1623,1535	1238, 1235			[74]
CeO_2-TiO_2	1297, 1280	1560, 1535,	1601, 1244	1613		[75]
CeO_2-TiO_2	1530 1290	1571, 1550,	1240		1620	[76]

3. Fundamentals and experimental

3.1. Chemicals, gases, and instruments

The main chemical reagents used for catalyst preparation and performance tests are listed in Table 3, the gases used in the experiments are listed in Table 4, and the instruments and equipment used for catalyst preparation, characterization and reactivity tests are listed in Table 5.

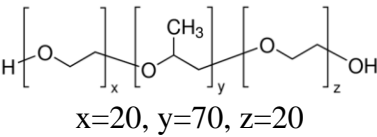Table 3. List of chemicals used in this thesis.

Name	Chemical formula	Specification	Manufacturer
Pluronic P123	x=20, y=70, z=20	Analytical pure	Aldrich Sigma
Tetraethylorthosilicate (TEOS)	$Si(OEt)_4$	>99 %	Aldrich Sigma
Titanium tetrachloride	$TiCl_4$	>99 %	Aldrich Sigma
Silicon tetrachloride	$SiCl_4$	>99 %	Aldrich Sigma
Vanadium oxychloride	$VOCl_3$	>99 %	Aldrich Sigma
Pyridine	C_5H_5N	99.8 %	Aldrich Sigma
Cerium nitrate hexahydrate	$Ce(NO_3)_3 \cdot 6H_2O$	99 %	Aldrich Sigma
Copper nitrate trihydrate	$Cu(NO_3)_2 \cdot 3H_2O$	99 %	Aldrich Sigma
Manganese nitrate tetrahydrate	$Mn(NO_3)_2 \cdot 4H_2O$	> 97 %	Aldrich Sigma
Nickel nitrate hexahydrate	$Ni(NO_3)_2 \cdot 6H_2O$	99.999 %	Aldrich Sigma
Magnesium nitrate hexahydrate	$Mg(NO_3)_2 \cdot 6H_2O$	99 %	Aldrich Sigma
Lanthanum nitrate hexahydrate	$La(NO_3)_3 \cdot 6H_2O$	99.999 %	Aldrich Sigma
Magnesium oxide	MgO	> 99.99 %	Aldrich Sigma

Table 4. List of gases used in this thesis.

Name	Chemical formula	Specification	Manufacturer
Nitrogen	N_2	$\geq 99.999\%$	Westfalen
Oxygen	O_2	$\geq 99.999\%$	Westfalen
Nitrogen monoxide / Nitrogen	NO / N_2	2000 ppm $\pm$ 0.25% abs.	Air Liquide
Ammonia / Nitrogen	NH_3 / N_2	2000 ppm $\pm$ 0.25% abs.	Air Liquide
Sulfur dioxide / Nitrogen	SO_2 / N_2	1000 ppm	Air Liquide

Table 5. Instruments and equipment used in this thesis.

Name	Equipment model	Manufacturer
Raman spectrometer	Argon ion laser (514 nm)	Melles Griot Inc.
	Nd:YAG laser (532 nm)	Cobolt Inc.
Gas-phase FTIR spectrometer	Tensor-27	Bruker
DRIFT spectrometer	Vertex	Bruker
Gas adsorption analysis	NOVA 3000e	Quantachrome
X-ray powder diffractometer	StadiP	Stoe & Cie GmbH
DR UV-Vis spectrometer	V-770	Jasco
X-ray photoelectron spectrometer	SSX 100 ECSA	Surface Science Laboratories Inc.
Transmission electron microscope	JEOL JEM-2100F	Akishimashi
Reactor cell I	CRA-1000	Linkam
Reactor cell II	DRP-ASC	Harrick

3.2. Characterization methods

The structure and physical properties of the samples were characterized by X-ray diffraction (XRD), nitrogen adsorption-desorption measurements, Transmission electron microscopy (TEM), and X-ray photoelectron spectra (XPS).

XRD. X-ray diffraction experiments were carried out in transmission geometry on an X-ray powder diffractometer (StadiP, Stoe & Cie GmbH) with a Mythen 1K (Dectris) detector. For the measurements, Cu Kα1 radiation (λ = 1.540598 Å) and a Ge[111] monochromator were used.

N$_2$ adsorption isotherm. Nitrogen adsorption-desorption measurements were carried out on a NOVA 3000e (Quantachrome) to determine the surface area and pore size of the mesoporous samples. The Brunauer-Emmett-Teller (BET) method was employed to calculate the specific surface area, and nonlocal density functional theory (NLDFT) was used to calculate the adsorption branch to obtain the porosity characteristics.

TEM. TEM measurements were performed with a JEOL JEM-2100F (JEOL, Akishimashi, Tokyo, Japan) equipped with a FEG, operating at 200kV. ED spectra and mappings were recorded using an Oxford XMax 80 silicon drift detector (Oxford Instruments plc, Tubney Woods, Abingdon, U.K.). TEM grids were prepared by dispersing a small amount of sample in 2ml Ethanol with an ultrasonic bath. 3-4 droplets of the suspension were applied on a carbon coated gold grid (Plano GmbH, Wetzlar, Germany) and allowed to dry. The charged grids were lightly carbon coated to avoid charging under the electron beam.

XPS. X-ray photoelectron spectra were recorded on an SSX 100 ECSA spectrometer (Surface Science Laboratories Inc., Minneapolis, MN, USA), equipped with a monochromatic Al-Kα X-ray source (1486.6 eV), in constant analyzer energy (CAE) mode at a 36° detection angle with 0.1 eV resolution. The C 1s peak of ubiquitous carbon (284.9 eV) was used to correct the binding energies. Data analysis included subtraction of a Shirley background and a peak-fit analysis using Gaussian−Lorentzian product functions with 45% Lorentzian share. The degree of reduction of ceria was determined based on the ratio $Ce^{3+}/(Ce^{3+}+Ce^{4+})$ using the sum of integrated peaks for Ce^{3+} and Ce^{4+}, respectively.

To analyse the formation of ceria during the calcination process, thermogravimetric analysis (TGA) and *in situ* spectroscopies were applied.

Thermogravimetric analysis (TGA). TGA was performed on a TGA/SDTA851-e (Mettler Toledo). In order to record TGA curves, samples were exposed to a flow of synthetic air or pure N$_2$ gas (100 ml/min) while being heated from room temperature to 500 °C at a rate of 1.5 °C/min.

Samples were then calcined at 500 °C for 5 h. At the same time, derivative thermogravimetry (DTG) profiles were obtained.

Gas-phase Fourier transform infrared (FTIR) spectroscopy. FTIR spectroscopy was performed on a Bruker Tensor 27 equipped with a DLaTGS (deuterated and L-alanine-doped triglycine sulfate) detector, and a low volume gas cell (25 ml, 0.5 m path-length, Axiom). The gas cell was heated to 120 °C to avoid the condensation of water produced by the catalytic reaction. IR spectra were continuously recorded every minute with a resolution of 4 cm^{-1}. The backgrounds used for the analysis were recorded under pure nitrogen gas at room temperature. For online IR gas-phase detection, the Tensor was connected to the SCR reactor (commercial CCR1000 catalyst cell, Linkam Scientific Instruments). The gas-phase concentrations were determined based on a set of calibration curves.

Diffuse reflectance (DR) UV-Vis spectroscopy. DR UV-Vis spectra were recorded on a Jasco V-770 UV-Visible/NIR spectrometer with a praying mantis mirror cell and a high-temperature reaction chamber (Harrick Scientific Products Inc.). Halogen and deuterium light sources were adopted to transmit wavelengths in the visible and ultra-violet, respectively, and a Peltier-cooled PbS detector was employed. Spectra were recorded from 800 to 200 nm with a spectral resolution of 0.5 nm. MgO was used as the white standard.

Raman spectroscopy. Raman spectra were recorded in a backscattering geometry. For excitation, an argon ion laser (514.5 nm, Melles Griot) or a Nd:YAG laser (532 nm, Cobolt Inc., Germany) was employed and for collection of the backscattered light a transmission spectrometer (Kaiser Optical) equipped with a charge-coupled device (CCD) detector was employed. The spectrometer was calibrated using the emission lines of a standard argon lamp. The resolution of the spectrometer was 5 cm^{-1} and the wavelength stability was better than 0.5 cm^{-1}. The laser power was set to 2.5 mW and measured by a power meter (Ophir). The Raman features were fitted by Voigt functions using a Gaussian linewidth of 6 cm^{-1} to account for the instrumental broadening.

Diffuse reflectance infrared Fourier transform spectroscopy (DRIFTS). DRIFT spectra were recorded on a Vertex 70 (Bruker) equipped with a liquid N_2 cooled mercury cadmium telluride (MCT) detector and a commercial Harrick cell. As a background standard, KBr powder was used. The spectral resolution of DRIFTS was 1 cm^{-1}, the temporal resolution was 60 s. *In situ* DRIFT spectroscopy was combined with gas-phase analysis, by analyzing the gas phase at the outlet of the *in situ* cell by gas-phase FTIR spectroscopy (see above).

3.3. Synthesis methods

Metal oxides (e.g. CeO_2 based) are effective catalysts for NH_3-SCR of NO. The reactivity is proportional to the number of active sites on the surface. Thus, a smaller size (nano size) is beneficial for the metal oxides to achieve high specific surface area. On the other hand, the high operation temperature can sinter the tiny oxides together which decreases the catalytic performance with increasing catalytic time. SBA-15 is used as support with high surface area and inert silicate substrate to stabilize the ceria-based oxides. In order to disperse the oxides on the mesoporous SBA-15, two synthesis methods are adopted, i.e. solid state impregnation (SSI) and atomic layer deposition (ALD).

Solid state impregnation. For the solid state impregnation (SSI) method, the precursors of the active metal oxides are mixed with the mesoporous support directly followed by calcination to remove the ligands and obtain the oxides dispersed on the support. Different from the conventional wetness impregnation method, the SSI method is solvent free which makes the technique environmentally friendly and easy to operate. Scheme 1 shows an example of the general process of the SSI method for preparing CeO_2@SBA-15 using the cerium precursor $Ce(NO_3)_3 \cdot 6H_2O$. The cerium nitrate powder and SBA-15 are mixed according to the weight proportion and grand in a mortar for 30 mins. After that, the obtained mixture is calcined in a furnace with a specific temperature program.
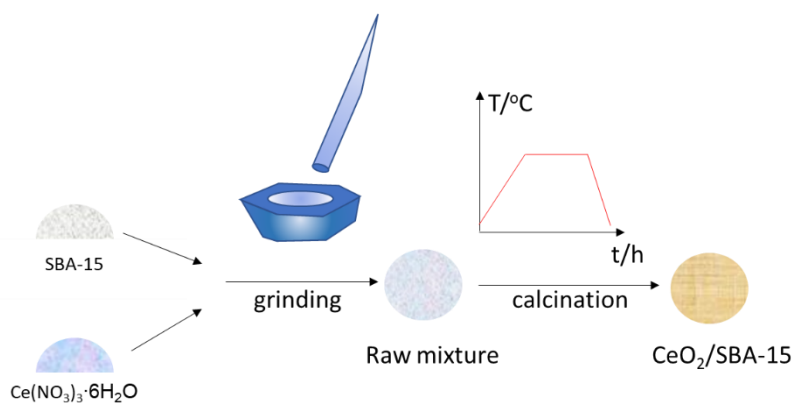
Scheme 1. General process of the SSI method for preparing CeO_2@SBA-15 using the cerium precursor $Ce(NO_3)_3 \cdot 6H_2O$.

Atomic layer deposition. Atomic layer deposition (ALD), also known as atomic layer epitaxy (ALE), is a chemical vapor deposition technology based on ordered, surface self-limiting reactions. ALD technology originated in the 1960s- 1970s. It was first reported by former Soviet scientists Aleskovskii and Koltsov.[79] Then based on the demand for high-quality ZnS:Mn thin film materials for

electroluminescent thin-film flat-panel displays, it was developed and improved by Suntalo from Finland. However, due to its complex surface chemical processes and other factors, ALD technology did not achieve great development at the beginning. In the 1990s, with the rise of the semiconductor industry, the requirements for the size and integration of various components and parts became higher and higher, and ALD technology ushered in the golden stage of development. In the 21st century, with the successful development of commercial ALD instruments to meet various preparation needs, ALD technology has attracted more and more attention in both basic research and practical applications.[79]

Typically, ALD refers to a process of forming thin films by feeding alternating pulses of gas-phase precursors into the reaction chamber followed by gas-solid chemical reactions on the surface of the deposited substrate. Figure 8 shows the process which includes four steps in more detail: (i) Feed of precursor MB pulse for adsorption reaction on the surface with an initial group (such as -AC); (ii) Use of inert gas (N_2 or Ar) to purge excess reactants and by-products; (iii) Feed of precursor AC pulse (which always acts as an oxidant) for adsorption reaction with adsorbed -B; (iv) Use of inert gas to purge excess reactants and by-products.

$$-AC + MB_3 \rightarrow -AMB_2 + BC \tag{3-1}$$

$$(-AM)-B + AC_2 \rightarrow (-AM)-AC + BC \tag{3-2}$$

where M is the metal element for coating, B the coordinated ligand, AC is the oxidant with A is oxygen when metal oxide AM is wanted. These steps are then repeated to realize the film layer by layer growth on the substrate surface.
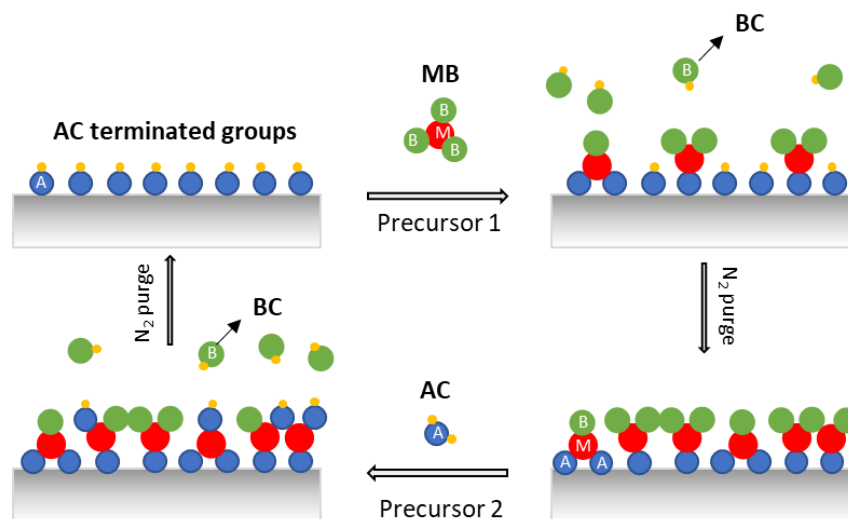

Figure 8. Schematical diagram of the ALD procedure.

Here, the ALD technology is adopted to deposit oxide SiO_2, Al_2O_3, TiO_2, and VO_x using as precursors $SiCl_4$ (+pyridine), $Al(CH_3)_3$, $TiCl_4$, and $VOCl_3$, respectively. H_2O is adopted as an oxidizing agent. In Figure 9, the ALD system used in this thesis is presented. The powder samples are loaded in a customized opened container with filters. The feed system and reactor can be heated by thermal controllers (red lines).
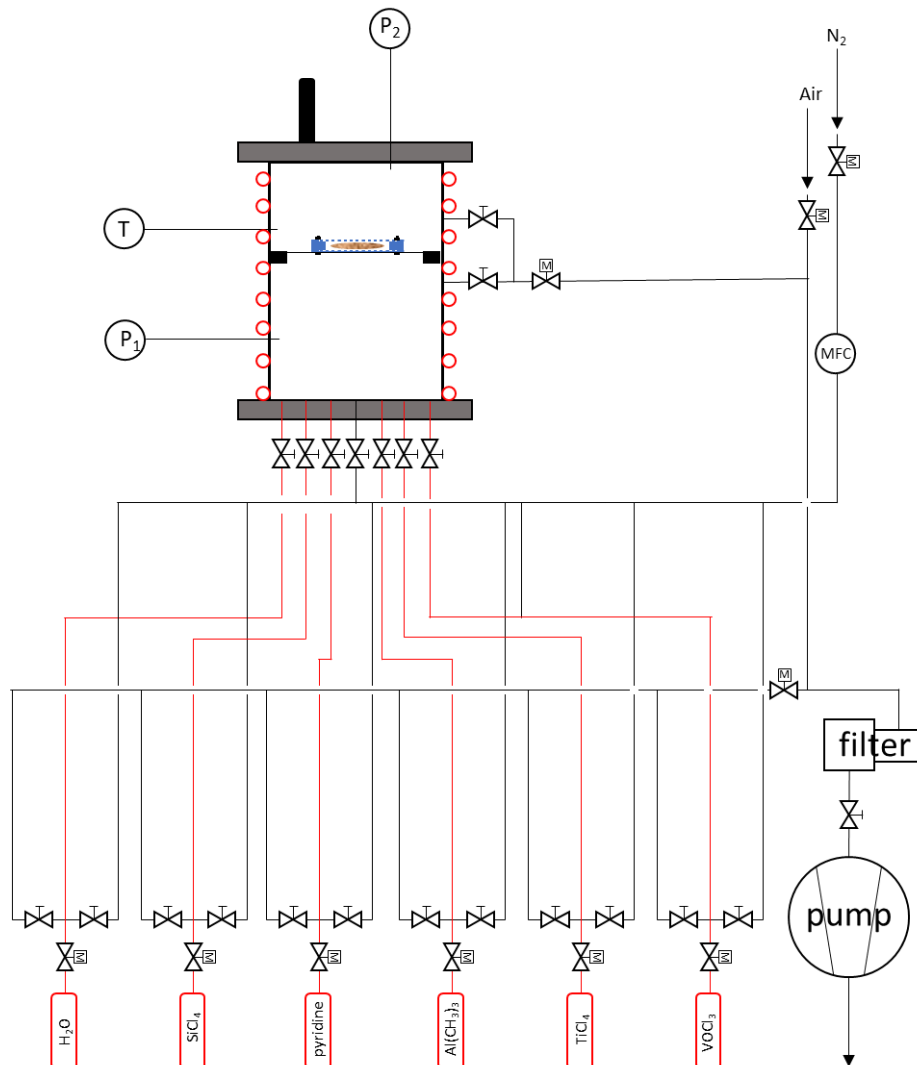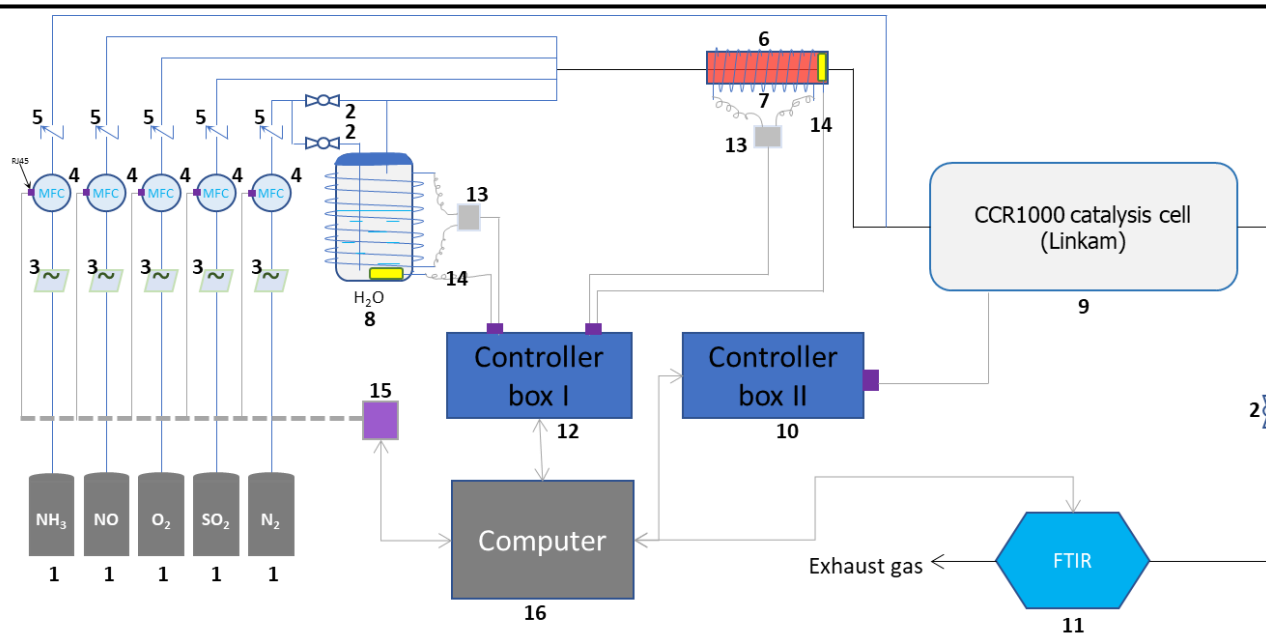

Figure 9. Customized ALD instrument used in this thesis.

3.4. NH$_3$-SCR reaction system

The NH$_3$-SCR reaction was studied by using the reaction platform shown schematically in Figure 10 which was developed within this thesis.

1. Gas bottle; 2. Ball valve; 3. Filter; 4. Mass flow controller; 5. Back pressure valve; 6. Mixing reactor; 7. Gas preheater; 8. Steam generator; 9. Catalysis cell; 10. Controller box for catalysis cell; 11. FTIR gas analyzer; 12. Controller box for heater band; 13 Heater band; 14. Thermocouple; 15. RJ45 hub; 16. Computer.

Figure 10. Schematic diagram of the NH$_3$-SCR reaction system.

Several points should be noted here. Firstly, the exhausted gas is detected by gas phase FTIR. Different from the specifically integrated detector for NH$_3$-SCR, from which the gas component values can be obtained directly, the FTIR is advantageous in recording all the possible gas products except for the IR-inactive N$_2$. In order to quantitatively determine the amount of the exhausted components, suitable IR signals are chosen and via calibration the relation between IR intensity and gas component concentration is evaluated, which is shown in the next section.

Secondly, the NH$_3$-SCR reaction is examined by using a Linkam cell. Regarding the *in situ* spectroscopy work, both a Linkam cell and a Harrick cell were used, which will be specified when discussing the results.

In general, the NH$_3$-SCR catalytic performance, including the NO$_x$ conversion and N$_2$ selectivity, is conducted by putting a certain amount of catalyst into the fixed bed cell and feeding the experimental gas at a certain temperature with a known inlet gas composition and detected outlet exhausted composition. In detail, firstly, the catalyst is dehydrated at 550 $^{\circ}$C and N$_2$+ 20 vol.% O$_2$ for 1 h. Afterwards the typical SCR reaction gas is fed into the cell chamber as 500 ppm NH$_3$, 500 ppm NO, 5 vol.% O$_2$ and balanced with N$_2$. When considering the effect of vapor and sulfur, 5 vol. % H$_2$O and 200 ppm SO$_2$ are added in the typical SCR inlet gas and balanced with N$_2$. The gas flow is set as 50 mL/min and the corresponding gas hour space velocity (GHSV) is about 60000 h^{-1} unless noted otherwise.

Considering the deadtime of the gas transport in the pipe and the reaction time for reaching a stable equilibrium, 20 mins (or 30 mins) are adopted for each reaction condition.

The catalytic performances are evaluated as below,

$$\text{NO conversion} = \frac{[\text{NO}]_{in} - [\text{NO}]_{out}}{[\text{NO}]_{in}} \times 100\% \tag{3-3}$$

$$\text{NO}_x \text{ conversion} = \frac{[\text{NO}_x]_{in} - [\text{NO}_x]_{out}}{[\text{NO}_x]_{in}} \times 100\% \tag{3-4}$$

$$\text{N}_2 \text{ selectivity} = \frac{[\text{N}_2]_{out}}{[\text{N}_2]_{out} + [\text{N}_2\text{O}]_{out}} \times 100\% \tag{3-5}$$

where the subscripts in and out indicate the inlet and outlet flows of the reactor, respectively.

3.5. Temperature calibration

Temperature is an important factor affecting the NH$_3$-SCR behavior as well as the reaction mechanism. Typically, the NH$_3$-SCR reaction is ought to be tested in a temperature range from low temperature (about 150 $^{\circ}$C) to high temperature (about 450 $^{\circ}$C). Thus, accurately anchoring the tested temperature is the foundation for the understanding of NH$_3$-SCR reaction especially at low temperature. Here, two reactor cells are adopted, the Linkam cell and the Harrick cell, which are each calibrated.

For the temperature calibration of the reactor, it should be noted that the temperature in the cell space is not even for the side heating mode. In this case, the calibration point is fixed in the center and near the upper surface of sample (see Figure 11). Although it is typically lower than the wall side temperature which would result in a higher apparent temperature, the surface region acts as an important role in the *in situ* spectroscopy characterization which is sensitive to the temperature. In addition, during the calibration, the cell is opened (the glass window is removed) and the convective heat transfer makes great effect on the detected temperatures. Therefore, the SBA-15 is used as a filler above to simulate an closed atmosphere.

Figure 11. Scheme of the temperature calibration setup.
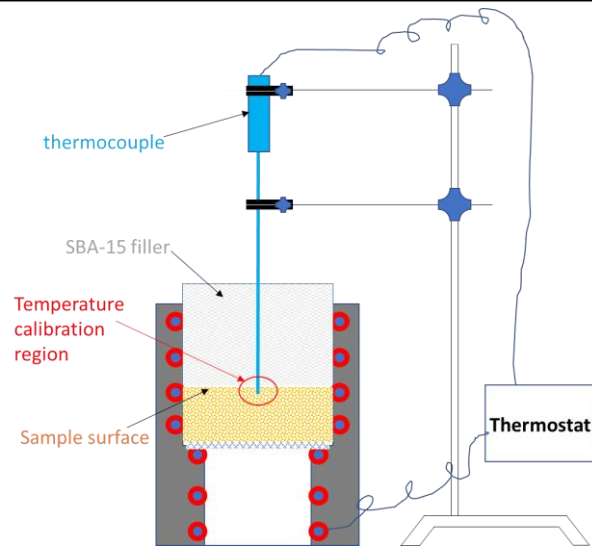
The temperature calibration results are recorded and subjected to a least square fit analysis yielding a relation between the actual temperature (T_{act}) and the apparent temperature (T_{app}), as shown in Figure 12. In the following, all temperatures given refer to actual temperatures.
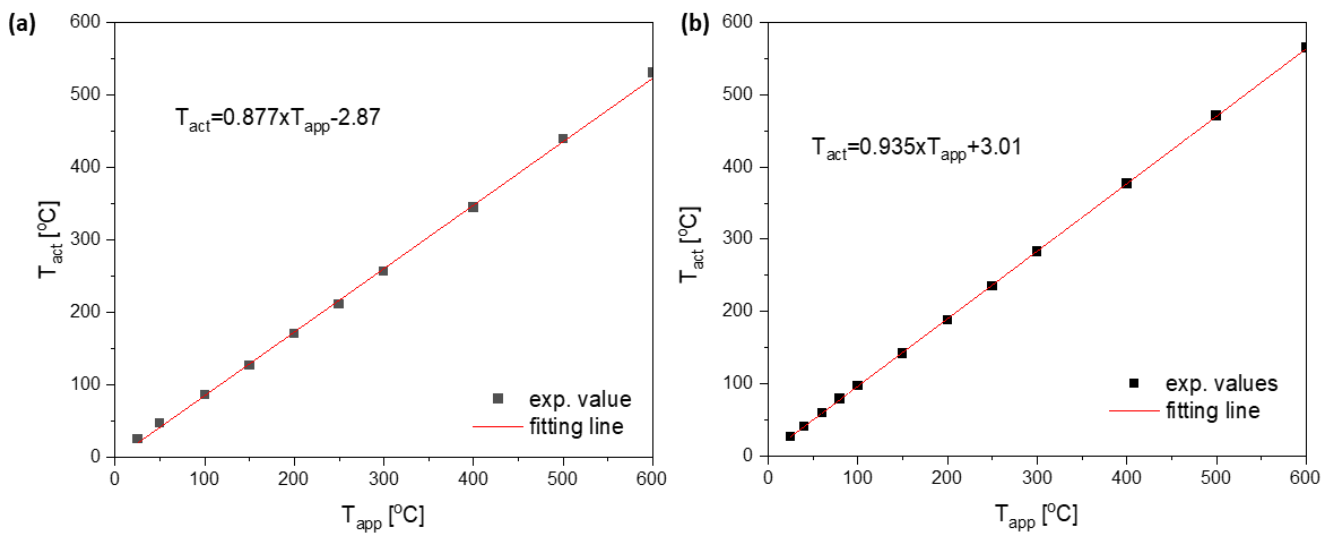

Figure 12. Temperature calibration of the (a) Linkam cell and the (b) Harrick cell.

4. Synthesis of CeO₂ loaded on mesoporous SBA-15 and its application for NH₃-SCR

As discussed in the last section, mesoporous SBA-15 has been widely adopted as catalyst support due to its high specific surface area and chemically inertness. Synthetic approaches leading to catalytically active mesoporous silicates are following mostly two routes, that is, the "one-pot" strategy and the "loading" strategy.[45] In the case of the "one-pot" strategy (or pre-synthesis method), the silicon source is mixed with the precursor of the active composition, which then both interact with the template to co-assemble into a porous framework.[80, 81] The "loading" strategy (or post-synthesis method) mainly involves the preparation of a stable mesoporous silica matrix, followed by its loading with the active composition.[82] Besides, the intermediate route between the pre- and post-synthesis approaches, denoted "med-synthesis", in which the template remains in the pore (see Figure 6), has been applied owing to its potential to combine the advantages of the pre- and post-synthesis approaches, such as good active phase distribution and defined structure, as well as improved catalytic activity.

In this section, the preparation of active metal oxide catalysts supported on SBA-15 by solid-state impregnation with the assistance of a template is described, corresponding to the "med-synthesis". Based on the catalytic test comparing the template-assisted method (med-synthesis) with the template-free method (post-synthesis), the former apparently yielded an improved SCR performance which was the motivation to explore how the template assistance made an effect and why the prepared catalysts showed distinct SCR reactivities, which were corresponding to the mechanisms of the synthesis process and SCR reaction process, respectively. Firstly, *in situ* characterizations were adopted to monitor the synthesis of CeO₂ loaded on SBA-15 by the SSI method with/without a template.[41] Secondly, the SCR reaction mechanism was explored for the CeO₂/SBA-15 catalyst. In order to exclude the effect of support, bare CeO₂ exploration was inserted before the CeO₂/SBA-15 to show the general mechanism of NH₃-SCR on ceria.

4.1. Controlling the dispersion of ceria using nanoconfinement: application to CeO₂/SBA-15 catalysts for NH₃-SCR

Ceria-based materials have been considered as potential catalysts for the NH₃-SCR reaction, due to their high oxygen storage capacity (OSC) and excellent redox properties.[83] Since crystalline CeO₂ cannot provide a sufficiently high specific surface area, especially after high-temperature aggregation, SBA-15 has been employed previously as a support material to disperse and stabilize CeO₂ particles,[84] but also other NH₃-SCR-related materials.[85]

Recently, the positive effect of surfactants on the loading of active components in mesoporous silicates has attracted considerable attention. To this end, previous studies have shown that 3 nm-sized ceria particles dispersed on SBA-15, as achieved with the assistance of H$_3$Cit, caused an enhanced reducibility and defect concentration of the particles, influencing the catalytic performance.[86] Besides, surfactant-assisted impregnation has been widely applied in the context of Ni/SBA-15 catalysts for CO$_2$ reforming of CH$_4$.[87] These studies have revealed that the use of surfactant P123 yields a catalytic performance superior to that of other surfactants,[87-89] which was explained by the coordination of Ni atoms by the OH groups of P123, thus preventing their aggregation.[88] Considering that P123 is the template of SBA-15, a method was put forward that used as-made SBA-15 for wetness impregnation after partial removal of P123. This method was employed for the synthesis of Cu/SBA-15 materials, enabling a good dispersion of copper even at high loadings.[90] Yin et al. suggested an improved method to use the P123-contained SBA-15 combined with solid-state impregnation methods to avoid the extra step of partial removal of P123, which was applied to the synthesis of CuO/SBA-15 for thiophene capture,[91] CeO$_2$/SBA-15 for sulfur capture,[92] Pt/SBA-15 for hydrogen storage,[93] Co/SBA-15 for the oxidation of organic pollutants,[94] and Fe/SBA-15 for phenol degradation.[95] Also composite catalysts, i.e., Ag-CeO$_2$/SBA-15, were prepared by using P123-contained SBA-15, showing good dispersion and catalytic performance for room-temperature reduction of 4-nitrophenol.[96] Summarizing, previous studies have demonstrated the great potential of the template P123-assisted synthesis of mesoporous catalysts containing highly dispersed metals or metal oxides.

Although the med-synthesis approach towards improved supported catalysts has received increasing attention, a detailed mechanistic understanding of the template P123-assisted synthesis is still lacking. One hypothesis is that P123 remaining in the pores of SBA-15 forms a confined space between the silica walls and residual P123 in the intra-wall pores,[90, 92-95] while another proposes an interaction between P123 and the metal precursors, influencing their decomposition behavior.[88] However, due to a lack of direct experimental evidence, particularly *in situ* analysis, none of the above hypotheses have been verified so far. Besides, it was found that the dispersion effect of P123 was limited to samples with high loadings.[92] Thus, elucidating the mechanism of the template assistance will be of great importance to further improve its applicability to catalyst synthesis.

In the following, the preparation of CeO$_2$/SBA-15 catalysts by solid-state impregnation methods starting from bare and template-containing SBA-15 is reported, aiming at a mechanistic understanding of the synthesis. To monitor the calcination process in detail, *in situ* Raman, DRIFT, and DR UV-Vis spectroscopies were applied, revealing details of the transformation of the cerium precursor to the supported oxide. Additional thermogravimetric analysis (TGA) and exhaust gas analysis by FT-IR

spectroscopy allowed the temperature-dependent decomposition of the P123 template and the cerium precursors to be monitored. The differently prepared samples were characterized regarding their structural and surface properties and tested in NH_3-SCR. Based on these combined results, a synthesis mechanism was proposed and used to develop a novel synthesis protocol to yield catalysts with improved ceria dispersion and superior NH_3-SCR performance. This work mainly follows the published paper "Controlling the dispersion of ceria using nanoconfinement: application to CeO_2/SBA-15 catalysts for NH_3-SCR".[41]

4.1.1. Catalyst preparation

asSBA-15 and tfSBA-15. Mesoporous SBA-15 was synthesized according to the methods reported by Zhao et al. (see Figure 5).[40] Briefly, 4 g of pluronic $EO_{20}PO_{70}EO_{20}$ (P123) was dissolved in 150 ml of 1.6 M HCl solution and stirred at 35 °C and a speed of 250 r/min for 2.5 h. Then, 11 ml of tetraethylorthosilicate (TEOS) was added and the obtained mixture was stirred at 35 °C at an increased speed of 400 r/min for 20 h. The stirred mixture was then transferred to a Teflon bottle for hydrothermal treatment and crystallization at 85 °C for 24 h. Vacuum filtration of the suspension at room temperature yielded a white powder, which is referred to as as-made SBA-15 (asSBA-15) and which contains the templating agent P123 in the mesoporous matrix. Calcination of asSBA-15 at 550 °C for 12 h with a heating rate of 1.5 °C/min in air yields a white powder, referred to as template-free SBA-15 (tfSBA-15), from which the templating agent P123 has been removed.

asSBA-L/H-CeO₂-Air/N₂. Cerium nitrate was employed as the cerium source for the preparation of CeO_2/SBA-15 catalysts. The precursor $Ce(NO_3)_3·6H_2O$ was mixed with asSBA-15 (see above) via solid-state grinding at room temperature for 30 min. The thoroughly mixed powder was then calcined in a muffle furnace at 500 °C for 5 h (heating rate: 1.5 °C/min) in air (denoted by -Air) or N_2 (denoted by -N₂) to remove the P123 template and form the CeO_2 phases. To explore the effect of CeO_2 loading, CeO_2/SBA-15 catalysts with low and high CeO_2 loading were prepared. The sample resulting from a mixture of 0.173 g of $Ce(NO_3)_3·6H_2O$ and 0.225 g of asSBA-15 will be referred to as L-CeO₂, while that resulting from a mixture of 0.346 g of $Ce(NO_3)_3·6H_2O$ and 0.225 g of asSBA-15 will be labelled as H-CeO₂. Thus, as an example, mixing 0.173 g of $Ce(NO_3)_3·6H_2O$ with 0.225 g of asSBA-15, followed by calcination in air, gave the sample *asSBA-L-CeO₂-Air*.

tfSBA-L/H-CeO₂-Air/N₂. Similarly, tfSBA-L/H-CeO₂-Air/N₂ samples were prepared by following the above protocol, except that asSBA-15 was replaced by tfSBA-15. To ensure comparable CeO_2 loadings, 0.225 g of asSBA-15 was calcined yielding 0.108 g of tfSBA-15. Thus, as an example, mixing

0.173 g of Ce(NO$_3$)$_3 \cdot$ 6H$_2$O with 0.108 g of tfSBA-15 followed by calcination in air resulted in the sample *tfSBA-L-CeO$_2$-Air.*

Prior to catalytic testing in NH$_3$-SCR, all samples treated in N$_2$ during synthesis were calcined in air for 2 h at 500 °C to remove residual template.

4.1.2. Characterization of dispersed CeO$_2$ on SBA-15

Three CeO$_2$/SBA-15 samples were prepared by calcination of the cerium oxide precursor Ce(NO$_3$)$_3 \cdot$ 6H$_2$O and the SBA-15 support following different routes, as detailed in Scheme 2. The sample tfSBA-CeO$_2$-air was synthesized by grinding template-free SBA-15 (tfSBA-15) with cerium nitrate and subsequent calcination in air to obtain ceria crystallites grown inside SBA-15 pores. For the sample asSBA-CeO$_2$-air, P123-containing SBA-15 (asSBA-15) was employed as support material. Using the same calcination step in air results in ceria dispersed inside the SBA-15 pores. Moreover, a third route was designed, which yields the sample asSBA-CeO$_2$-N$_2$, by starting from asSBA-15 but changing the gas atmosphere to inert N$_2$.
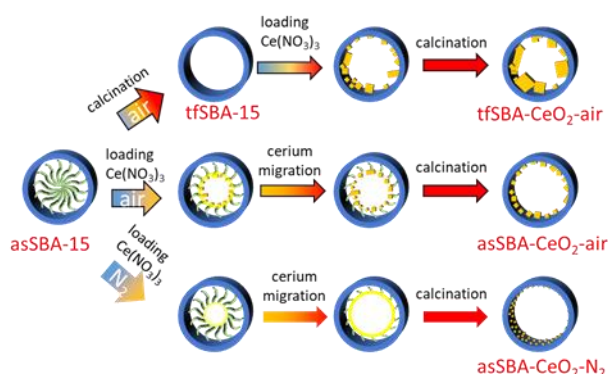
Scheme 2. Different synthesis routes for CeO$_2$/SBA-15 catalysts using the solid-state impregnation method.

Figure 13(a) summarizes the temperature program of the calcination process, which is characterized by two stages, i.e., heating from room temperature to 500 °C at a rate of 1.5 °C/min and keeping the temperature at 500 °C for 5 h.
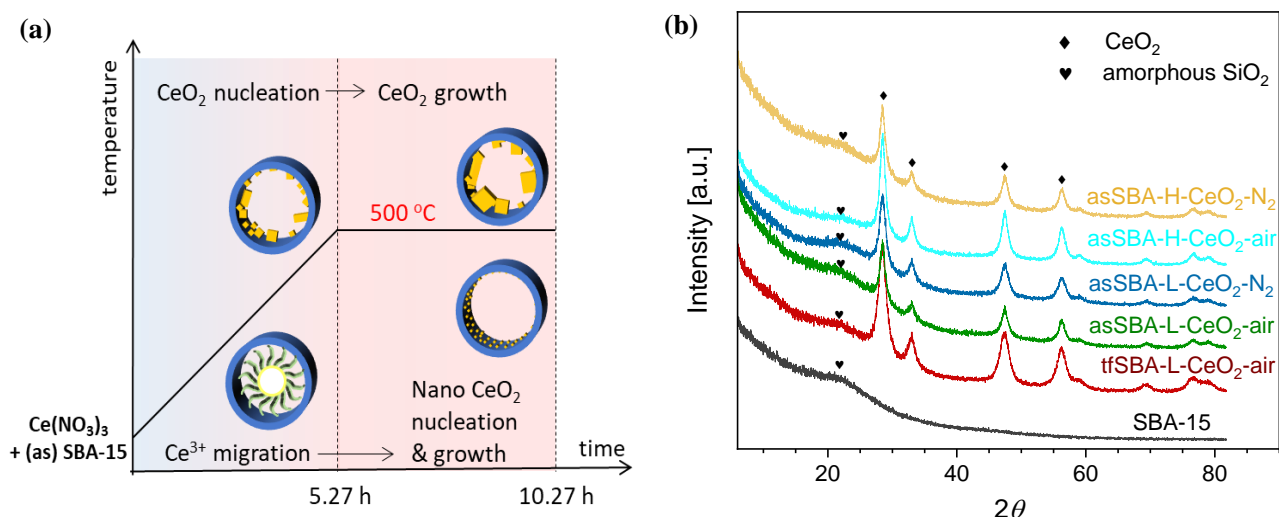
Figure 13. (a) Temperature program of the calcination process, and (b) XRD patterns of the calcined CeO_2/SBA-15 materials, after starting from different SBA-15 matrixes (tfSBA-15 and asSBA-15) and cerium contents (low and high), and applying different atmospheres (air and N_2). For comparison the XRD pattern of bare SBA-15 is shown. The CeO_2-related peaks are marked. XRD patterns are offset for clarity.

Figure 13(b) shows wide-angle XRD patterns of the calcined samples. Starting with bare SBA-15, the broad diffraction peak at $2\theta = 23°$ is assigned to amorphous silica. For the samples with CeO_2 loading, new peaks appear at 2θ values of 28.5°, 33.2°, 47.5°, and 56.3°, which can be attributed to different planes of crystalline CeO_2, i.e., (111), (200), (220), and (311), respectively. Detailed analysis reveals that the peaks show a full width at half maximum (FWHM) in the order tfSBA-L-CeO_2-air < asSBA-L-CeO_2-air < asSBA-L-CeO_2-N_2. Based on a fit analysis of the ceria (111) diffraction peak and application of the Scherrer formula,[97] the grain sizes are found to decrease as tfSBA-L-CeO_2-air > asSBA-L-CeO_2-air > asSBA-L-CeO_2-N_2 (see Table 6), reflecting the suppression of ceria crystal growth when the use of template P123 is combined with a N_2 calcination atmosphere. Similarly, with increasing CeO_2 loading, the grain sizes decreased as asSBA-H-CeO_2-air > asSBA-H-CeO_2-N_2, indicating that an inert calcination atmosphere can further improve the CeO_2 dispersion compared to the effect of the surfactant template alone.

Table 6 summarizes some physical properties of the CeO_2/SBA-15 samples as determined on the basis of N_2 adsorption isotherms, including the specific surface areas, pore volumes, and pore sizes. The CeO_2-containing samples exhibit smaller specific surface areas than bare template-free SBA-15 (tfSBA-15), decreasing in the order tfSBA-L-CeO_2-Air > asSBA-L-CeO_2-Air > asSBA-L-CeO_2-N_2, owing to

micropore blocking and, in the case of asSBA-L-CeO$_2$-N$_2$, also the reduction of mesopore diameter by ceria loading onto the inner surface of the porous matrix.

Table 6. Composition, specific surface area, and porosity characteristics of the CeO$_2$/SBA-15 samples compared to bare SBA-15.

Samples	CeO$_2$ (wt.%)	S$_{total}$ [m^2/g][a]	D$_p$ [nm][b]	V$_{total}$ [cm^3/g][c]	d$_{CeO2}$ [nm][d]
tfSBA-15	0	616	6.3	0.64	--
tfSBA-L-CeO$_2$-air	39	414	6.3	0.43	7.8
asSBA-L-CeO$_2$-air	39	359	6.3	0.39	6.4
asSBA-L-CeO$_2$-N$_2$	39	280	5.8	0.32	5.4

[a] Total BET surface area.
[b] Pore diameter determined from the adsorption branch by NLDFT.
[c] Total pore volume.
[d] Calculated from XRD results using the Scherrer formula.

The N$_2$ adsorption/desorption isotherms of the SBA-15 and CeO$_2$/SBA-15 samples all show profiles typical for mesoporous materials (see Figure 14(a)), but with variations in the shape of the hysteresis loop. Bare SBA-15 powder shows the typical shape of a mesoporous material with an H1 hysteresis loop at the relative pressure p/p^o of 0.55-0.75, reflecting uniform hexagonal pores with a narrow pore size distribution centered around 6.3 nm diameter. For samples loaded with CeO$_2$, a decrease in the micropore area compared to bare SBA-15 is observed. Also, the closing point of the hysteresis loop shifts to lower relative pressure values of about 0.45, which implies that CeO$_2$ is formed inside the pores, resulting in open and narrowed mesopores.[98] The desorption branch of the hysteresis loop of tf-SBA-L-CeO$_2$-air shows two steps, representing open mesopores (p/p^o of 0.53-0.70) and narrowed mesopores (p/p^o of 0.45-0.53), respectively. For asSBA-L-CeO$_2$-air, a weak feature from open mesopores and a forced closure of the hysteresis loop at $p/p^o = 0.46$ is observed, which is attributed to ink-bottle type pores. In contrast, the desorption branch of asSBA-L-CeO$_2$-N$_2$ is characterized by a smoother decrease, which is somewhat similar to that of SBA-15, representing a more uniform pore size along the channels, while the shift of the curve to lower relative pressure values compared to bare SBA-15 results from the decreased pore size after the coating with CeO$_2$.

Figure 14(b) shows the pore size distributions calculated from the adsorption branches of the isotherms. The samples treated in air, tfSBA-L-CeO$_2$-air and asSBA-L-CeO$_2$-air, exhibit a maximum at

a pore size of around 6.3 nm, i.e., at the same diameter as the original SBA-15, implying that a considerable amount of surface area inside the pores is uncoated. Especially the pore sizes of tfSBA-L-CeO$_2$-air are distributed over a wider range towards lower values, suggesting the presence of CeO$_2$ crystallites inside the pores. In contrast, asSBA-L-CeO$_2$-N$_2$ shows a maximum at a decreased pore diameter of 5.8 nm, as a result of a more even coating of the pores with nano-scale CeO$_2$. For illustration, Fig. S4-1 in the Supporting Information provides schematic diagrams of the pore structures of these three samples, as proposed on the basis of the above analysis. In summary, for tfSBA-L-CeO$_2$-air, the growth of crystalline ceria results in the presence of narrowed pores, while in the case of asSBA-L-CeO$_2$-air the limited diffusion of the cerium precursor leads to the formation of ink-bottle pores. By contrast, for asSBA-L-CeO$_2$-N$_2$, extensive diffusion of cerium ions results in an evenly coated porous matrix.
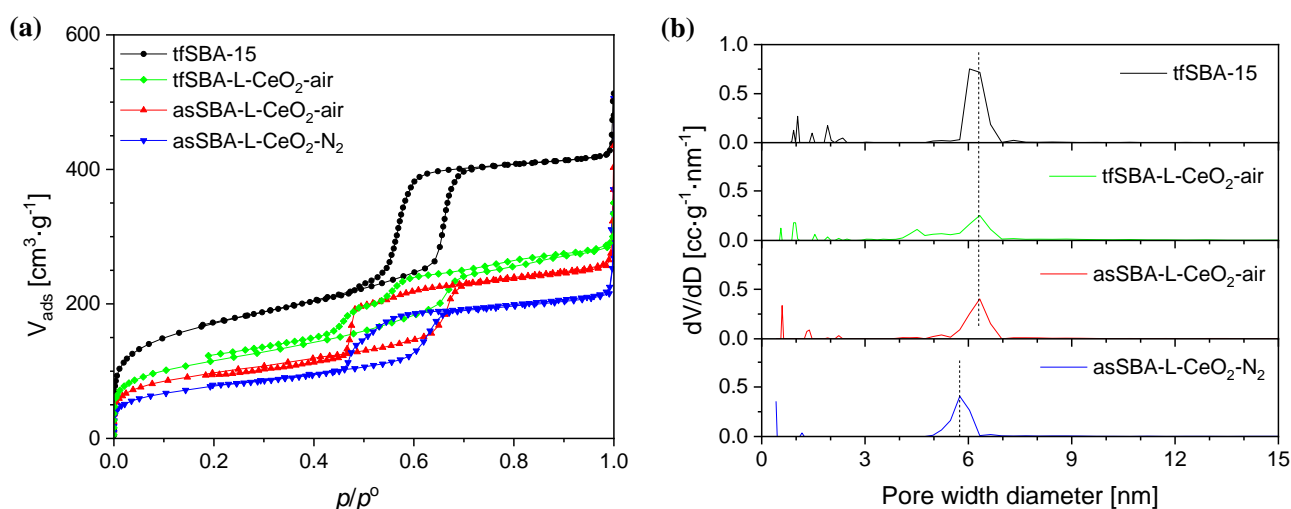
Figure 14. (a) N$_2$ adsorption/desorption isotherms and (b) NLDFT pore size distributions of template-free SBA-15 and CeO$_2$/SBA-15 materials prepared by different synthesis routes.

4.1.3. Mechanism of CeO$_2$ dispersion during calcination

Previously, the good dispersion on asSBA-15 has been proposed to be due to the existence of template P123, resulting in confined spaces for CeO$_2$ crystal growth, however, without providing direct evidence. To elucidate the interaction between the SBA-15 support and the ceria species during calcination, TG analysis and online gas-phase FTIR spectroscopy, as well as *in situ* Raman, DR UV-Vis, and DRIFT spectroscopies were applied.

First, TG analysis were applied to gain detailed insight into the decomposition of the template-containing SBA-15 during calcination, compared to bare asSBA-15 and the cerium precursor

$Ce(NO_3)_3 \cdot 6H_2O$ as reference (see Figure 15(a)), following the temperature program given in Figure 13(a). The observed thermal decomposition of bare as-made SBA-15 shows a single weight loss of 47 wt. % at about 120 °C, which is associated with the decomposition of triblock copolymer P123 slightly embedded in the siliceous pore walls.[99] Previous studies have addressed the decomposition mechanism of bare cerium nitrate $Ce(NO_3)_3 \cdot 6H_2O$ in air by TGA, as summarized in Fig. S4-2.[100, 101] Here, by combining TG and DTG analysis (see Figure 15(a) and S4-3), It is identified 221 °C as a critical temperature point, attributed to the onset of cerium nitrate decomposition. Weight losses observed below 221 °C are assigned to the release of surface water and structural water, while at temperatures above 221 °C the decomposition of nitrate resulted in the release of NO_x gas (see below, Figure 15(b)) and a further substantial weight loss of 35 wt.%. Sample tfSBA-L-CeO$_2$ calcined in air shows a substantial decrease in weight below 200 °C due to lower onset temperatures for the release of water and cerium nitrate decomposition compared to bare cerium nitrate.

However, because, for the mixed samples (cerium nitrate/SBA-15), the weight loss reflects a more complex interplay of different processes, the exhaust was continuously monitored by gas-phase FTIR spectroscopy. To this end, Figure 15(b) depicts the temperature-programmed evolution of NO_2 gas (at 1629 cm^{-1})[67] resulting from cerium nitrate decomposition. As a reference, the NO_2 evolution of bare $Ce(NO_3)_3 \cdot 6H_2O$ salt is shown (see light-blue curve), which is characterized by a sharp increase at 240 °C and a slower decline up to ~500 °C, in agreement with the literature.[101] There is an additional small peak at about 120 °C, indicating the evaporation of aqueous acid azeotrope, as discussed in the context of Fig. S4-2. Compared to the bare cerium salt, the NO_2 signal of tfSBA-L-CeO$_2$-air appears within a much narrower temperature range, suggesting the influence of SBA-15 on the decomposition of cerium nitrate. The lack of NO_2 features at lower temperatures, i.e., at around 120 °C and at 190-230 °C, suggests the inhibition of azeotrope formation by dry SBA-15. In contrast, the sample asSBA-L-CeO$_2$-air shows an increasing signal at 160-250 °C, which is attributed to template P123 decomposition, producing water to form the HNO_3 azeotrope, as well as a stronger nitrate decomposition peak with an onset at ~250 °C. For asSBA-L-CeO$_2$-N$_2$, the cerium nitrate precursor is observed to decompose within a very narrow temperature window (250 °C-300 °C), indicating differences in the interaction between precursor and template as a function of the calcination conditions.

Fig. Figure 15(c) depicts the temperature-programmed evolution of exhaust CO_2 gas (at 2350 cm^{-1})[102] resulting from the decomposition of template P123. For bare as-made SBA-15, the decomposition starts at around 155 °C and extends up to 500 °C. Sample tfSBA15-L-CeO$_2$-air shows a small feature at 240-350 °C, originating from residual P123 after calcination. By comparison of Figure 15(b) and Figure 15(c), it can be seen that the temperature range of the CO_2-related band overlaps with that of the NO_2

band, possibly leading to synergetic effects in the decomposition and oxide formation processes. The sample asSBA-L-CeO$_2$-air exhibits several CO$_2$-related peaks. Compared to the single broad CO$_2$ band detected for bare asSBA-15, these more discrete features indicate the presence of different intermediate states during P123 decomposition. In contrast, when the calcination is performed in N$_2$, a significant amount of CO$_2$ is released within a very narrow temperature window (270-275 °C), strongly overlapping with that of the NO$_2$ release (see Figure 15(b)), reflecting an interaction between the decomposition of P123 and that of cerium nitrate, while the CO$_2$ emission at higher temperatures can be ascribed to the decomposition of oxygen-containing fragments of the template.

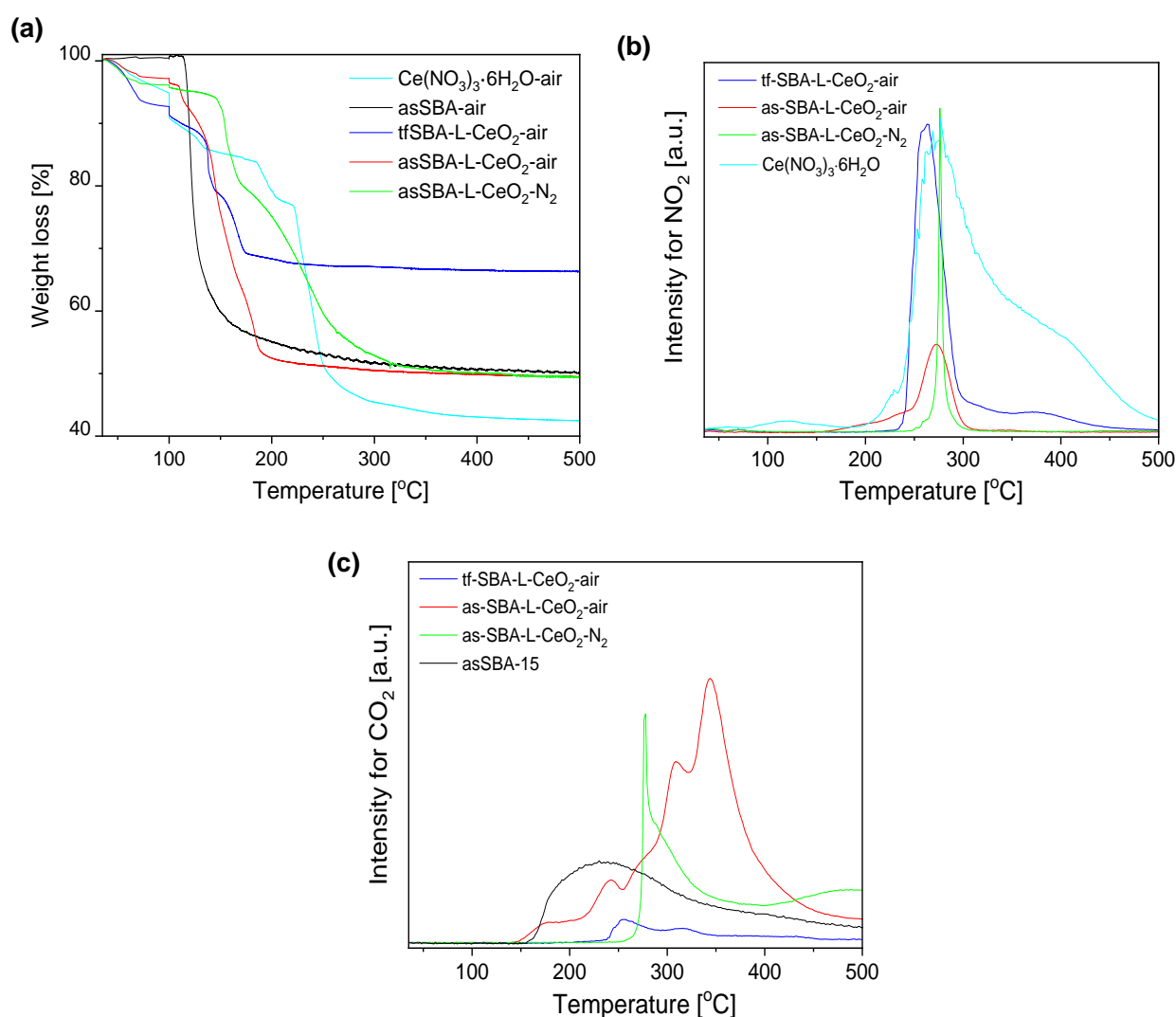Figure 15. TGA profiles (a), and IR intensities of exhaust NO$_2$ (b), and CO$_2$ (c) during calcination of bare asSBA-15, bare cerium nitrate, and cerium nitrate/SBA-15 mixtures, following the protocol given in Figure 13a.

To gain more detailed insight into the decomposition processes, Figure 16 shows the temporal evolution of all exhaust gases during calcination, as detected by online gas-phase IR analysis. Features

at around 1150-1250 cm^{-1} are assigned to C-O-C stretching modes,[103] those at 1350 cm^{-1} and 2800-3000 cm^{-1} to C-H bending and stretching modes, respectively.[103] and those at 1750 and 3638 cm^{-1} to C=O and O-H stretching modes, respectively.[102]

For bare asSBA-15, the P123 decomposes directly to gaseous CO_2 as well as C1 or C2 fragments, starting at around 170 °C. In the case of tfSBA-L-CeO$_2$-air, the decomposition of cerium nitrate, leading to NO_2 formation, and small amounts of CO_2 and C_n ketone are observed from 260 °C onwards. The exhaust gas evolution of asSBA-L-CeO$_2$-air is characterized by four stages, beginning at about 160 (I), 240 (II), 300 (III), and 350 °C (IV), respectively, consistent with the discrete CO_2 peaks in Figure 15(c): In stage I, C_n fragments (including ketone, alcohol, and ether) are formed, while NO_2 shows a gradual increase, indicating that P123 fragments may affect the decomposition of cerium nitrate, considering the higher onset temperature for decomposition observed for tfSBA-L-CeO$_2$-air. In stage II, which corresponds to the temperature range of the original cerium nitrate decomposition, a facilitated decomposition of P123 compared to bare asSBA-15 is observed, which may be attributed to a catalytic effect by the formed ceria (see below). In stage III, most of the residual P123 is catalytically converted by ceria to CO_2 and H_2O, while in stage IV more stable fragments are decomposed.

Summarizing, from the above *in situ* gas-phase results, it is concluded that P123 fragments facilitate the decomposition of cerium nitrate, while in turn the formed ceria catalyzes the decomposition of P123. Interestingly, for sample asSBA-L-CeO$_2$-N$_2$, P123 and cerium nitrate decompose almost simultaneously within a narrow temperature window at about 280 °C, which equals the decomposition temperature of cerium nitrate, according to the tfSBA-L-CeO$_2$-air and asSBA-L-CeO$_2$-air results. Thus, it is concluded that the inert atmosphere inhibits the decomposition of P123 at low temperatures (see also Fig. S4-4), allowing an increased catalytic interaction between cerium nitrate and P123 at elevated temperature, boosting the nucleation of nano ceria.
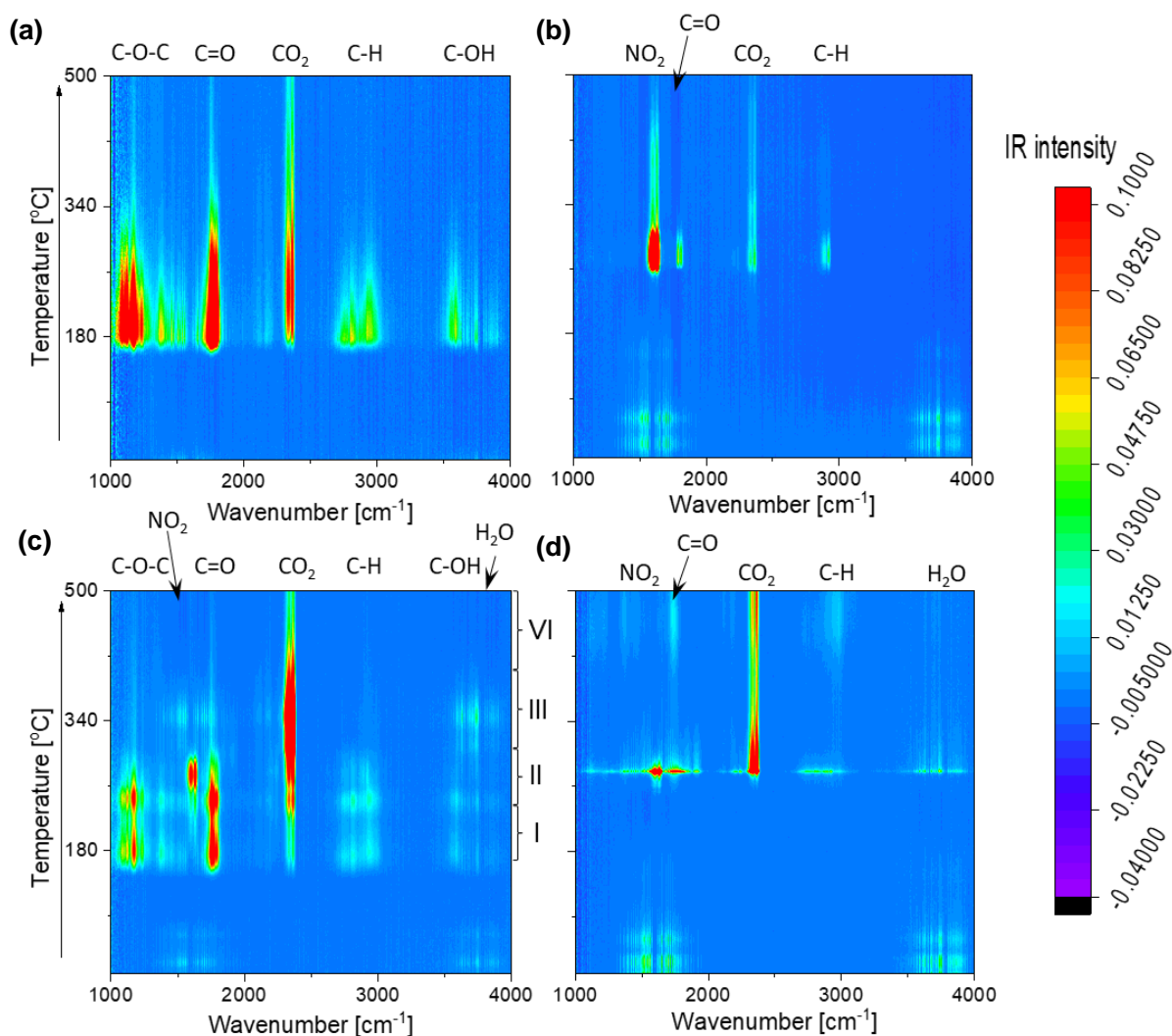
Figure 16. Online IR detection of exhaust gases during calcination of the samples (a) asSBA15-air, (b) tfSBA-L-CeO2-air, (c) asSBA-L-CeO2-air, and (d) asSBA-L-CeO2-N2. The low-temperature features at around 1600 and 3750 cm^{-1} can be attributed to water released from cerium nitrate. For details see text.

The *in situ* Raman spectra of tfSBA-L-CeO$_2$-air, asSBA-L-CeO$_2$-air, and asSBA-L-CeO$_2$-N$_2$ during calcination are mainly characterized by Raman features at 457, 745, and 1046 cm^{-1} (see Fig. S4-5). The band at about 460 cm^{-1} is assigned to the triply degenerate symmetrical stretching mode (F$_{2g}$) of ceria,[62] and its position and shape are known to depend on the detailed ceria lattice structure.[104] The Raman features at 745 cm^{-1} and 1046 cm^{-1} originate from bending and stretching vibrations of free nitrate, respectively.[105] Figure 17 compares the temperature-dependent transformation of cerium nitrate into ceria for the three samples, focusing on the nitrate stretching mode at 1046 cm^{-1} to monitor the precursor decomposition (a) and the F$_{2g}$ mode at 457 cm^{-1} to describe formation of crystalline ceria (b).

For tfSBA-L-CeO$_2$-air, the cerium nitrate features disappear at 300 °C, while those for ceria start to appear at 250 °C, implying simultaneous cerium nitrate decomposition and ceria formation. Initially, a broad F$_{2g}$-related band is detected at about 450 cm^{-1}, which undergoes a narrowing and red-shift to 457 cm^{-1} with increasing temperature, thus indicating the growth of ceria crystallites (see Fig. S4-5(a)). The additional smaller features at about 250 and 279 cm^{-1} are attributed to nitro- and ceria-related vibrations and discussed in the context of Fig. S4-5.
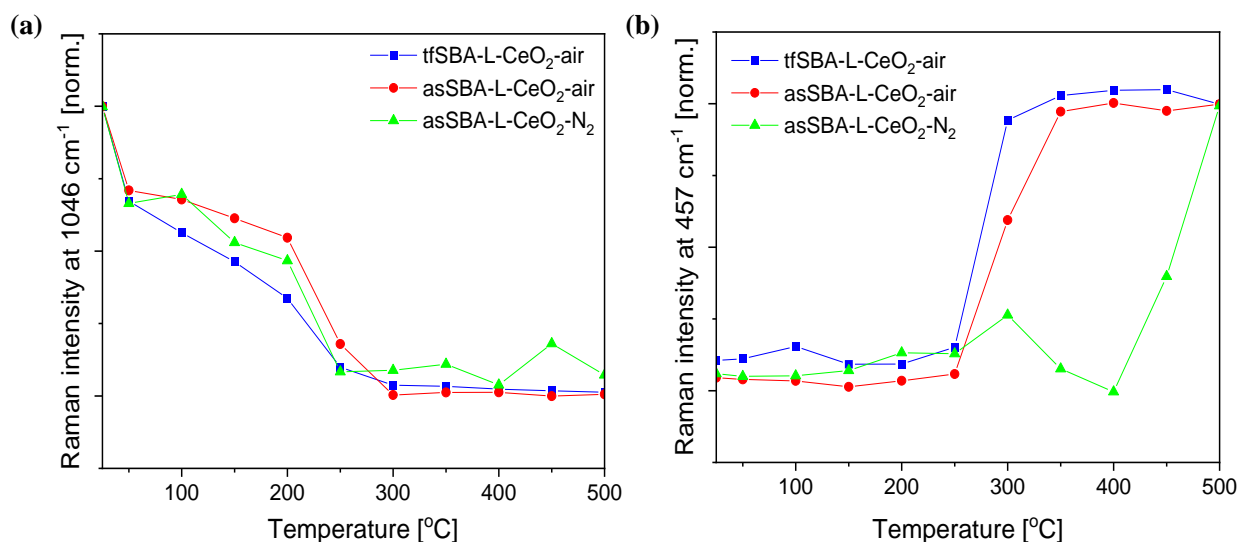
Figure 17. Temperature-dependent Raman intensities (514.5 nm) at 1046 cm^{-1}, representing cerium nitrate (a), and at 457 cm^{-1}, representing CeO$_2$ (b), recorded during calcination, following the protocol given in Figure 13a. The corresponding Raman spectra are shown in Fig. S4-5.

In the case of the asSBA-L-CeO$_2$ samples, temperature windows of about 250-300 °C (in air) and 250-450 °C (in N$_2$) were detected. Sample asSBA-L-CeO$_2$-air shows the F$_{2g}$ band only at about 300 °C, suggesting an inhibited ceria growth process. In contrast, in the case of asSBA-L-CeO$_2$-N$_2$, a F$_{2g}$ band is only indicated, consistent with the presence of amorphous ceria and/or very small ceria crystallites.

Previously, a possible ion-exchange reaction on silicate adsorbent has been reported:[88, 106]

$$Ce\text{-}O\text{-}NO_2 + OH^- \rightarrow Ce\text{-}OH + NO_3^- \tag{4-1}$$

Thus, one may deduce that the dispersion of cerium within the pores is related to the extent of migration of soluble Ce^{3+}, stabilized by hydroxyl groups of P123, prior to forming solid CeO$_2$ crystallites at higher temperatures. Thus, a wide temperature window is expected to facilitate the migration process of cerium ions within the pores, resulting in a better dispersion.

In situ DR UV-Vis spectra were recorded to gain information about changes in the coordination environment of cerium ions during the transformation from $Ce(NO_3)_3$ to CeO_2 (see Figure 18). The initial DR UV-Vis spectra of tfSBA-L-CeO$_2$-air, asSBA-L-CeO$_2$-air, and asSBA-L-CeO$_2$-N$_2$ at low temperature are characterized by typical features of $Ce(NO_3)_3$ at 218, 255, and 314 nm, which correspond to a $4f^1$-$5d^1$ electronic transfer of Ce^{3+}, a charge transfer (CT) of O^{2-} 2p to Ce^{3+} 4f/5d, and a CT of Ce^{3+} 5d to O^{2-} 2p, respectively.[107] At higher temperature, spectra show a broad absorption band at 220-320 nm, which can be attributed to a CT band of O^{2-} to Ce^{4+} (at ~270 nm) and inter-band transitions (at ~310 nm) of ceria. With increasing temperature from room temperature to 500 °C, tfSBA-L-CeO$_2$-air (see Figure 18(a)) shows an increase of the bands at 320 nm and 255 nm, but a decrease of the band at 220 nm, which is attributed to the transformation of nitrate to oxide. In addition, there is a shift of the absorption edge from 370 nm for $Ce(NO_3)_3$ to 470 nm for CeO_2. For the samples asSBA-L-CeO$_2$-air (see Figure 18(b)) and asSBA-L-CeO$_2$-N$_2$ (see Figure 18(c)) similar overall changes were observed, i.e., the band at 260 nm increased, while the shoulder band at 320 nm disappeared. The presence of noise signals in the UV region can be explained by the strong absorption of the carbon-containing P123 template. Similarly, the absorption edge shifted from 370 nm to 450 nm for asSBA-L-CeO$_2$ calcined in air or in N$_2$/air. The intensity at about 380 and 250 nm has been reported to be proportional to the amount of Ce^{4+} ions in an octahedral/polymeric and a tetrahedral coordination environment of CeO_2, respectively.[108] Thus, it is concluded that there is more tetrahedrally coordinated cerium present in asSBA-L-CeO$_2$-air/N$_2$ than in tfSBA-L-CeO$_2$-air after calcination (see Fig. S4-6).

Figure 18. *In situ* DR UV-Vis spectra during the calcination of (a) tfSBA-L-CeO$_2$-air, (b) asSBA-L-CeO$_2$-air, and (c) asSBA-L-CeO$_2$-N$_2$, following the protocol given in Figure 13a.

For bare CeO$_2$, the direct band gap energy (E$_g$) can be calculated from the DR UV-Vis spectra according to[109]

$$\alpha h\nu = A(h\nu - E_g)^{1/2} \tag{4-2}$$

where α is the absorption coefficient, which is described by the absorbance here. Using Tauc's method, the evolution of the E$_g$ value during calcination can be derived (see Fig. S4-7). In the low-temperature range, the gradual wavelength blueshift in the UV absorption (i.e., E$_g$ decrease) is due to the removal/dissociation of crystal water and chelated NO$_3^-$ according to[110]

$$Ce(NO_3)_3 \cdot xH_2O \rightarrow Ce(NO_3)_3(s) \rightarrow CeONO_3\ (s) \rightarrow CeO_{2-x}(s) \tag{4-3}$$
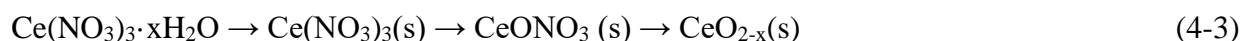
The E$_g$ values decrease rapidly for tfSBA-L-CeO$_2$-air to reach a relatively stable state at about 275 °C, while asSBA-L-CeO$_2$-air and asSBA-L-CeO$_2$-N$_2$ require higher temperatures of ~375 °C and 500 °C to reach their final state, respectively. In addition, with increasing temperature from 300 to 500 °C,

the band gap energy increases from 2.90 eV to 3.12 eV for tfSBA- L-CeO$_2$-air, suggesting the growth of CeO$_2$ crystallites. In contrast, for asSBA-L-CeO$_2$-air, the band gap reaches its minimum value of 2.85 eV at about 375 °C and then stays unchanged at higher temperature, indicative of a stable ceria crystallite size. Finally, for asSBA-L-CeO$_2$-N$_2$, the determined E$_g$ value suggests that there is no dominant ceria crystal phase formation with N$_2$ at 500 °C, while subsequent calcination for 2 h in air at 500 °C induces an E$_g$ red-shift to 2.71 eV, which may indicate the formation of tiny CeO$_2$ crystallites.

Figure 19 shows *in situ* DRIFT spectra of tfSBA-L-CeO$_2$-air, asSBA-L-CeO$_2$-air, and asSBA-L-CeO$_2$-N$_2$ during the calcination process. The assignments for the observed IR features are summarized in Table S4-1. Briefly, in the low-wavenumber region (1400-1800 cm^{-1}), mainly bands of nitrogen-containing species, and in the high-wavenumber region (>3000 cm^{-1}) hydroxyl-related features are detected. In addition, there are features attributed to vibrational modes of organic groups, such as C-O, C=O, and C-H, originating from P123 in the case of the asSBA-15-based samples, and from a small amount of residual P123 in the case of the tfSBA-15-based sample. As can be seen in Figure 19, all three samples exhibit a distinct change in vibrational structure at a critical temperature. In detail, at low temperatures, sample tfSBA-L-CeO$_2$-air shows a broad band at about 3200-3600 cm^{-1}, originating from H-bonded hydroxyl groups, which disappears when the temperature is raised from 225 °C to 275 °C, suggesting the removal of crystal water from Ce(NO$_3$)$_3$·6H$_2$O. Simultaneously, a strong decline of the nitrate features (at 1400-1800 cm^{-1}) is detected,[110] indicating the decomposition of cerium nitrate. Similarly, for asSBA-L-CeO$_2$-air and asSBA-L-CeO$_2$-N$_2$, there are rather sudden spectral changes within 225-275 °C and 275-300 °C. These observations further prove that the inert gas causes a delay in the decomposition of the cerium precursor. The asymmetric peak at 3740 cm^{-1} is typical for Si-OH groups, while the feature at 3700 cm^{-1} is attributed to Ce-OH.[104] It is noteworthy that tfSBA-L-CeO$_2$-air shows a peak at 3740 cm^{-1} over the whole temperature range, providing evidence for the presence of uncovered silica, even after CeO$_2$ formation. For asSBA-L-CeO$_2$-air, at the beginning no peak at 3740 cm^{-1} is detected, but at temperatures >275 °C, indicating that surface Si-OH is initially covered by the template, but emerges after the removal of P123. At low temperatures, the sample asSBA-L-CeO$_2$-N$_2$ shows spectra similar to those of asSBA-L-CeO$_2$-air, but the appearance of the Ce-OH peak at 3700 cm^{-1} evidences that the silica surface is coated by ceria. Based on these changes of the surface hydroxyl groups, it is concluded that P123 inside the pores shrinks to the pore wall when the temperature is increased. After reaching a critical temperature, surface Si-OH is exposed. On the other hand, the observation of Ce-OH in the absence of silanol features clearly shows that the formed ceria coats the silica surface.
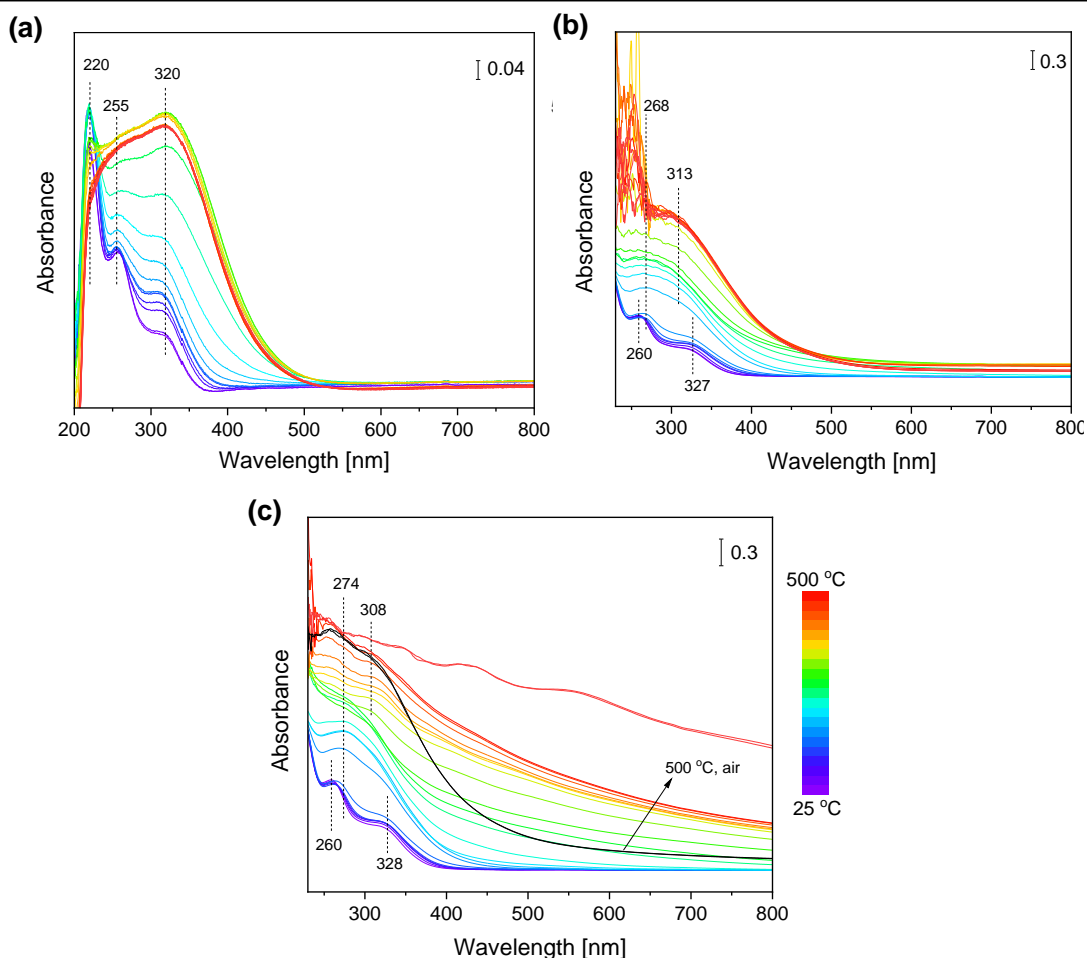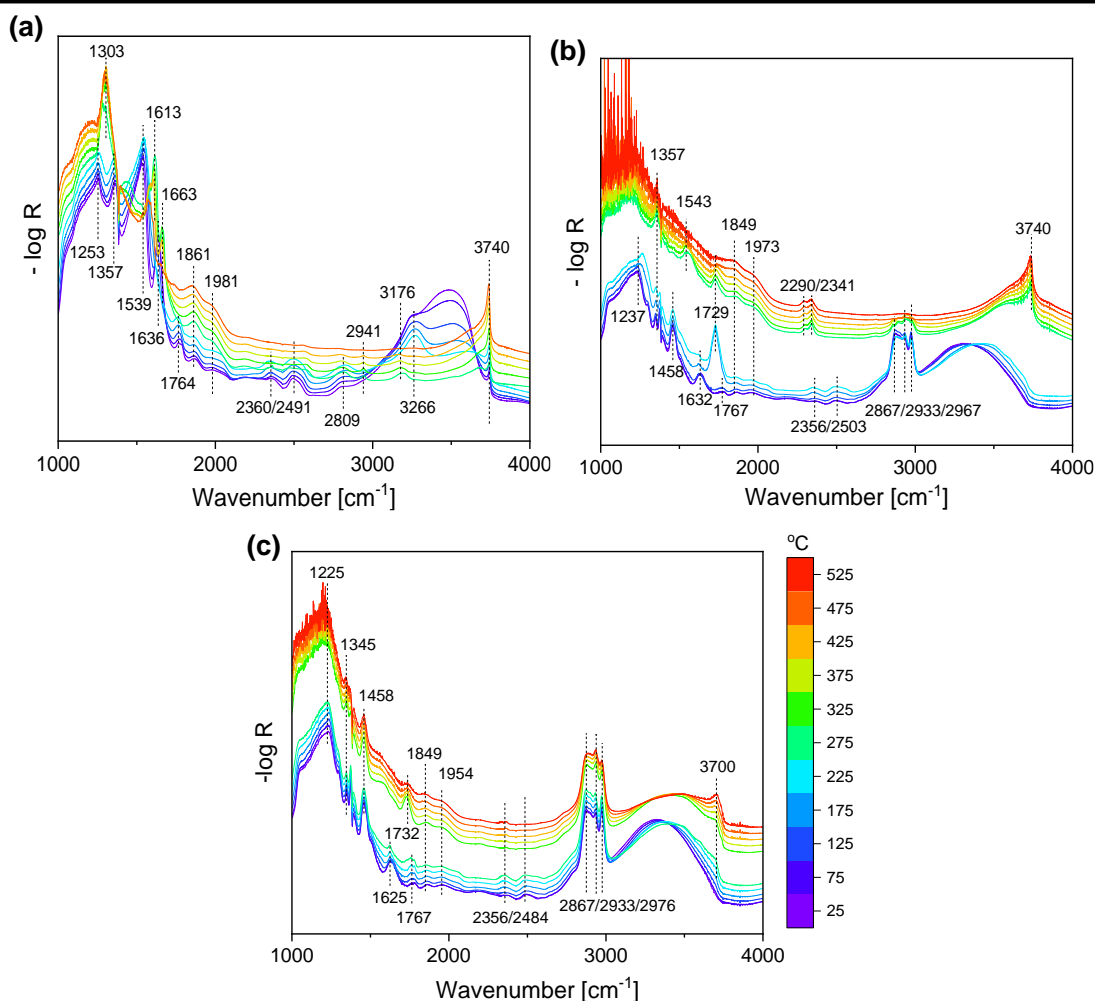
Figure 19. *In situ* DRIFT spectra during calcination of (a) tfSBA-L-CeO$_2$-air, (b) asSBA-L-CeO$_2$-air, and (c) asSBA-L-CeO$_2$-N$_2$, following the protocol given in Figure 13a.

4.1.4. The roles of P123 template

Previously, it had been proposed that the template could form a confined space to hinder the growth of larger crystallites. An unverified hypothesis was that the confined space was formed between the P123 micelles and the inner wall of SBA-15. As part of the detailed analysis, *in situ* DRIFT spectra show Si-OH-related signals at about 3734 cm-1, which appear after the removal of P123, strongly suggesting that P123 shrinks to the wall with increasing temperature. Especially, at low temperatures, the P123 chains are stabilized by their integration into the silica wall, while in the shrinkage stage, the water loss would break the central micelle structure (see Scheme 3). Thus, P123 tends to shrink to the inner wall, forming a confined space in the pore center, and cerium ions entering the pore are coordinated by P123, as shown in Scheme 3, overturning previous hypotheses.[95] In the further course of the synthesis, cerium,

initially coordinated by P123 in the central confinement, is dispersed onto the silica surface when the template is removed at higher temperatures (see Scheme 3).
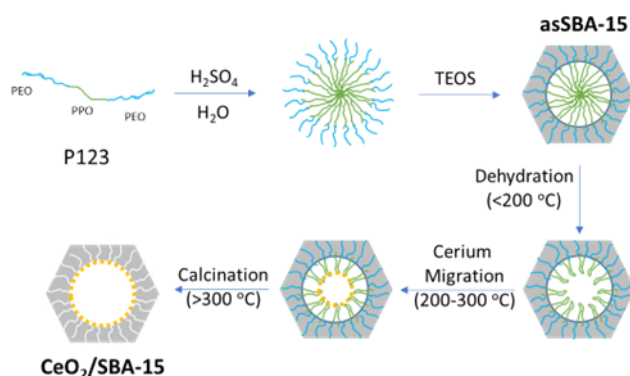
Scheme 3. Schematic diagram of the template-assisted processes leading to ceria dispersion within the mesopores matrix.

Based on the findings described above, the calcination process involves three steps, i.e., decomposition of cerium nitrate, migration of cerium species, and nucleation/growth of ceria. The final dispersion of ceria is shown to depend on the relative decomposition temperatures of P123 and cerium nitrate. The TG and FTIR results have revealed that the decomposition behavior of cerium nitrate/SBA-15 mixtures significantly deviates from that of bare cerium nitrate and P123 containing SBA-15, confirming the presence of interactions between cerium nitrate and the P123 template.

Calcination of mixed samples in air with the assistance of P123 results in the coordination of cerium ions by P123, while cerium nitrate migrates into the pores.[88] Due to the catalytic reaction between cerium ions and P123, ceria nanoparticles are formed by oxidation in air, while without P123, thermal decomposition of cerium nitrate occurs over a wide temperature range, accompanied by nucleation and growth of ceria crystallites (see Scheme 4). The catalytic reaction facilitates the oxidation of P123-coordinated cerium to ceria nuclei at even lower temperature than the critical decomposition temperature of bare $Ce(NO_3)_3 \cdot 6H_2O$. Meanwhile, reduction by P123 consumes lattice oxygen, which slows down the growth of ceria nanocrystals, thus increasing dispersion of ceria on SBA-15.
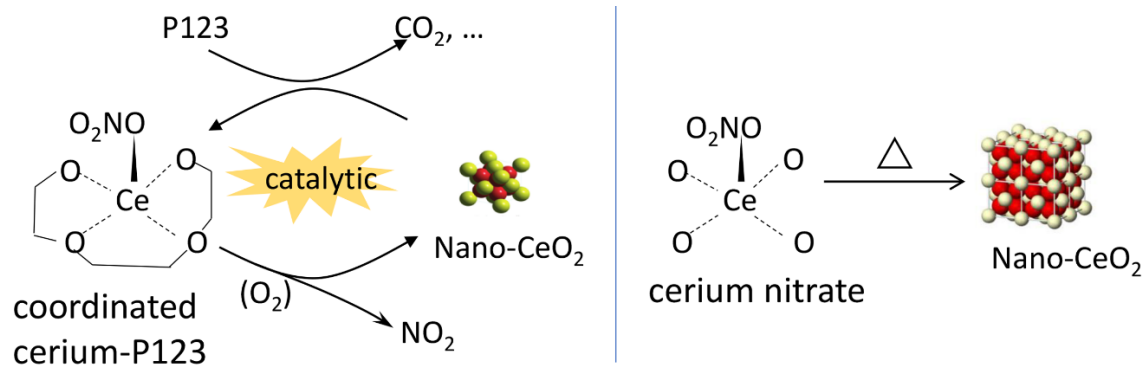
Scheme 4. Calcination of cerium nitrate with (left) or without (right) the assistance of template P123.

Based on the knowledge of the catalytic effect of P123, the synthesis protocol for CeO_2/SBA-15 was modified by application of an inert N_2 atmosphere to further improve the ceria dispersion. Considering the low thermal stability of P123, which decomposes at a temperature of about 115 °C (TGA) in air, the nitrogen atmosphere could delay the decomposition of P123 into carbon chain fragments, thus inhibiting the catalytic oxidation induced formation of ceria nuclei at an early stage until the decomposition temperature of cerium nitrate. Reaching this temperature results in an explosive nucleation of ceria and catalytic decomposition of P123, which is favorable for the formation of a homogeneous nanoscale grain structure.

4.1.5. DeNO$_x$ performance

Figure 20 summarizes the catalytic performance of CeO_2/SBA-15 samples in NH_3-SCR within a temperature range of 100-450 °C. Sample tfSBA-L-CeO_2-air shows the lowest NO conversion (<30 %) over the whole temperature range (see Figure 20(a)) and the lowest N_2 selectivity in the high-temperature range (see Figure 20(b)). The low reactivity in NH_3-SCR is in agreement with that of bare CeO_2 reported previously.[62] Sample asSBA-L-CeO_2-air, which is based on as-made SBA-15 and is calcined in air atmosphere, shows a dramatic improvement in NO conversion and N_2 selectivity, exhibiting a maximum in NO conversion of about 60% at 300 °C. Combining the template interaction with a calcination in inert N_2 atmosphere yields sample asSBA-L-CeO_2-N_2, which shows a further significant increase in NO conversion compared to asSBA-L-CeO_2-air, and even the N_2 selectivity slightly improves. Thus, the NH_3-SCR performance of these three samples follows the order asSBA-L-CeO_2-N_2 > asSBA-L-CeO_2-air >> tfSBA-L-CeO_2-air, which resembles the extent of ceria dispersion on the SBA-15 surface, as discussed above. At high ceria loading, similar trends were observed (see Fig. S4-8), with overall higher

NO conversions compared to low cerium loading. Especially, the N_2 selectivity of asSBA-H-CeO$_2$-N$_2$ was significantly higher than that of asSBA-H-CeO$_2$-air, demonstrating that an inert calcination atmosphere could further improve the CeO$_2$ dispersion and thus the catalytic performance even at high ceria loading.
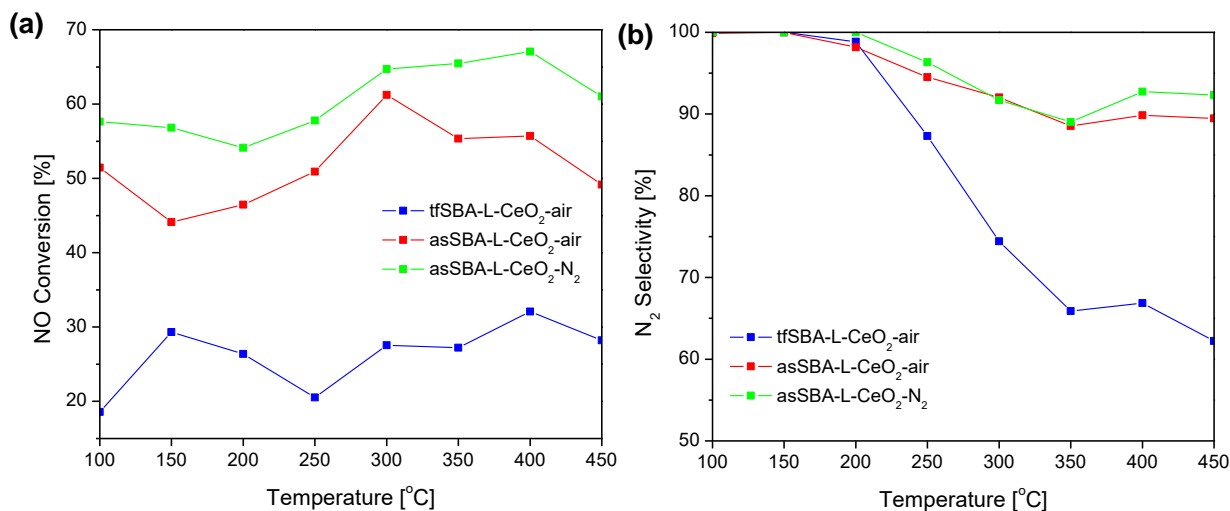
Figure 20. Catalytic performance of CeO$_2$/SBA-15 samples in NH$_3$-SCR. (a) NO conversion and (b) N_2 selectivity. Feed: 500 ppm NO, 500 ppm NH$_3$, 5% O$_2$, balanced with N$_2$; total gas flow: 50 Nml·min^{-1}, GHSV=30000 h^{-1}. The data points were determined based on an average of five gas-phase IR spectra.

4.1.6. Conclusion

Herein, Studies of the synthesis mechanism of CeO$_2$/SBA-15 catalysts are reported by the solid-state impregnation method using a combination of TG and IR gas-phase analysis, as well as *in situ* Raman, DR UV-Vis, and DRIFT spectroscopies. These studies have revealed that ceria formation on mesoporous SBA-15 during calcination involves first cerium precursor decomposition, then migration of cerium species, and finally ceria formation at high temperature. Based on the findings the roles of the template inside the mesoporous matrix can be explained: on one hand P123 acts as a physical barrier to prevent the growth of ceria, on the other, P123 acts as a chemical reactant, which interacts with cerium ions, thus enabling the catalytic decomposition of the cerium precursor.

With the gained mechanistic knowledge of the formation of CeO$_2$/SBA-15 materials, a new calcination protocol was developed based on an intended retardation of the decomposition of the template and the cerium precursor, leading to a higher dispersion of ceria inside the pores and thus a significant improvement of catalytic performance in NH$_3$-SCR.

An important finding of the study is that the precursor itself can facilitate the synthesis of the catalyst, as demonstrated here for a ceria-based catalyst, by using both the template and the gas atmosphere to control the catalytic reaction conditions. The results underline the importance of the details of the calcination process for defining the catalyst properties. Application of *in situ* spectroscopy allows one to monitor the preparation process, including calcination, thus facilitating a rational synthesis of supported catalysts as shown here in the context of NO_x abatement. The outlined approach is expected to trigger more studies on the development of improved catalysts based on a careful design of the catalytic preparation reactions.

4.2. Reaction mechanism of CeO_2/SBA-15 in NH_3-SCR studied by *in situ* DRIFTS

Ceria is known to contain abundant oxygen vacancies and coordinated unsaturated cerium ions on the surface and bulk, providing superior oxidative properties and the potential to function as catalyst for low-temperature NH_3-SCR.[111] Considering the poor NH_3-SCR reactivity of bare CeO_2,[112, 113] composite oxide catalysts were introduced to improve the $DeNO_x$ performance, such as binary systems including CeO_2-MnO_x,[70] CeO_2-TiO_2,[76] CeO_2-WO_3,[114] and CeO_2-MoO_3,[115] ternary systems including CeO_2-WO_3-TiO_2,[116] CeO_2-CuO-TiO_2,[117] CeO_2-MnO_x-Nb_2O_5,[118] or even quaternary catalyst such as CeO_2-MnO_x-Nb_2O_5-TiO_2.[119] While improvements in catalytic performance (NO conversion, N_2 selectivity) were observed, the results reflected different reaction kinetics among these ceria-based catalysts.[18] For example, addition of MnO_x to CeO_2 was reported to improve the redox properties of bare ceria, resulting in high NO conversion but low N_2 selectivity, and to enhance the L-H route compared with bare ceria at low temperatures.[120] On the other hand, modification of CeO_2 with WO_3 was reported to increase the number and strength of acid sites, resulting in a broader operating temperature window but little improved NO conversion.[121] The above examples illustrate that the added oxides promote the reaction differently, highlighting the importance of first clarifying the SCR reaction mechanism on bare ceria to allow for rational development of improved ceria-based SCR catalysts. However, considering the lower activity of bare ceria, its mechanism was rarely explored despite its relevance for the discussion of ceria-based mixed oxide catalysts and the fact that ceria may play multiple roles such as main active site,[70] promotor,[122] and/or support.[65]

Like in many other mechanistic studies on NH_3-SCR, previous work on ceria focused on the following two aspects: (i) The site where NH_3 is adsorbed and activated, i.e., either Lewis acid sites (L acid sites) or Brønsted acid sites (B acid sites). (ii) The reaction route of adsorbed NH_3 was, i.e., either the reaction with gaseous NO to form an NH_2NO intermediate (E-R route) or the reaction with nitrate species to form an NH_3NO intermediate (L-H route). Previous studies on NH_3-SCR over bare ceria concluded that the reaction followed the E-R mechanism,[123] essentially in accordance with the amide-nitrosamine mechanism typically reported for V_2O_5/TiO_2 catalysts.[124] On the other hand, based on kinetic experiments, Zhang et al. concluded that E-R and L-H routes were operative. Besides, CO-pretreated ceria was shown to increase the L-H share,[125] implying the existence of an active NO adsorbate on the ceria surface. To this end, DFT calculations on $CeO_2(110)$[126] and experimental results have demonstrated that the interaction of NO or NO_2 with ceria gives rise to diverse N-containing species.[127] Considering the temperature-dependent distribution of N_xO_y species (such as gaseous N_2O, NO_2, N_2O_4 or adsorbed N_3^-, NO^-, NO, NO^+, nitrite, and nitrate) on the surface,[128] it stands to reason to assume the existence of a L-H mechanism within a specific temperature range, comprising adsorbed NO

species and NH_3 adsorbed on surface acid sites. In principle, L and B acid sites coexist on the ceria surface.[129] However, previous experimental results showed only the presence of L acid sites,[130] which implies that the surface -OH group (B acid sites) show a poor protonation activity. Even for the L acid sites, the acid strength was shown to be weak,[131] which was invoked as reason for the lower catalytic performance. While increasing the ceria acidity was considered to be a good strategy to improve ammonia adsorption,[69] it was further noticed that the increased acid strength would inversely weaken the interaction of NO with the ceria surface. It is therefore essential to identify the contribution of acidity and redox properties of ceria for the catalytic performance in NH_3-SCR, thus providing guidance for the rational development of ceria-based composite catalysts.

Herein, CeO_2/SBA-15 catalysts were prepared by solid-state impregnation. Inert mesoporous SBA-15 was chosen as support material to achieve a higher surface area and thus a larger number of active ceria sites. *Operando* vibrational spectroscopy was applied to monitor the surface dynamics by combining DRIFTS with simultaneous gas-phase FTIR characterization. Kinetic experiments were conducted to explore the contribution of L-H and E-R mechanisms. The results of the combined spectroscopic and kinetic approach provide new insight into the interaction of NO and/or NH_3 with the ceria surface, allowing us to unravel the mechanism of NH_3-SCR over ceria catalysts.

4.2.1. Catalyst preparation

For the preparation of SBA-15,[41] 4.0 g P123 was completely dispersed in a mixture of 120 ml HCl solution (2 M) and 30 ml water in a PP bottle at 35 °C with 250 r/min stirring for 2 h. Then 10 ml TEOS was added at 35 °C with 400 r/min stirring for 20 h. After that the bottle was placed in an oven at 85 °C for 24 h for hydrothermal crystallization treatment. After vacuum filtration, the as-made SBA-15 was calcined in a muffle furnace heated to 550 °C for 12 h (heating rate: 1.5 °C/min). CeO_2 was loaded onto SBA-15 by solid-state impregnation by grinding a mixture of 0.173 g $Ce(NO_3)_3 \cdot 6H_2O$ and 0.108 g SBA-15 under ambient conditions for 30 min. The resulting mixed powder was calcined in air flow at 500 °C for 5 h (heating rate: of 1.5 °C/min). It will be referred to as CeO_2/SBA-15. The specific surface area of CeO_2/SBA-15 was determined as 345 $m^2 \cdot g^{-1}$ (BET method), and the pore volume as 0.447 $cm^3 g^{-1}$ (nitrogen adsorption).

4.2.2. Catalytic performance

Figure 21 depicts the catalytic performance of CeO_2/SBA-15 for the NH_3-SCR reaction at temperatures ranging from 100 to 500 °C. The conversion is characterized by an increase between 100 and 300 °C, a

plateau at 300 - 450 °C (maximum conversion: 58%), and a decline at temperatures > 450 °C. The N_2 selectivity decreased from 100% at 100 °C to 89 - 91% at 300 - 450 °C, and finally to 82% at 500 °C, as a result of increased generation of N_2O.
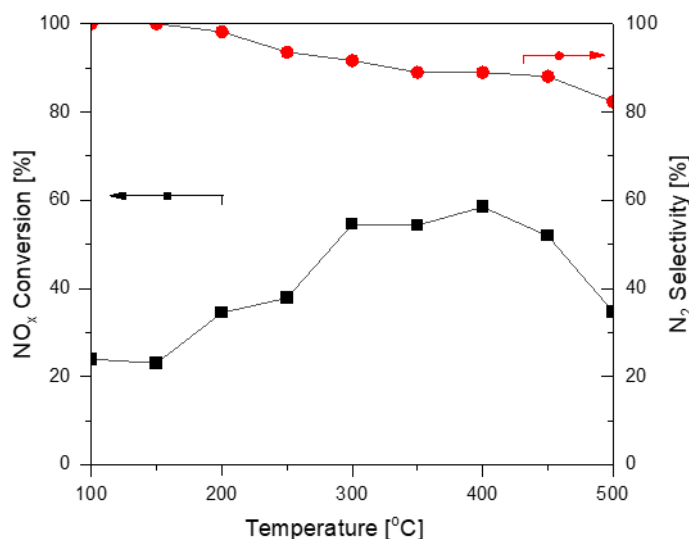

Figure 21. Catalytic performance of CeO_2/SBA-15 for the NH_3-SCR reaction at 100-500 °C. The feed gas composition was 500 ppm NO, 500 ppm NH_3, 5% O_2, balanced with N_2; total gas flow: 50 Nml·min^{-1}, GHSV=60000 h^{-1}.

4.2.3. *Operando* DRIFT spectroscopy

Low temperature adsorption. The *in situ* DRIFT spectra for NH_3 adsorption and $NO+O_2$ co-adsorption over CeO_2/SBA-15 at 200 °C are shown in Figure 22, respectively. The sample was first calcined at 500 °C for 1h for dehydration and then cooled down to 200 °C in N_2+20 % O_2 atmosphere before recording spectrum, which was used as reference.

As presented in Figure 22(a-b) after NH_3 adsorption, three features appear at around 1445, 1600 and 1673 cm^{-1} in the DRIFT spectra, increasing with NH_3 exposure time. In detail, the band at 1600 cm^{-1} is ascribed to the asymmetric deformation mode of coordinated NH_3 to L acid sites, $\delta_{as}(NH_3)$, while the weak features at around 1445 and 1673 cm^{-1} are assigned to the asymmetric and symmetric deformation mode of NH_4^+ bound to B acid sites, $\delta_{as}(NH_4^+)$ and $\delta_{sym}(NH_4^+)$, respectively.[132-134] Correspondingly, the strong peaks at 3281 and 3364 cm^{-1} are attributed to the symmetric and asymmetric stretching mode of N-H of NH_3-L acid sites, v(N-H, NH_3).[135, 136] The other bands at about 3007, 3053, 3160 are tentatively assigned to the N-H stretching vibration interacting with the overtone of $\delta(NH_3)$ via a Fermi resonance. The strong peak at 1513 cm^{-1} is assigned to -NH_2 species resulting from H-abstraction of adsorbed NH_3.[135, 137] which reduces the intensity of the surface M-OH (M=Si and Ce) groups due to

hydrogen bond formation, which is verified by negative peaks of isolated Si-OH at 3740 cm^{-1} and Ce-OH at 3610 cm^{-1}.
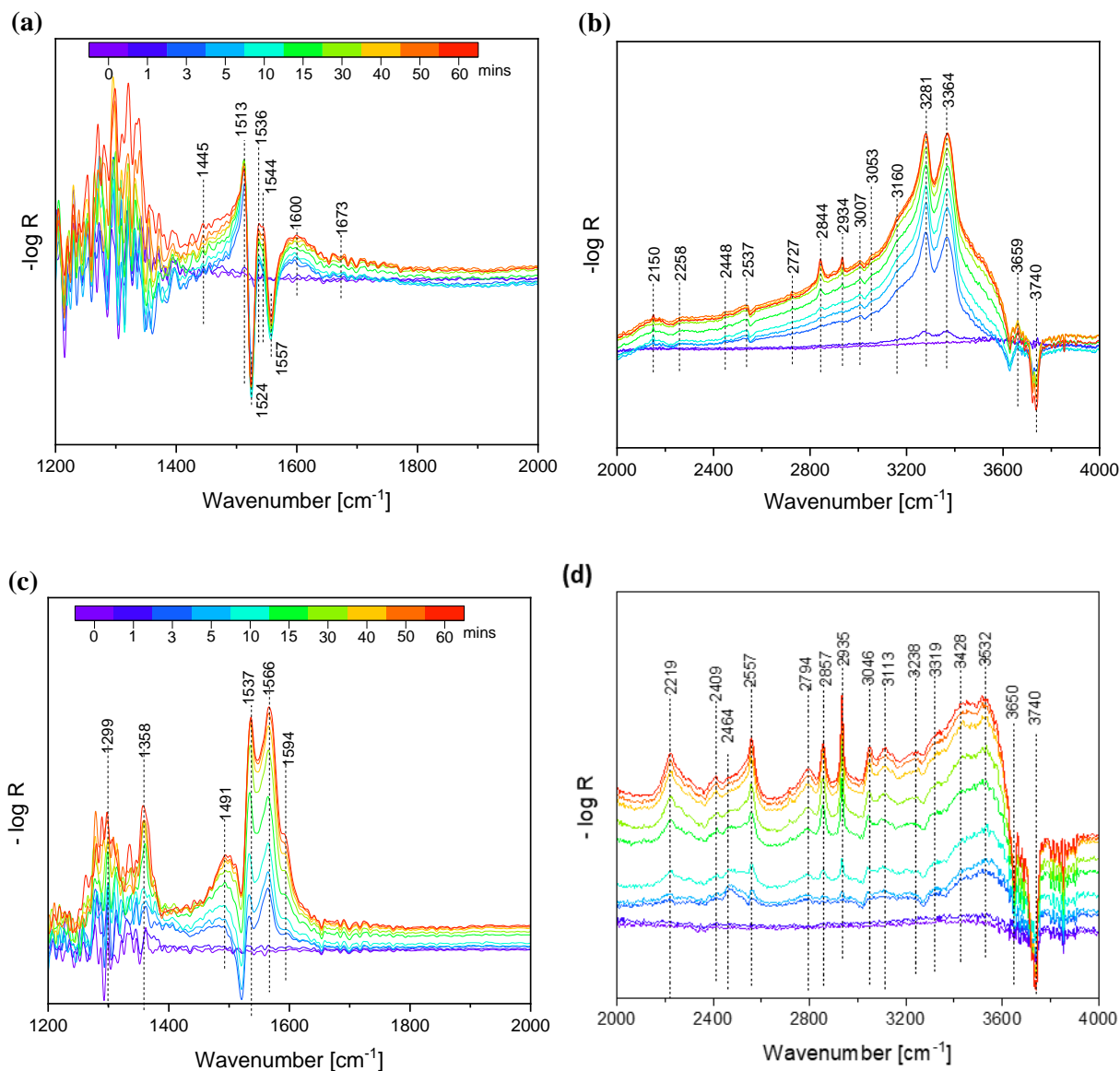
Figure 22. *In situ* DRIFT spectra of CeO$_2$/SBA-15 during (a-b) NH$_3$ adsorption, and (c-d) NO+O$_2$ adsorption at 200 °C.

The bands at 1536 and 1544 cm^{-1} are tentatively assigned to the interaction between NH$_3$ with CeO$_2$ crystal surface. For the NH$_3$ adsorbate, the infrared spectra exhibits typical vibrational modes for N-H of both NH$_3$ and NH$_4^+$ species at 1603 and 1440 cm^{-1}, respectively,[76] which implied no possibility to assign the bands at 1536 and 1544 to these two species. Ramis et al, reported a band at 1480-1490 cm^{-1} after ammonia adsorbed on CuO/TiO$_2$ followed by thermal desorption and assigned it to NO stretching of nitroxyl HNO species.[138, 139] Thus, it is supposed that NH$_3$ molecules are coordinated on Lewis acid

sites Ce^{4+} but bonded with adjacent oxygen site as Ce-O-NH_2 or chelating Ce-[O]$_2$-N by oxidation. In detail, it is noted that the 1536 cm^{-1} band appeared at 3 min and 1544 cm^{-1} band at 15 min, and the NH_2 feature at 1513 cm^{-1} turned to decrease at 15 min. Thus, a two-step process was deduced in which NH_3 is adsorbed first on L acid site Ce^{4+} and then oxidized by adjacent lattice oxygen to Ce-O-NH_2 in a fast step. Furthermore, the monodentate Ce-O-N species is further oxidized to be chelating bidentate Ce-[O]$_2$-N with slower rate according to:

In addition, the negative peaks at 1524 and 1575 cm^{-1} are attributed to the monodentate and bidentate nitrate, which are residual from the preparation process and interact with NH_3. Thus, the adsorbed NH_3 on the metal site is suggested to be oxidized by the lattice oxygen and then generates an O-N vibration. It should be noted that the continuous increase of features at 3281 and 3364 cm^{-1} for NH_3-L acid sites proves that the lattice oxygen reservoir is limited and the majority of ammonia is still adsorbed on cerium cations in such a reductive atmosphere.

There are two weak features at 2150 and 2258 cm^{-1}, which are tentatively assigned to the stretching mode of N≡N, ν(N≡N), differing in their anchoring sites. Previously, regarding the detailed assignment of features in the range of 2100-2300 cm^{-1}, Martra et al. assigned these to N_2^- ions,[140] while Matyshak et al. assigned a similar band at about 2200 cm^{-1} to adsorbed N_2O (asymmetric N-N-O stretching),[141] which is close to the typical feature of the gas phase N_2O vibration at about 2216/2234 cm^{-1}.[142] On the other, the negative inductive effect of O-N_2 should also cause a higher wavenumber than the positive inductive effect of Ce-N_2. Thus, the two bands at about 2150 and 2258 cm^{-1} observed for NH_3 adsorption (Figure 22 (b)), are tentatively assigned to the Ce-N≡N and O-N≡N, respectively.

There are two possible routes for the dinitrogen formation from ammonia. According to Route I, first hydrazine forms from two NH_3, followed by H-abstraction on the surface,[134]

$$2Ce^{4+} + 2NH_3 \rightarrow 2Ce^{3+} - (N_2H_4) + 2H^+ \rightarrow 2Ce^{3+} - (N_2) + 6H^+ \qquad (4\text{-}4)$$

Another possible process is that the NH_3 is oxidized to bind to oxygen sites and then reacts with the second NH_3 to form a N≡N bond (Route II),

$$Ce^{4+}\text{-}O + 2NH_3 \rightarrow Ce^{3+}\text{-}[O]_2\text{-}N + 3H^+ + NH_3 \rightarrow \text{Ce-O-}N_2 + 6H^+ \qquad (4\text{-}5)$$

The abstracted H^+ from NH_3 combined with surface Si-OH groups to form H_2O, which resulted in a decrease of the intensity at 3740 cm^{-1}. The band at 3659 cm^{-1} assigned to Ce-OH, increased, which is attributed to the reduction of Ce-O by NH_3.

For the former route I, Amores et al. compared the ammonia and hydrazine adsorption and oxidation behavior on the metal oxides and proposed that one hydrogen could easily be removed from ammonia giving rise to radical-like NH_2 species (band at 1513 cm^{-1}),[134] which can undergo a radical-like coupling, giving rise to hydrazine, which is easily oxidized further to nitrogen by high-valence cations like Ce^{4+}. For the latter route II, NH_3 is oxidized as nitrate/nitrite like species (bands at 2448/2537/2727 cm^{-1}) and anchored to surface lattice oxygen (bands at 1536/1544 cm^{-1}) was proved above, and then the NO_x species reacts with another NH_3 following the L-H mechanism of the SCR reaction. Thus, both routes offer a reasonable explanation for the formation of N≡N containing species.

Another interesting point is the presence of the peaks near 2844 and 2934 cm^{-1} (in Figure 22(b)) which are typically assigned to C-H stretching mode.[143] However, these peaks exhibited an increased intensity with NH_3 exposure time, in conflict with this assignment. Considering the combination v_1+v_3 modes (v_1=1322 cm^{-1} for symmetric N-O stretching and v_3=1616 cm^{-1} for asymmetric N-O stretching) of NO_2 observed at 2905 cm^{-1},[144] the peaks could be assigned to bidentate nitrito -[O]$_2$-N vibration for the deeply oxidized NH_3, as described above.

As presented in Figure 22(c) after NO+O$_2$ co-adsorption, peaks appear at 1491 and 1537 cm^{-1}, 1299 and 1566 cm^{-1}, and 1594 cm^{-1} which were assigned to monodentate, bidentate, and bridging nitrate vibration, respectively.[132, 145] The peak at 1358 cm^{-1} was attributed to the NO$^-$ or dimer $N_2O_2^{2-}$ species, which was tend to adsorb on strong reductive sites.[128, 146] In Figure 22(d) there are various features increasing in intensity with NO+O$_2$ adsorption. The peak at 2219 cm^{-1} was assigned to the N≡O vibration of adsorbed NO$^+$ species.[147, 148] The band at 2557 cm^{-1} was attributed to NO_2^-, while the bands at 2409 and 2794 were assigned to NO_3^-.[149] The peaks at 2857 and 2935 cm^{-1} were assigned to NO_2 species resulting from oxidation of NO.[150, 151] The bands in the range of 3046-3532 cm^{-1} were all attributed to vibrations of the -OH group linked to NO_x species as HNO_x.[152] The bands at 3650 and 3740 cm^{-1} were assigned to vibrations of the Ce-OH and Si-OH species, respectively. After the adsorption of NO+O$_2$, the negative intensities for both Ce-OH and Si-OH indicate a decrease of these species due to the oxidation of the surface and the desorption of H_2O, which is consistent with the increasing negative noise features for adsorbed water.

The adsorption results of both NH_3 and NO+O$_2$ suggest the high reactivity of surface lattice oxygen of ceria oxidized both NH_3 and NO to various N_xO_y species, which exhibited vibrational features in the fingerprint range below 2000 cm^{-1} and in the characteristic range above 2000 cm^{-1}. In addition, for the

same species, different binding sites (O- or Ce- site) give rise to distinct IR features in the spectrum. It was deduced that NH_3 mainly coordinated on L acid site Ce^{4+} cation and $-NH_2$ species formed via H-abstraction by oxidation interaction on the surface. Most importantly, ammonia transforms on a Ce-site ($Ce-NH_3$) to a nitro-nitrito species ($[Ce-O]-NH_2$) and finally to a nitrato species on an O-site ($Ce-[O]_2-N$).[128] These two types of coordinated sites also give rise to the definition of two kinds of dinitrogen species as N_2^- and N_2O. For the $NO+O_2$ adsorption, diverse N_xO_y species are expected to be formed with different oxidation states and coordination structures on the surface sites.

Thermal stability. In this experiment, the $CeO_2/SBA-15$ sample was pretreated in NH_3 or $NO+O_2$ for 1h at room temperature to reach a saturated adsorption state, and was then, while keeping the gas flow, subjected to increasing temperatures from 25 to 400 °C. In-situ DRIFT spectra were recorded to explore the thermal stability of the adsorbed species as shown in Figure 23. The sample exposed to N_2 at 25 °C was used to measure the background spectrum.
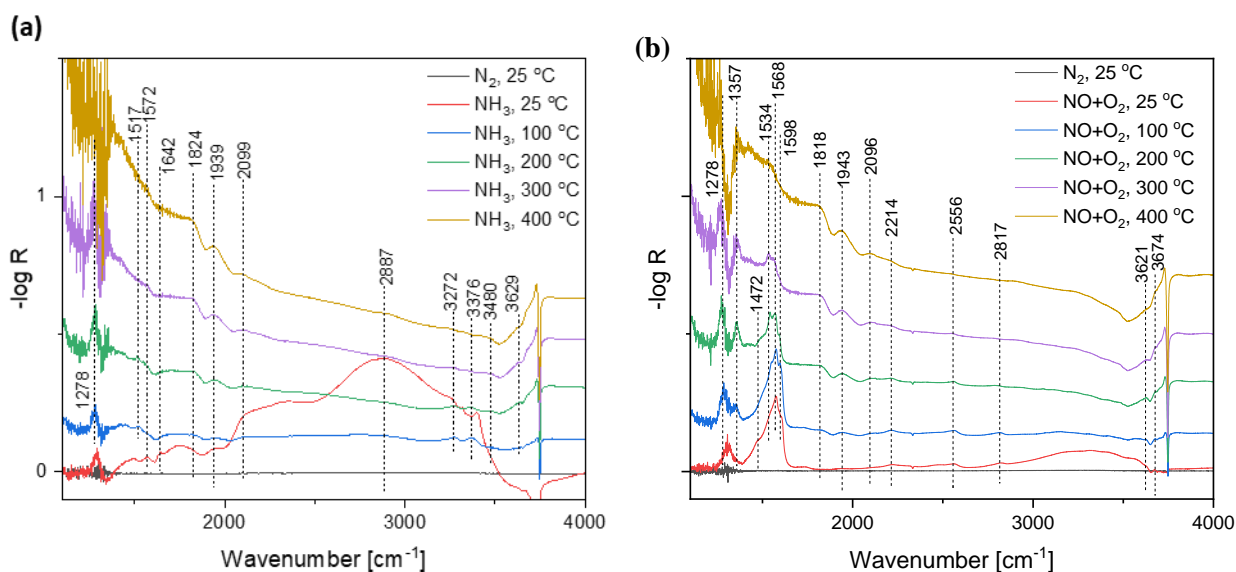
Figure 23. *In situ* DRIFT spectra of $CeO_2/SBA-15$ exposed to (a) NH_3, and (b) $NO+O_2$ at increasing temperature within 25°C-400 °C.

Figure 23(a) shows the spectra of surface species after NH_3 adsorption at increasing temperatures. The spectrum at room temperature is characterized by a broad and strong band at 2887 cm^{-1} due to the formation of nitric acid hydrates at room temperature.[153] The peaks at 3258, 3320, and 3399 cm^{-1} are assigned to the N-H stretching of adsorbed NH_3 on L acid sites. With the temperature increasing, these three peaks are blue-shifted to 3272, 3376, and 3480 cm^{-1}, which indicates the shortening of N-H bonds and is further attributed to $-NH_2$ generated for the preliminary oxidation of NH_3, consistent with

computational results.[129] The decreasing intensity with temperature rising from 100 to 400 $^{\circ}$C implies that NH$_3$ adsorbed on the surface is not stable at high temperature. The features at 1824 and 1939 cm^{-1} were assigned to N-O stretching of nitrosyl,[128] and the peak at 2099 cm^{-1} was assigned to adsorbed NO$_2$,[154] all of which show that NH$_3$ on L acid sites (Ce^{4+}) prefers to be oxidized as NO$_x$ by binding to oxygen sites via N-O bonds. Their increased intensity with increasing temperature indicates the disappearance of ammonia or amine at high temperature is mainly attributed to an enhanced oxidation of NH$_3$ on the surface.

In Figure 23(b), the adsorption of NO+O$_2$ at room temperature results in typical bands at 1534, 1568, and 1598 cm^{-1}, attributed to monodentate, bidentate and bridging nitrate vibrations, respectively. It can be seen that the bands decrease with increasing temperature due to decomposition of nitrate. On the other hand, the appearance and enhancement of features at 1357 cm^{-1} (NO$^-$), 1818 and 1943 cm^{-1} (v(N-O)),[128, 155] and 2096 cm^{-1} (NO$_2$) indicate that the NO adsorbed on Ce^{3+} sites is thermally stable, while the O^{2-} site bound NO leads to the formation of oxidated products including nitrate (1534-1598 cm^{-1}), NO$_2$ (2214 cm^{-1}), and NO$_2^-$ (2556 cm^{-1}), which decrease in intensity with increasing temperature. The spectrum at room temperature shows a feature at about 1750 cm^{-1} due to NO dimers.[128] With increasing temperature, two peaks at 1818 and 1943 cm^{-1} are observed due to N-O stretching of mononitrosyl, as well as bands at 2096 cm^{-1} for NO$_2$ and at 1357 cm^{-1} for NO$^-$ species. It is found that the N-bound species all show a positive correlation with temperature which may be explained based on the highly oxidized Ce^{4+} ions and the stronger coordinative N-Ce^{4+} bond. The empty orbital of Ce 4f and Ce 5d also decreased the π-back donation of N=O, which reduces v(N-O) but strengthens the coordinated bond. Thus, it is deduced that NO can be adsorbed both on oxygen sites as N-O-M^{n+} and on metal cation as N-M^{n+}. It is also found that the O-bound products at low temperature contain nitrogen with high oxidation state (+III or +V), while that of N-bound NO$^-$ at higher temperature contain nitrogen (+I) with low oxidation state. It is further deduced that the reduction of NO to NO$^-$ is associated with a high reaction barrier and the reduction product NO$^-$ is more reactive than the oxidation products NO$^+$, NO$_2^-$, or NO$_3^-$.

The temperature behavior of adsorbed NH$_3$ may be illustrated by ammonia being mainly adsorbed on L acid sites at low temperature, while increased temperature would promote the oxidation of NH$_3$ via hydrogen abstraction, probably contributing to the different products. In case of NO+O$_2$, it is found that both N-bound nitrito and O-bound nitro species are formed. At low temperature, NO prefers to adsorb onto oxygen sites to form nitrate species (+V) or NO$^+$ (+III), while at increasing temperature, NO tends to interact with cerium cations by accepting electrons to form coordinated N-bound nitrosyl (+I).

Interaction between NH₃ and NOₓ. In this experiment, catalyst samples were pretreated in 500 ppm NH₃ (balance N₂) at 200 °C for 60 min followed by exposure to a gas mixture of 500 ppm NO / 5% O₂ (balance N₂), or pretreated in 500 ppm NO / 5% O₂ (balance N₂) at 200 °C for 60 min, followed by exposure to a gas mixture of 500 ppm NH₃ (balance N₂), as shown in Figure 24. The sample exposed to N₂ at 200 °C was used to measure the background spectrum.
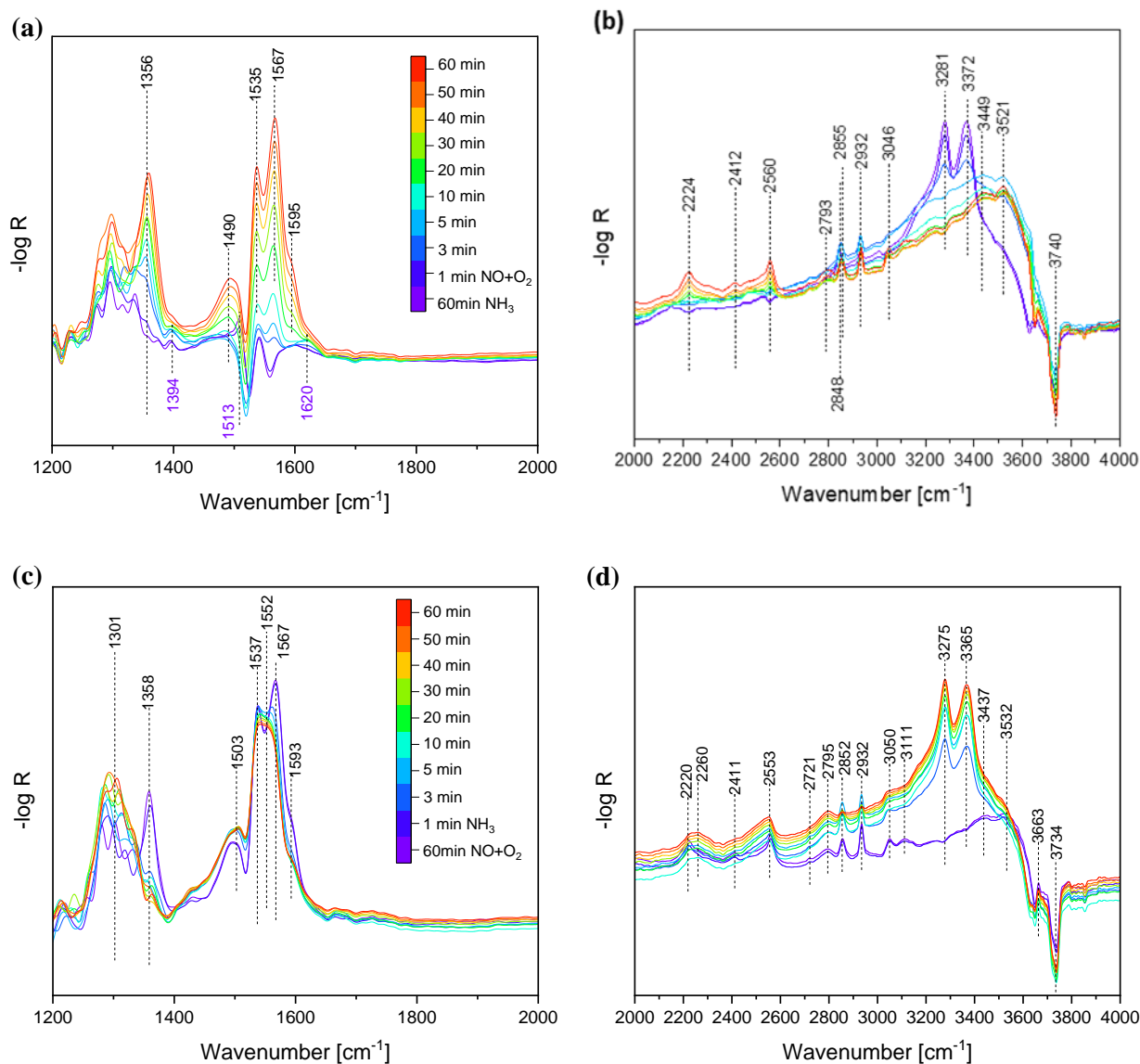

Figure 24. *In situ* DRIFT spectra of CeO₂/SBA-15 during (a-b) NH₃ reaction with pre-adsorbed NOₓ, and (c-d) NOₓ reaction with pre-adsorbed NH₃ at 200 °C.

As presented in Figure 24(a), exposure to NO+O₂ leads to reaction with adsorbed NH₃ and the peaks for -NH₂ (at 1513 cm⁻¹) disappears within 3 min exposure, after which the spectra show a similar behavior as for NOₓ adsorption in Figure 22(c-d). This indicates that the adsorbed -NH₂ should be the active species to react with NOₓ. It is worth noting that the relative intensity of the peak at 1358 cm⁻¹ for

NO$^-$ species is higher than that in Figure 22(c). The reason is that the NH$_3$ pre-treated surface owns more reduced Ce^{3+} sites, allowing for more NO adsorption and electron acceptance facilitating NO$^-$ formation.

In Figure 24(b), the peaks at 3281 and 3372 cm^{-1} attributed to the L acid site coordinated NH$_3$ disappear after 10 mins exposure to NO+O$_2$ gas. Thus, it can bes deduced that L acid sites rather than B acid sites should be the active adsorption sites for ammonia. In addition, the peaks of -ON$_2$ species (at 2260 cm^{-1}) and N$_2^-$ species (at 2150 cm^{-1}) disappears due to competitive adsorption of NO$^+$ (at 2220 cm^{-1}) and NO$^-$ (at 1356 cm^{-1}) by NO adsorption on oxygen sites and metal cation sites, respectively. The peak for NO$_2$ (at 2848 cm^{-1}) is blue-shifted to 2855 cm^{-1} after reaction indicating a structural change from bridged O$_{lattice}$-N-O$_{lattice}$ to monodentate nitrite O$_{lattice}$-N-O, in agreement with the formation of NO$_2^-$ (at 2560 cm^{-1}) after 5 min, and upon further oxidation, of NO$_3^-$ (at 2411 and 2795 cm^{-1}) after 20 min, indicating that the surface adsorbed NH$_3$ is oxidized to NO$_x$ species.

In Figure 24(c), NH$_3$ reacting with adsorbed NO$_x$ species results in the fast disappearance of the peak at 1358 cm^{-1} (NO$^-$ or N$_2$O$_2^{2-}$ species),[128] while the peaks for nitrate species (1503-1593 cm^{-1}, 1301 cm^{-1}) show little change after reaction with NH$_3$. This implies that N$_2$O$_2^{2-}$ or NO$^-$ should be the active NO$_x$ species which is able to react with NH$_3$ via the L-H route. The discrete peaks for monodentate (1537 cm^{-1}) and bidentate (1567 cm^{-1}) nitrate transform into a broad band at about 1552 cm^{-1}, indicating that the ammonia iss adsorbed on the surface and oxidized by lattice oxygen to HNO$_x$ species (1544 cm^{-1}) the signal of which overlaps with the original NO$_x$ signal. In the 2000-4000 cm^{-1} range (see Figure 24(d)), the appearance of peaks at 3275 and 3365 cm^{-1} due to N-H stretching of coordinated NH$_3$ in L acid sites indicates the competitive adsorption of NH$_3$. A broad band at about 2220-2260 cm^{-1} is observed, including intact NO$^+$ (at 2220 cm^{-1}) and newly generated dihydrogen -ON$_2$ species (at 2260 cm^{-1}), indicating that NO$^+$ species is inert towards reaction with NH$_3$, and that excessive NH$_3$ is anchored to the oxygen sites. The absence of a band at about 2150 cm^{-1} implies that the route via hydrazine, interacting with metal cations and forming N$_2^-$, is blocked in this case. The reason might be attributed to the activated surface by NO$_x$ occupying the metal cation sites, preventing the generation of hydrazine-M^{n+}. The peaks at 2852 and 2932 cm^{-1} are assigned to NO$_2$ resulting from NO bound to the M-O site as M-O-NO. It is found that with NH$_3$ proceeding, these two peaks gradually disappear. Combining the changes at 1358 cm^{-1}, 2220-2260 cm^{-1} and 2852-2932 cm^{-1}, it is deduced that NO adsorbs on the oxides surface to form N-bound Ce-NO 1358 cm^{-1}) and O-bound Ce- ONO$^+$ (2220 cm^{-1}). The former one (Ce-NO species) can react with H-abstracted NH$_3$ (Ce-O-NH$_2$) to from N$_2$+H$_2$O, or react with over-oxidized NH$_3$ (Ce-(O$_2$)-N)) to form N$_2$O species (2260 cm^{-1}), while the latter one (Ce-ONO species) is further oxidized to NO$_2^-$ (2553 cm^{-1}) and NO$_3^-$ (2411 and 2795 cm^{-1}), which are inert towards NH$_3$.

Thus, from the *in situ* IR spectroscopic analysis of the interaction of NH_3 and $NO+O_2$, NH_2 and NO^- are evidenced to be the active species for adsorbed NH_3 and NO_x. In detail, NH_3 prefers to adsorb on L acid sites (Ce cation), is oxidized to NH_2 and finally consumed by NO quickly. The other species (such as unoxidized NH_3, dinitrogen species) seems to be oxidized by oxygen to yield NO_x. The adsorption of NO forms a variety of N_xO_y species, of which NO^- can react with ammonia via the L-H route, while the NO_2^- and NO_3^- are inactive.

Temperature dependent NH_3-SCR. Figure 25 shows *in situ/operando* DRIFTS results of CeO_2/SBA-15 exposed to NH_3-SCR reaction conditions at various temperatures increasing from room temperature to 450 ^{o}C. The sample exposed to expgas at 25 ^{o}C was used to measure the background spectrum.

At room temperature, the bands at 1604 cm^{-1} and 3281, and 3369 cm^{-1} are assigned to NH_3 on L acid sites, while the bands at 1532 and 1572 cm^{-1} and a weak shoulder band at 1590 cm^{-1} aree assigned to O-bound nitrate species. The feature at 1358 cm^{-1} is attributed to N- bound NO^- on the metal cation. With increasing temperature, the amount of adsorbed ammonia decreases, in agreement with the desorption peak of ammonia at the heating steps (Figure 25(b)), which further shows that the amount of adsorbed NH_3 is sufficient at low temperatures (100-250 ^{o}C); at higher temperatures the disappearance of NH_3 is due to its oxidation to form irreversibly N_xO_y species instead of desorption, accounting for the low level of NH_3 concentration in the exhaust. The band at 1513 cm^{-1} (-NH_2) is absent, as compared with NH_3 adsorption, implying that the H-abstraction of NH_3 to NH_2 might be the rate determining step. The nitrate-related features (1500-1600 cm^{-1}) increase at low temperature (100-200 ^{o}C), followed by decomposition at 200-500 ^{o}C. Especially, only monodentate NO_x exists at high temperature and the other two structural nitrates have disappeared. The feature at 2222 cm^{-1} is assigned to the stretching mode of -NO^+ species on M-O- sites. The unchanged band explains that NO^+ is formed due to NO adsorption on oxygen sites, but does not react with NH_3. Another band resulting from NO adsorption is observed at 1358 cm^{-1} which originates from NO^- on reduced Ce^{3+} sites. Although the NO^- was active to react with NH_3, the residual of NO^- on the surface implies that the NH_3 is not sufficient, which is consistent with the absence of NH_2 species.

Figure 25(b) shows that N_2O is formed at lower temperatures such as 200 ^{o}C. It has been discussed in the literature that the production of N_2O was due to the over-oxidation of NH_3 at high temperature. Here, more details are provided which show that NH_3 is coordinated to a Ce site first, and one H is abstracted by lattice O yielding a Ce-O-NH_2 species which further reacts with gaseous NO or adsorbed NO^- to form an NH_2NO intermediate finally N_2 and H_2O. However, the Ce-O-NH_2 can be over- oxidized

by near-neighbor lattice O to Ce-[O]$_2$-N, which reacts with gaseous NO to form chelating coordinated [O]$_2$-N-N-O, and then desorbed as N$_2$O.
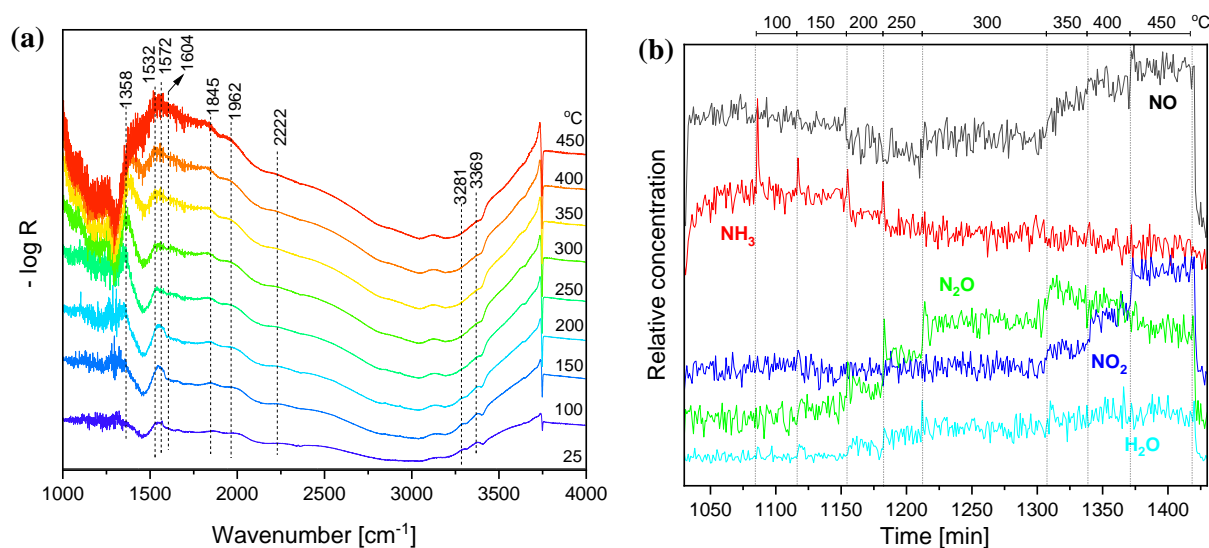

Figure 25. (a) *In situ/operando* DRIFT spectra and (b) simultaneous gas phase FTIR analysis over CeO$_2$/SBA-15 upon exposure to NH$_3$-SCR reaction conditions: 500 ppm NH$_3$, 500 ppm NO, 5% O$_2$ and N$_2$ balanced. The gas flow rate is 50 NmL/min with GHSV=60000 h^{-1}.

4.2.4. Kinetics

As discussed above, for the SCR reaction an E-R route and a L-H route have been proposed. Here, a simple model for the reaction rate is established,

$$r_{tot} = r_{E-R} + r_{L-H} \tag{4-6}$$

where the r_{tot}, r_{E-R}, and r_{L-H} represent the rate of the total reaction, the reaction via the E-R route, and the reaction via the L-H route, respectively. Considering that the gas reactions involve adsorption and reaction steps, and a large amount of source gas is provided to ensure a sufficient number of reactant molecules adsorbed on the surface, then the reaction orders of the adsorbed reactants are 0 and that of gaseous reactants aree 1. Thus, one obtains,

$$r_{tot} = k_{E-R}[NO] + r_{L-H} \tag{4-7}$$

Here, the k_{E-R} is the rate constant for the E-R route and [NO] represents the gaseous NO concentration which is approximately equal to the inlet gas concentration. From the equation, the reaction rate is known to be proportional to the NO concentration. Therefore, a series of gas mixtures with varying NO concentration (500 ppm NH$_3$ / 5% O$_2$ with 100 to 600 ppm NO) was applied to CeO$_2$/SBA-15 to examine the reaction rates, as shown in Figure 26(a). The reaction rate was found to

show an approximate linear relationship with NO concentration in the gas mixtures. The slope follows the order: 200 °C < 300 °C < 400 °C. From equation (4-7), it is known that the slope is associated with the rate constant of the reaction via the E-R route, and the intercept with the reaction rate via the L-H route although there is no physical meaning to set [NO] to zero. Thus, the data were only fitted at higher concentrations (400-600 ppm) to obtain the values of k_{E-R} close to the applied NH$_3$-SCR reaction conditions. Then, r_{E-R} and r_{L-H} can be calculated by k_{E-R}[NO] and r_{tot} - k_{E-R}[NO] by substituting [NO]=500 ppm, respectively. (Figure 26(b).
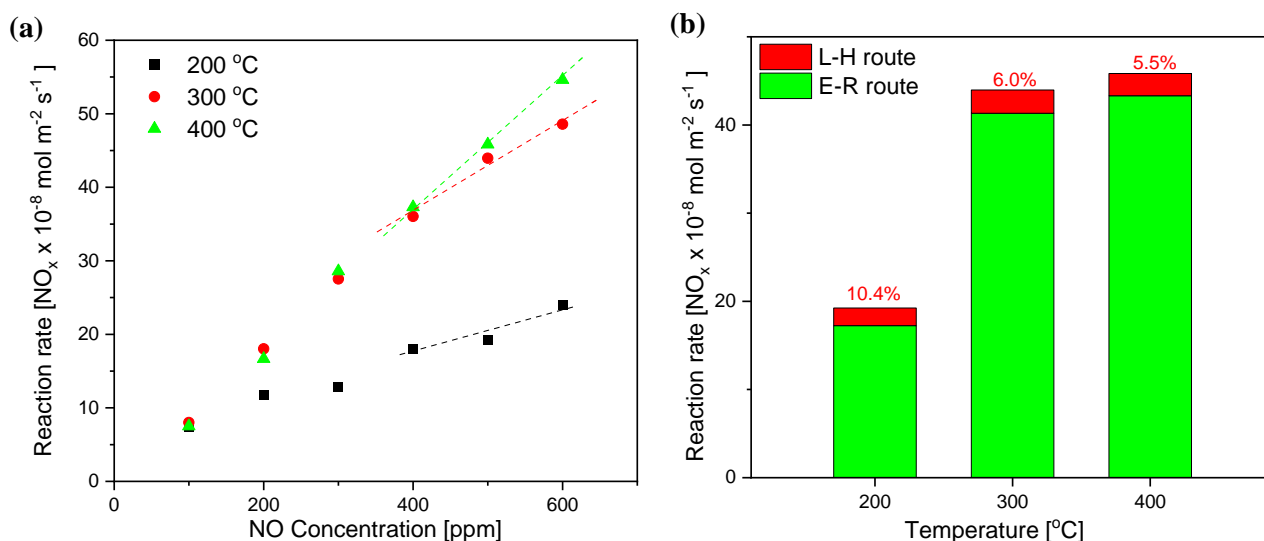
Figure 26. (a) NH$_3$-SCR reaction rate for CeO$_2$/SBA-15 upon exposure to gas mixtures with NO concentrations from 100 to 600 ppm. (b) Contribution of the L-H and the E-R route to the total reaction rate.

Figure 26(b) shows the contribution of the L-H route to the total reaction at different temperatures. It is apparent that at low temperature (200 °C), the L-H mechanism contributes 10.4 % to the NO conversion, while at temperatures of 300 °C or even 400 °C, the contribution of the L-H route decreases to less than 6 % of the whole reaction rate, which explains why some previous works that NH$_3$-SCR on bare ceria follows only the E-R route.[28, 66, 125]

4.2.5. Reaction mechanisms

Based on the discussion above, an outline of the NH$_3$-SCR reaction on ceria can be provided. In broad terms, the reaction proceeds via two mechanisms, the E-R and L-H routes, simultaneously. The E-R mechanism plays the main role and involves the adsorption of NH$_3$ which then reacts with gaseous NO, while the L-H mechanism involves two adsorbed molecules, NH$_3$ and NO, which react on the surface

and contributes especially at low temperatures. The proposed reaction mechanism is shown in Scheme 5.
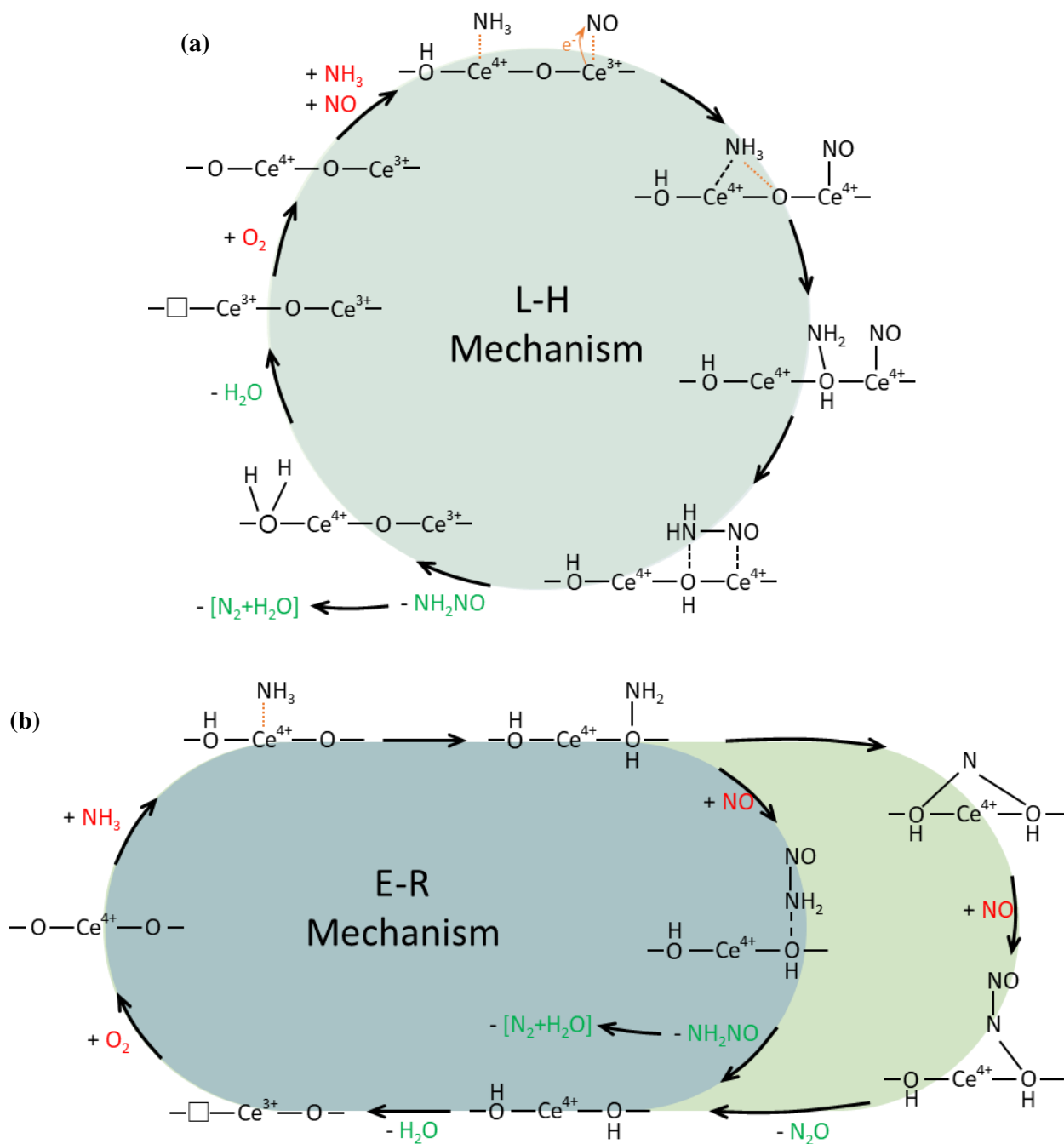
Scheme 5. Proposed NH₃-SCR mechanism over CeO₂/SBA-15 catalysts according to the (a) L-H route and (b) E-R route.

For the L-H mechanism, NO and NH_3 are adsorbed on the ceria surface at different sites. NH_3 owns a lone electron pair as electron donor to coordinate with a cerium cation. NO can be adsorbed on different surface sites forming a variety of N_xO_y species, of which NO⁻ which accepts one electron from a reduced

Ce^{3+} ion shows a high reactivity to ammonia. Thus, an adjacent cerium ion pair is necessary for providing nearby activated sites. NH_3 is oxidized by adjacent oxygen to NH_2 anchoring on the O sites which are in closer distance to the adsorbed NO^- group. By reaction of adjacent NH_2 and NO, a N-N bond is formed, leading to NH_2NO as an intermediate which may desorb from the surface and further decompose to N_2 and H_2O. With temperature increasing, the NH_2 is further H-abstracted as bidentate Ce-$[O]_2$-N and thus the L-H route is inhibited due to the increased distance between the adsorbed Ce-$[O]_2$-N and NO. On the other hand, during the H-abstraction of NH_3, the surface O or surface -OH may further react to -OH and H_2O which is desorbed from the surface and forms an oxygen vacancy $V_O^{\cdot\cdot}$, which is re-oxidized by oxygen from the gas phase.

For the E-R mechanism, NH_3 is also adsorbed on the L acid sites (cerium cation) and is oxidized to NH_2 (O site), which then further reacts with gaseous NO to form an NH_2NO intermediate which desorbs from the surface leading to N_2 and H_2O. However, at high temperature, the adsorbed NH_2 may be over-oxidized to chelating Ce-$[O]_2$-N by two adjacent oxygen ions, which by reaction with gas phase NO via E-R route can form N_2O at high temperature. Similarly to the L-H mechanism, the oxidation of NH_3 results in the formation of oxygen vacancies which are re-oxidized by gas phase oxygen.

4.2.6. Conclusion

In situ DRIFT spectroscopy was applied to CeO_2/SBA-15 catalysts exposed to different gas compositions and temperatures related to the NH_3-SCR reaction. The results provide deep insight into the mechanism of the SCR reaction on ceria catalysts. Firstly, it is evidenced that both E-R and L-H mechanisms coexist on the surface, especially at low temperatures. In detail, NH_3 is adsorbed on oxidative sites and transformed into active NH_2, which can react with adsorbed NO via the L-H route and with gaseous NO via the E-R route. Furthermore, in the low-temperature range, the oxidation of NH_3 by surface lattice oxygen might be rate-determining rather than the poor acidity or the adsorption of ammonia. The H-abstracted O-NH_2 can quickly react with NO to form first NH_2NO and then N_2 and H_2O products, while over-oxidized NH_3 can produce chelating nitrito -$[O]_2$-N which reacts with NO to form N_2O at high temperature.

5. Synthesis of binary ceria-based catalysts and their application for NH₃-SCR

In the previous studies, the P123-assisted solid-state impregnation method was adopted to prepare CeO$_2$/SBA-15 materials and used *in situ* spectroscopy to elucidate the role of P123 in the loading of CeO$_2$ on SBA-15.[41] However, due to the overall poor NH$_3$-SCR reactivity of CeO$_2$-only catalysts,[112, 113] bimetallic oxides were added to form MO$_x$-CeO$_2$ catalysts, such as WO$_3$-CeO$_2$, TiO$_2$-CeO$_2$, MnO$_x$-CeO$_2$, and so on, which were reported to own improved NH$_3$-SCR reactivity due to synergistic effects. Thus, the goal was to prepare bimetallic oxides on mesoporous SBA-15 and then apply them to the NH$_3$-SCR reaction.

Herein, firstly, a preliminary screening was performed by preparing various CeO$_2$-MO$_x$ mixtures supported on SBA-15 in order to identify possible SCR-active combinations. After that, copper oxide was added to form CuO-CeO$_2$/SBA-15 binary oxide catalysts, which are expected to improve the NH$_3$-SCR performance due to the redox equilibrium Ce^{3+}+Cu^{2+} ↔ Ce^{4+}+Cu$^+$.[156] It is a challenge to disperse bimetallic oxides on mesoporous supports. Here, the SSI method is adopted for the preparation of CeO$_2$-CuO/SBA-15 catalysts and the role of P123 is explored in controlling the synthesis conditions, as well as the resulting product structures and NH$_3$-SCR performances. To unravel the synthesis mechanism and to relate the preparation to the catalytic performance, *in situ* DRIFT, DR UV-Vis, and Raman spectroscopies are employed, besides online FTIR monitoring of the gas-phase composition. Similarly, MnO$_x$-CeO$_2$/SBA-15 catalysts are prepared accompanied by *in situ* characterization. Interestingly, a higher reactivity was observed compared with CuO-CeO$_2$/SBA-15 catalysts. Finally, the mechanism of NH$_3$-SCR over MnO$_x$-CeO$_2$/SCR was studied in detail by *in situ* DRIFT spectroscopy.

5.1. Exploring bimetallic oxides supported on SBA-15 for NH₃-SCR applications

As noted above, ceria itself can not satisfy current DeNO$_x$ requirements and thus bimetallic oxides are widely applied to the NH$_3$-SCR. This involves the question of how to choose a suitable second metal element to improve the catalytic reactivity of ceria. To evaluate possible promotion of material properties,[157] five metal oxides (CuO, MnO$_x$, NiO, MgO, and La$_2$O$_3$) were tested in combination with ceria. Among them, Cu ($3d^{10}4s^1$) has the redox pair Cu$^+$/Cu^{2+}, Mn^{n+} ($3d^54s^2$) shows various valence of the manganese element, Ni^{n+} ($3d^84s^2$) also shows several valent species (Ni^{1+}, Ni^{2+}, Ni^{3+}), Mg^{2+} ($3s^2$) is an alkaline-earth metal, and La^{3+} ($6s^25d^1$) is a rare earth metal. The former three metal elements can adjust both the acidity and redox properties in different degrees, while the latter two show lower but permanent valence which only makes effect on the acidity.

5.1.1. Sample preparation

Silica SBA-15 was prepared as described previously.[158] 0.173 g Ce(NO$_3$)$_3$·6H$_2$O (0.4 mmol) was used as ceria precursor. 0.100g Mn(NO$_3$)$_2$ 4H$_2$O, 0.096 g Cu(NO$_3$)$_2$ 3H$_2$O, 0.116 g Ni(NO$_3$)$_2$ 6H$_2$O, 0.103 Mg(NO$_3$)$_2$ 6H$_2$O, and La(NO$_3$)$_3$ 6H$_2$O was adopted as the second metallic oxide precursor and the prepared samples are denoted as CeMO (M=Mn, Cu, Ni, Mg, La), respectively. The moral ratio of Ce: M is equal to 1:1. The solid-state impregnation (SSI) method was applied to load the bimetallic oxides on 0.108 g SBA-15. As a reference, 0.346 g Ce(NO$_3$)$_3$ 6H$_2$O (0.8 mmol) was also used to load the CeO$_2$ on 0.108 g SBA-15. All the precursor were nitrate salts in order to exclude the effect of different ligands.

5.1.2. Catalytic test

Figure 27 summarizes the catalytic performance of these five mixed samples (plus bare ceria) applied to NH$_3$-SCR for temperatures ranging from 100 to 500 °C. The GHSV was set as 60000 h^{-1}. It is found CeO$_2$/SBA-15 shows a typical volcano curve for NO$_x$ conversion with the maximum peak at about 300 °C. while CeNiO and CeMnO show better NO$_x$ conversions at all temperatures, with maxima at around 200 °C. Their N$_2$ selectivity shows a similar temperature-dependent behavior, going through a minimum at around 300 °C. At higher temperature (500 °C), the N$_2$ selectivity increases while the NO$_x$ conversion decreases which is attributed to the generation of NO$_2$ instead of N$_2$O. CeCuO shows a volcano curve for the NO$_x$ conversion as bare ceria but with a lower optimal temperature window. The N$_2$ selectivity decreases monotonically with increasing temperatures due to the generation of N$_2$O. For the CeMgO and CeLaO samples, lower NO$_x$ conversions and N$_2$ selectivity in NH$_3$-SCR are observed.
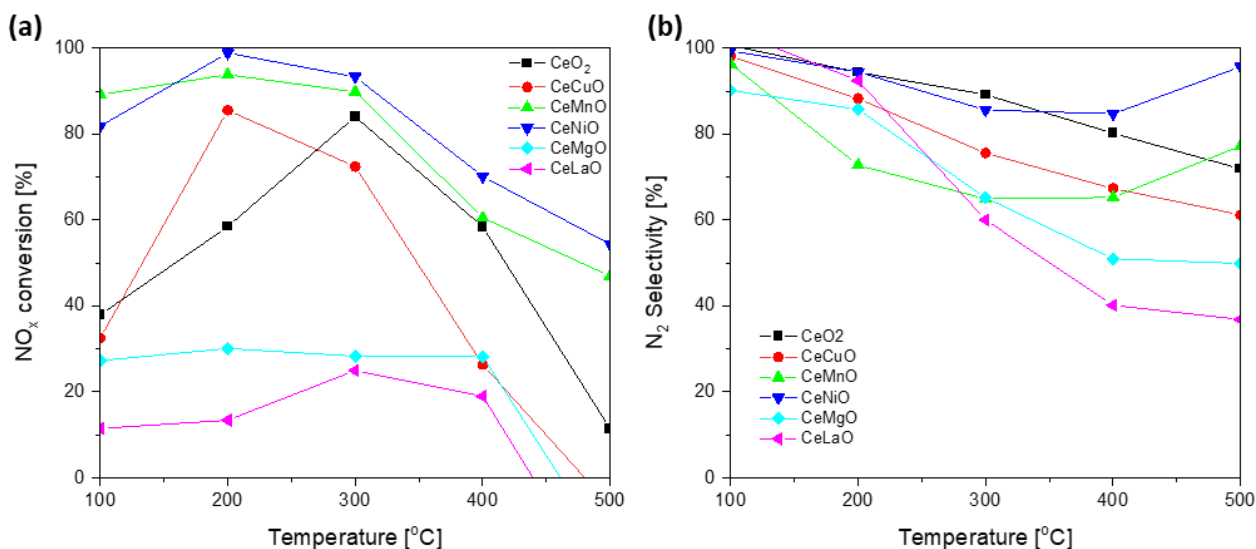
Figure 27. (a) NOx conversion and (b) N2 selectivity for NH3-SCR reaction over different bimetallic oxide samples at temperatures within 100-500 °C (GHSV=60000 h^{-1}).

Figure 28 shows the *in situ* monitoring of the exhaust gas during exposure of the bimetallic oxide samples to NH3-SCR conditions for step-wise increase in temperature from 100 to 500 °C. The CeO2 and CeCuO catalysts share a similar behavior: at low temperature, there are strong NH3 desorption peaks implying a reduced surface and sufficient NHx on the surface. For CeCuO. at 200 °C, NO strongly decreases while NO2 and N2O appear, indicating that the Cu doping increases the oxidation of CeO2. For CeMnO and CeNiO, high NO conversions as well as NH3 removal due to their high oxidation ability. To this end, the appearance of NO2 and N2O indicates over-oxidation, especially for CeMnO. At high temperatures, the NO signals appear again with NO2 replacing the N2O, which is tentatively attributed to the oxidation of NO with NH3 to N2O at medium temperature but the oxidation of NH3 to NO2 at high temperature. For CeMgO and CeLaO, the strong desorption peak of NH3 and the high NH3 level at constant temperature imply that the low reactivity at low temperature is due to the low oxidation ability instead of the acidity. At high temperature, the NO concentration is even higher than the inlet gas indicating that NH3 is catalytically oxidized to NO, NO2, and N2O.
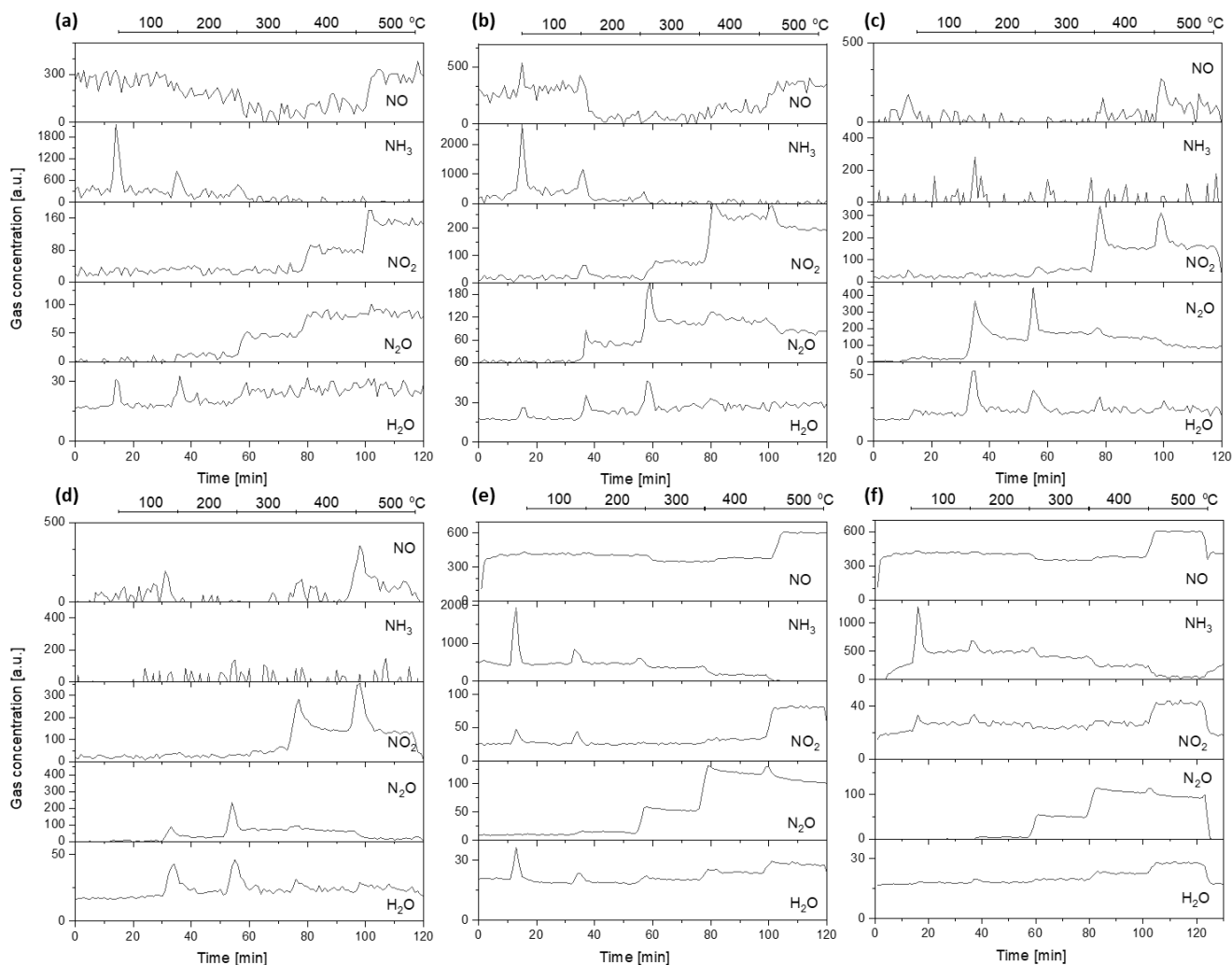
Figure 28. *in situ* monitoring of the exhaust gas for NH₃-SCR reaction over the (bi)metallic oxide samples (a) CeO₂, (b) CeCuO, (c) CeMnO, (d) CeNiO, (e) CeMgO, (f) CeLaO, applying a step-wise increase in temperature from 100 to 500 °C.

5.1.3 Characterizations

Figure 29 shows *ex situ* Raman spectra of CeO₂, CeCuO, CeMnO, and CeNiO supported on SBA-15. Only CeO₂ exhibits a peak at 464 cm⁻¹ due to the F$_{2g}$ mode of fluorite ceria. It illustrates that the secondary metal element is completely with ceria under the present preparation methods.
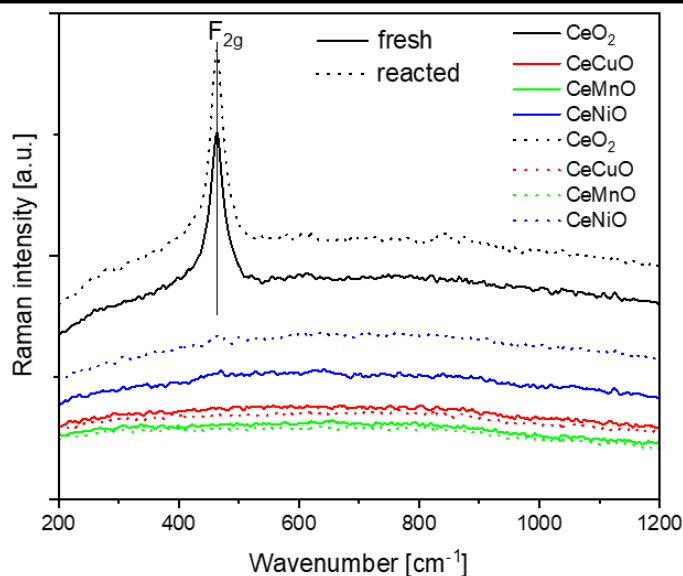
Figure 29. Raman (514 nm) spectra of prepared MO_x-CeO_2/SBA-15 before and after NH_3-SCR reaction.

5.1.4. Discussion

In this part, six ceria-containing samples were prepared to explore the synergistic effect of a second metal oxide with CeO_2. It is found that the low activity of CeO_2, CeCuO, CeMgO, and CeLaO can be attributed to the weak oxidation but not the acidity. Conversely, the samples CeMnO and CeNiO show good NO_x conversion (> 90%) with very clean NH_3 emission indicating their strong oxidation towards NH_3 to complete the H-abstraction step. In the following, CeCuO and CeMnO catalysts were chosen for further exploration. This is because CeCuO shows a similar behavior as CeO_2 but a low-temperature shift of the volcano curve, which reflects the low temperature NH_3-SCR potential of bimetallic oxide catalysts. CeMnO shows a high reactivity and a broad temperature window due to synergistic effects between active CeO_2 and MnO_x.

In addition, the six samples tested here also prove the importance of redox properties of the catalysts. Comparison of CeCuO, CeMnO, and CeNiO with CeMgO and CeLaO shows that the catalytic performance could be divided into two categories. In case of various valent metal doping, an enhanced catalytic performance is observed, while permanent valent metal doping leads to low NH_3-SCR reactivities. On the one hand, the various valent metal can be coupled with cerium ion to improve the redox properties, such as $Cu^+ + Ce^{4+} = Cu^{2+} + Ce^{3+}$. For doping with both various valent metal and permanent valent metal, there may be an increase in the acidity for the different valences with Ce^{4+}. Thus, from the preliminary tests, it can be deduced that it is the redox properties but not the acidity that determine the NH_3-SCR reactivity.

5.2. Rational design of mesoporous CuO-CeO$_2$ catalysts for NH$_3$-SCR applications guided by multiple *in situ* spectroscopies

Due to the overall poor NH$_3$-SCR reactivity of CeO$_2$-only catalysts,[112] copper oxide was added to form CuO-CeO$_2$/SBA-15 binary oxide catalysts, which are expected to improve the NH$_3$-SCR performance due to the synergetic effect through the redox equilibrium Ce^{3+} + Cu^{2+} ↔ Ce^{4+} + Cu$^+$.[117] In the previous work,[41] the P123-assisted solid-state impregnation method was adopted to prepare CeO$_2$/SBA-15 materials and used *in situ* spectroscopy to elucidate the role of P123 in the loading of CeO$_2$ on SBA-15 including a physically formed confined space for the growth of nano-oxides and chemically catalyzing the decomposition of active precursors. To the best of our knowledge, this was the first time to use *in situ* spectroscopy to characterize the solid synthesis process of oxides supported on mesoporous materials. Based on the understanding of the synthesis mechanism, it is probable to design the template-assisted SSI method for the preparation of more relevant CuO-CeO$_2$ catalysts for NH$_3$-SCR applications. Compared with the preparation of CeO$_2$/SBA-15, for the common situation of a coloaded system, the role of the template needs to be evaluated, as not only the dispersion but also the distribution of the two oxides needs to be taken into account. Thus, clarifying the chemical reaction processes occurring during the loading and formation of the final catalyst is of great importance for a controllable synthesis of bimetallic and more complex oxides.

For the synthesis of metal-oxide catalysts for SCR reactions, mainly two approaches are applied: (i) direct condensation from a metal precursor, or (ii) exchange with another coordination ligand, followed by condensation as the metal oxide. Both routes involve the thermal decomposition of metal compounds and form the final oxide products at high-temperature calcination. For the SSI method applied here, the cerium and copper nitrate precursors are mixed with the support (SBA-15), followed by a calcination step, which includes the metal ion immigration to the pores and their interaction with the support surface, the decomposition of the metal precursor, and the nucleation and growth of metal oxides. Due to the occurrence of a large number of processes, calcination has often been considered as a "black-box".

In situ analysis is essential to elucidate the mechanisms of these processes, but it has proved difficult to use standard analytical techniques (*e.g.*, thermogravimetric analysis (TGA) /differential thermal analysis (DTA)) for direct monitoring. To this end, the use of optical spectroscopy is of great interest, allowing continuous data collection from outside the furnace (reaction) chamber, not affecting the calcination process. Applying *in situ* X-ray spectroscopy to nanomaterial synthesis has previously been shown to allow a description of the direct structural phase transformation.[159] For a detailed understanding of the processes underlying the synthesis, the use of other techniques would be highly desirable, such as

Raman spectroscopy, which probes the extended structure *via* phonons but also the short-range structure of solids, diffuse reflectance infrared Fourier transform (DRIFT) spectroscopy, providing information on surface and adsorbed species, and UV-Visible (UV-Vis) spectroscopy, which gives details on the metal coordination environment.

In this contribution, to unravel the synthesis mechanism of CuO-CeO$_2$-based catalysts and to relate their preparation to the catalytic NH$_3$-SCR performance, *in situ* DRIFT, UV-Vis, and Raman spectroscopies, as well as online Fourier transform infrared (FTIR) monitoring of the gas-phase composition were used. To allow for a detailed understanding of the aspects controlling the synthesis and reactivity behavior, the focus will be on samples with a Ce/Cu mole ratio of 1:1 loaded on silica SBA-15 by solid-state impregnation. Based on the results, the role of the oxide dispersion and distribution for NH$_3$-SCR reactivity will be discussed. This work follows mainly the published paper "Rational design of mesoporous CuO-CeO$_2$ catalysts for NH$_3$-SCR applications guided by multiple *in situ* spectroscopies".[111]

5.2.1. Sample preparation

Silica SBA-15 was prepared as described previously.[158] Briefly, 4.0 g P123 was completely dispersed in a mixture of 120 ml 2 M HCl solution and 30 ml water in a PP bottle at 35 °C (250 r/min; 2 h). Then 10 ml TEOS was added at 35 °C and stirred at 400 r/min for 20 h. After that, the bottle was placed in an oven at 85 °C to allow hydrothermal crystallization for 24 h. The as-made SBA-15 (asSBA-15) was collected using vacuum filtration, followed by calcination for 12 h in a muffle furnace heated to 550 °C at 1.5 °C /min to remove the template P123, yielding template-free SBA-15 (tfSBA-15). CeO$_2$ and CuO were loaded onto asSBA-15 or tfSBA-15 by one-pot solid-state impregnation (SSI) by grinding a mixture of 0.173 g of Ce(NO$_3$)$_3$·6H$_2$O, 0.096 g of Cu(NO$_3$)$_2$·3H$_2$O, and SBA-15 (0.225 g of asSBA-15 or 0.108 g of tfSBA-15) under ambient conditions for 30 min (molar ratio Ce:Cu = 1:1). The completely mixed powder was calcined in a stream of air at 500 °C for 5 h (heating rate: 1.5 °C/min). The final powder materials will be referred to as tfSBA-CeCuO and asSBA-CeCuO in the following.

As reference samples, CeO$_2$ and CuO were separately loaded onto SBA-15 by the same procedures as described above, and will be referred to tfSBA-CeO$_2$, asSBA-CeO$_2$, tfSBA-CuO and asSBA-CuO, respectively.

5.2.2. Characterization

Figure 30 shows the N_2 isotherm adsorption/desorption curves, providing insight into the mesoporous and microporous structure of the SBA-15 supported samples. The curve for bare SBA-15 in Fig. 1a is given as a reference and shows typical H1 type behavior with a hysteresis loop at 0.55-0.75 p/p^0, reflecting uniform hexagonal pores and a narrow pore size distribution centered at around 6.3 nm diameter (see Figure 30(b)). After cerium or copper oxides were loaded onto the SBA-15 support, the pore volume declined compared with the unloaded sample, resulting from the blocking of surface pores especially micropores. The shapes of the hysteresis loops changed, indicating the transport of oxides solid into the porous matrix. In detail, for the tfSBA-CeO$_2$ sample, the desorption branch shows two stages: one at p/p^0 of 0.55-0.7 p/p^0, corresponding to open pores, and another one at 0.4-0.5 p/p^0, suggesting narrow pores due to the local growth of CeO$_2$. This behavior is consistent with the wide pore size distribution (see Figure 30(b)). The tfSBA-CuO sample shows a similar behavior, but with less pronounced stages, which may be attributed to the lower degree of CuO crystallization and agglomeration compared to CeO$_2$ (see Fig. S5-1). For tfSBA-CeCuO, the pore volume further declined as compared to the single cerium or copper oxide loaded samples. In comparison, samples calcined with asSBA-15 (asSBA-CeO$_2$ and asSBA-CeCuO) showed a better preservation of the pore structure. Similarly, the first stage at 0.6-0.7 p/p^0 is attributed to the open pores, while the second stage, at 0.45-0.6 p/p^0, results from a decreased pore diameter due to the presence of oxides. Overall, the isotherm profiles and porosity characteristics indicate that the asSBA-15-based samples contain more dispersed oxides than the ones based on tfSBA-15. Table 7 summarizes the BET surface area and porosity results of bare SBA-15 and SBA-15 supported cerium and/or copper oxides samples.
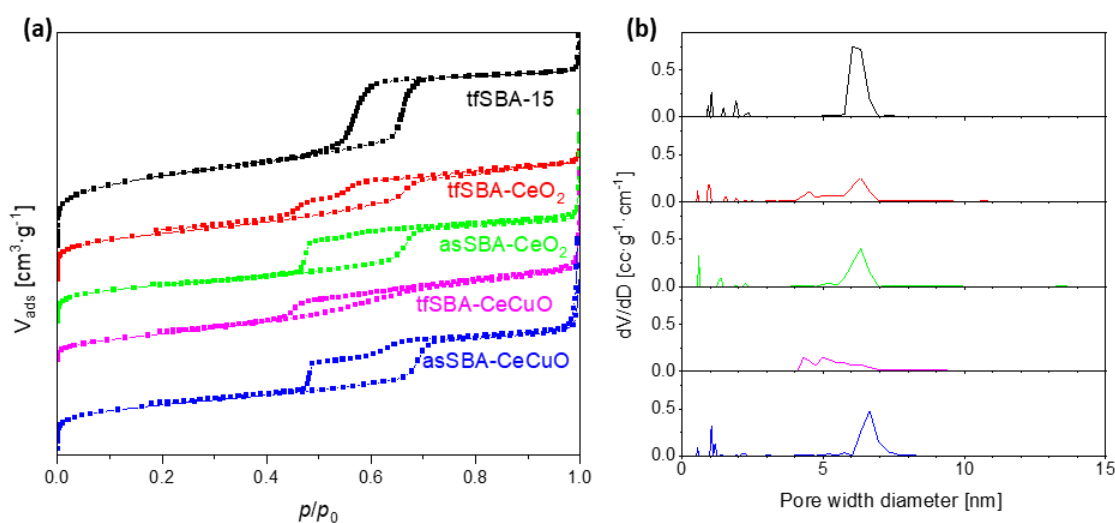

Figure 30. (a) N$_2$ adsorption/desorption isotherms, and (b) NLDFT pore size distributions of template-free SBA-15- and SBA-15-based materials.

Table 7. Composition, specific surface area, and porosity characteristics of the SBA-15 supported oxide samples compared to bare SBA-15

Samples	CeO$_2$ (wt.%)	CuO (wt.%)	S_{total} [m^2/g]^a	D_p [nm]^b	V_{total} [cm^3/g]^c	d_{CeO2} [nm]^d	d_{CuO} [nm]^d
tfSBA-15	0	0	616	6.3	0.64	--	--
tfSBA-CeO$_2$	39	0	414	6.3	0.43	7.8	--
asSBA-CeO$_2$	39	0	359	6.3	0.39	6.4	--
tfSBA-CuO^e	0	23	445	5.8	0.55	--	29.5
asSBA-CuO^e	0	23	315	5.4	0.45	--	--
tfSBA-CeCuO	32	18	285	6.3	0.35	4.8	--
asSBA-CeCuO^f	32	18	400	6.6	0.44	4.7	9.7

^{a} Total BET surface area.

^{b} Pore diameter determined from the adsorption branch by NLDFT.

^{c} Total pore volume.

^{d} Calculated from XRD results using the Scherrer formula.

^{e} N$_2$ adsorption analysis performed on an Autosorb-3B device.

^{f} For sample preparation a different SBA-15 batch was used (S_{total} = 739 m^2/g; D_p = 6.6 nm), explaining the systematically higher surface area and porosity values.

Figure 31 depicts TEM results of the calcined tfSBA-CeCuO sample. The bright field image in Figure 31(a) verifies the channel structure of SBA-15, whereby the dark traces represent copper and cerium oxides. The dark field image in Figure 31(b) provides an enlarged view, with bright spots representing oxide phases. Element mapping of Cu and Ce (see Figure 31(c-d)) reveals that Cu and Ce are well mixed and distributed within SBA-15.
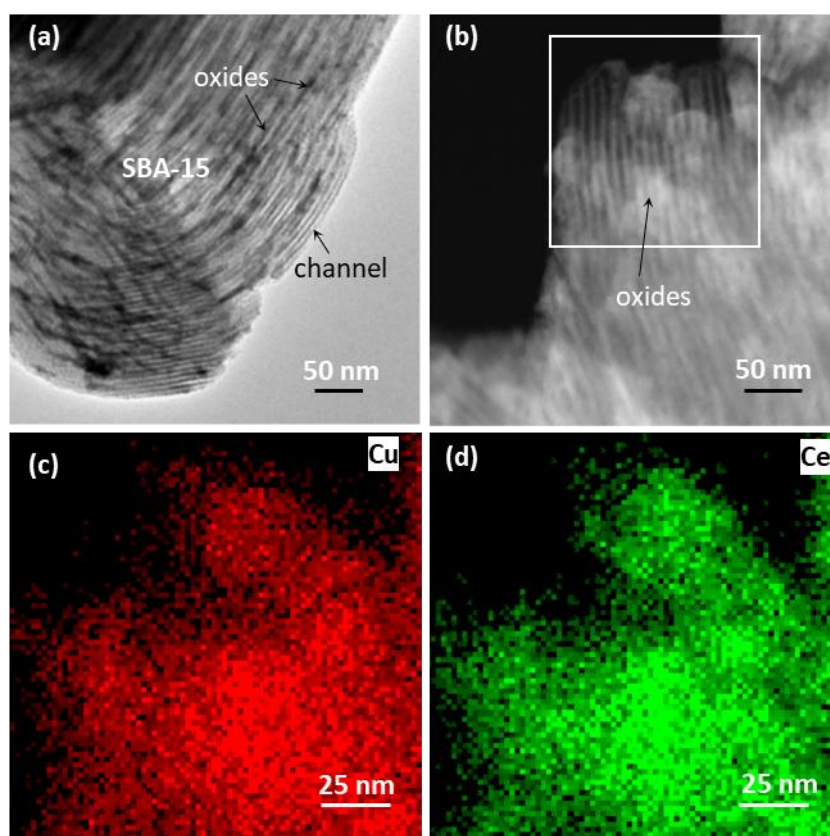
Figure 31. TEM analysis of tfSBA-CeCuO. (a) Bright field, (b) dark field, and elemental mapping of (c) Cu, and (d) Ce, based on the area outlined in (b).

Figure 32 shows the wide-angle XRD patterns of the SBA-15 supported ceria or/and copper oxide samples. The broad diffraction peak at $2\theta = 23°$ observed for template-free SBA-15 is assigned to the amorphous silica framework.[85] After ceria loading, new peaks appear at 28.5°, 33.2°, 47.5°, and 56.3° for both tfSBA-CeO$_2$ and asSBA-CeO$_2$, which are readily attributed to crystalline CeO$_2$.[41] After copper oxide loading, sample tfSBA-CuO shows a series of peaks at 32.67° (110), 35.63° (111), 38.90° (022), 48.83° (202), 53.60° (020), 58.24° (202), 61.59° (113), 66.5° (022), and 68.19° (220), corresponding to different planes of monoclinic CuO.[160] In contrast, sample asSBA-CuO shows no copper oxide-related signals, which indicates that the presence of template P123 makes a difference regarding the copper oxide dispersion, consistent with the different colors observed for tfSBA-CuO (grey) and asSBA-CuO (green). For the co-impregnated sample tfSBA-CeCuO, XRD shows only CeO$_2$ features with a higher FWHM than those of tfSBA-CeO$_2$. This implies that Cu^{2+} ions can enter the CeO$_2$ crystal lattice due to their smaller radius (Cu^{2+}: 72 pm; Ce^{4+}: 92 pm),[161] or form highly dispersed CuO clusters.[162] In contrast, asSBA-CeCuO shows XRD peaks of both CeO$_2$ and CuO, evidencing the coexistence of crystalline

CeO$_2$ and CuO. Table 7 summarizes the corresponding crystallite sizes, as estimated from the Scherrer equation.
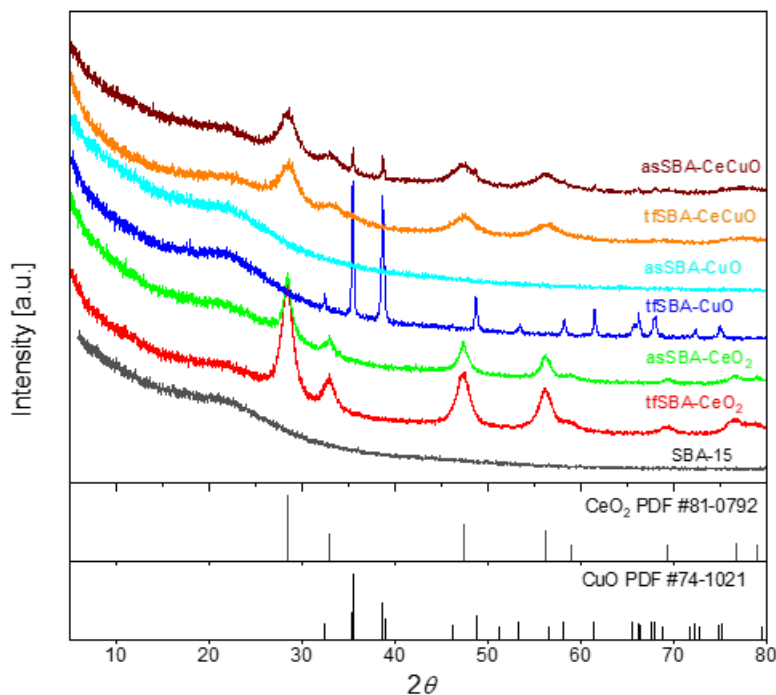
Figure 32. X-ray diffraction patterns of bare SBA-15 and the SBA-15 supported samples.

The XP spectra of the calcined samples provide insight into the surface chemical states of the loaded CeO$_2$ and CuO. The Ce 3d photoemission presented in Figure 33(a) is characterized by two sets of peaks from spin-orbit coupling (d$_{3/2}$, d$_{5/2}$), labelled u and v, corresponding to the mixing of Ce^{4+} final states (u, v, u″, v″, u‴, v‴) as well as Ce^{3+} final states (u′, v′, u$_0$, v$_0$).[163] On the basis of the Ce 3d XPS data, the surface Ce^{3+} content is determined as 1.4 at.% and 1.5 at.% for tfSBA-CeCuO and asSBA-CeCuO, respectively (see Table 8). Detailed analysis of the Cu 2p photoemission reveals contributions from Cu$^+$ and Cu^{2+}, as shown in Figure 33(b). The peaks at 953.7 eV and 933.6 eV are assigned to Cu^{2+} 2p$_{1/2}$ and Cu^{2+} 2p$_{3/2}$ of CuO, respectively.[164] The contributions at lower binding energies can be attributed to the Cu$^+$ ion in Cu$_2$O , while the features at higher binding energies are assigned to Cu^{2+} in Cu(OH)$_2$ formed via thermohydrolysis, in agreement with the literature.[165] The surface compositions of tfSBA-CeCuO and asSBA-CeCuO are summarized in Table 8. The Cu/Ce surface ratio is close to 1 for tfSBA-CeCuO, but equal to 0.6 for asSBA-CeCuO, indicating that tfSBA-CeCuO is characterized by a uniform mixture of metals and asSBA-CeCuO rather than by a phase-separated structure. In addition, asSBA-CeCuO contains a higher fraction of Cu(OH)$_2$ and Cu$_2$O, which may originate from hydrolysis and a reducing atmosphere in the presence of P123.
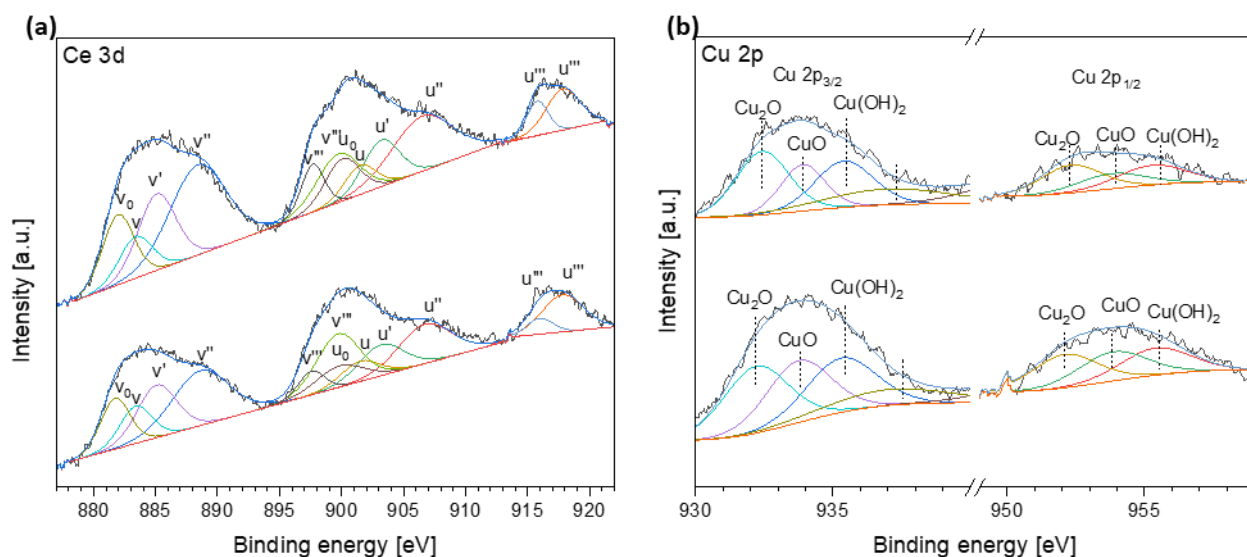
Figure 33. X-ray photoelectron (XP) spectra of tfSBA-CeCuO and asSBA-CeCuO, showing the (a) Ce 3d and (b) Cu 2p photoemission, together with the results of a least-squares fitting analysis. For details see text.

Table 8. Surface composition of tfSBA-CeCuO and asSBA-CeCuO from XPS analysis

	Elements (at.%)			$Ce^{3+}/$ $(Ce^{3+}+ Ce^{4+})$	Cu species (at.%)		
	Cu	Ce	Si		$Cu(OH)_2$	CuO	Cu_2O
tfSBA-CeCuO	1.5	1.4	23.8	0.33	31.3	32.7	36.0
asSBA-CeCuO	0.9	1.5	25.0	0.34	33.3	25.2	41.5

5.2.3. Catalytic test

Figure 34 and Fig. S5-2 show the catalytic performance of the synthesized samples for NH_3-SCR within the temperature range 100-500 °C. From Figure 34 it can be clearly seen that e.g. the mono-metallic oxides tfSBA-CeO$_2$ and tfSBA-CuO are characterized by a low level of NO_x conversion (maximum: ~30%), while the bimetallic oxides tfSBA-CeCuO and asSBA-CeCuO show a strongly improved NO_x conversion up to ~80 % (see Figure34(a)). Furthermore, tfSBA-CeCuO shows a better low-temperature NO_x conversion at 200-250 °C, while the SCR performance of asSBA-CeCuO spans a wide temperature window ranging from 250 to 450 °C and peaks at around 350 °C. Within the regions of maximum NO_x conversion, both catalysts show N_2 selectivity of 80% or higher (see Figure 34(b)). Please note that at

500 °C, the NO_x conversion of the tfSBA-15 samples takes negative values, leading to increased NO_x ($NO+NO_2$) compared with the inlet gas, implying that NH_3 was over-oxidized to NO_2.
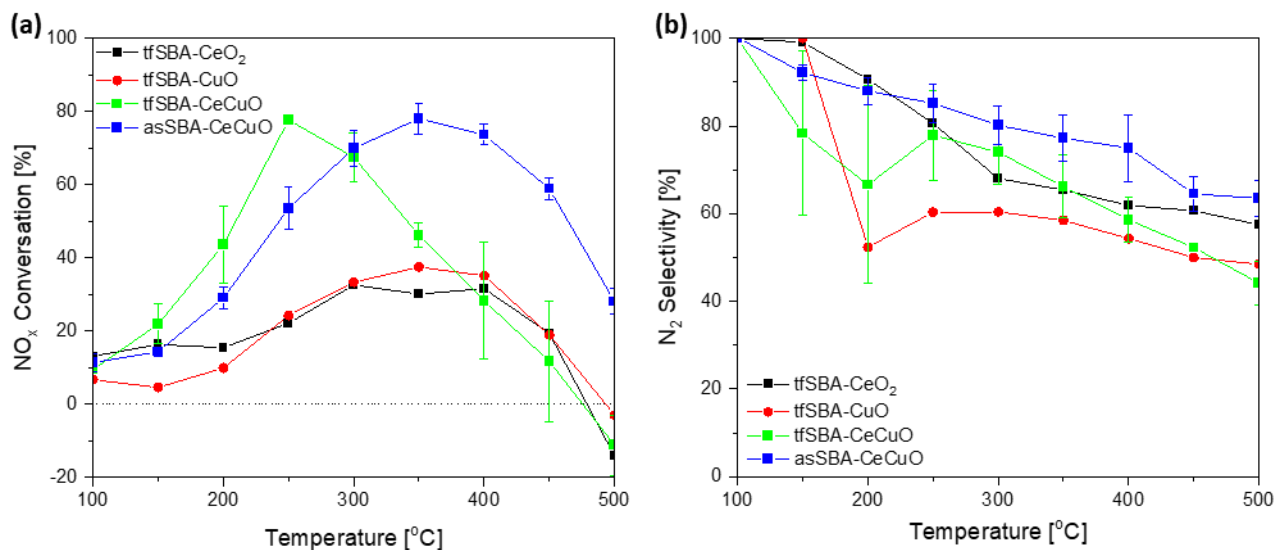

Figure 34. Temperature-dependent NH_3 SCR performance for the synthesized samples: (a) NO_x conversion, (b) N_2 selectivity.

A more detailed view of the NH_3-SCR reactivity behavior of tfSBA-CeCuO and asSBA-CeCuO is provided by Fig. S5-2, showing the online gas-phase IR during a stepwise increase in temperature. Within the low-temperature range of 150-250 °C, tfSBA-CeCuO clearly shows NO desorption peaks when the temperature is raised, in contrast to asSBA-CeCuO, implying a better low-temperature NO_x conversion by reaction of adsorbed NO with NH_3. Both samples exhibit similar NH_3 peaks, indicating extensive NH_3 adsorption on the surface, which excludes acidity effects. Regarding the NO_2 emission behavior, major differences between the samples are detected. For tfSBA-CeCuO, NO_2 desorption peaks appear within the whole temperature range studied, while asSBA-CeCuO shows only low-temperature NO_2 peaks. From the observed behavior it is deduced that tfSBA-CeCuO is characterized by a stronger oxidizing power, which facilitates the NO_x conversion at low temperatures but increases the transformation of NH_3 into NO_2 at high temperatures, resulting in lower high-temperature NO_x conversion and N_2 selectivity.

5.2.4. Mechanism of co-dispersion of cerium and copper within the SBA-15 matrix

As discussed above, the samples tfSBA-CeCuO and asSBA-CeCuO present two types of $CuO-CeO_2$ materials with improved SCR performance compared to monometallic oxides. While different reactivities of $CuO-CeO_2$ catalysts have been reported in the literature, a knowledge-based synthesis

approach aiming at dedicated surface and catalytic properties is still lacking, hampering further catalyst development. To gain insight into the mechanism of catalyst preparation, a multiple *in situ* spectroscopy study was conducted, as described in the following.

Figure 35 depicts results from the TG analysis of cerium and/or copper nitrate mixed with tf/asSBA-15, using the same experimental conditions as during catalyst preparation. As a reference, the decomposition behavior of bare cerium nitrate, copper nitrate and asSBA-15 are shown in Fig. S5-3a. To identify the critical temperatures, the first derivatives of the TG curves were taken (see Fig. S5-3b). The critical temperature for template removal of asSBA-15 is about 130 °C. Both cerium nitrate and copper nitrate exhibit two weight losses: The first band at 0-150 °C originates from the loss of water of crystallization, and the second one from decomposition of nitrate salt, which was detected at about 220 °C for $Ce(NO_3)_3$ and 180 °C for $Cu(NO_3)_2$ due to different electronic interactions between metal and nitrate.[100] The higher charge density of Cu^{2+} effectively polarizes nitrate, facilitating the decomposition compared to Ce^{3+}. In addition, nitrate decomposition is sensitive to other factors, such as the support effect and the calcination atmosphere. For tf/asSBA-CeO_2, the catalytic interaction between the SiO_2 support or template P123 with cerium nitrate facilitates the nitrate decomposition by changing the metal-nitrate electronic structure, as discussed previously.[88, 100] On the other hand, the decomposed P123 creates a reduced atmosphere for asSBA-CeO_2 that can inhibit the nitrate salt decomposition.[166] Thus, the weight loss for the decomposition of $Ce(NO_3)_3$ moves to 200 °C for tfSBA-CeO_2 but is delayed to 250 °C for asSBA-CeO_2. For tf/asSBA-CuO, dehydration is accompanied by thermohydrolysis, leading to the appearance of $Cu_2(OH)_3NO_3$.[167] The existence of P123 provides more -OH and free water for the thermohydrolysis products. The final product of the thermolysis, CuO, is formed at 200-250 °C. Finally, for the bimetallic tf/asSBA-CeCuO, the nitrate decomposition temperatures are influenced by the mixed metal cations and the chemical surroundings, including support surface, reduced atmosphere, and moisture.[168] For tfSBA-CeCuO, the weight loss at low temperature (<150 °C) is attributed to water evaporation. After that, $Ce(NO_3)_3$ and $Cu(NO_3)_2$ are gradually decomposed to their oxides at lower decomposition temperatures compared to bare nitrate, owing to the support effect. In the case of asSBA-CeCuO, the increasing temperature makes template P123 lose water and shrink to the silica surface, facilitating the thermohydrolysis of Ce^{3+} and Cu^{2+} as $M(OH)_x(NO_3)_y$, which disperses and fixates the metal ions within the pores. When the temperature reaches about 250 °C, the intermediate $M(OH)_x$ is calcined, thereby forming oxide crystals, as indicated by a sharp decrease in the weight loss curve (see Figure 35).
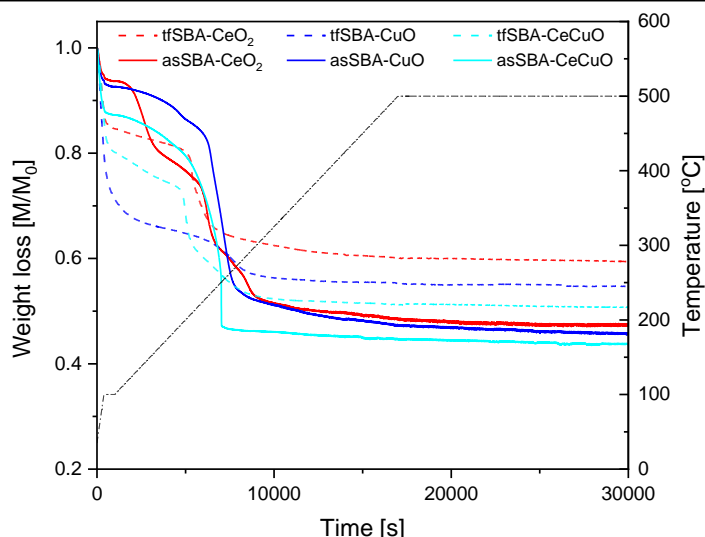
Figure 35. Thermogravimetric analysis (TGA) of the precursor samples using an airflow of 100 ml/min and the same heating program as during the calcination treatment.

Figure 36 shows online gas-phase IR spectra during air calcination of the precursor samples to tfSBA-CeCuO and asSBA-CeCuO in the temperature range 25-500 °C. In the case of calcination of the tfSBA-CeCuO precursor (see Figure 36(a)), low temperature bands (~80 °C) bands are detected at 1316/1340 cm^{-1} and 1698/1716 cm^{-1}, which are assigned to C-O-C bending and C=O stretching vibrations, respectively, accompanied by minor water-related features (1300-1800 cm^{-1}; 3500-4000 cm^{-1}). This implies that the residual template in tfSBA-15 is catalytically decomposed and oxidized by the Ce^{3+} and/or Cu^{2+} nitrate salts. Compared with the results for tfSBA-CeO$_2$ (see Fig. S5-4), the presence of copper decreases the critical decomposition temperature of the residual template and changes the reactivity behavior, leading to products containing both C-O-C and C=O groups rather than only C=O groups, as a result of enhanced oxidation. After the catalytic decomposition of residual template, there are two stages of nitrate salt decomposition via MO$_x$(NO$_3$)$_y$ (M = Ce and Cu), leading to the release of NO$_2$ gas at about 170 °C and 200 °C, as observed by IR signals at 1625 cm^{-1}.[167] Figure 36(a) also shows that when the temperature reaches 180 °C and 205 °C, bands due to C-containing products appear at 1316/1340 cm^{-1} (C-O-C), 1698/1716 cm^{-1} (C=O), 2870-2930 cm^{-1} (C-H), and 2338/2362 cm^{-1} (CO$_2$), indicating that the produced intermediate MO$_x$(NO$_3$)$_y$ and their oxides MO$_x$ can catalyze the decomposition of residual P123 or its segments left inside the pore. For the calcination of the asSBA-CeCuO precursor (see Figure 36(b)), weak signals appear at low temperature (90 °C), which are related to C-O-C (1316/1340 cm^{-1}) and C=O (1689/1716 cm^{-1}) vibrations, followed by NO$_2$-related signals in the range 100-210 °C. At temperatures >200 °C, H$_2$O and CO$_2$ bands are detected together with CH$_n$ stretching features (2790-3950 cm^{-1}) within a narrow temperature range at around 195 °C, in agreement

with the TGA results discussed above. Based on the TGA and gas phase IR results, it is proposed that $Ce(NO_3)_3$ and $Cu(NO_3)_2$ are transferred into the pores to undergo thermohydrolysis and coordinate with -OH groups of P123 as $M(OH)_x(NO_3)_y$ and further hydroxides $M(OH)_x$. Finally, the coordinated metal cations catalytically decompose the P123 template bed with a large number of contact sites while transforming themselves into oxide phases. Summarizing, for tfSBA-CeCuO, a gradual emission is observed, which is attributed to the thermal decomposition of nitrate ligands, while the formation of tfSBA-CeCuO is characterized by low temperature NO_2 and high temperature H_2O emission, originating from the hydrolysis of nitrate to hydroxides and condensation of hydroxides to oxides, respectively.
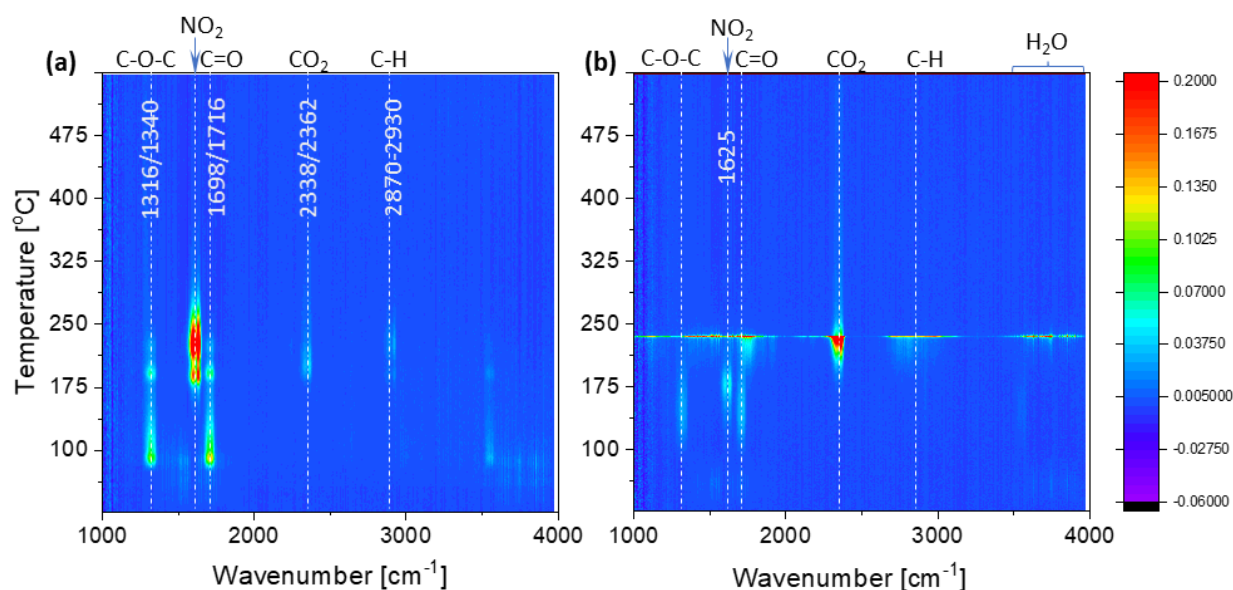
Figure 36. Online IR detection of exhaust gases during air calcination of the (a) tfSBA-CeCuO, (b) asSBA-CeCuO precursor samples. The temperature was raised from 25 °C to 500 °C at a heating rate of 1.5 °C /min.

To examine the adsorbed species during air calcination, the DRIFT spectra of the precursors to samples tfSBA-CeCuO and asSBA-CeCuO were recorded, while the temperature was increased from 25 to 500 °C. For the tfSBA-CeCuO precursor, at room temperature, strong adsorption bands are observed at 3000-3600 cm^{-1} (see Figure 37(a)), which are assigned to H-bonded hydroxyl groups.[106] The presence of water is indicated by the bending and stretching features at around 1640 cm^{-1} and 3442.[106] The sharp but asymmetric peak at 3740 cm^{-1} is characteristic of isolated Si-OH on the surface of silica (SBA-15),[41, 169] whereas the bands at 1036 and 1216 cm^{-1} are attributed to stretching vibrations of the mesoporous framework (Si-O-Si).[170] The DRIFT spectra of the tfSBA-CeCuO precursor show a series of peaks at 1235, 1342, 1552, 2482/2788, and 2583 cm^{-1}, which are assigned to O-N-O stretching of nitrite, N-O stretching of nitrate, N=O stretching, nitrate species, and nitrite species, respectively.[128] The

negative peaks at 2357/2287 cm^{-1} originate from pre-adsorbed CO_2, which gradually desorbs with increasing temperature.[41] The bands at 1759 and 2057 cm^{-1} are attributed to adsorbed nitric oxide and carbon monoxide, respectively,[128] which disappear at temperatures > 235 °C. The nearby bands at 1842 and 1982 cm^{-1} are tentatively assigned to nitrosyl groups coordinated to metal cations.[128] In addition, weak features appear in the NIR region (4000-5000 cm^{-1}), originating from the $\nu+\delta$ overtone of M-OH and M-O-M (M = Si, Ce, and Cu) vibrations.[171] When the temperature is increased to 200 °C, the band related to monodentate nitrate at 1522 cm^{-1} decreases, while those related to bidentate nitrate (1554 cm^{-1}) and bridging nitrate (1617 cm^{-1}) increase, indicating a change in coordination from isolated M-O-NO$_2$ to bridged M-O(NO$_2$)-M. The band at 1342 cm^{-1} (N-O) shifts to 1296 cm^{-1} (nitrite M-ONO) at 235 °C and finally to 1260 cm^{-1} (chelating nitrate M-(O)$_2$-NO) at 400 °C, reflecting the decomposition of nitrate salts. As a result of dehydration, starting at 130 °C, the hydroxy-related features in the range 3000-3600 cm^{-1} decrease in intensity. Two weak bands at 3205 and 3489 cm^{-1}, which have been attributed to stretching vibrations of -OH on copper and cerium cations,[171] disappear at temperatures above 235 °C.

The above findings demonstrate that DRIFT spectra provide detailed information on the surface chemistry of tfSBA-CeCuO during calcination. Previously, the thermal decomposition of metal nitrate to metal oxides had been studied by TGA, DTA, conductometric, and thermometric titration methods and proposed to proceed according to the sequence: $M(NO_3)_x \cdot yH_2O \rightarrow M(NO_3)_x \rightarrow MONO_3 \rightarrow CeO_2$.[172] To this end, the IR results of this study provide new insight into the mechanism of metal nitrate decomposition (see Scheme 6), including chelating and bridging rearrangements and final condensation.
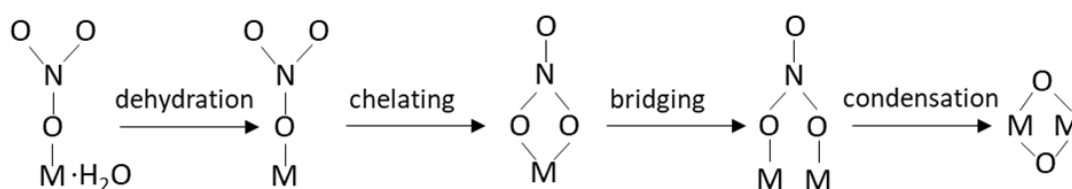
Scheme 6. Schematic process of thermal decomposition of copper and cerium nitrates for tfSBA-CeCuO.

For asSBA-CeCuO (see Figure 37(b)), the characteristic C-H stretching features at 2879-2975 cm^{-1} confirm the presence of template P123. The peaks at about 3740 cm^{-1}, which suddenly appear when a critical temperature of 235 °C is reached, are attributed to surface silanol groups.[41] The observed spectral behavior implies that P123 covers the silica surface at low temperature, thereby blocking Si-OH species, while, with increasing temperature, P123 gradually shrinks to the surface and silanol starts to appear (at 235 °C). Correspondingly, the (noisy) features at 800-1500 cm^{-1}, detected at high temperatures, are assigned to C-C bonds resulting from P123 decomposition.[173] The blue-shift of the Ce-OH stretching

band from 3373 to 3460 cm^{-1} is assigned to the gradual replacement of nitrate by hydroxyl during the ion-exchange reaction.[106] The spectral region 1500-1600 cm^{-1}, typically assigned to different nitrate structure, reveals that the structure of the nitrate ligands remains unchanged with increasing temperature until 235 °C, where the (intermediate) formation of chelating nitrate (1560 cm^{-1}) is observed. In addition, at temperatures > 235 °C, two new bands appear, at 3232 and 3587 cm^{-1}, which have been attributed to the OH-stretch vibration of copper and cerium hydroxide, respectively.[171, 174] Compared with the apparent spectral changes observed for tfSBA-CeCuO, related to the transformation from monodentate to bridging nitrate and the disappearance of -OH species at high temperature, the presence of P123 (in the case of asSBA-CeCuO) changes the mechanism of nitrate salt decomposition from solid calcination to a hydrothermal-like process,[100] as shown in Scheme 7. To this end, P123 provides abundant -OH and -O- sites to coordinate the metal cations and replace the nitrate by hydroxide ligands by ion exchange.[88] Finally, the metal hydroxides condense to form their oxides.
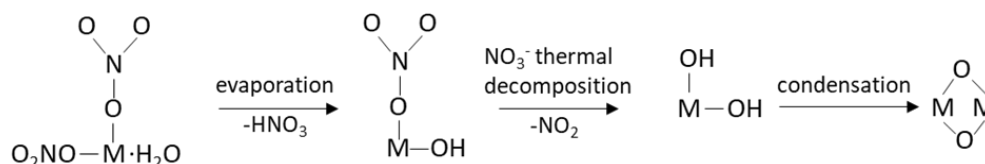
Scheme 7. Schematic process of the hydrothermal-like mechanism for decomposition of copper and cerium nitrate for asSBA-CeCuO.
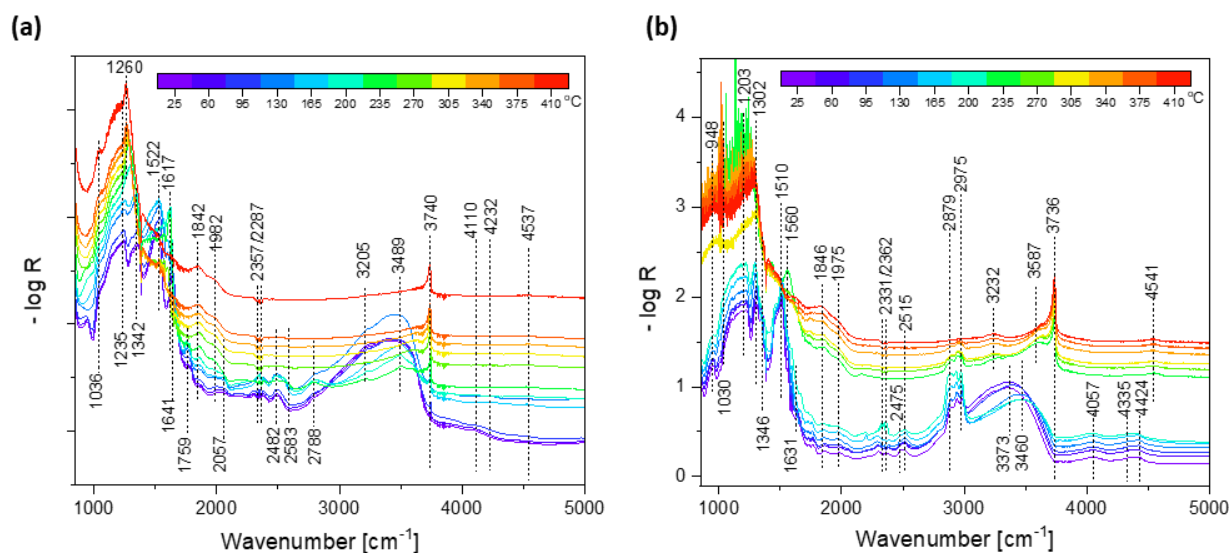

Figure 37. *In situ* DRIFT spectra of the (a) tfSBA-CeCuO and (b) asSBA-CeCuO precursor samples during air calcination from 25 to 500 °C at a heating rate of 1.5 °C /min.

Figure 38 depicts *in situ* UV-Vis DR spectra of the tfSBA-CeCuO and asSBA-CeCuO precursor samples, providing information about changes in the coordination environment of cerium and copper ions during the calcination process. The initial spectra of precursor samples tfSBA-CeCuO and asSBA-CeCuO at low temperature show typical features of $Ce(NO_3)_3$ at 218, 257, and 310 nm, corresponding to a $4f^1$-$5d^1$ electronic transfer of Ce^{3+}, a charge transfer (CT) of O^{2-} 2p to Ce^{3+} 4f/5d, and a CT of Ce^{3+} 5d to O^{2-} 2p, respectively.[107] The broad, weak feature at 600-800 nm is attributed to d-d transitions of Cu^{2+} ions.[175] The ligand metal charge transfer (LMCT) of O^{2-} 2p to Cu^{2+} 3d shows an absorption band at about 300 nm,[176] which overlaps with the CeO_2 absorption. With increasing temperature, the peak at 257 nm disappears gradually as a result of copper and cerium nitrate decomposition. For tfSBA-CeCuO, the absorption bands at 257 nm and 310 nm increase with increasing temperatures until 225 °C. In the case of asSBA-CeCuO, the peak at 257 nm increases to a stable value at about 250 °C and the bands at about 280-310 nm show an overall increase but an intermediate decrease at 125-175 °C, which is similar to the behavior of the tail bands at 600-800 nm. This behavior suggests that the decomposition of cerium and copper nitrate occurs in different stages, leading to the separate formation of CeO_2 and CuO crystallites. On the other hand, for tfSBA-CeCuO, both nitrates tend to decompose simultaneously and form an amorphous CeO_2-CuO solid solution. A different behavior is also observed for the peaks at about 218 nm, assigned to nitrate ligands, in agreement with the different decomposition routes discussed above. For tfSBA-CeCuO, the features decrease gradually throughout the whole calcination process, corresponding to the successive thermal release of NO_2, while for asSBA-CeCuO, the features show little change until about 250 °C, where a sudden change in the spectral profile is observed due to the formation of oxides, in agreement with the TGA results.

The band gap energy (E_g) was calculated from the DR UV-Vis spectra using Eq. 5-1:[177]

$$\alpha h\nu = A(h\nu - E_g)^n \tag{5-1}$$

where α is the absorption coefficient, which is determined by the absorbance. A is a constant. In this study, n was taken to be 1/2 for evaluation of the direct bandgap of the CeO_2-CuO samples.[177] Using Tauc's method, the evolution of the E_g value during calcination can be derived (see Fig. S5-5). In the low-temperature range, the gradual redshift of the energy gaps is due to the removal/dissociation of the water of crystallization and chelated NO_3^-. The smaller (final) band gap of tfSBA-CeCuO (2.55 eV) compared to asSBA-CeCuO (2.80 eV) implies that the ceria-copper oxide mixture exhibits a better reducibility, in agreement with the improved catalytic activity at low temperature but minor NO_x conversion at high temperature due to eased oxidation.
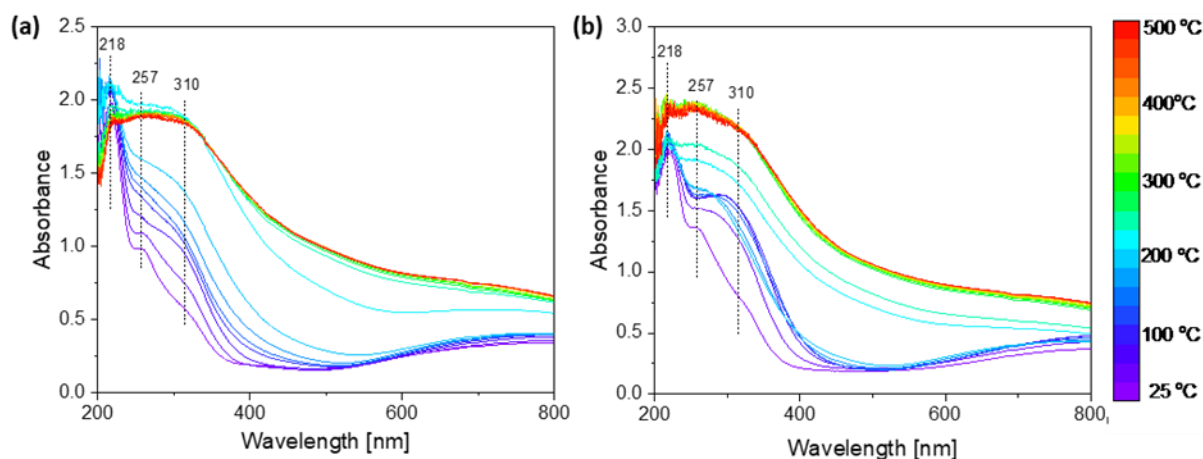
Figure 38. *In situ* UV-Vis DR spectra of the (a) tfSBA-CeCuO, (b) asSBA-CeCuO precursor samples during air calcination from 25 to 500 °C at a heating rate of 1.5 °C /min.

Figure 39 shows *in situ* Raman spectra of the tfSBA-CeCuO and asSBA-CeCuO precursor samples, facilitating the identification of structural changes during the calcination process. Free nitrate is planar and possesses D_{3h} symmetry, resulting in the following vibrational modes: v_1, symmetric NO stretch at ~1049 cm^{-1}; v_2, out-of-plane rocking mode at ~830 cm^{-1}; v_3, antisymmetric N-O stretch at ~1370 cm^{-1} and v_4, in-plane deformation at ~719 cm^{-1}. The v_2 mode is Raman inactive and the v_3 and v_4 vibrations are doubly degenerate, i.e., they might split upon symmetry lowering.[178] For bulk metal nitrates, NO_3^- ions can be coordinated in different ways, e.g. as monodentate, bidentate chelating, bidentate bridging or tridentate nitrate. For mono- and bidentate nitrates the symmetry is lowered to C_{2v}. As a result, six vibrational modes are expected.[178] Starting with precursor tfSBA-CeCuO, the bands at 720/741 cm^{-1} originate from nitrate in-plane deformation and the strong peak at 1038 cm^{-1} from the symmetric stretch vibration of NO_3^-.[179] The broad feature at 1337 cm^{-1} is attributed to NO_3^- asymmetric stretching,[180] while that at about 1501 cm^{-1} is assigned to the asymmetric N-O stretching of monodentate nitrate.[178] The weak Raman bands in the range 200-400 cm^{-1} are attributed to M-O (M = Ce and Cu) vibrations, and the peak at 1609 cm^{-1} to bidentate bridging nitrate.[178] For the asSBA-CeCuO precursor, the peaks at 735 and 1040 cm^{-1} are again assigned to the bending and stretching of nitrate ions, respectively. In contrast, for tfSBA-CeCuO, instead of asymmetric nitrate features (1337, 1501 cm^{-1}), split bands are detected at 1258/1347 and 1455/1513 cm^{-1}. Since the doublet has been found to be insensitive to the nature of the cation, it seems unlikely that the doublet structure is due to ion-pair formation. As the origin of the band splitting, it is rather proposed the presence of specific $NO_3^- \cdots H_2O$ hydrogen-bond interactions.[181]

In the case of asSBA-CeCuO, additional bands are detected due to the presence of P123. In particular, the features at 814, 854, 930, 956, and 1127 cm^{-1} are attributed to C-O-C symmetric stretching, -CH$_3$ wagging, C-C symmetric stretching, -CH$_3$ out of plane bending, and -CH$_3$ rocking,

respectively.[182] The band at 294 cm^{-1} is attributed to Cu-ONO$_2$ or Ce-ONO$_2$ vibrations.[183] With increasing temperature, the Raman bands of the tfSBA-CeCuO precursor continuously decrease in intensity and disappear at about 250 °C, indicating thermal decomposition of Ce(NO$_3$)$_3$ and Cu(NO$_3$)$_2$ to their amorphous oxides. In the case of asSBA-CeCuO, the nitrate redshift from 1040 to 1019 cm^{-1} indicates major changes in the vicinity of the nitrate ligands. Previously, Xu et al. discussed metal-nitrate interactions such as hydration and ion pairing effects on the basis of Raman spectra.[179] Jackson et al. reported on the shift of the nitrate symmetric stretch due to partial replacement of nitrate by hydroxyl ligands.[180] Thus, it is reasonable to conclude that the migration of metal cations is supported by P123 and that M(NO$_3$)$_n$ is coordinated to P123 molecules as MO(OH)$_x$(NO$_3$)$_y$.[41, 88] With increasing temperature P123 is then further catalytically transformed to amorphous carbon (band at ~1600 cm^{-1}), which may confine the growth of ceria and copper oxides. After calcination of the asSBA-CeCuO precursor at 500 °C for 5 h, only one peak is detected at 447 cm^{-1}, which is characteristic of the F$_{2g}$ mode of fluorite CeO$_2$.
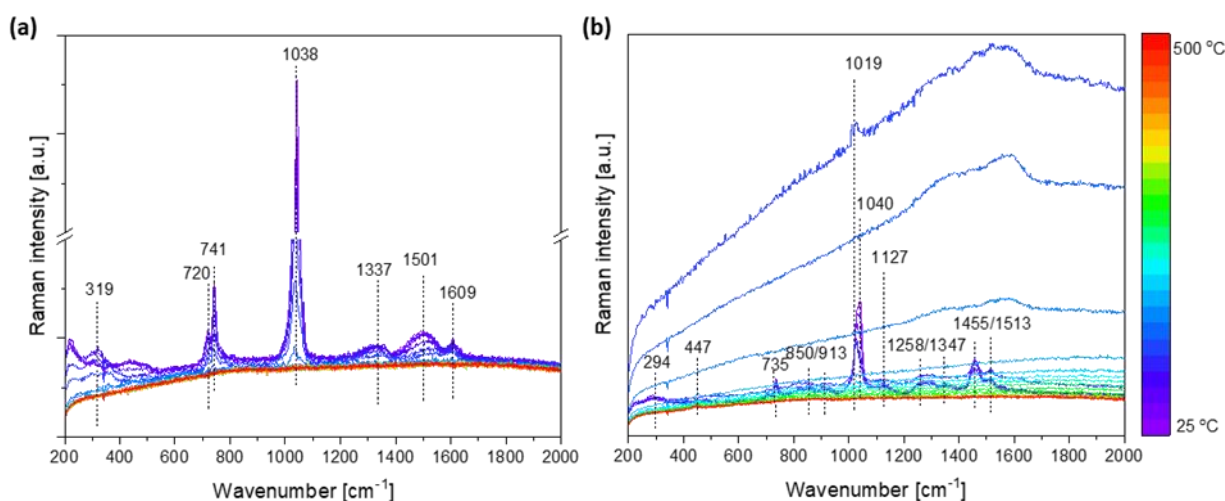

Figure 39. *In situ* Raman spectra of the (a) tfSBA-CeCuO and (b) asSBA-CeCuO precursor samples during air calcination from 25 to 500 °C at a heating rate of 1.5 °C /min. The spectra were recorded using 532 nm laser excitation.

5.2.5. Discussion of the synthesis mechanism and its relevance for the catalytic properties

In the following, it is first combining the results of the multiple *in situ* analyses during synthesis of CuO-CeO$_2$ catalysts to develop a comprehensive mechanistic picture, and then discussing their relevance for the catalytic properties. The gas-phase IR results during calcination reveal that tfSBA-CeCuO undergoes a multi-staged release of NO$_2$ within a wide temperature range (175-320 °C), while asSBA-CeCuO shows NO$_2$ emission at lower temperature (~175 °C) and a rapid release of H$_2$O, hydrocarbon, and CO$_2$ at higher temperature (230 °C) within a narrow temperature window (at about 220-250 °C). This is

further supported by TGA showing a multiple step weight loss for tfSBA-CeCuO but a rapid weight loss in one step for asSBA-CeCuO.

The DRIFT spectra provide important information on the transformation and exchange of ligands and the surface chemistry. It is shown that during calcination the tfSBA-CeCuO precursor decomposes by stepwise NO_2 release, whereas the residual NO_3^- ligands transform from a monodentate (M-ONO_2) to a bridging (M-O-(N=O)-O-M) structure, which further condenses to mixed metal oxide particles. On the other hand, the decomposition of asSBA-CeCuO follows the hydrothermal-like route, i.e., NO_2 is released during replacement of -ONO_2 by -OH followed by the formation of metal hydroxide M(OH)$_x$, which further condenses as metal oxide.

The *in situ* DR UV-Vis spectra of tfSBA-CeCuO provide evidence for synchronous Ce-O and Cu-O changes, including the formation of bridged Ce-O-(NO)-O-Cu, resulting in an evenly mixed CeCuO$_x$ phase. In contrast, asSBA-CeCuO shows a different behavior supported by the different intermediates during the calcination process, including separated Ce(OH)$_3$ and Cu(OH)$_2$ hydroxyls. *In situ* Raman spectroscopy further specifies the differences of the two routes. The spectra of tfSBA-CeCuO are characterized by features of different nitrate species with monodentate and bridging structures, while for asSBA-CeCuO, a splitting of the asymmetric vibration is observed, implying the presence of hydrolyzed M(OH)$_x$(NO$_3$)$_y$ by ligand exchange between NO_3^- and H_2O.
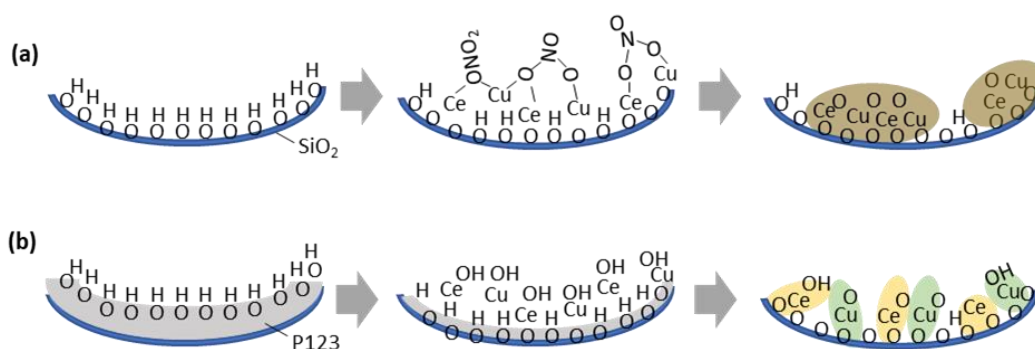
Scheme 8. Mechanism of CuO-CeO2/SBA-15 catalyst synthesis as deduced from multiple *in situ* analyses without (a) and with (b) the presence of template P123.

Scheme 8 summarizes the mechanism of CuO-CeO$_2$ catalyst synthesis as derived from the multiple *in situ* analysis discussed above. In the case of tfSBA-CeCuO (a), cerium and copper nitrates are anchored to the silica surface and nitrates transform into oxides, which involves the conversion of monodentate to bridging nitrate at increasing temperatures and finally the generation of a CeCuO$_x$ solid solution. During the calcination of the asSBA-CeCuO (b) precursor, the nitrate salt is coordinated by

OH groups of P123, thereby replacing nitrate ligands. With increasing temperature, P123 shrinks to the silica surface and separates the -OH coordinated metal ions. Finally, $Ce(OH)_3$ and $Cu(OH)_2$ condense separately as CeO_2 and CuO, respectively.

In previous studies on CuO-CeO_2 catalysts in the context of CO-PROX, WGS, VOCs, and SCR,[184-186] the superior reactivity of CuO-CeO_2 has been attributed to synergistic effects, originating from strong copper-ceria interactions.[187] To this end, Electronic Metal Support Interactions (EMSI) were proposed to explain the outstanding catalytic performance rather than Strong Metal Support Interactions (SMSI).[188] In the EMSI concept, the alteration of the chemical properties of metal sites are related to perturbations in their electronic properties via bonding interactions with the ceria support. In this regard, the fine-tuning of the copper and ceria oxide morphological characteristics can notably affect the metal-support interactions and, as a consequence, alter the catalytic performance.[187] When copper ions enter the ceria lattice or form smaller clusters on the ceria surface, the interaction between CuO and CeO_2 improves the surface reducibility, while the formation of larger copper oxide aggregates is expected to attenuate the interaction with ceria. Previously,[22] CuO-CeO_2 prepared by Cu doping was investigated for NH_3-SCR of NO, showing an enhanced low-temperature activity, but decreased high-temperature activity owing to NH_3 oxidation. On the other hand, for $CuO/Ce_{0.8}Zr_{0.2}O_2$ catalysts used for NO reduction by CO, the maximum catalytic activity was found to be related to moderate sizes of bulk CuO.[189] Thus, consistent with the literature, the sample tfSBA-CeCuO, which is characterized by a $CeCuO_x$ solid solution, shows considerable improvement of the low-temperature NO_x conversion, but lower N_2 selectivity due to its strong oxidation. The asSBA-CeCuO contains separated CuO and CeO_2 particles, exhibiting a moderate EMSI effect, which results in an improved SCR catalytic performance at high temperatures and over a wide temperature range.

5.2.6. Conclusion

Bimetallic oxides CeO_2-CuO supported on mesoporous SBA-15 for NH_3-SCR applications were prepared by solid-state impregnation and structure-activity relations were established. It is demonstrated that templates can be employed in a targeted manner to influence the structure of the oxides, resulting in different NH_3-SCR properties. The catalyst from the template-free synthesis (tfSBA-CeCuO) is characterized by a CeO_2-CuO solid solution showing better low-temperature NO_x conversion but increased high-temperature NH_3 oxidation, owing to its enhanced oxidation properties by coupled Ce^{3+}/Ce^{4+} and Cu^{+}/Cu^{2+} pairs. The catalyst formed in the presence of the template (asSBA-CeCuO) exhibits smaller but separated oxides phases of CeO_2 and CuO, showing an improved SCR performance within a wide temperature range due to the moderate EMSI effect.

A series of *in situ* analyses was performed to directly monitor the precursor decomposition during calcination, including gas-phase, surface, and bulk changes. In addition to conventional TG analysis, *in situ* spectroscopy evidenced two decomposition routes of the metal nitrates to their oxides: the tfSBA-CeCuO precursor followed a nitrate-bridging mechanism via a Ce-O-(N=O)-O-Cu intermediate and ended as CeO_2-CuO solid solution, while the asSBA-CeCuO precursor followed a hydrolysis-based mechanism, forming hydroxides $M(OH)_x$ on the route towards separated CeO_2 and CuO.

As a general remark, the results presented here can be used as a guideline for the development of mesoporous composite oxides by solid-state impregnation methods. The change of synthesis conditions using template assistance enables the dedicated formation of different oxide structures with different catalytic properties. In any case, an *in situ* understanding of the preparation process is a *conditio sine qua non* for the rational synthesis of highly active and selective catalysts.

5.3. *In situ* characterization of CeO_2-MnO_x/SBA-15 catalysts during synthesis and NH_3-SCR

Besides the CuO-CeO_2 system, another bimetallic oxide combination, MnO_x-CeO_2, was tested. Attributed to the multivalent states of manganese, the MnO_x-based oxides have been widely used for the NH_3-SCR reaction in the previous works and exhibit outstanding catalytic performance, especially regarding the low-temperature activity.[190] The intimate contact between the components can effectively accelerate the charge transfer to enhance the electron-hole separation efficiency. Thus, it can be expected that the fabrication process could affect the structure, especially the relative position of Ce and Mn, which may further result in the different catalytic reactivity for NH_3-SCR. It was proved in the last section that changing preparation conditions (with/without P123) could controllably prepare two types of CeCuO catalysts. Here, the same route was adopted that the SSI method with/without P123, to synthesize MnO_x-CeO_2 on mesoporous SBA-15, and then applied the prepared catalysts to the NH_3-SCR reaction. Importantly, *in situ* characterizations were applied to monitor the whole process including both the preparation stage and the SCR catalytic reaction stage.

5.3.1. Sample preparation

Silica SBA-15 was prepared as described previously.[158] The as-made SBA-15 (asSBA-15) was collected using vacuum filtration, followed by calcination for 12 h in a muffle furnace heated to 550 °C at 1.5 °C /min to remove the template P123, yielding template-free SBA-15 (tfSBA-15). CeO_2 and MnO_x were loaded onto asSBA-15 or tfSBA-15 by one-pot solid-state impregnation (SSI) by grinding a mixture of 0.173 g of $Ce(NO_3)_3 \cdot 6H_2O$, 0.100g of $Mn(NO_3)_2 \cdot 4H_2O$, and SBA-15 (0.225 g of asSBA-15 or 0.108 g of tfSBA-15) under ambient conditions for 30 min (molar ratio Ce:Mn = 1:1). The completely mixed powder was calcined in a stream of air at 500 °C for 5 h (heating rate: 1.5 °C/min). The final powder materials will be referred to as tfSBA-CeMnO and asSBA-CeMnO in the following.

5.3.2. Catalytic test

Figure 40(a) depicts the catalytic performance of tfSBA-CeMnO and asSBA-CeMnO catalysts for NH_3-SCR at temperature ranging from room temperature to 500 °C (GHSV = 60000 h^{-1}). The two samples show volcano curves for the NO_x conversion but the optimal temperature window for tfSBA-CeMnO is lower than that for asSBA-CeMnO. Figure 40(b-c) shows the *in situ* monitoring of the exhaust gas during exposure to the NH_3-SCR reaction mixture over the two catalysts for a step-wise increase in temperature from 25 °C to 500 °C.
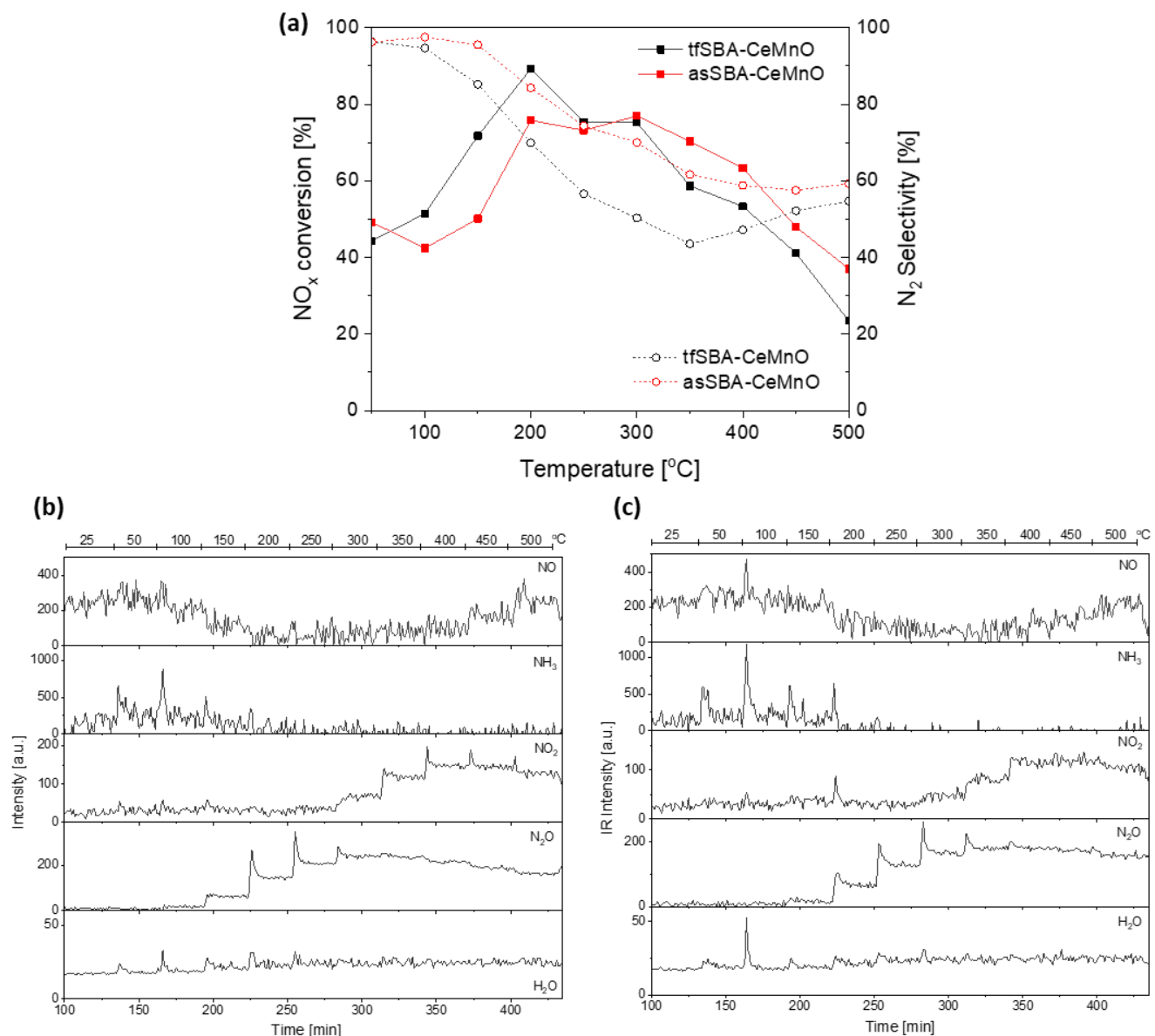
Figure 40. (a) Temperature-dependent catalytic performance of SBA-CeMnO catalysts in NH₃-SCR (GHSV = 60000 h⁻¹). (b-c) *In situ* monitoring of the exhaust gas during exposure to the NH₃-SCR reaction mixture over tfSBA-CeMnO (left) and asSBA-CeMnO (right) at a step-wise increase in temperature from 25 ℃ to 500 ℃.

5.3.3. *In situ* characterization of the synthesis process

Figure 41(a) shows the TGA curves for the calcination of raw tfSBA-CeMnO and asSBA-CeMnO (red lines). For detailed analysis, the exhausted gas during calcination was detected by gas phase FTIR spectroscopy as shown in Figure 41(b-c). The calcination of raw tfSBA-CeO and asSBA-CeO was analyzed in the last section, which revealed the catalytic oxidation of carbon-containing material with cerium ions as catalyst. Here, the tfSBA-CeMnO sample shows a sharp weight loss at low temperature

(100 °C) due to water emission (at two typical IR ranges from 1000-2000 cm^{-1} and 3500-4000 cm^{-1}) especially for the condensed or physically adsorbed water in the channels. The TGA curve then shows two main weight loss stages at about 160-180 °C and 180-280 °C, which correspond to the two stages of NO$_2$ emission (at about 1629 cm^{-1}). For calcination of raw asSBA-15, the lower free water emission at low temperature is due to the occupation of hydrophobic fragments of P123 in the channels. The continuous weight loss at 130-290 °C is attributed to the release of carbon-containing fragments from P123 decomposition. It is found that at temperatures of about 150 °C-170 °C the decomposed product signals mainly consist of C-O-C (1320 cm^{-1}) and C=O (1700 cm^{-1}), reflecting the preliminary decomposition of macromolecular P123. At higher temperature of about 175 °C, the observed NO$_2$ emission implies that cerium or manganese nitrate is decomposed. Meanwhile, the decomposition of P123 speeds up to release large amounts of carbon-containing gas and CO$_2$ which are tentatively attributed to the catalytic effect of metal ions in the oxidation of P123.
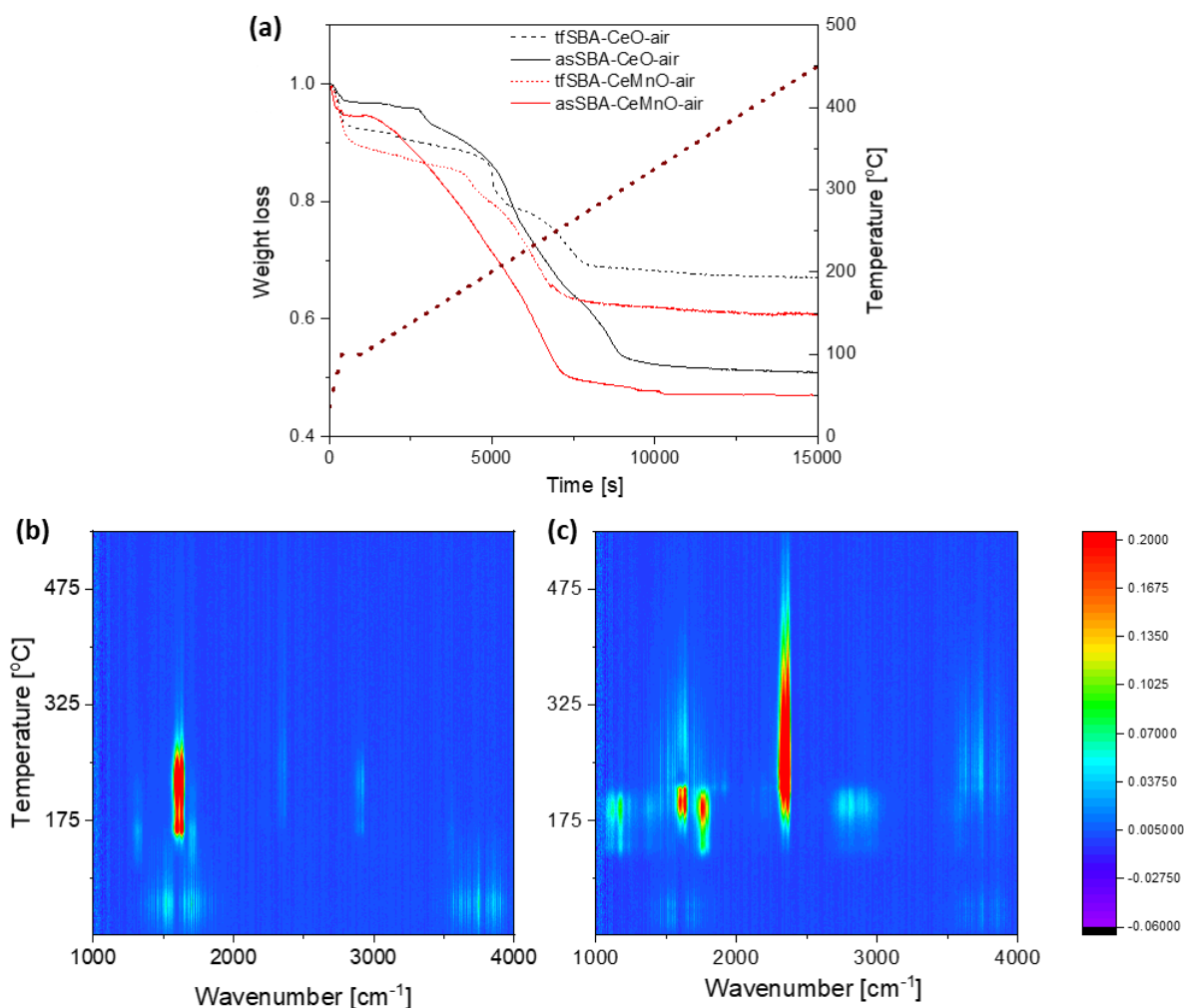

Figure 41. (a) TGA of raw samples calcined in air with a heating rate of 1.5 °C/min. *In situ* monitoring of the exhaust gas during the calcination of (b) tfSBA-CeMnO and (c) asSBA-CeMnO.

Figure 42 depicts the UV-Vis DR spectra of the raw tfSBA-CeMnO and asSBA-CeMnO during the calcination process. As previously reported,[191] peaks at 250 and 300 nm can be attributed to the $Ce(NO_3)_3$, and peaks at 245 and 320 nm to $Mn(NO_3)_2$, which related to the broad bands at about 257 and 320 nm for the initial raw samples in Figure 42(a-b) at room temperature.

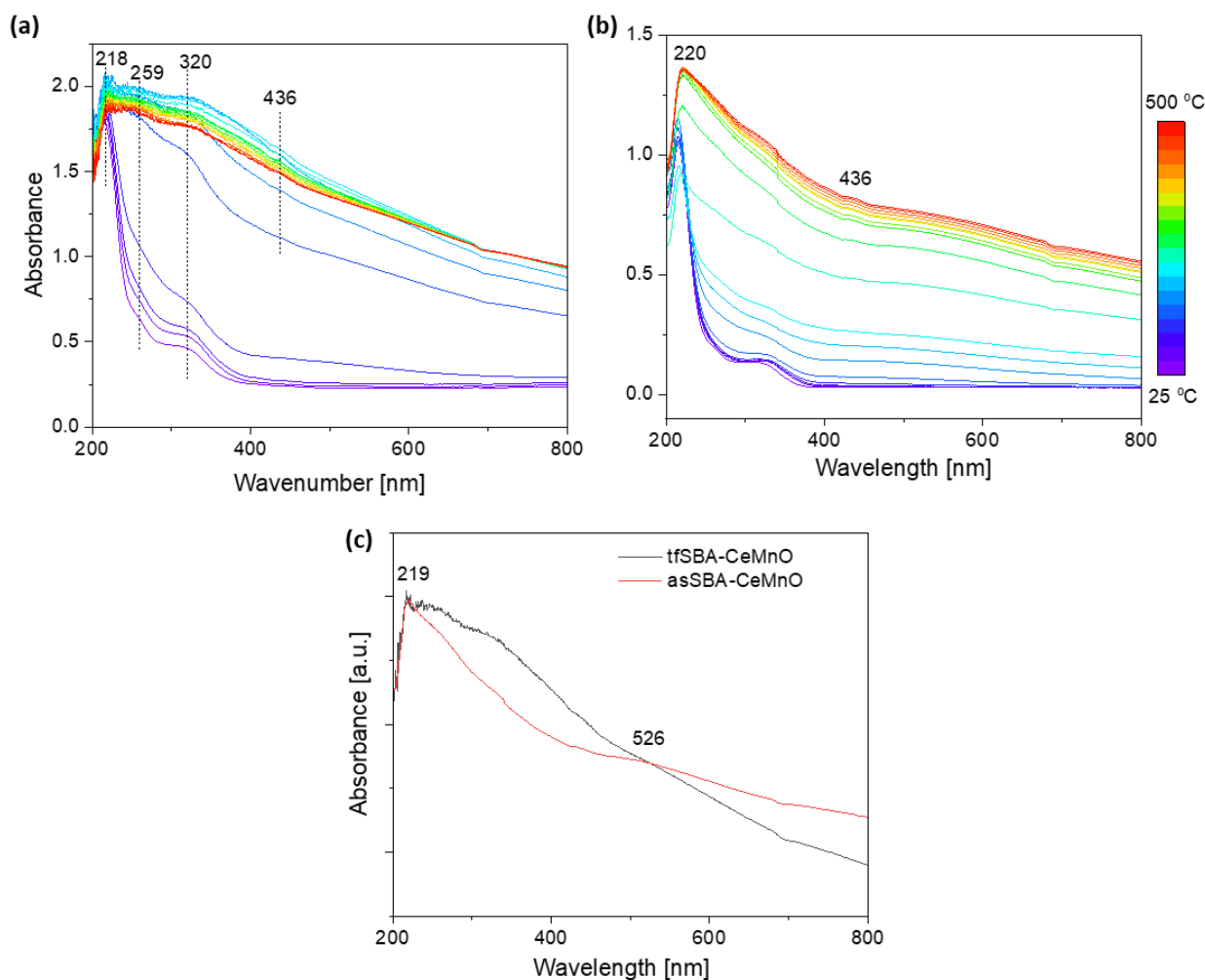Figure 42. *In situ* DR UV-Vis spectra of (a) tfSBA-CeMnO and (b) asSBA-CeMnO during calcination in N_2+20% O_2 from 25 to 500 °C at a heating rate of 1.5 °C/min. (c) Spectra of the calcined samples after cooling down to room temperature in N_2+20% O_2.

Generally, the UV-Vis spectra of bare CeO_2 exhibit three band centers at around 255, 285 and 340 nm, originating from $O^{2-} \rightarrow Ce^{3+}$, $O^{2-} \rightarrow Ce^{4+}$ and interband (IBT) transitions, respectively.[192] In addition, crystalline Mn_3O_4 has a band gap of 2.18 eV and a corresponding absorption wavelength of about 570

nm. The bands at about 500 nm and 270 nm were assigned to the $^6A_{1g} \rightarrow {}^4T_{2g}$ crystal field transitions of Mn^{2+} and the charge transfer transition of $O^{2-} \rightarrow Mn^{3+}$.[193]

With increasing temperature, for tfSBA-CeMnO, the adsorption curve increases sharply until 200 ^{o}C, with the highest level being characterized by features at 218, 259, 320 and 435 nm, due to f→d transitions of Ce^{3+}, $O^{2-} \rightarrow Ce^{3+}$ CT, $O^{2-} \rightarrow Mn^{4+}$ CT, and d→d transitions of Mn^{4+}, respectively. In contrast, for asSBA-CeMnO the change in adsorption varied only slowly with increasing temperature. Importantly, the adsorption reversely decreases at higher temperature for tfSBA-CeMnO which corresponds to the decreased adsorption edge and indicates that the CeO_2 and MnO_x were coupled, leading to a narrow band gap during the high temperature sintering process. For the asSBA-CeMnO sample, on the other hand, the adsorption increased evenly in the whole wavelength range, implying the formation of separate CeO_2 and MnO_x without close interaction.

Figure 42(c) shows the spectra of prepared tfSBA-CeMnO and asSBA-CeMnO after cooling down to room temperature (25 ^{o}C) in 20 % O_2/N_2. The high and broad adsorption in the low wavelength range (<500 nm) for calcined tfSBA-CeMnO is attributed to the narrow band gap from the doping effect of mixed CeO_2 and MnO_x. For calcined asSBA-CeMnO on the other hand, the spectrum shows a higher adsorption at wavelengths > 500 nm, which is assigned to the presence of nano δ-MnO_2.[194] As reported previously, the absorption edge of the CeO_2 interband transition is sensitive to the crystal size and blue shifts with decreasing size, especially when the size is smaller than 10 nm.[193] Thus, the asSBA-CeMnO owns smaller size of CeO_2 than the tfSBA-CeMnO for its left position of the spectrum ranging 219-526 cm^{-1}.

The DR UV-Vis spectra prove that the calcination of tfSBA-CeMnO is accompanied by complex interactions of Ce^{3+}/Ce^{4+} and $Mn^{2+}/Mn^{3+}/Mn^{4+}$, while asSBA-CeMnO exhibits a gradual decomposition of cerium nitrate and manganese nitrate to obtain ceria and separated MnO_x nanoparticles. Moreover, the smaller size of ceria for asSBA-15 is due to the confined space effect of the template P123 limiting the oxide growth.

Figure 43 depicts *in situ* DRIFT spectra during the calcination process of tfSBA-CeMnO and asSBA-CeMnO, which provides information on the surface reactions during the decomposition of nitrate salts and generation of ceria and manganese oxide. A standard KBr sample exposed to air at room temperature was used to measure the background spectrum.
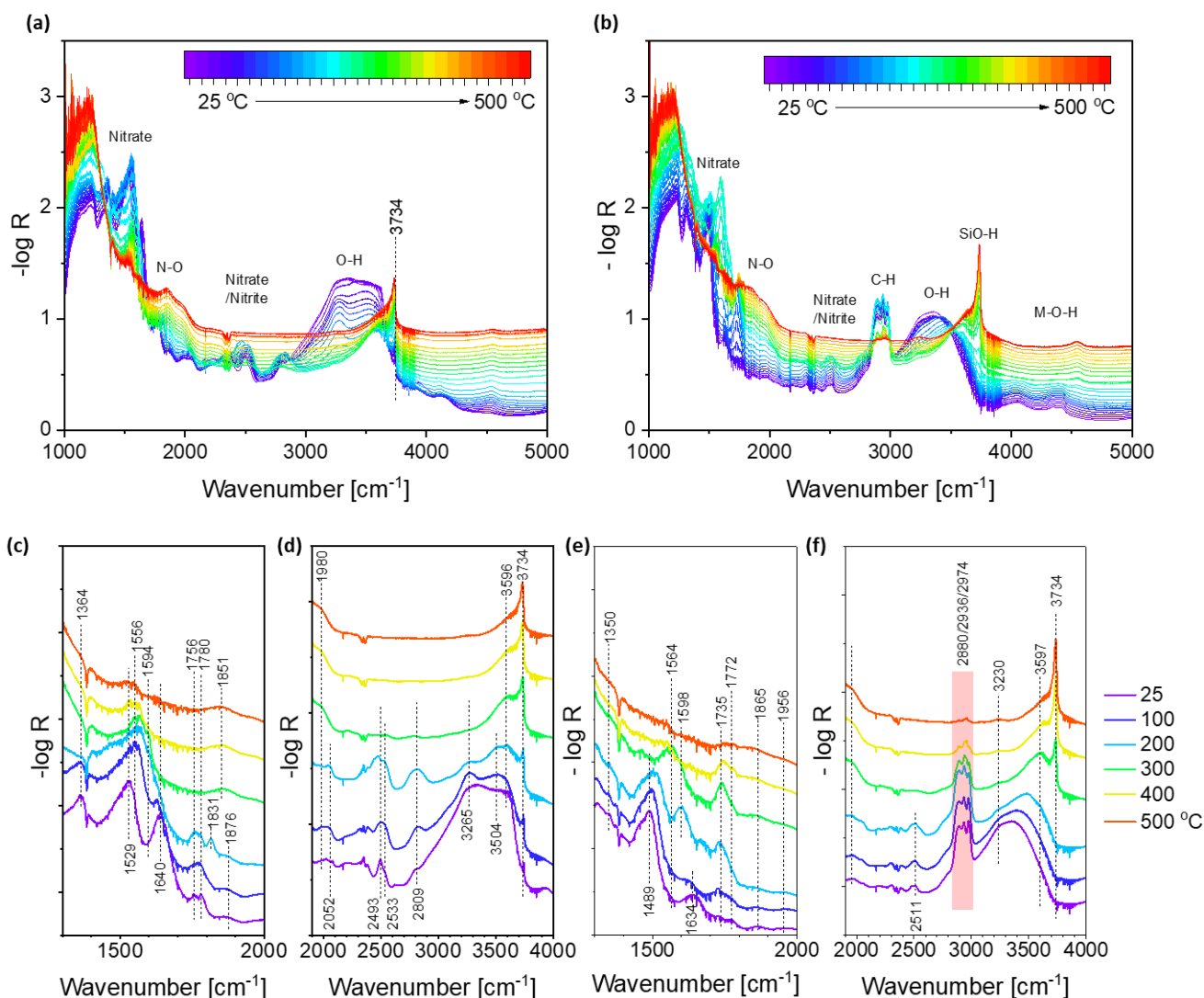
Figure 43. *In situ* DRIFT spectra recorded during the preparation of (a) tfSBA-CeMnO and (b) asSBA-CeMnO by calcination in N_2+20% O_2 from 25 to 500 °C at a heating rate of 1.5 °C/min, while (c) and (d) are enlarged views of (a), and (e) and (f) enlarged view of (b).

Generally, the calcination of cerium nitrate involves the decomposition of nitrate salt to form oxides. In Figure 43(a) and Figure 43(b), the *in situ* DRIFT spectra for both tfSBA-CeMnO and asSBA-CeMnO are characterized by features of various nitrate species (at 1500-1600 cm^{-1}), of N-O vibrations (at 1700-2000 cm^{-1}), of nitrate and nitrite species gathered together (2400-2800 cm^{-1}), of O-H vibrations of hydrogen bonded water (at 3200-3700 cm^{-1}) and of isolated silanol (at 3734 cm^{-1}), and of the combination mode of O-H with the anchoring bond (at 4000-5000 cm^{-1}).[128, 171] In addition, the bands at 2880-2974 cm^{-1} in Figure 43(b) for asSBA-CeMnO are typically assigned to C-H stretching, which is attributed to the P123 template.

In detail, for tfSBA-CeMnO preparation (see Figure 43(c)), the band at 1364 cm^{-1} is assigned to the asymmetric vibration of NO$_3^-$ which gradually disappears above 300 °C.[195] The peaks at 1529, 1556, and 1594 cm^{-1} are attributed to monodentate, bidentate, and bridging nitrate, respectively. At 25 °C, the nitrate species mainly shows the monodentate structure coordinated with a central cerium ion. With increasing temperature, the bidentate and bridging nitrates all appear, indicating a bridging effect to form the M-O-(N=O)-O-M structure. t should be noted that the calcined sample (at 500 °C) still shows features originating from monodentate and bidentate nitrates. The peak at 1640 cm^{-1} is attributed to adsorbed H$_2$O which desorbs after 100 °C. The peaks within 1700-2000 cm^{-1} are typically assigned to N-O vibrations, and the variation results from the vibrational mode and the chemical environment of the -NO species. Following the reported assignment, the peaks at 1700-1800 cm^{-1} are assigned to the asymmetric vibration, and the bands at 1800-1900 cm^{-1} are assigned to the symmetric vibration.[128] Another important factor affecting the surface NO species is the metal ion adsorbent. Being rich in d-electrons, the π-back donation is possible for low valent Mn^{2+} ions and the N-O stretching mode can decrease compared with cerium (d^0). On the other hand, the oxidation of the metal ion to its high valence does not form nitrosyls upon NO adsorption. Here, the bands at 1756 and 1876 cm^{-1} are assigned to Mn^{2+}-NO, while the bands at 1780 and 1965 cm^{-1} are assigned to Ce^{3+}-NO. The peak at 1831 cm^{-1} appearing at 200 °C is assigned to Mn^{3+}-NO.[128] At low temperature (25-200 °C), these features exist for nitrosyls on low valent ions (Mn^{2+}-NO and Ce^{3+}-NO). With increasing temperature (above 300 °C), the features disappear due to the oxidation of Mn^{2+} to Mn^{3+} and further high valent Mn^{n+} in MnO$_x$ and of Ce^{3+} to Ce^{4+} in CeO$_2$. The features at 1851 cm^{-1} are tentatively assigned to nitrosyls on mixed Ce-O-Mn sites which provide low valent Ce^{3+} ions due to doping with high valent Mn^{n+} ions.

In Figure 43(d), the peaks at 2493 and 2809 cm^{-1} are assigned to nitrate salt and the peak at 2533 cm^{-1} which gradually increases with increasing temperature to 200 °C is assigned to nitrite. Initially, the sample shows features at 2493 and 2809 cm^{-1} due to nitrate; increasing temperature results in a broadening of these peaks, as well as the appearance of a shoulder peak at 2533 cm^{-1} which is attributed to nitrite species. This behavior implies that the O transfers from the nitrate group to the metal ion. The broad band within 3000-3700 cm^{-1} is assigned to O-H stretching of adsorbed water, while the peaks at 3265, 3596, and 3374 cm^{-1} are attributed to O-H stretching of Mn-OH, Ce-OH, and Si-OH, respectively.[171]

For asSBA-CeMnO (see Figure 43(e)), the weak feature at 1350 cm^{-1} is assigned to the asymmetric stretch vibration of NO$_3^-$. The peaks ranging from 1489 to 1598 cm^{-1} are assigned to various differently structured nitrate species. It is noted that at room temperature the nitrate peak appears at 1489 cm^{-1} and is tentatively assigned to monodentate nitrate. The low wavenumber of this feature, compared with the

common value at 1525 cm^{-1}, is due to the interaction between the nitrate ligand with template P123.[196] At 200 ℃, a peak at 1598 cm^{-1} appears which is assigned to bridging nitrate while at 300 ℃, a peak at 1564 cm^{-1} appears which is assigned to bidentate nitrate accompanied by the disappearance of the features at 1489 and 1598 cm^{-1}, indicating that the nitrate precursor was partially replaced by O-H ligands during the grinding stage even at room temperature. The feature due to bridging nitrate at 1598 cm^{-1} observed at 200 ℃ may result from the condensation of adjacent metals and the presence of bidentate nitrate at 300 ℃ can be explained by its thermal stability. The peaks at 1735 and 1865 cm^{-1} are attributed to Mn^{2+}-NO, while those at 1772 and 1956 cm^{-1} are attributed to Ce^{3+}-NO species. It should be noted that the N-O vibration at 1735 cm^{-1} persists until 400 ℃, originating from nitrosyl on reduced Mn^{n+} in reductive atmosphere, while the features related to the cerium site disappear at high temperature (above 300 ℃). This indicates that the decomposition of cerium nitrate and manganese nitrate occurs via separated processes.

In Figure 43(f), the peak at 2511 cm^{-1} is attributed to nitrite species, reflecting the reduction effect of template P123 on the nitrate precursor. As discussed above, the bands at 3230, 3597, and 3734 cm^{-1} are attributed to hydroxyl groups on Mn, Ce, and Si sites, respectively.

Comparing the spectra of the two samples, the feature at 1489 cm^{-1} for monodentate nitrate observed for asSBA-CeMnO sample is red shifted to that at 1529 cm^{-1} due to the tfSBA-CeMnO sample. This is attributed to the different ligands, which means that the nitrate ligands are partially replaced even at room temperature, changing the metal-ligand distance and electron donor power of the ligand. In addition, in the range 2400-3000 cm^{-1} assigned to nitrate or nitrite species, tfSBA-CeMnO shows features of both nitrate and nitrite (2493/2533/2809 cm^{-1}), An initial strong peak at 2493 cm^{-1} is assigned to free nitrate ions at room temperature. This peak gradually broadens due to contributions at 2471 (nitrate) and 2521 cm^{-1}(nitrite) at 25-175 ℃, originating from the mixture of nitrate and nitrite due to the multivalence of Ce and Mn, especially reduced Mn^{2+}. When the temperature increases to 175-225 ℃, the band at 2471 cm^{-1} (nitrate) becomes stronger and then all these peaks disappear due to the complete decomposition of the nitrate salts at higher temperatures. This behavior indicates that the M(NO$_3$)$_x$ precursors decompose by a redox reaction producing a NO$_2^-$ intermediate, followed by re-oxidation to NO$_3^-$. On the contrary, the asSBA-CeMnO sample shows only a feature of nitrite species (2511 cm^{-1}) due to the interaction with P123 at the grinding stage. At higher wavenumbers (see Figure 43(a)), the peaks at 4049, 4339, and 4428 cm^{-1} are assigned to the combination mode of M-OH species, implying the formation of both Ce(OH)$_4$ and Mn(OH)$_4$, which further condense as metal oxides. Thus, template P123 can react with the nitrate precursor at room temperature and coordinate the metal ions and fixed them onto the SBA-15 surface.

Secondly, with increasing temperature, tfSBA-CeMnO shows an evolution of surface nitrate species from monodentate to bridging nitrate. The N-O vibrations for nitrosyl attached to Ce^{3+} and Mn^{2+} ions disappear at high temperature due to the oxidation of the metal ions, while a mixed substrate (Ce-O-Mn) is formed, giving rise to a nitrosyl feature at 1851 cm^{-1}. For asSBA-CeMnO, the metal ion is coordinated onto the substrate by P123 and the nitrate ligand of manganese and cerium shows separated behaviors, especially, the Mn-NO feature remains present until 400 ^{o}C due to the presence of reduced Mn^{2+}, while Ce-NO almost disappears at temperatures above 300 ^{o}C. Thus, tfSBA-CeMnO tends to form a mixture of cerium dioxide and manganese oxide, while asSBA-CeMnO shows separated oxides.

The third difference is the surface -OH group, especially the isolated Si-OH group. For tfSBA-CeMnO sample, this feature exists at all times. However, for asSBA-CeMnO, the feature at 3734 cm^{-1} appears only above 300 ^{o}C which can be explained by the coverage of P123 on the SBA-15 surface at low temperature, while the removal of P123 leads to the appearance of the Si-OH feature.

In summary, the *in situ* results reveal details of the calcination process for the tfSBA-CeMnO and asSBA-CeMnO samples. With the assistance of template P123 (asSBA-CeMnO), the cerium nitrate and manganese nitrate interact with the P123 of asSBA-15 during the grinding stage. leading to a separated growth of the oxides. Without P123 (tfSBA-CeMnO), the mixture of nitrate precursors is thermally decomposed, showing a highly mixed oxide. In addition, the P123 inside the pore can also provide confined space for the growth of oxides, facilitating the formation of well dispersed oxides on the SBA-15 support.

5.3.4. Using *in situ* DRIFTS to elucidate the SCR reaction mechanism

In situ DRIFT spectroscopy was also employed to unveil the mechanism of prepared asSBA-CeMnO by monitoring the changes of the surface species. The sample exposed to N_2 at the experimental temperature (200 ^{o}C) was used to measure the background spectrum.

Prior to the adsorption of the reactant gases, the catalyst was pretreated at 500 $°C$ in N_2 (50 mL/min) for 1 h. After the catalyst was cooled to 200 $°C$, the N_2 gas was replaced by a gas mixture of 500 ppm NH_3/N_2 (50 mL/min), and *in situ* DRIFT spectra of the asSBA-CeMnO catalyst were taken; the results are shown in Figure 44(a). Similarly, the N_2 gas was replaced by a gas mixture of 500 ppm NO/5 vol. % O_2/N_2 (50 mL/min), and the corresponding *in situ* DRIFT spectra are shown in Figure 44(b).
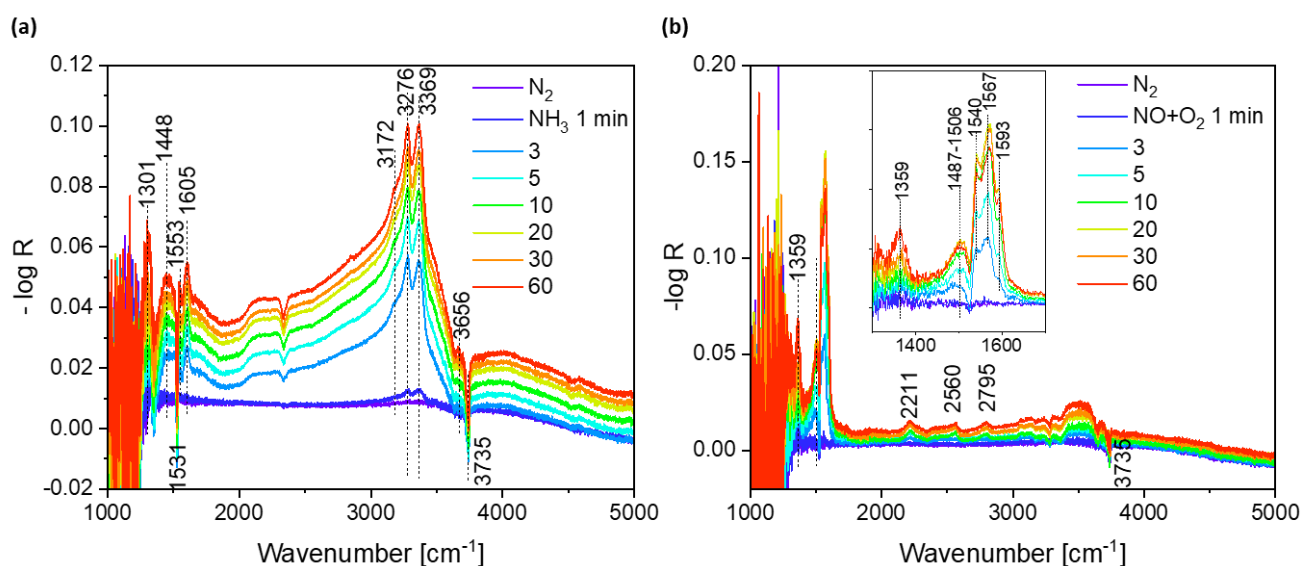
Figure 44. *In situ* DRIFT spectra of asSBA-CeMnO during exposure to (a) NH₃, (b) NO/O₂ at 200 °C.

As shown in Figure 44(a), upon gas exposure to NH_3/N_2 eight bands at 1301, 1448, 1553, 1605, 3172, 3276/3369, 3656, and 3735 cm^{-1} appear. The bands at 1448 cm^{-1} and 1605 cm^{-1} are assigned to NH_4^+ bound to Bronsted acid sites (B acid site) and NH_3 bound to Lewis acid sites (L acid site), respectively.[76] The band at 1553 cm^{-1} is assigned to NH_2 species.[76] The bands at wavenumbers > 3000 cm^{-1} are assigned to stretching vibrations of N-H or O-H, of which the 3172 cm^{-1} feature is assigned to N-H of NH_4^+ on B acid site, the 3276/3369 cm^{-1} features to N-H of NH_3 on L acid site, the 3656 cm^{-1} feature to O-H bond of Ce-OH, and the 3735 cm^{-1} feature to O-H of isolated silanol group (Si-OH) at the surface.[85] The peak at 1301 cm^{-1} is tentatively assigned to bidentate nitrate species although it NH_3 is adsorbed, suggesting that adsorbed NH_3 is oxidized by surface lattice oxygen.[197] Note that all bands appear and increase in intensity with increasing adsorption time. These results indicate that NH_3 species may be adsorbed on both the L and B acids sites surface of the CeMnO oxides at 200 °C, and NH_3 may be oxidized to NH_2.

Figure 44 (b) shows the spectra upon exposure to $NO/O_2/N_2$ which are characterized by nitrate bands at 1359, 1487-1506, 1540-1593, 2560, and 2795 cm^{-1}, of which the 1359 cm^{-1} peak is assigned to NO$^-$,[128] the broad peak at 1487-1506 cm^{-1} is assigned to bidentate nitrate.[198] and the peaks at 1540, 1567, and 1593 cm^{-1} are typically assigned to monodentate, bidentate, and bridging nitrates, respectively. The bands at 2560 and 2790 cm^{-1} are attributed to nitrite and nitrate. With increasing exposure, the nitrate/nitrite species increased in intensity except for the reverse decrease of monodentate (1540 cm^{-1}) and bidentate (1500 and 1567 cm^{-1}) nitrate after reaching the maximum value at about 20-30 mins. This

indicates that NO is first adsorbed onto the surface and oxidized to form surface adsorbed nitrate species (1487-1593 cm^{-1}). The decrease of these features after a long-time exposure might be due to the formation of the low valent species NO^- (1359 cm^{-1}) and N_2O (2211 cm^{-1}). In detail, NO is catalytically oxidized to NO_2 by surface lattice oxygen and the desorption of NO_2 leaves an oxygen vacancy and two reduced Ce^{3+} sites, which serves as adsorption site for NO to form NO^- as discussed above. The formation and increase of low valent NO^- (I) and N_2O (I) implies that the activation of O_2 on the surface might be the rate determining step.

Figure 45 depicts the *in situ* DRIFT spectra of asSBA-CeMnO during exposure to (a) $NO+O_2$ after pre-adsorption of NH_3, and to (b) NH_3 after pre-adsorption of $NO+O_2$ at 200 ºC. The pretreatment operations are the same as described in Figure 44. As shown in Figure 45(a), the intensity of the bands at 1550 and 1605 cm^{-1} assigned to NH_2 and NH_3 bound to L acid sites decreases with an increase in the exposure time to 500 ppm NO/O_2, whereas the intensities of the bands at 1440 cm^{-1} assigned to NH_4^+ bound to B acid sites decreases initially and then increases again, indicating that L acid sites are the active sites for the SCR reaction via E-R route. On the other hand, the strong N-H stretching features (3280, 3359 cm^{-1}) gradually disappear while the features for nitrate/nitrate species increase in intensity.

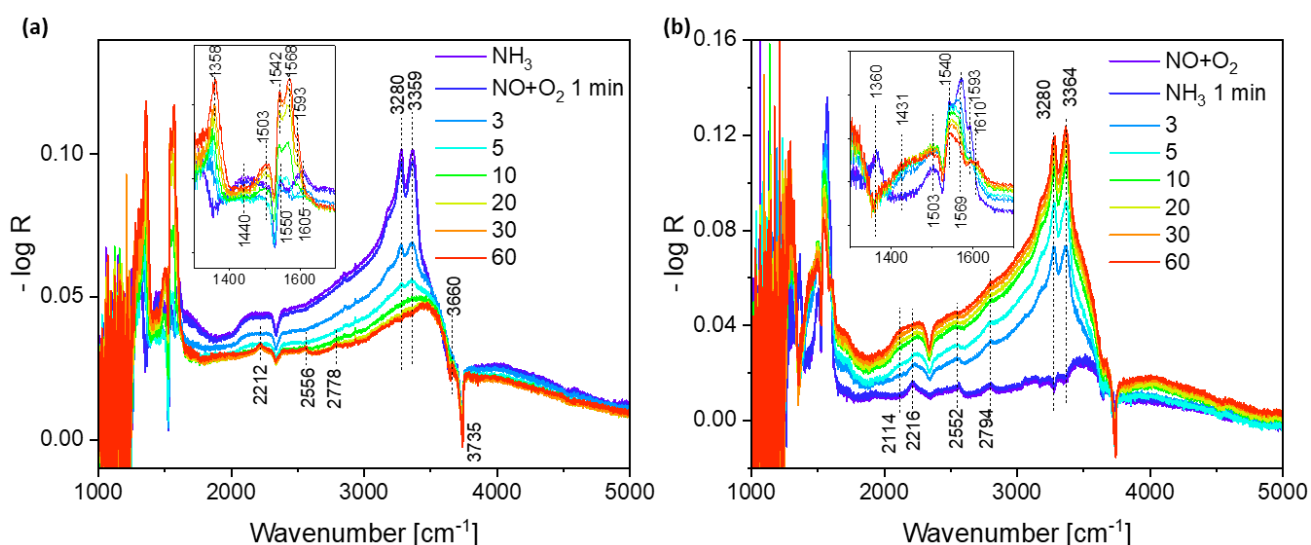Figure 45. *in situ* DRIFT spectra of asSBA-CeMnO during exposure to (a) $NO+O_2$ after pre-adsorption of NH_3, (b) NH_3 after pre-adsorption of $NO+O_2$ at 200 ºC.

As shown in Figure 45(b), the intensity of the band at 1593 cm^{-1} assigned to bidentate nitrate decreases with an increase in the exposure time to 500 ppm NH_3, whereas the intensities of the bands at 1540 and 1593 cm^{-1} assigned to bridged nitrate and monodentate nitrate, respectively, hardly change, especially when comparing their relative intensity, indicating that bidentate nitrates are the most reactive

among the different adsorbed nitrate species to react with NH_3. It should be noted that the feature at 1358 cm^{-1} assigned to NO^- quickly disappears due to its high reactivity towards NH_3, while the features at 2552 cm^{-1} and 2794 cm^{-1}, assigned to nitrite and nitrate species, are stable even after 1 h exposure to NH_3. Thus, the adsorbed NO_x species is partially reactive towards NH_3 via the L-H route, especially the NO^- species, although the bidentate nitrate shows also activity.

In order to clarify the interaction between NH_3 and NO_x on the catalyst surface, different pre-treated surfaces were characterized by DRIFT spectroscopy as shown in Figure 46.
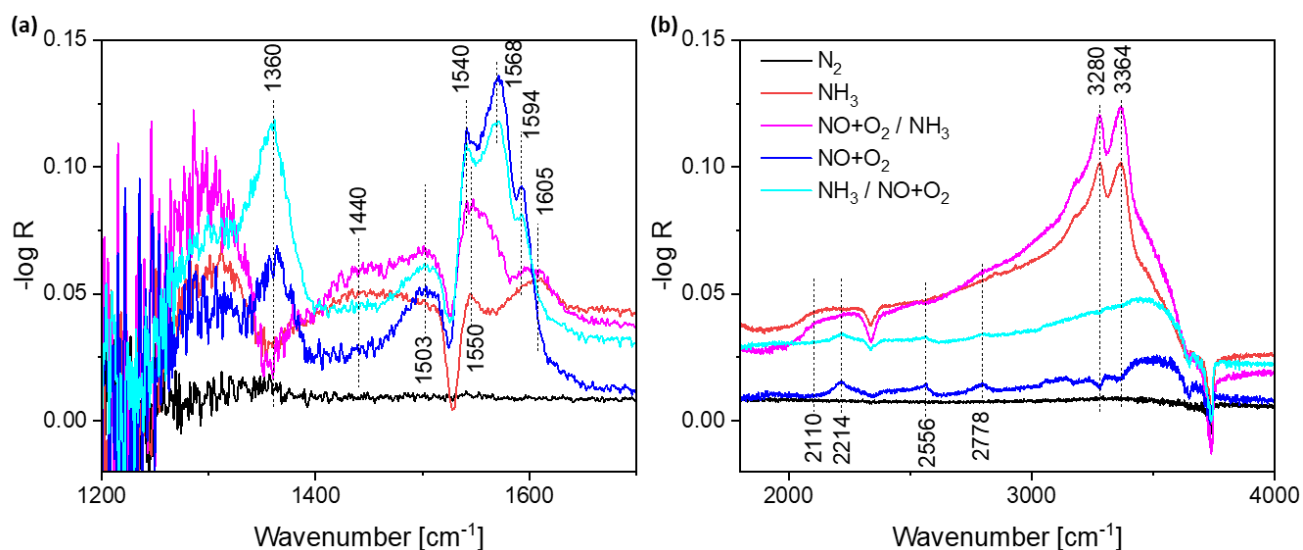

Figure 46. *In situ* DRIFT spectra of asSBA-CeMnO after different surface treatments at 200 °C. N_2: original surface, NH_3: treated in NH_3 for 1 h, NO/O_2/NH_3: reacted in NO/O_2 for 1 h and then treated in NH_3 for 1 h, NO/O_2: treated in NO/O_2 for 1 h, NH_3/NO/O_2: treated in NH_3 for 1 h and then treated in NO/O_2 for 1 h.

Comparing the NH_3 treated (red curve) and the (NO/O_2)/NH_3 treated (pink curve) sample, the pink curve shows higher intensity of features (see Table 9 and Table 6) at about 1440 cm^{-1} (B site bounded NH_4^+), 1503 cm^{-1} (bidentate nitrate), 1550 cm^{-1} (monodentate nitrate) and 3280/3364 cm^{-1} (N-H stretching), indicating the $NO+O_2$ treated surface owns nitrate species which is inert to NH_3 and prefers to adsorb NH_3 on its surface.

Comparing the NO/O_2 treated (blue curve) and NH_3/(NO/O_2) treated (cyan curve) sample, almost the same features over the whole wavenumber range are observed, indicating that the surface pre-adsorbed NH_3 completely reacted. It should be noted that the cyan curve shows a higher intensity in the lower wavenumber range (<1520 cm^{-1}), such as 1360 cm^{-1} (NO^-), but a lower intensity in the higher wavenumber range (>1520 cm^{-1}). Considering the presence of a reduced surface due to NH_3 pre-

treatment, it is concluded that NO is oxidized to high valent nitrate/nitrite species on the original catalyst surface but partially reduced to low valent NO^- species on reduced surface.

Comparing the NH_3 treated (red curve) and NH_3/(NO/O_2) treated (cyan curve) sample, the peak at 1550 cm^{-1}, assigned to amine species, disappears after NO/O_2 treatment (cyan curve), implying that NH_2 is the active intermediate. The peak at 1360 cm^{-1} (NO^-) appears for the cyan curve, indicating that this feature was from the NO_x instead of the ammonia related species.

Comparing the NO/O_2 treated (blue curve) and (NO/O_2)/NH_3 treated (pink curve) samples, the peak at 1360 cm^{-1} (NO^-) disappears from the blue to pink curve, implying the reactivity of NO^- species towards NH_3. The peaks at 1503 and 1568 cm^{-1}, assigned to bidentate nitrate species, decrease in intensity, implying the reactivity of part of the bidentate nitrate towards NH_3.

From the DRIFT spectra above, it can be concluded that the L-H and E-R routes are co-existent for the NH_3-SCR reaction. In detail, for the E-R route, adsorbed NH_3 can completely react with gaseous NO_x and NH_2 is proposed to be the active species. For the L-H route, NO is adsorbed on the surface as NO_x species and partially reacts with NH_3 and NO^- is proposed to be the reactive species. Oxidized NO as nitrate or nitrite is almost inert to react with NH_3 except for part of the bidentate nitrates.

5.3.5. Conclusion

In this section, bimetallic oxide catalysts based on Mn and Ce, MnO_x-CeO_2, were loaded onto SBA-15. The synthesis of tfSBA-CeMnO and asSBA-CeMnO shows different formation routes of the CeO_2 and MnO_x from their nitrate salts. For tfSBA-CeMnO, the cerium nitrate and manganese nitrate are decomposed as nitrite first and then as their oxides at higher temperature, while for asSBA-CeMnO the decomposition went through the ion exchange between nitrate ligands and hydroxyl groups, forming cerium hydroxide and manganese hydroxide first with release of carbon-containing fragments of P123. These two different routes result in different structures and properties of the prepared tfSBA-CeMnO and asSBA-CeMnO catalysts, and further lead to different catalytic performances in the NH_3-SCR reaction. Moreover, when *in situ* DRIFT spectroscopy was applied to get insight into the mechanism of NH_3-SCR reaction on asSBA-CeMnO, it was found that the reaction mainly follows the E-R route, although part of the adsorbed NO_x (NO^- and bidentate nitrate) is active towards NH_3 via the L-H route.

6. Surface modification by Atomic Layer Deposition (ALD) methods

In the last two chapters, the solid-state impregnation (SSI) method was introduced and employed to prepare ceria-based oxide catalysts supported on mesoporous SBA-15. However, with the addition of more complicated components, conventional impregnation methods would lead to serious pore blockage and a sharp decrease of the surface area which goes against the original intention to design the mesoporous structure. To this end ALD methods have been widely applied to the preparation of catalysts due to the flexibility and control of structure and composition.[199] Although the economy of using ALD for the catalysis industry may be questioned, the controlled surface modification makes it an ideal approach to design model catalysts at the laboratory level and explore the active sites, which further helps to gain insight into the catalytic mechanism. On the other hand, in the studies described above, the reaction during the catalyst preparation is proved to be important to determine the final state of the prepared catalyst. Compared with calcination-involved methods (e.g. SSI), ALD relies more on the reaction between the active precursor and the substrate surface, and is therefore a good tool to explore the controllability of the synthesis by adjusting the deposition reaction.

In this chapter, using ALD VO_x and TiO_2 supported on SBA-15 were prepared as a model catalyst to obtain a high surface area vanadia-based catalyst for the NH_3-SCR reaction. Then, several atomic layers of SiO_2 were coated on prepared CeO_2@SBA-15 to form a $SiO_2/CeO_2/SiO_2$ sandwich structure, and the effect of Ce-O-Si species on the NH_3-SCR reactivity is discussed. At last, active VO_x is site-selectively deposited on prepared CeO_2@SBA-15 by pretreating the CeO_2@SBA-15 with different surface reactions followed by ALD of VO_x.

6.1. VO$_x$-TiO$_2$/SBA-15 catalysts for NH$_3$-SCR applications by ALD

Selective catalytic reduction (SCR) of NO$_x$ with NH$_3$ is proved to be the most effective technology for the removal of NO$_x$ from stationary and mobile sources. Commercial vanadia-based ammonia SCR catalysts are typically based on vanadia and tungsten oxide (or molybdenum oxide) on TiO$_2$ anatase, but vanadia supported on TiO$_2$ has been extensively studied as a model catalyst system [200].

It is known from the literature, that SCR activities depend on the vanadia structure and the support material [201, 202]. Mesoporous materials such as silica SBA-15 provide higher surface area than conventional powder or planar supports [203, 204], and the controlled synthesis of vanadia supported on SBA-15 was reported [205]. However, SiO$_2$ supported VO$_x$-based catalysts were reported to show only poor SCR performance compared to titania-based systems [201, 206]. On the other hand, Segura et al. studied vanadia/titania supported on SBA-15 and attributed the good catalytic NH$_3$-SCR reactivity to isolated VO$_x$ or TiO$_2$ species [207]. Reiche et al. prepared high surface area TiO$_2$, SiO$_2$, and TiO$_2$-SiO$_2$ supported vanadia systems using sol-gel methods and selective vanadia grafting, and found TiO$_2$-based catalysts to show the highest SCR activity. In mixed TiO$_2$-SiO$_2$ aerogels, vanadia was reported to be preferentially grafted to Ti sites [201]. Compared to these conventional synthesis techniques, atomic layer deposition (ALD) enables accurate control at the atomic scale without damaging the structure of the original matrix [204, 208]. Although ALD has been widely applied to metal-oxide deposition, such as SiO$_2$ [209], TiO$_2$ [210], and VO$_x$ [204, 211, 212], there are only very few studies on the deposition of vanadia and titania on mesoporous SBA-15 [213], and its application to NH$_3$-SCR.[212]

In the previous work, a hierarchical NH$_3$-SCR model catalyst was developed using low surface area silica particles as a platform [206]. Here, it reports on a new model catalyst system based on high surface area mesoporous silica SBA-15. In particular, ALD technique is employed for controlled synthesis of titania and vanadia layers within the pores of the silica matrix and demonstrate its catalytic activity in NH$_3$-SCR. Using UV-Vis and Raman spectroscopy and, in particular, *in situ* DRIFTS, the nature of the surface sites upon exposure to different gas atmospheres and temperatures were explored, including NH$_3$-SCR reaction conditions, were explored. This work mainly follows the published paper "High Surface Area VO$_x$/TiO$_2$/SBA-15 Model Catalysts for Ammonia SCR Prepared by Atomic Layer Deposition".[85]

6.1.1. Sample preparation

The preparation of SBA-15 was the same as introduced above. VO$_x$/TiO$_2$/SBA-15 samples were prepared by ALD using a deposition system d escribed in detail elsewhere [206]. Briefly, three ALD cycles

of titania were deposited onto silica SBA-15. Finally, VO_x was deposited with 1, 3, and 5 cycles leading to different V loadings. For the ALD of TiO_2, the $TiCl_4$ precursor was evaporated in a feeding bottle at 40 °C and reacted in the reaction chamber at 120 °C for 60 s. Similarly, for VO_x ALD, the $VOCl_3$ precursor was evaporated at 40 °C and reacted at 60 °C for 60 s. In both processes, water at room temperature acted as oxidant. Between reaction steps the system was purged (N_2, 60 s).

The sample with 3 cycles of TiO_2 on SBA-15 is labeled as 'TiO$_2$/SBA-15', and samples with different cycles of VO_x on TiO_2/SBA-15 as 'TiO$_2$/SBA-15 + $n \times VO_x$' (n=1, 3, 5). Hydrated samples correspond to samples exposed to ambient conditions for at least one week after synthesis. Samples labeled as 'dehydrated' were heated at 500-600 °C for 1 h under a controlled atmosphere (20% O_2/80% N_2) and then cooled to room temperature.

6.1.2. Characterization results

Table 9 gives a summary of the prepared samples and their surface area and porosity characteristics. The ALD deposition of TiO_2 and VO_x on mesoporous silica SBA-15 leads to a significant decrease in specific surface area, accompanied by a reduction in pore diameter. The observed decrease in specific surface area is attributed to a coating of the (rough) mesoporous channels but also to a closure of SBA-15 micropores, as discussed previously [214]. Increasing VO_x deposition leads to a further (but much smaller) overall decrease of the specific surface area and pore volume (see Table 9). As shown in Figure S6-1, after TiO_2 and VO_x deposition, the nitrogen adsorption-desorption isotherms show variations of the hysteresis loop compared to bare SBA-15. In particular, the desorption branches exhibit a bulge towards lower p/p° values, indicating the presence of narrowed mesopores [98]. Thus, despite the use of ALD the pores of the silica matrix are not evenly coated, resulting in pore narrowing and possibly pore blocking, consistent with the observed overall decrease in surface area.

Table 9. Surface, porosity, and V loading characteristics of the prepared samples.

Samples	S_{total} [m^2/g]	D_p [nm]	V_{total} [cm^3/g]	L_V [V/nm^2]	V:Ti (wt. %)[a]
SBA-15	952	6.96	0.82	--	--
TiO$_2$/SBA-15+1x VO$_x$	410	6.33	0.49	0.4	1.4 : 5.8
TiO$_2$/SBA-15+3x VO$_x$	366	6.33	0.43	1.6	5.1 : 5.9
TiO$_2$/SBA-15+5x VO$_x$	355	6.33	0.43	2.0	6.0 : 5.6

[a] From ICP-OES.

Figure 47(a) depicts wide-angle XRD patterns of TiO$_2$/SBA-15+n×VO$_x$ (n = 1, 3, and 5) and TiO$_2$/SBA-15. None of the diffractograms shows any peaks, thus indicating the absence of crystalline titania and vanadia phases and confirming the amorphous nature of the SBA-15 silica matrix. The broad feature at around 23° has been attributed to the walls of mesoporous silica [215]. To check for microcrystalline domains the sample TiO$_2$/SBA-15 +3×VO$_x$ was examined in more detail using UV Raman spectroscopy (see Fig. S6-2), which was shown to be a sensitive indicator for small (micro)crystalline titania contributions in the previous work [206]. According to Fig. S6-2, there is no indication for the presence of titania microcrystals due to the absence of characteristic anatase (394, 514, and 634 cm^{-1}) and rutile (443 and 610 cm^{-1}) bands [216], or V$_2$O$_5$ microcrystals. In the context of Raman detection of V$_2$O$_5$, it should be mentioned, however, that visible Raman spectroscopy is typically more sensitive to V$_2$O$_5$ microcrystals than UV Raman spectroscopy (see discussion below).
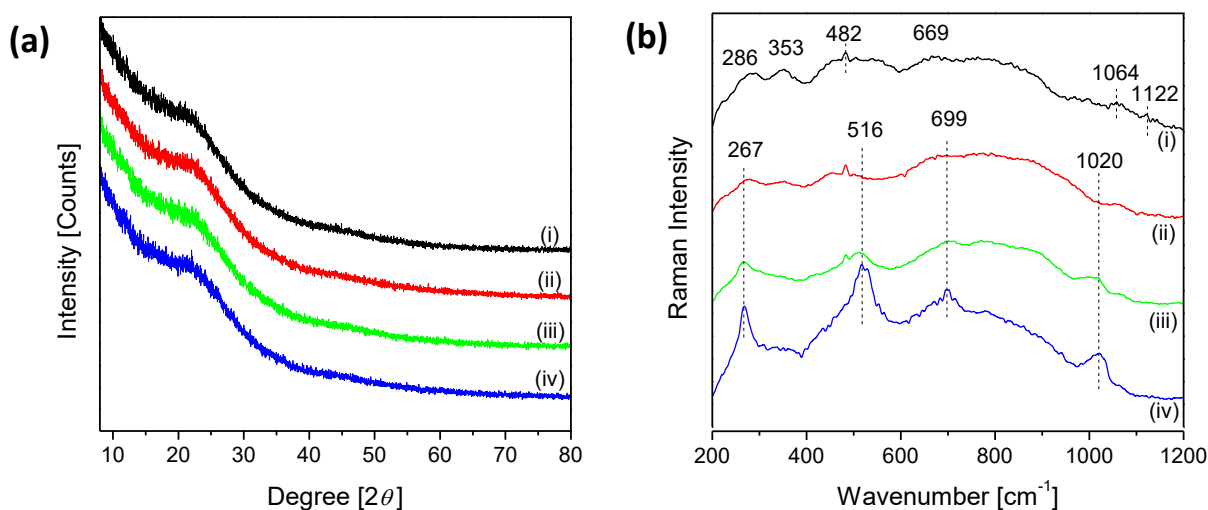

Figure 47. (a) XRD patterns and (b) Raman spectra of the samples TiO$_2$/SBA-15+nxVO$_x$ (n = 1, 3 and 5) compared to TiO$_2$/SBA-15 under ambient conditions. (i) TiO$_2$/SBA-15, (ii) TiO$_2$/SBA-15+1xVO$_x$, (iii) TiO$_2$/SBA-15+3xVO$_x$, (iv) TiO$_2$/SBA-15+5xVO$_x$.

Figure 47(b) shows the corresponding Raman spectra at 532 nm excitation. The spectrum of TiO$_2$/SBA-15 is characterized by broad features typical for amorphous silica dominating the weaker (surface) titania contributions[217]. Major features include the band at around 450-550 cm^{-1} associated with four-membered rings (D$_1$), and the broadband at around 600-900 cm^{-1} assigned to symmetrical Si-O-Si stretching and three-membered rings (D$_2$) [218], respectively. The band located at 353 cm^{-1} is assigned to bending in Si-O-Si bridges [219], whereas the band at 286 cm^{-1} has been attributed to the A$_1$ mode of TiO$_6$

octahedra [220]. The small feature at 1064 cm^{-1} is characteristic of silica TO phonons [221], whereas the weak Raman peak observed at 1122 cm^{-1} for TiO$_2$/SBA-15 is attributed to framework Ti-O-Si species [222]. Importantly, the addition of increasing amounts of vanadia leads to the appearance of new Raman signals at around 267, 516, 699, and 1020 cm^{-1}. At first sight, the signals at around 267, 516, and 699 cm^{-1} show some similarity with those observed for crystalline V$_2$O$_5$, however, closer inspection reveals significant differences. The observed signals rather indicate the presence of hydrated vanadia forming xerogels V$_2$O$_5 \cdot n$H$_2$O, resembling those discussed previously in the context of silica-supported vanadia, and the peak at 1020 cm^{-1} is attributed to the V=O stretching vibration mode of tetrahedral VO$_x$ species [223]. Based on the above results from XRD and Raman spectroscopic characterization, it is concluded that the ALD-prepared samples contain amorphous titania and vanadia on silica SBA-15 and that titania at the loading studied here (2 Ti/nm^{-2}) does not form a conformal layer on the silica surface allowing vanadia to interact with titania and silica. According to a previous ALD study [212], deposition of 3 Ti nm^{-2} and 7 Ti nm^{-2} onto SiO$_2$ leads to the formation of sub-monolayer titania, in agreement with the results obtained here.
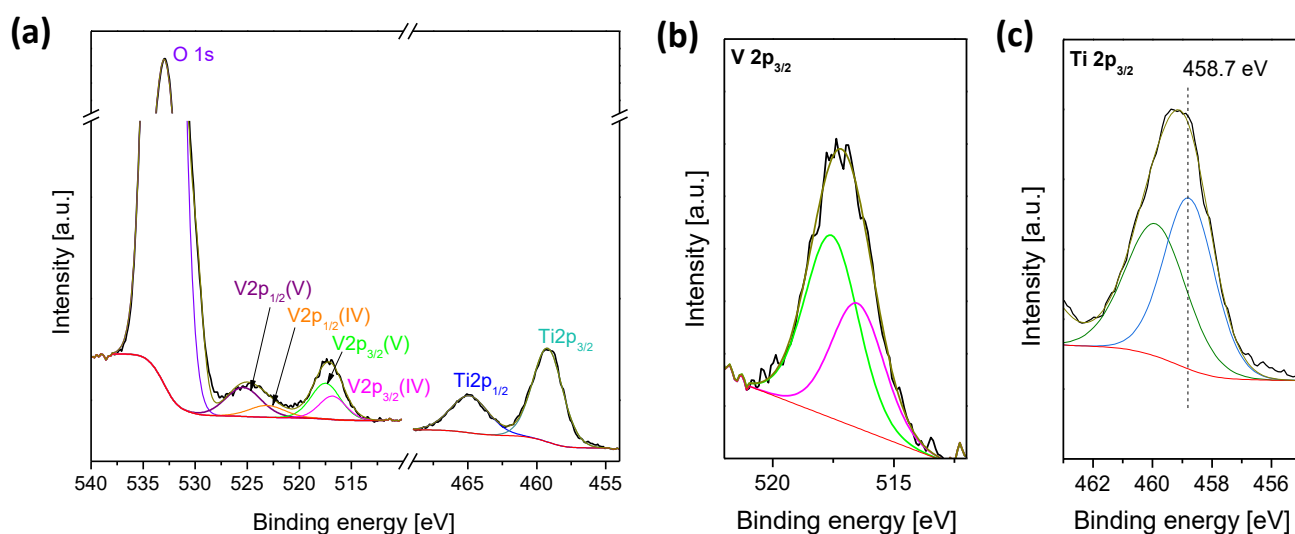

Figure 48. (a) O 1s, V 2p, and Ti 2p photoemission of TiO$_2$/SBA-15+3xVO$_x$. Detailed view of (b) the V 2p$_{3/2}$ region (c) the Ti 2p$_{3/2}$ region. The colored lines represent the result of a least-square fit analysis.

In the following, it is focused on the structural and catalytic properties of sample TiO$_2$/SBA-15+3×VO$_x$ with a vanadium loading density of 1.6 V/nm^2. Table S6-1 and Figure 48 summarize the results of the XPS analysis. As shown in Table S6-1, Si, O, Ti, and V are detected at the catalyst surface, besides C. The Ti/Si and V/Si ratios correspond to 0.10 and 0.12, respectively, suggesting the presence of similar amounts of Ti and V on the surface. The results are consistent with the above picture of a

mixed layer and rule out the exclusive formation of large titania or vanadia (3D) aggregates, which would strongly reduce the visibility of Ti and V in XPS. The left of Figure 48 depicts the O 1s, V $2p_{1/2,}$ and V $2p_{3/2}$ photoemission located at 532.9 eV, 524.9 eV, and 517.4 eV, respectively. As expected, the former is dominated by the O 1s contribution from SiO_2, by comparison with the literature [223]. Detailed analysis of the V $2p_{3/2}$ region based on literature data for binary vanadia compounds (V_2O_5, V_2O_4, V_2O_3) reveals the presence of V^{5+} at 517.6 eV (60%) and V^{4+} at 516.3 eV (40%), while a small contribution from V^{3+} at 515.7 eV cannot be ruled out [224]. The Ti $2p_{3/2}$ peak is composed of (at least) two contributions located at 458.7 and 459.9 eV, which can be attributed to TiO_2 domains and to Ti-O-Si bonds, respectively [201, 225].

Figure 49(a) depicts DR UV-Vis spectra of TiO_2/SBA-15+3×VO_x in comparison to TiO_2/SBA-15. To clarify the influence of water from ambient on the catalyst structure, spectra were recorded under ambient (hydrated) and dehydrated conditions. Please note that bare silica SBA-15 does not show any significant UV-Vis absorption. The UV-Vis spectrum of Ti/SBA-15 is characterized by strong absorption at around 280 nm, which has been attributed to charge transfer between an oxygen ligand and the central Ti^{4+} ion [226], whereas the position of the absorption band is consistent with higher coordinated or oligomeric titania species [227]. The presence of oligomeric species would be in agreement with the literature on SiO_2-supported titania, reporting two-dimensional oligomers of TiO_5 domain at a loading density of about 4 Ti nm^{-2}, which is higher than the density used in this work (2 Ti nm^{-2}) [228].
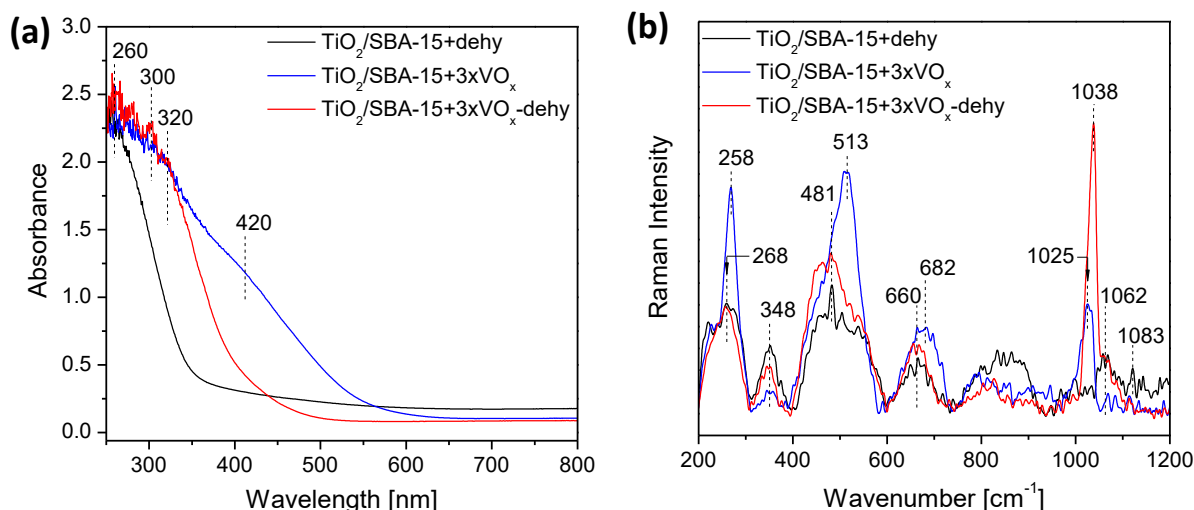

Figure 49. (a) DR UV-is and (b) Raman spectra of TiO_2/SBA-15+3xVO_x under ambient (hydrated) and dehydrated conditions in comparison to dehydrated TiO_2/SBA-15.

Regarding the vanadia structure, the observed UV-Vis absorption was analyzed based on the ligand-to-metal charge transfer (LMCT) transitions observed for bulk vanadia reference compounds [229]. To this

end, bands at around 240 and 290 nm were reported to originate from isolated tetrahedrally coordinated mono-vanadate ions [230], while the bands at about 270, 340, and 412 nm were assigned to poly-vanadate ions [231]. In the literature, the bands at 308, 371, and 406 nm were assigned to LMCT transitions of monomeric tetrahedral VO_4^{3-}, oligomeric tetrahedral VO_3^-, and polymeric distorted tetrahedral VO_3^- ions, respectively [232]. It was also reported that the bands at around 440-510 nm and 545-650 nm were due to LMCT transitions and d-d transitions of V^{5+} and V^{4+} species with square pyramidal structure, respectively. For crystalline V_2O_5, a broad absorption band with maxima ranging from 440 to 490 nm was observed [229]. The presence of V^{3+} and/or V^{4+} species was shown to lead to d-d transitions ranging from 600 to 800 nm [233]. A comparison of the hydrated and dehydrated state of the sample reveals the presence of a broad band at around 380-450 nm, which has been attributed to the coordination of water to V sites leading to major structural changes [226].

After dehydration, the UV-Vis absorption behavior is characterized by contributions at around 280 nm, 320 nm, and 400 nm, which, based on the above literature results, are attributed to monomeric/dimeric, oligomeric, and polymeric VO_x species, respectively, while the intensity increase at around 260 nm was attributed to Ti-O-Ti from Ti-OH or possibly V-O-Ti from V-OH. Because of the overlap of charge transfer bands of titania and vanadia [232, 234], removal of the titania contribution facilitates the analysis of the surface vanadia structure (see Fig. S6-3) [235]. As a result, Fig. S6-3 shows the presence of an asymmetric broad absorption band located between 250-550 nm for the hydrated and between 250-450 nm for the dehydrated sample, together with the result of a fit analysis based on the above reference data [235]. Besides, the ratio of monomeric/dimeric/oligomeric VO_x with tetrahedral coordination to polymeric VO_x with (pseudo-)octahedral coordination was estimated to increase from 0.31 to 12.5 upon dehydration, underlining the structural changes associated with the removal of coordinated water.

Based on the UV-Vis spectra the bandgap energy E_g was determined using the general power-law expression suggested by Davis and Mott based on the absorbance α [236]:

$$\alpha \hbar v \propto (\hbar v - E_g)^n \tag{6-1}$$

The value of the parameter n in eq. 6-1 was set to 2 following the literature [234], showing a linear relationship when plotting $(\alpha h v)^{1/2}$ vs hv (Tauc's method) [237]. Extrapolation of the linear region to $(\alpha h v)^{1/2} = 0$ yields E_g values of 2.99 and 3.30 eV for the hydrated and dehydrated state of the catalyst, respectively. As the E_g value is negatively correlated to the number of covalent V-O-V bonds (CVB) via the relation CVB = $14.03-3.95\ E_g$ [234], an increase in E_g implies a decrease in the degree of VO_x polymerization upon dehydration.

Figure 49(b) depicts Raman spectra of TiO_2/SBA-15+3×VO_x under hydrated and dehydrated conditions in comparison to the spectrum of TiO_2/SBA-15. As discussed above VO_x-related features are observed at 268, 513, 682, and 1025 cm^{-1}. Upon dehydration, the vanadyl (V=O) stretching mode shows an intensity increase and blueshift from ~1025 to 1038 cm^{-1}, consistent with previous work on VO_x/SiO_2 and VO_x/(TiO_2+SiO_2) [212, 223]. The position of the V=O band at 1038 cm^{-1} in the visible Raman spectrum is characteristic for tetrahedrally coordinated vanadium ions, and has been associated with monomeric and/or small oligomeric VO_x species, consistent with the results from UV-Vis spectroscopy (see above). The presence of (micro)crystalline V_2O_5 in the dehydrated state of the catalyst can be excluded due to the absence of the characteristic vanadyl feature of V_2O_5 at 994 cm^{-1} [223]. The shoulder observed at around 1062 cm^{-1} has been attributed to V-O-Si bridging bonds [238]. The Raman bands observed at 268, 513, and 682 cm^{-1} for the hydrated state are consistent with the presence of hydrated vanadia forming xerogels $V_2O_5 \cdot n H_2O$, as discussed above. Upon dehydration, these bands disappear due to the structural transformation of surface vanadia, leading to an increased visibility of the support-related bands at 258, 481, and 660 cm^{-1} discussed below.

To gain insight into the NH_3-SCR mechanism, DRIFT spectroscopy is applied in the presence of different gas environments and at different temperatures including reaction conditions (*operando*). Figure 50 shows DRIFT spectra of TiO_2/SBA-15+3xVO_x exposed to a gas mixture of 500 ppm NH_3, 500 ppm NO, and 5 % O_2 (balanced with N_2) at different temperatures from 100 °C to 450 °C at a flow rate of 50 Nml/min. In Figure 50(a), the black curve (labeled 'N_2, 300°C') corresponds to the catalyst in a nitrogen flow at 300 °C before exposure to the reaction gas mixture. Features located at around 919 and 1036 cm^{-1} and at around 1849 and 2002 cm^{-1} have previously been assigned to V-O-V and V=O stretching modes of surface VO_x species and their first overtones, respectively [56, 200]. The feature at 1203 cm^{-1} has been ascribed to L acid sites on TiO_2 [239]. The shoulder at around 1640 cm^{-1} and the broad band within the range 3500-3800 cm^{-1} can be attributed to OH bending and stretching of water, respectively [200]. In the OH stretching region, the sharp peak at 3745 cm^{-1} is characteristic of isolated Si-OH groups, while the small feature at 3656 cm^{-1} can be associated with V-OH [226]. The Si-OH feature shows an asymmetric broad tail at around 3650 cm^{-1}, which has been assigned to Ti-OH [240]. Upon exposure to the reaction gas mixture, two new features appeared at 1418 and 1455 cm^{-1}, which can be attributed to the asymmetric N-H bending vibration of NH_4^+ linked to B acid sites, while the shoulder and small feature at 1176 and 1606 cm^{-1} have been associated with the symmetric and symmetric N-H bending vibrations of NH_3 linked to L acid sites, respectively [241]. According to Figure 50(a), the observed N-H modes show a different temperature-dependent behavior. Whereas the feature at 1606 cm^{-1} decreased with temperature and disappeared at about 250 °C, the band at about 1418 cm^{-1} kept intact.

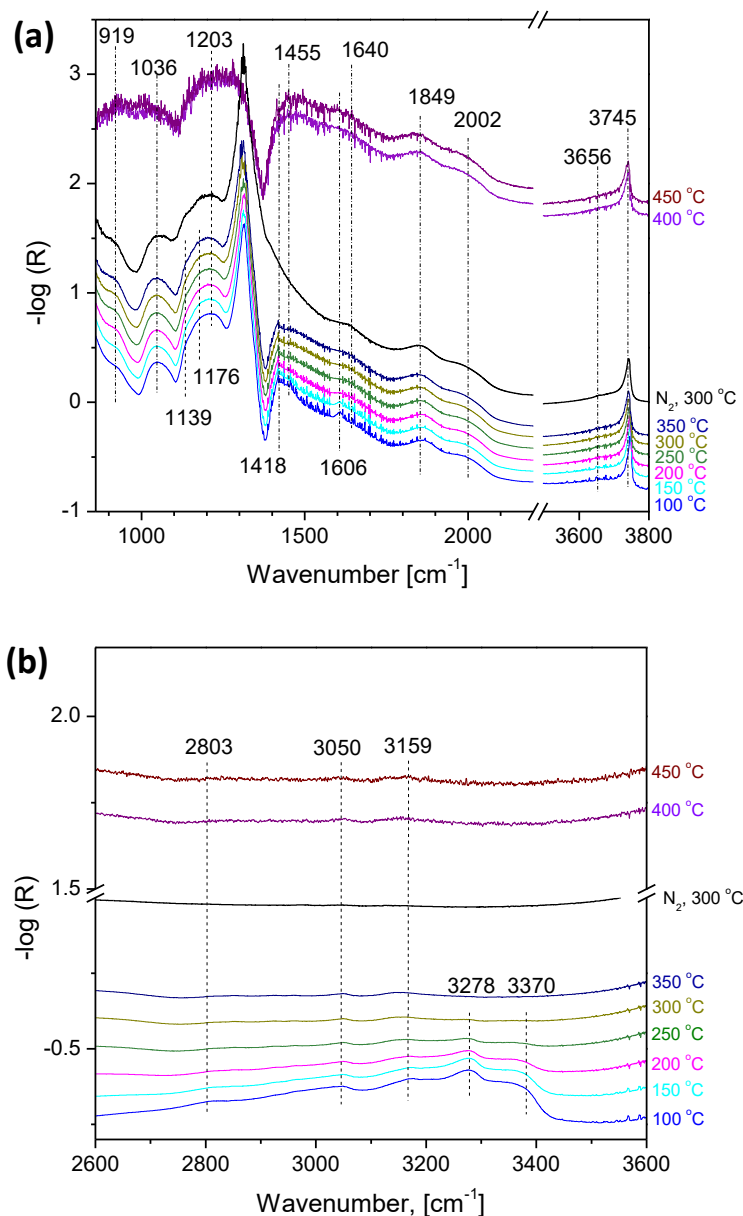Figure 50. DRIFT spectra of TiO$_2$/SBA-15+3xVO$_x$ exposed to a gas mixture of 500 ppm NH$_3$, 500 ppm NO, and 5% O$_2$ (balanced with N$_2$) at temperatures from 100 °C to 450 °C within (a) 850-3800 cm^{-1}, (b) 2600-3600 cm^{-1}. The total flow rate was 50 Nml/min (GHSV = 40000 h^{-1}).

In Figure 50(b), upon exposure to the reaction gas mixture, new IR bands are observed at 2803 and 3050 cm^{-1}, which can be attributed to N-H stretching of NH$_4^+$ linked to B acid sites, while the bands located at 3159, 3278, and 3370 cm^{-1} are assigned to N-H stretching modes of NH$_3$ coordinated to L acid sites [47, 49, 241]. As the temperature increases, the bands at 3278 and 3370 cm^{-1} show an intensity decrease and completely disappear at temperatures above 300 °C, while the feature at 3159 cm^{-1} is detectable until 450 °C. Similarly, the bands at 2803 and 3050 cm^{-1} related to NH$_4^+$ on B acid sites can be observed within the whole temperature range.
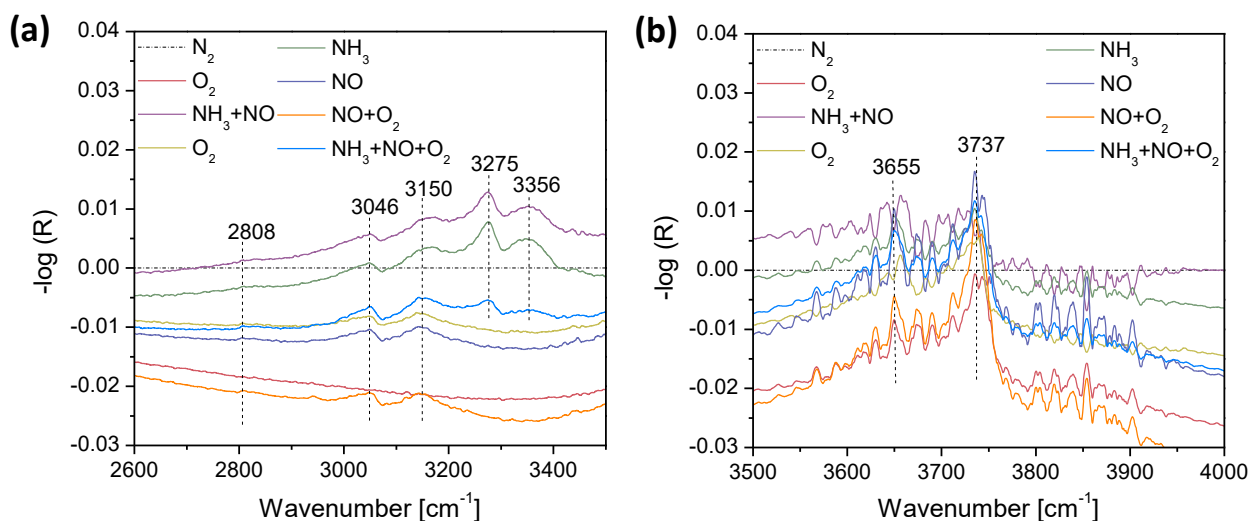
Figure 51. DRIFT spectra of TiO$_2$/SBA-15+3xVO$_x$ exposed to different gas environments at 300 °C and at a total gas flow rate of 50 Nml/min (GHSV = 40000 h^{-1}) within (a) 2600-3500 cm^{-1}, (b) 3500-4000 cm^{-1}.

Figure 51 depicts DRIFT spectra of TiO$_2$/SBA-15+3×VO$_x$ exposed to different gas environments at 300 °C at a total flow rate of 50 Nml/min within (a) 2600-3500 cm^{-1} and (b) 3500-4000 cm^{-1}. Following the assignments discussed in the context of Figure 50, the features at 2808 and 3046 cm^{-1} are assigned to NH$_4^+$ coordinated to B acid sites, and those at 3150, 3275, and 3356 cm^{-1} to NH$_3$ bound to L acid sites (see Figure 51(a)). Similar to the effect of temperature, the bands linked to B acid sites (2808 and 3046 cm^{-1}) and the band linked to L acid sites at 3150 cm^{-1} are observed independent of the composition of the gas atmosphere, while those at 3275 and 3356 cm^{-1} can only be detected upon exposure to gas mixtures containing NH$_3$. That is to say, that NH$_4^+$ on V-OH sites is stable towards reaction no matter which redox conditions, while NH$_3$ adsorbed on specific L acid sites was proved to be reactive. In the corresponding high-wavenumber region (see Figure 51(b)) IR bands are observed at 3655 and 3737 cm^{-1} in all gas mixtures and are attributed to V-OH and Si-OH stretching vibrations, respectively, as discussed above, while the broad absorption band extending to ~3600 cm^{-1} originates from Ti-OH (see above) and the background from the fine structure of adsorbed water.

Upon closer inspection, the IR spectra in Figure 51 show gas phase-dependent variations. Upon the first exposure to 20 vol.% O$_2$, no acid site-related bands are observed. However, water-related background peaks are detected indicating the rearrangement of surface hydroxyl groups into water under oxidizing conditions [59]. Switching to the reductive atmosphere, i.e., NH$_3$/NO, results in the appearance of the five N-H stretching modes related to L and B acid sites (see above), while during the following O$_2$ treatment the L site related features at 3275 and 3356 cm^{-1} disappear. On the other hand, the 3150

cm^{-1} band assigned to NH$_3$ coordinated to V=O sites, is still detected under oxidizing conditions. In the high-wavenumber region, the Si-OH, Ti-OH, and V-OH signals first show a decrease and then a partial recovery in oxygen. Next, the catalyst was exposed separately to NH$_3$ and NO, and then to a NO/O$_2$ mixture oxidation. In the presence of NH$_3$ reduction, the L site related features completely re-appear and the water-related peaks show a weak positive increase indicating that NH$_3$ itself could be reduced to NH$_n$ thereby transferring hydrogen atoms to adjacent hydroxyl groups to form water. Upon oxidation by NO or NO+O$_2$ the features at 3275 and 3356 cm^{-1} disappeared, while the water-related peaks significantly increased, suggesting the promotional effect of NO regarding NH$_3$ oxidation, leading to intermediate formation (e.g. NH$_2$-NO or NH-NO), consistent with results from DFT [242], and mass spectroscopy [243].

Finally, the catalyst was exposed to reaction conditions, i.e., an NH$_3$/NO/O$_2$ mixture, leading to the re-appearance of all five acid site-related features, while the peaks for Si-OH, Ti-OH, and V-OH decreased in intensity. It is worth mentioning that there is a distinct difference in the IR spectra for exposure to the NH$_3$/NO mixture and the subsequent exposure to NH$_3$ and NO. In the former case, the presence of NH$_3$ was sufficient to competitively adsorb on the surface resulting in H$_2$O desorption, while in the latter case, NH$_3$ initially adsorbed on the surface was oxidized by NO resulting in NH$_2$-NO/N-NO and water formation with reduced competitive adsorption [243]. These above results are consistent with the strength of adsorption following the order NH$_3$ > H$_2$O > NH$_2$-NO intermediate, in agreement with the literature [244]. Interestingly, the addition of oxygen (NH$_3$/NO/O$_2$) leads to a different, distinct state of the catalyst regarding the presence of surface species, which falls between the behavior observed for NH$_3$ exposure and subsequent exposure to NH$_3$ and NO, and is also different to that obtained by subsequent exposure to NH$_3$/NO and oxygen.

In summary, the DRIFTS results shown in Figure 50 and Figure 51 reveal important differences in the adsorption/reactivity behavior of NH$_3$ species attached to acid sites. The N-H stretching linked to B acid sites at 2803 and 3050 cm^{-1}, which have been assigned to coordinate and suspended N-H bonds [49], respectively, did not respond to the different atmospheres and different temperatures, suggesting that the B acid sites were active for adsorption but not for reaction. On the other hand, the L acid site related N-H stretching features at 3275 and 3356 cm^{-1}, assigned to -NH$_2$ and -NH species, showed a more distinct response to the nature of the gas environment and the temperature, while the 3150 cm^{-1} feature, assigned to adsorbed NH$_3$ species, remained passive towards reaction. Regarding the reaction mechanism, it is drawn the following conclusions: (a) NO reacts with NH$_3$ connected to the inert site (3150 cm^{-1}). (b) NH$_3$ adsorbs to active L acid site forming NH$_2$ by H-abstraction (3275 and 3356 cm^{-1}), followed by its interaction with NO leading to NH$_2$NO intermediate formation and further reaction to N$_2$ and H$_2$O. (c) In case of N$_2$O formation, NH$_2$NO may be expected to lead to NHNO intermediates and finally N-NO.
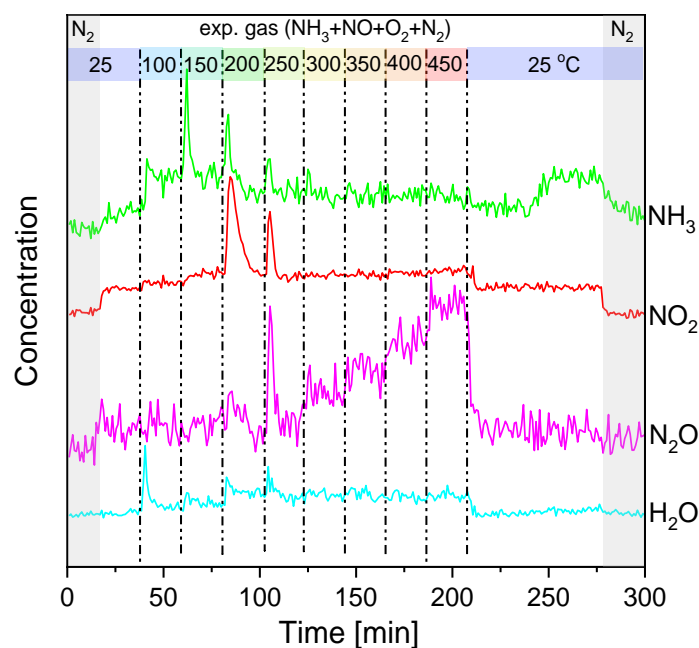
Figure 52. *In situ* detection of the exhaust gas during NH_3-SCR reaction of TiO_2/SBA-15+3x VO_x at 100-450 °C. The feed consisted of 500 ppm NH_3, 500 ppm NO, and 5% O_2 (balanced with N_2) at a total flow rate of 50 Nml/min (GHSV = 40000 h^{-1}).

Figure 52 depicts the results of the *in situ* detection of the exhaust gas during different temperature SCR experiments from 100 to 450 °C. Each temperature was kept for 20 minutes to reach an equilibrium state. When increasing the temperature, desorption peaks were observed indicating changes in the surface concentration as a function of temperature. At lower temperatures, the presence of NH_3 peaks but absence of NO desorption peaks (not shown) suggests a surface reaction following the E-R rather than the L-H route, in agreement with the literature [245]. In addition, insight into the reaction mechanism can be obtained. To this end, three steps have been distinguished, i.e., adsorption of reactants (mainly NH_3), reaction, and desorption of products (such as H_2O, NO_2, and N_2O). According to Figure 52, there are low temperature desorption peaks of NH_3 at 25/100 °C and 100/150 °C, which are attributed to NH_3 desorption from the B acid site, while high temperature NH_3 peaks above 150 °C are assigned to desorption from L acid site [201, 246]. These peaks disappeared at about 300/350 °C, consistent with the disappearance of L acid sites in DRIFTS (see Figure 51). The strong water desorption peak at 25/100 °C originates from condensation of OH groups, e.g. after desorption of NH_3 bound to B acid sites [201]. The first desorption peak of NO_2 at 150/200 °C can be attributed to the distortion and release of NO_2 from nitrite/nitrate species by NO molecules connected to surface oxygen sites [247]. The second peak at 200/250 °C shows that NO oxidation is faster than NO_2 desorption at 200 °C. Similarly, the first desorption peak

for N_2O detected at 200/250 °C is indicative of its formation on active sites and subsequent chemisorption at temperatures <250 °C [248].

6.1.3. Catalytic test

The NH_3-SCR activity was examined within 100-450 °C using a mixture of 500 ppm NH_3, 500 ppm NO, 5% O_2, and N_2 (balance). The temperature was increased from 100 °C to 450 °C in 50 °C steps keeping each temperature for 20 min for equilibration. Analysis of the gas phase at the reactor outlet was performed by quantitative FT-IR spectroscopy. Figure 53 depicts the catalytic performance for NO_x conversion over TiO_2/SBA-15+3×VO_x as a function of temperature. The NO_x conversion follows a volcano shape with an increase from 100 to 250 °C, a maximum conversion level at 250-350 °C, and a decrease above 350 °C.

Despite the similar shape of the conversion, the TiO_2/SBA-15+3×VO_x sample shows significantly higher catalytic activity (shown in Table 10) as VO_x/(SiO_2+TiO_2) samples prepared by sol-gel methods [201]. In this context, it was reported that doping TiO_2 with Si may result in an increase in NO_x conversion and a decrease of the lower temperature limit from 360 °C for pure TiO_2 to 300 °C or lower for Si-doped samples [225]. Interestingly, the catalyst exhibits an excellent N_2 selectivity with values higher than 90% even at 450 °C. This behavior may be attributed to the microporous structure of the SBA-15 support, which was proved to effectively inhibit the formation of N_2O [203]. In contrast to the results shown in Figure 53, VO_x/SiO_2 samples (prepared by ALD) showed only low NO conversions. In fact, the presence of titania was reported to enable V-O-Ti bond formation, which was related to the number and strength of surface acid-base sites [212]. Thus, it is concluded conclude that besides the influence of (micro)structural effects, the improved catalytic performance may be attributed to the controlled preparation of dispersed active sites and a submonolayer of TiO_2 on SiO_2.
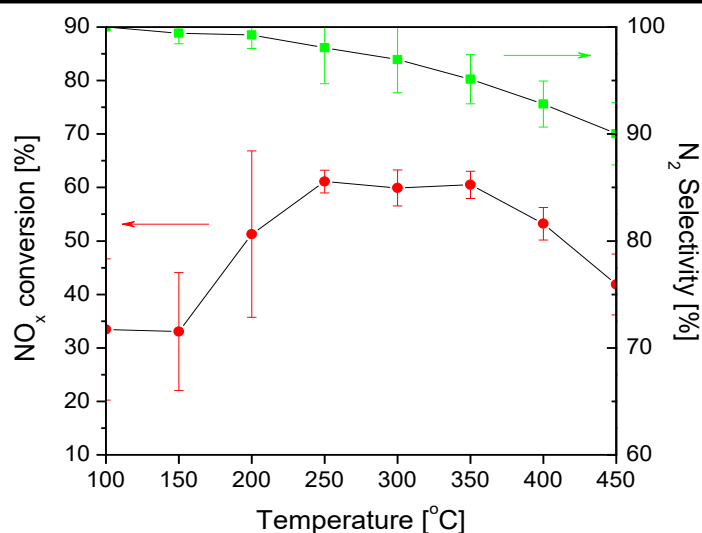
Figure 53. Catalytic performance of TiO_2/SBA-15+3×VO_x in NH_3-SCR. The temperature was increased from 100 °C to 450 °C. The feed gas consisted of 500 ppm NH_3, 500 ppm NO, and 5% O_2 balanced with N_2. The total flow rate was 50 Nml min^{-1} (GHSV = 40000 h^{-1}).

Table 10. Catalytic performance of TiO_2/SBA-15+3×VO_x in NH_3-SCR as a function of temperature. The feed gas consisted of 500 ppm NH_3, 500 ppm NO, and 5% O_2 balanced with N_2. The flow rate was 50 Nml min^{-1} (GHSV = 40000 h^{-1}).

Temperature, °C	100	150	200	250	300	350	400	450
NO_x conversion, %	33.4	33.1	51.3	61.1	59.9	60.5	53.2	41.9
N_2 selectivity, %	100	99.4	99.3	98.1	97.0	95.1	92.8	90.0

6.1.4. Discussion about surface vanadia structure

Previously, highly dispersed vanadia and titania on SBA-15 have been studied in detail under hydrated and dehydrated conditions [226]. Despite the lower loading ranges discussed (V: 0.00001-0.7 V/nm^2; Ti: 0.001-0.7 Ti/nm^2) valuable structural information for the present sample (1.6 V/nm^2; 2 Ti/nm^2) was obtained regarding the nature of the surface species, in particular, as all samples are well below monolayer coverage [211, 249]. This is supported by the absence of Raman features due to crystalline V_2O_5 and TiO_2, implying the presence of amorphous domains, consisting of dispersed titania and vanadia species on the silica surface. On the other hand, the detailed surface composition after successive deposition of titania and vanadia needs closer examination, especially as it was reported that vanadium is preferentially deposited on titanium sites [211, 250].

For TiO$_2$ deposited on SBA-15, the Ti loading was quantified as 2 Ti/nm^2, which is significantly below monolayer coverage (6-8 Ti/nm^2) [249]. DR UV-Vis spectra show an absorbance band at about 260 nm, attributed to titanium in 5-fold coordination (see Figure 49) [228]. The UV-Vis edge energies were determined to be 3.2 and 3.0 for the hydrated and dehydrated state, respectively. Comparison with edge energies of titania structures ranging from isolated tetrahedrally coordinated TiO$_4$ (4.3 eV) to oligomeric TiO$_5$ species (3.4 eV), suggests the presence of oligomeric TiO$_5$ species in the VO$_x$/TiO$_2$-SiO$_2$ sample. Regarding the effect of water on the titania structure, no difference was found between the dehydrated and hydrated state at extremely low Ti loading (<0.05 Ti/nm^2), in contrast to higher loadings (>0.1 Ti/nm^2) [226]. In fact, adsorbed water was reported to interact with adjacent titanium atoms (Ti-O-Ti) in oligomeric titania, leading to an edge energy 0.2 eV higher than in the dehydrated state, consistent with the behavior observed here [226]. High temperature calcination is expected to lead to an increase in Ti-O-Ti linkages as part of domain TiO$_2$ [211] without formation of crystalline TiO$_2$, as discussed above (see above). While anatase and rutile related Raman bands are absent, the feature at 286 cm^{-1} is attributed to TiO$_6$ octahedra as part of amorphous TiO$_2$ domains on the silica surface.

After vanadia deposition, adsorption-desorption isotherms are characterized by a steep hysteresis, attributed to cavitation-controlled evaporation in a narrow range of the pore neck, while some pore blockage or seepage may not be excluded. The surface area shows only a small decrease with increasing VO$_x$ deposition, while no significant differences in the NLDFT pore-size distribution were observed. This behavior implies that the ALD deposited VO$_x$ did not block the pore openings, but was rather selectively deposited inside the matrix on TiO$_2$ domain sites, forming ink-bottle pore [251].

Although the ALD method permitted the vanadium precursor to react with all surface adsorption sites, including Ti-OH and Si-OH hydroxyls, preferential deposition seems to be inevitable [212]. According to Table 6-1, the sample with 1×VO$_x$ deposition shows a lower V:Ti ratio of 0.24, at which vanadium is expected to be mainly loaded on TiO$_2$ domains [211]. For the 3×VO$_x$ and 5×VO$_x$ samples close to unit V:Ti ratios of 0.85 and 1.08 are observed, which can be interpreted as sub- and over-saturated coverages of VO$_x$ on TiO$_2$, respectively. It should be mentioned that the VO$_x$ deposition rate showed differences among the three samples. In fact, based on the growth rate for 1xVO$_x$, leading to a V/Ti ratio of 0.24, the extrapolated V/Ti ratio for 3×VO$_x$ should be 0.72, which is slightly smaller than the actual value of 0.85, while the extrapolated V/Ti ratio for 5×VO$_x$ should be 1.20, a value slightly larger than the observed value of 1.08. The increase in VO$_x$ growth rate is attributed to a change in deposition site from titania to silica when approaching TiO$_2$ saturation coverage. On the other, the mobility of surface VO$_x$ species was reported to reach its lowest surface free energy (SFE) at elevated temperature under reaction conditions, resulting in a two-dimensional spreading of VO$_x$ species on silica

and titania [252]. To this end, it is worth mentioning that the IR spectra recorded at elevated temperature under reaction conditions reveal a hydroxyl signal at 3740 cm^{-1} due to surface Si-OH groups (see Figure 50), indicating that the deposition of TiO_2 and VO_x did not lead to complete coverage of the silica surface.

The DR UV-Vis and Raman spectra provide structural information on the VO_x surface species (see Figure 49 and Fig. S6-3). It is well known that the structure of surface VO_x depends sensitively on the gas environment [253]. UV-Vis spectra of the hydrated state are characterized by a 250-550 nm band, consistent with polymeric VO_x with pseudo-octahedral coordination, and by a band at 250-450 nm for the dehydrated catalyst, reflecting the presence of tetrahedrally coordinated oligomeric VO_x species. overlapping with the signal of the TiO_2/SiO_2 substrate in the dehydrated state. The presence of H_2O can hydrate the surface VO_x species leading to the formation of $V_2O_5 \cdot nH_2O$-like gels, as evidenced by Raman features at 267, 516, 699, and ~1020 cm^{-1} under ambient conditions (see Figure 47 and Figure 49). Regarding the position of the V=O stretching bands (~1020 and 1038 cm^{-1}) also the effect of moisture needs to be taken into account [223]. Upon dehydration, a 13 cm^{-1} blueshift of the V=O feature is observed (see Figure 53), consistent with the literature [223], leading to the formation of tetrahedrally coordinated vanadium ions. In the dehydrated state, the position of the V=O band at 1038 cm^{-1} is located between the values 1031 cm^{-1} and 1042 cm^{-1} reported for bare TiO_2 and SiO_2, respectively [12, 212], suggesting the simultaneous existence of vanadia species on both oxides attached via V-O-Ti and V-O-Si bands.

Summarizing, regarding the structure of the VO_x surface species proposed, based on the findings that (i) titania is dispersed on the silica surface in domains containing low oligomerized TiO_5, (ii) VO_x is preferentially deposited on titania sites at low VO_x loadings ($1xVO_x$), inducing the formation of dispersed oligomeric species, (iii) increasing VO_x loading results in the deposition of V on both Ti and Si sites ($3\times VO_x$, $5\times VO_x$).

6.1.5. Discussion about rate-determining step

In agreement with the literature, the observed temperature-dependent efficiency for NO removal follows a volcano shape, with a maximum NO conversion at 250-350 °C. N_2 selectivities are near 100% within 100-300 °C and decrease to 90% as temperatures rise to 450 °C (see Figure 53).

The reason for the reactivity changing with temperature was related to the different processes determining the rate. Generally, the SCR reaction process on the VO_x catalyst could be divided into three steps, i.e., adsorption of reactants, redox reaction, and desorption of products. On the one hand, it was

stated that the redox reaction was rate-determining at low temperature, while adsorption of NH_3 on surface acid sites was the rate-determining step (RDS) at high temperature [201]. On the other hand, desorption of generated H_2O was considered the low-temperature RDS, and the reductive reaction of NH_3 the high-temperature RDS [254]. To explore possible structural factors related to catalytic reactivity, *operando* DRIFT was applied.

Based on the DRIFT spectra in Figure 50 and Figure 49 part of the L acid sites is proposed as active sites, due to their gas phase and temperature dependent behavior. These sites can be associated with the N-H stretching of coordinated amide, while the stable L acid sites can be related to the N-H vibration of coordinated NH_3. Thus, the detailed H-abstraction ability is important even for the same type of adsorption sites. According to the literature, dispersed oligomeric VO_x species are believed to be the main active species, providing oxygen (V=O or V-O-V) [60, 202, 255], for H-abstraction of adsorbed NH_3 to form an amide intermediate [243]. To this end, the samples TiO_2/SBA-15-3$\times VO_x$ and TiO_2/SBA-15-5$\times VO_x$ with a larger fraction of oligomeric VO_x show a better NO_x conversion than TiO_2/SBA-15-1$\times VO_x$ (not shown). Also, the changes of the acid site-related signals with increasing temperature demonstrate that at temperatures <300 °C the H-abstraction step is slower than the adsorption of NH_3 (see Figure 50). The presence of adsorbed NH_3 at low temperatures was evidenced by NH_3 desorption peaks. On the other hand, desorption of water was observed at very low temperatures, indicating that its desorption was slower than its formation by reaction. Thus, it is proposed that the RDS at low temperatures to be related to the desorption of products, especially water.

Except for the redox properties surrounding the acid site, the acid strength is another important factor concerning the SCR reaction, relevant for both the adsorption of reactants (mainly NH_3 in E-R route) and the desorption of products (such as H_2O, NO_2, and N_2). The acidity of binary oxides and ternary oxides $VO_x/TiO_2/SiO_2$ has been the subject of previous studies, both on solid solutions and supported systems [201, 212, 213, 250]. For binary systems, the surface acidity was found to increase as $VO_x/SiO_2 < TiO_2/SiO_2 < VO_x/TiO_2$ [213]. Regarding $VO_x/TiO_2/SiO_2$ systems prepared by ALD [212], samples with lower VO_x loading (1 V/nm^2, 3 Ti/nm^2) and higher VO_x loading (2 V/nm^2, 3 Ti/nm^2) were compared towards their acidity behavior, showing a decrease (increase) in weak/medium (strong) strength acid sites with loading. Furthermore, strong acid sites were assigned to VO_x species on titania and weak acid sites to VO_x species on silica [212]. In the study, NH_3 desorption peaks for TiO_2/SBA-15+1$\times VO_x$ were detected at higher temperature as compared to 3$\times VO_x$ and 5$\times VO_x$ (see Fig. S6-4), consistent with the formation of stronger acid sites at lower V loading on titania. The N_2O desorption signal also follows the trend of the VO_x acid sites as 1$\times VO_x$ > 3$\times VO_x$ > 5$\times VO_x$. For the 1$\times VO_x$ sample, even at 300/350 °C, a weak N_2O desorption peak was detected. The 3$\times VO_x$ and 5xVO_x samples showed

a very similar desorption behavior of reactants and products. At temperatures >300 °C, no more desorption of NH$_3$ but an increase in the N$_2$O concentration was detected, reflecting an increase in the H-abstraction ability. Thus the RDS at high temperatures may be related to the adsorption of NH$_3$.

6.1.6. Discussion about Structure-Activity relationship

In the sections above, it was discussed the structure of VO$_x$ loaded on TiO$_2$/SBA-15 and several aspects affecting the NH$_3$-SCR activity. Compared to previous VO$_x$-based model systems with similar V loading on SiO$_2$, TiO$_2$, or SiO$_2$+TiO$_2$ prepared by other techniques, the VO$_x$/TiO$_2$/SBA-15 catalyst here shows an improved NO$_x$ conversion and operation window [201, 256]. For NH$_3$-SCR over supported VO$_x$ catalysts, high reactivity has been related to crystalline (anatase) TiO$_2$ [201]. Mixing SiO$_2$ with TiO$_2$, to be used as support for vanadia, introduces extra acid sites, and is accompanied by the transformation of crystalline into amorphous titania, resulting in a decrease in the catalytic performance compared to bare titania [201, 257]. However, by adjusting the Si/Ti ratio, a volcano-shape of the SCR reactivity with Si content was obtained [257], indicating synergetic effects regarding the reactivity, possibly related to the presence of Ti-O-Si surface sites. Kobayashi et al. studied the acidity of TiO$_2$-SiO$_2$ mixed systems, also showing a volcano-shaped relationship as a function of composition, with a maximum at a Si/Ti ratio of 1 [257]. On the other hand, according to other studies, using the same sol-gel method, the best SCR activity was observed for lower Si/Ti ratios such as 2/8 [225, 257]. The mismatch between the acidity and reactivity may be explained by the RDS discussion above, as within the low and medium temperature range, the desorption step was rate determining for the strong acid sites. In present work, ALD deposition of TiO$_2$ onto SiO$_2$ results in the formation of oligomeric TiO$_2$ domains, with a limited boundary between TiO$_2$ and SiO$_2$, in contrast to the more uniform mixture of Ti and Si obtained by the sol-gel method. The improved catalytic performance of the TiO$_2$/SBA-15+3×VO$_x$ compared to other SiO$_2$/TiO$_2$-based VO$_x$ catalysts can therefore be explained by the comparable amounts of V and Ti, allowing V to be deposited on TiO$_2$ and boundary sites (Ti-O-Si). This leads to the formation of VO$_x$ species supported by hybrid sites (V-O-Ti, V-O-Si), thus increasing the total number of acid sites. Consistent with this scenario, for lower V loading (1xVO$_x$), significantly lower NO$_x$ conversion is observed (not shown), due to the preferential deposition of V on (amorphous) TiO$_2$, while for higher V loading (5×VO$_x$), a similar behavior as for the 3×VO$_x$ catalyst was obtained, due accessibility of both TiO$_2$ and Ti-O-Si boundary sites.

Meanwhile, it is well-known that the SCR reactivity of VO$_x$/TiO$_2$ catalysts shows a narrow temperature window within the high temperature range, strongly decreasing below 300 °C,[258] VO$_x$/SiO$_2$ catalysts are characterized by low SCR reactivity but a wider temperature adaptability even at low

temperatures [259]. Besides, according to the literature, produced H_2O was adsorbed on surface active sites because the activation barriers of the NH_2NO decomposition on the catalyst surface were much lower than those calculated for the gas-phase reaction [260]. Thus, in the low temperature range, the desorption of water and other product molecules was considered rate-determining. Keranen et al. reported that VO_x supported on pure TiO_2 led to a larger number of strong acid sites but less weak/medium ones than on a mixture of TiO_2 and SiO_2,[212] implying strong adsorption of NH_3 and H_2O. In fact, Figure 52 reveals the appearance of desorption peaks of water during heating steps. Thus, a limited mixture of TiO_2 and SiO_2 decreases the surface acid strength, facilitates desorption of H_2O and other products and is therefore expected to improve the SCR activity at low temperatures.

Another aspect that is proposed to influence the low-temperature SCR performance is the preparation of the TiO_2 domains on the SiO_2 support[211]. In contrast to other methods used for the preparation of mixed SiO_2+TiO_2 supports, such as sol-gel based synthesis[201] and co-precipitation[257], the ALD approach enables controlled deposition of sub-monolayer titania and vanadia, resulting in micro-domain areas of TiO_2 and well dispersed VO_x species. The deposition of VO_x on small domains of an oxide less reducible than vanadia but more reducible than the support is expected to improve the dispersion of surface VO_x species [261]. Furthermore, the high surface area of the mesoporous matrix can be largely preserved by the low-temperature ALD approach and allows to further increase the VO_x loading for higher SCR catalytic performance.

6.1.7. Conclusion

An NH_3-SCR model catalyst was prepared by controlled deposition of titania and vanadia onto a mesoporous high surface area silica support by use of ALD. The final $VO_x/TiO_2/SBA$-15 catalyst retained a large surface area, characterized by domains of amorphous titania on silica and the formation of dispersed oligomeric VO_x surface species. While low V loadings resulted in the preferential deposition of VO_x on Ti sites with moderate catalytic performance, a significant improvement in performance was observed for catalysts containing a similar amount of deposited Ti and V, allowing vanadium to be anchored to both TiO_2 and Ti-O-Si boundary sites, thus increasing the total number of acid sites.

In situ and *operando* DRIFTS provided insight into the adsorbate dynamics as a function of temperature. At temperatures <300 °C, adsorbed NH_x species are evidenced by the detection of L and B acid site-related signals besides water, formed by SCR reaction and/or present as stable species. On the other hand, at higher temperatures (>300 °C), part of the NH_x species related to L acid sites could no

longer be detected in DRIFTS, indicating their involvement in the H-abstraction reaction and subsequent removal from acid sites. As a result, NH_3 adsorption is proposed to become rate-determining, which is consistent with the absence of NH_3 desorption peaks in the exhaust gas at higher temperatures.

Compared to other catalysts with similar composition, the SBA-15-based catalyst used in the present study shows a better NH_3-SCR performance and wider temperature window for operation. The superior catalytic behavior is attributed to several factors, including the controlled ALD synthesis leading to a high dispersion of VO_x oligomeric species due to the high surface area of the mesoporous structure. Considering the analysis of the RDS at low temperature, desorption of products is of great importance due to their strong interaction with acid sites. The structure of VO_x species with amorphous TiO_2 domains on the SiO_2 substrate, forming hybrid supports of V-O-Ti and V-O-Si, provided more acid sites, especially weak acid sites, thus leading to a better catalytic SCR performance than VO_x/TiO_2 and VO_x on atomically mixed SiO_2+TiO_2 prepared by sol-gel methods.

Our findings demonstrate the potential of using high surface area VO_x/TiO_2/SBA-15 model catalysts for gaining new insight into the factors determining the mode of operation of supported vanadia catalysts used for NH_3-SCR.

6.2. ALD SiO$_2$ coating on CeO$_2$/SBA-15 for SO$_2$ resistant NH$_3$-SCR

Ceria-based oxides have attracted much attention as SCR catalysts due to their excellent redox capacity of CeO$_2$ via the Ce^{4+}/Ce^{3+} couple.[120, 262] Bare CeO$_2$ applied to NH$_3$-SCR reaction was reported to follow an E-R (Eley-Rideal) mechanism, and the rate-determining step was the NH$_3$ adsorption due to its poor acidity.[64] On the other hand, the sulfur resistance of NH$_3$-SCR catalysts is of importance for industrial applications. It was reported that sulfated CeO$_2$ shows improved activity due to the enhanced surface acidity facilitating the adsorption of NH$_3$ in the E-R reaction process.[69] But, as observed for most metal oxides catalysts, the SO$_2$ poisoning process gives rise to the deposition of sulfate species and blocks the reaction sites, especially at temperatures below 300 ^{o}C.[66] Modifications of the catalyst by synthesizing complex oxides composites seem to be always effective to improve the catalytic activity as well as the SO$_2$ resistance and were fully reported in previous works.[1, 263] However, the mixing of multiple active metals complicates the analysis of the active species and the contribution of ceria, hindering the development of structure-activity relations and thus further catalyst improvement.

Along with promoting the NH$_3$-SCR catalytic performance, another challenge for bare CeO$_2$ is its poor thermal stability, which results in a significant decrease of the high oxygen mobility and catalytic activity of ceria at elevated temperatures.[264, 265] To this end, chemical inert silica (SiO$_2$) is widely used to stabilize the CeO$_2$ but without effect on the reactivity behavior.[41, 266] There are two strategies to synthesize binary CeO$_2$-SiO$_2$ catalysts, that is, co-crystallization of cerium and silicon ions by a one-pot method, and to deposit CeO$_2$ on the surface of SiO$_2$ by different kinds of methods, such as impregnation, precipitation, sol-gel, deposition, etc..[267-269] Although Si is considered to be a catalytically inert component, the addition of Si to ceria-based catalysts shows a positive effect on the SCR reactivity and SO$_2$ resistance, attributed to promoted Brønsted acid sites and active nitrates,[270] enhanced specific surface area and hydrothermal stability,[271] weakened alkalinity due to sulfate accumulation,[272] and synergetic effects between acid and redox catalysis.[273] For instance, Tan et al.[66] prepared Ce-Si oxides by coprecipitation (mixed CeSi$_2$) and wet impregnation (supported Ce/2Si) methods and found that mixed oxides (CeSi$_2$) show an excellent catalytic performance and SO$_2$ resistance for the NH$_3$-SCR reaction. Compared with bare CeO$_2$, the mixing with silicon leads to the formation of a Ce-O-Si structure and abundant Si-OH groups, enhancing the competitive adsorption of NH$_3$ versus inert NO$_x$ species, especially for the sulfated sample. Chen et al. proposed an interesting structure by coating Fe-ZSM with a layer of SiO$_2$ first before cerium species were introduced into the mesoporous SiO$_2$ shell, enhancing the oxidation of NO as well as the fast-SCR reaction, which was attributed to the confined growth of CeO$_2$.[274] Based on this knowledge, new strategies for the "molecular design" of improved catalysts for NO$_x$ removal and SO$_2$ resistance can be developed.

Herein, a novel Ce-Si oxide structure was proposed, in which CeO_2 is loaded onto mesoporous SBA-15 (for high surface area and stability), and then several atomic layers (0, 1, 3, 5, 10) of SiO_2 are deposited onto the surface by the ALD technique. With a suitable number of SiO_2 layers (5×cycles), the supported $CeO_2@SiO_2$ showed excellent NH_3-SCR reactivity and SO_2 resistance, compared with bare CeO_2 (0× cycle) and over-coated $CeO_2@SiO_2$ (10×cycles). The high reactivity is attributed to the presence of abundant acid sites (Ce-O-Si) and the strong redox behavior of nano CeO_2, while the excellent SO_2 resistance, especially at low temperatures, is attributed to the protection by the atomic layer(s) of SiO_2. The developed $CeO_2@SiO_2$ catalyst system provides a new strategy for the design of NH_3-SCR catalysts by surface atomic layer modification.

6.2.1. Sample preparation

The catalyst carrier, SBA-15, was prepared by in the same method as described previously.[158] CeO_2 was loaded onto asSBA-15 by one-pot solid-state impregnation (SSI) , yielding yellow samples denoted as $CeO_2@SBA-15$, the same way as introduced above (see section 4.2).

ALD of SiO_2 was performed on the home-made device introduced in the experimental section. $SiCl_4$ and H_2O were used as precursor for SiO_2 and oxidant, respectively. In order to achieve a low temperature deposition, pyridine was used as promoter to catalyze the oxidation reaction between silicon precursor and water. Due to the ready evaporation of $SiCl_4$ and pyridine, the feeding bottle could be employed at room temperature without assisted heating. The reactor temperature was set as 55 $^{\circ}$C; one cycle program includes (1) a pulse of pyridine for 5 s, (2) a pulse of $SiCl_4$ for 60 s, (3) purging with 200 mL/min N_2 for 60 s, (4) another pulse of pyridine for 5 s, (5) a pulse of H_2O for 60 s, (6) purging with 200 mL/min N_2 for 60 s to finish one cycle and recover surface hydroxyl groups. In order to explore the effect of the thickness of the deposited SiO_2, a series of samples was prepared containing n cycles of ALD deposition, which were denoted as $CeO_2@SBA-15 + n×SiO_2$ (n=0, 1, 2, 3, 5, 10).

6.2.2. Catalytic test

The catalytic activities of the $CeO_2@SBA-15+n×SiO_2$ (n=0, 1, 3, 5, and 10) catalysts for the NH_3-SCR reaction are shown in Figure 54. The results show that the bare $CeO_2@SBA-15$ sample exhibits a rather low catalytic activity ($< 45\%$) at all temperatures with a maximum NO conversion of only 31.5% and a N_2 selectivity below 60 % at high temperatures (500 $^{\circ}$C). After coating several atomic layers of SiO_2 (1-5 ALD cycles), the NO_x conversion and N_2 selectivity all increased especially within the medium temperature range (about 200-400 $^{\circ}$C), while further increasing the surface SiO_2 coated layer to 10 ALD

cycles led to an activity decrease. As can see in Figure 54(c), *in situ* monitoring of the exhaust gas shows a NH_3 desorption peak at the low temperature step for all five samples, implying that the adsorption ability of CeO_2@SBA-15 is not the rate-determining step at low temperature. On the other hand, at higher temperatures the amount of adsorbed NH_3 decreased and even disappeared at 500 ^{o}C, implying the oxidation of NH_3. Especially the increasing NO (reaching 500 ppm) and NO_2 indicate that NH_3 is over-oxidized to NO_2 instead of its reaction with NO to form N_2. N_2O appears above 200 ^{o}C and increases with temperature. In detail, the bare CeO_2@SBA-15 and $10\times SiO_2$ coated sample show the highest NH_3, indicating low oxidation of the surface. The $1\times SiO_2$ coated sample is interesting as it shows the highest N_2O signal at 300 ^{o}C and the highest NO_2 signal at 400-500 ^{o}C although its NO emission is not the lowest. This indicates that the coated SiO_2 forms Ce-O-Si bonds, truly increasing the oxidation ability. The $10\times SiO_2$ sample shows the highest N_2O level, implying that thick SiO_2 was facilitating the formation of N_2O. The emission of H_2O is another proof for the oxidation of NH_3 by either the SCR reaction or simple oxidation of NH_3. The $5\times SiO_2$ coated sample shows the lowest NO and highest H_2O level at 300-400 ^{o}C, indicating that the NH_3-SCR reaction is preferred on the optimized SiO_2 coated layers. In addition, Figure 54(d) shows the NO_x conversion for bare CeO_2@SBA-15 and the $5\times SiO_2$ coated sample for different gas space velocities. When the GHSV is decreased from 166667 $ml \cdot g^{-1} \cdot h^{-1}$ to 50000 $ml \cdot g^{-1} \cdot h^{-1}$, the NO_x conversation increased for both samples. Importantly, the NO_x conversion reached nearly 100 % for the $5\times SiO_2$ sample with a GHSV=50000 $ml \cdot g^{-1} \cdot h^{-1}$, which is better than the reported CeO_2-SiO_2 catalyst for NH_3-SCR under the same conditions.[66]
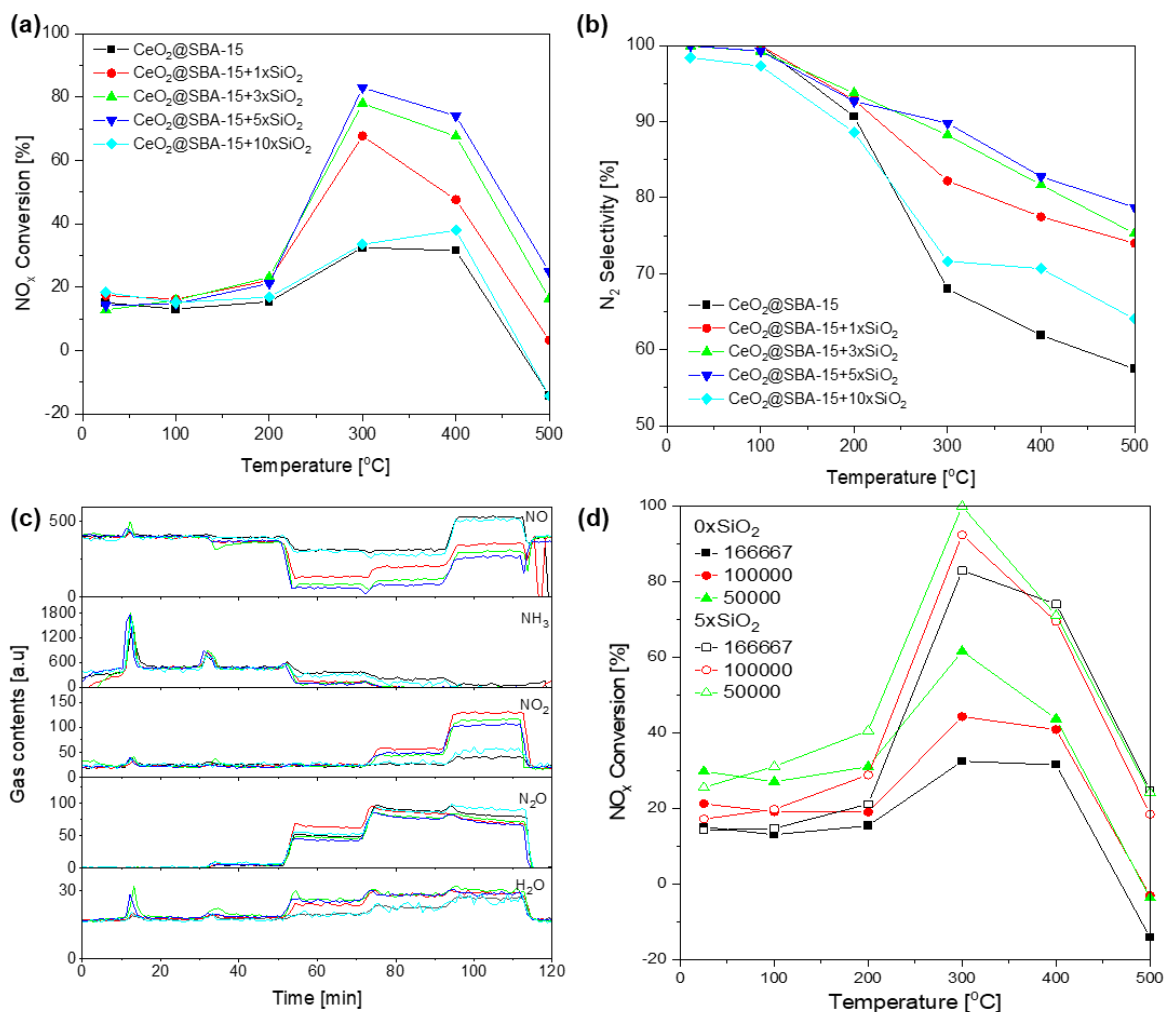
Figure 54. Temperature-dependent catalytic performance of CeO_2@SBA-15+nxSiO$_2$ samples for the NH$_3$-SCR reaction. (a) NO$_x$ conversion, (b) N$_2$ selectivity, (c) *in situ* monitoring of the exhaust gas (GHSV=166667 ml·g^{-1}h^{-1}). (d) NO$_x$ conversion of NH$_3$-SCR reaction on bare CeO_2@SBA-15 and 5×SiO$_2$ coated samples at different GHSV (ml·g^{-1}h^{-1}).

6.2.3. Characterization results

Considering the catalytic performances above, three samples (bare CeO_2@SBA-15, CeO_2@SBA-15+5×SiO$_2$, CeO_2@SBA-15+10×SiO$_2$) were chosen for further characterizations, i.e., to gain insight into the reaction mechanism and the role of coated SiO$_2$.

Figure 55 shows *in situ* DRIFT spectra of NH$_3$ pretreated samples reacting with NO/O$_2$ at 300 °C. In Figure 55(a), the peaks observed at about 1534, 1559, and 1593 cm^{-1} are typically assigned to monodentate, bidentate, and bridging nitrate species, respectively,[275] while the relative weak bands at 1514 and 1547 cm^{-1}, assigned to NH$_2$ and bidentate NO$_3^-$, disappear. The spectra in Figure 55(b) during

reaction with NO/O$_2$ show two features at 2220 and 2554 cm^{-1}, assigned to adsorbed N$_2$O species and nitrite species. These results for bare CeO$_2$@SBA-15 indicate that the reaction follows the E-R route and NO is oxidized to various nitrate and nitrate species on the surface. In Figure 55(c), the spectra of CeO$_2$@SBA-15 + 5×SiO$_2$ during reaction with NO/O$_2$ show interesting features including a strong peak at 1544 cm^{-1} due to monodentate nitrate but relative weak peaks at 1564 cm^{-1} and 1693 cm^{-1} due to bidentate and bridging nitrates, respectively. In addition, the peak at 1357 cm^{-1} is attributed to reduced NO$^-$ species, and the peak at 1486 cm^{-1} is tentatively assigned to adsorbed NO$_2$.[198] This implies that the 5 layers of SiO$_2$ coated on the surface of CeO$_2$@SBA-15 decrease the interaction between CeO$_2$ and NO, and especially the oxidized NO$_x$ species. At higher wavenumbers (see Figure 55(d)), the observed peaks above 3000 cm^{-1} can be attributed to the stretching vibrations of N-H or O-H bonds. In this range, the disappearance of N-H related vibrations at about 3273 and 3358 cm^{-1} but the appearance of NO$_x$-related features is observed. Thus, the high reactivity of the 5×SiO$_2$ sample might be attributed to the reaction between adsorbed NH$_3$ and NO/O$_2$. As shown in Figure 55(e), with increasing coating thickness of SiO$_2$, a strong signal due to monodentate nitrate is observed at 1541 cm^{-1} but little other features, indicating the weak interaction between NO$_x$ with the catalyst surface. Figure 55(f) shows that the N-H peaks at 3272 and 3342 cm^{-1} are weak and that after reaction with NO/O$_2$ much smaller spectral changes are observed than for the 5×SiO$_2$ sample (see Figure 55(d)), especially there is no appearance of a broad peak at about 3450-3550 cm^{-1}. In addition, the features at 2210 and 2558 cm^{-1} are absent in both NH$_3$ and NO/O$_2$ atmosphere, indicating that the thick coating (10×SiO$_2$) decreases the exposure of active CeO$_2$ species, and thus of active oxygen species.

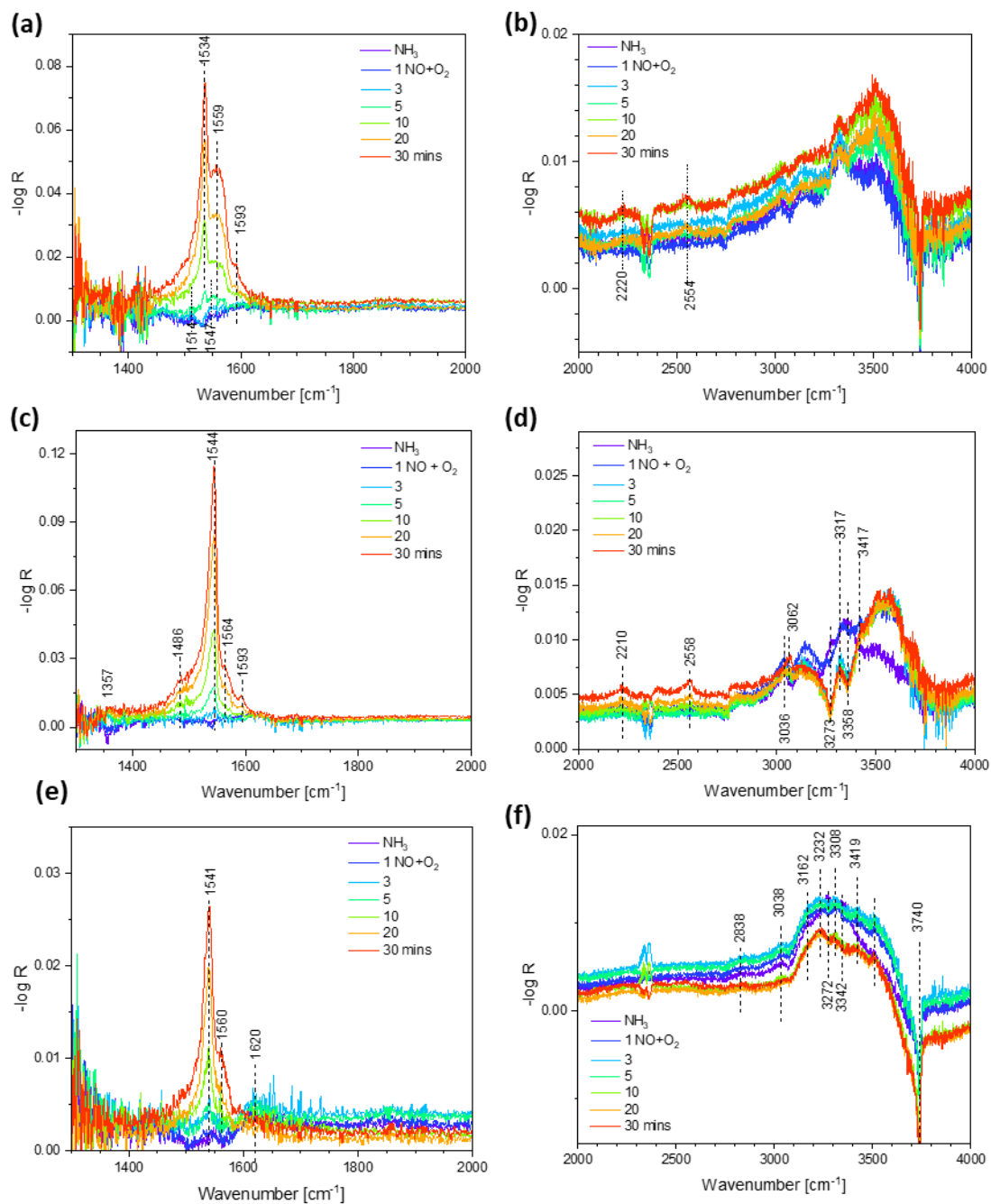Figure 55. *In situ* DRIFT spectra of NH$_3$ adsorbed samples reacting with NO/O$_2$ at 300 °C. (a-b) CeO$_2$@SBA-15, (c-d) CeO$_2$@SBA-15 + 5×SiO$_2$, and (e-f) CeO$_2$@SBA-15 + 10×SiO$_2$. For each series, the sample was first calcined in 500 °C for 1 h and then cooled down to 300 °C, and the corresponding spectrum was used as reference.

Afterwards, the reactants were passed into the reactor in the reverse order, that is, the samples were pretreated in NO/O$_2$ until saturation and then reacted with NH$_3$. As can be seen from Figure 56(a), the NO/O$_2$ pretreated samples show features at 1536, 1560, 1592 cm^{-1} which are typical for nitrate and a

nitrite-related feature at 2550 cm^{-1}. There is no 2210 cm^{-1} band, indicating that adsorbed N$_2$O results from the reaction between adsorbed NH$_3$ and NO (see Figure 55(b)). After the reaction with NH$_3$, new peaks appear at 1532 and 1549 cm^{-1} for amine (-NH$_2$) and bidentate nitrate, respectively. The peaks at 3039 and 3163 cm^{-1} are attributed to N-H stretching vibrations of B acid sites bound NH$_4^+$, while those at 3279 and 3368 cm^{-1} are due to L acid sites bound NH$_3$. From the temporal evolution of the spectra there is no indication for changes of the surface NO$_x$ species due to reaction with NH$_3$, suggesting that the surface nitrate or nitrite species are inert to react with NH$_3$ via the L-H route. For the 5×SiO$_2$ sample (see Figure 56(b)), the peak at 1544 cm^{-1} disappears quickly while a peak at about 1537 cm^{-1} appears, indicating the high reactivity for this nitrate species. It is found that the feature for nitrate (1544 cm^{-1}) is blue-shifted but the features for N-H (3036, 3157, 3270, and 3365 cm^{-1}) are all red-shifted compared with the same species on bare CeO$_2$@SBA-15 (see Figure 56(a)), reflecting the effect of different catalyst surfaces. Figure 56(c) also shows a gradual disappearance of the feature at 1537 cm^{-1}. It is concluded that the monodentate nitrate at higher wavenumbers (about 1544 cm^{-1}) is an active site for the L-H route while at lower wavenumber (about 1537 cm^{-1}) it was inactive towards NH$_3$. The N-H stretching features show the same wavenumbers for L sites bound NH$_3$ as observed for the 5×SiO$_2$ samples, but in case of the B sites bound NH$_4^+$, the features resemble the bare sample This behavior implies that NH$_3$ adsorbed on the same L acid sites (mainly Ce^{4+}), but that a major difference of the samples regarding catalyst surface properties is the presence of isolated silanol at about 3740 cm^{-1}, resulting from Ce-O(H)-Si species,[275] which shows a strong peak for the bare and the 10×SiO$_2$ sample, but is only very weak for the 5×SiO$_2$ sample.
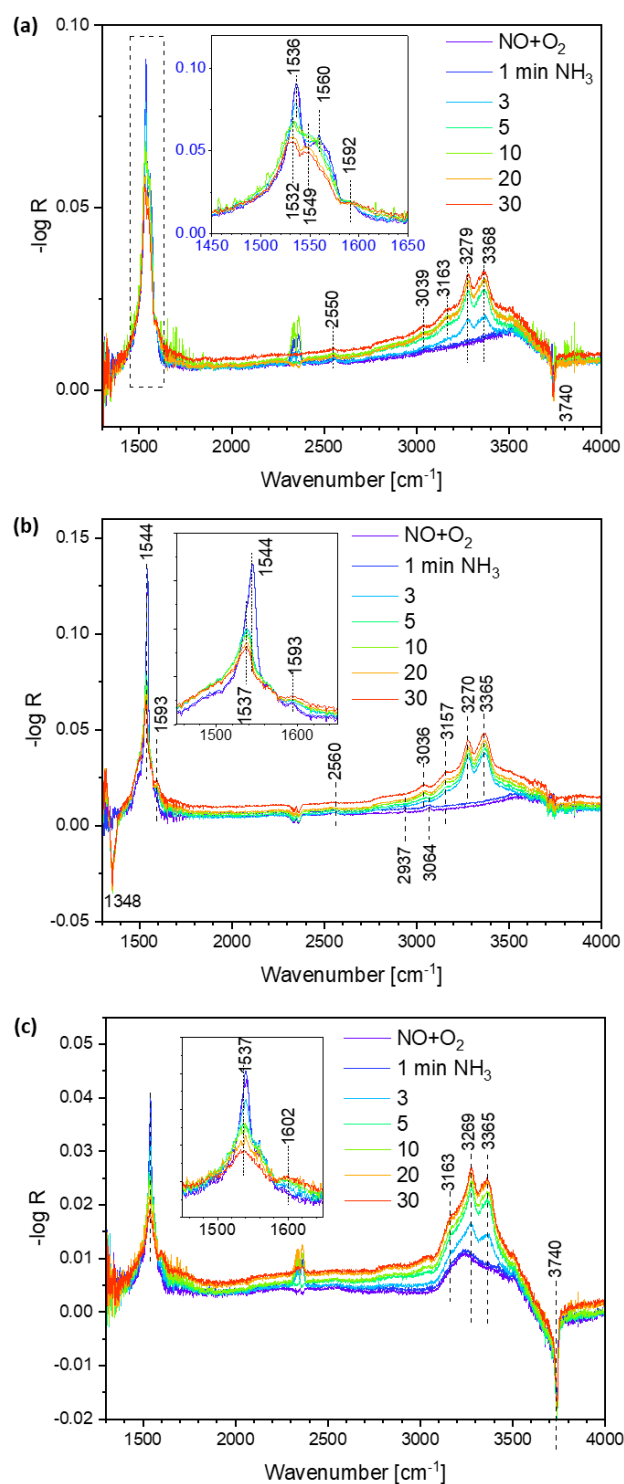
Figure 56. *In situ* DRIFT spectra of NO/O_2 adsorbed samples reacting with NH$_3$ at 300 °C. (a) CeO$_2$@SBA-15, (b) CeO$_2$@SBA-15+5xSiO$_2$, and (c) CeO$_2$@SBA-15+10xSiO$_2$. For each series, the sample was first calcined in 500 °C for 1 h and then cooled down to 300 °C, and the corresponding spectrum was used as reference.

6.2.4. Resistance towards sulfur poisoning

Figure 57 shows the catalytic performance of CeO_2@SBA-15 and the SiO_2-coated samples in NH_3-SCR including exposure to 200 ppm SO_2 to evaluate the effect sulfur poisoning. It is found that after SO_2 exposure all three samples at first exhibit an enhanced catalytic performance (for both the NO_x conversion and the N_2 selectivity), before the NO_x conversion then begins to gradually decrease. In case of with the SiO_2-coated samples, as lower decline is observed, especially for the thick SiO_2 (see Figure 57(c)). Moreover, when the SO_2 exposure is stopped, and the common NH_3-SCR gas atmosphere is applied, the $10 \times SiO_2$ sample shows a better SO_2 resistance than the other two samples because the SO_2 poisoned $10 \times SiO_2$ sample shows even higher NO_x conversion than the fresh one. It is concluded that the surface SiO_2 is effective for the SO_2 resistance.

To further explore the SO_2 resistance of bare CeO_2@SBA-15 and SiO_2-coated CeO_2@SBA-15 samples, in situ DRIFT spectra were recorded at low (200 ^{o}C) and high (300 ^{o}C) temperature (see Figure 58).

In Figure 58(a), the peaks at 1434 and 1672 cm^{-1} are assigned to ammonium ions bound to B acid sites, while the peak at 1593 cm^{-1} is assigned to NH_3 bound to L acid sites.[69, 145] Correspondingly, the peaks at 2822-3155 cm^{-1} and 3280-3372 cm^{-1} are attributed to N-H stretching vibrations of B-NH_4^+ and L-NH_3, respectively. Meanwhile, a negative peak appears at 1370 which may be assigned to sulfate on sulfated CeO_2, which is covered by NH_3.[69] This suggests that NH_3 is mainly adsorbed on SO_4^{2-} on sulfated CeO_2. In detail, after the NH_3 exposure at 200 ^{o}C, the B-NH_4^+ and L-NH_3 features appear with the L-NH_3 feature being stronger relatively dominant. After exposure to the experimental gas (NH_3+NO+O_2), it was found that the features show the same behavior as after NH_3 exposure but with increased intensity, implying that NH_3 further adsorbs on the surface and no NO_x is formed due to the low oxidation temperature for NO. The strong intensity of the B-NH_4^+ peak at 1434 cm^{-1} after adding SO_2 to the experimental gas indicates an increase of the surface Brønsted acidity. The peaks at 1593, 3280, and 3372 cm^{-1}also increase in intensity, indicating that the L-NH_3 also increased due to SO_2 addition, but the B-NH_4^+ features dominate the surface adsorption. The appearance of the peak at 2113 cm^{-1} assigned to N≡N of N_2O indicates that SO_2 activates the surface ammonia to react with NO at low temperature (200 ^{o}C). The following N_2 purge results in a decrease of the features at 1434, 1672, 2822-3722 cm^{-1} due to desorption of surface NH_3 species, while the increase of the peak at 1314 cm^{-1} suggests the exposure of bidentate sulfate. Here, the peak at 1314 cm^{-1} is tentatively assigned to sulfate species instead of NH_4^+ in previous work.[276]. The intensity increase of the peak at 3664 cm^{-1} indicates a change
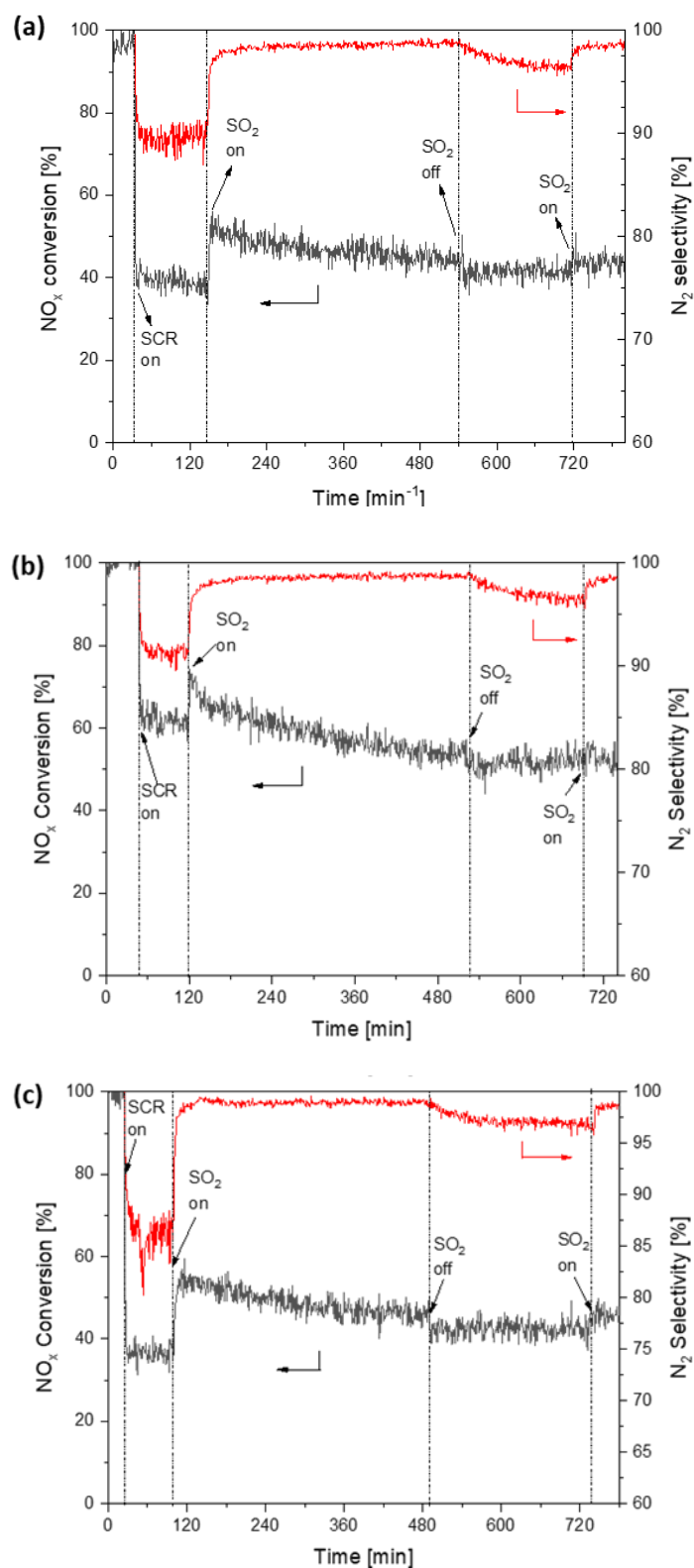
Figure 57. Evaluation of the effect of sulfur poisoning on the NH₃-SCR reactivity behavior, including the NOₓ conversion (black) and N₂ selectivity (red), at 300 °C. Feed gas: 500 ppm NH₃, 500 ppm NO, 5% O₂, 200 ppm SO₂ (if applied), and N₂; GHSV: 60000 h⁻¹. (a) 0xSiO₂, (b)5xSiO₂, (c) 10xSiO₂.
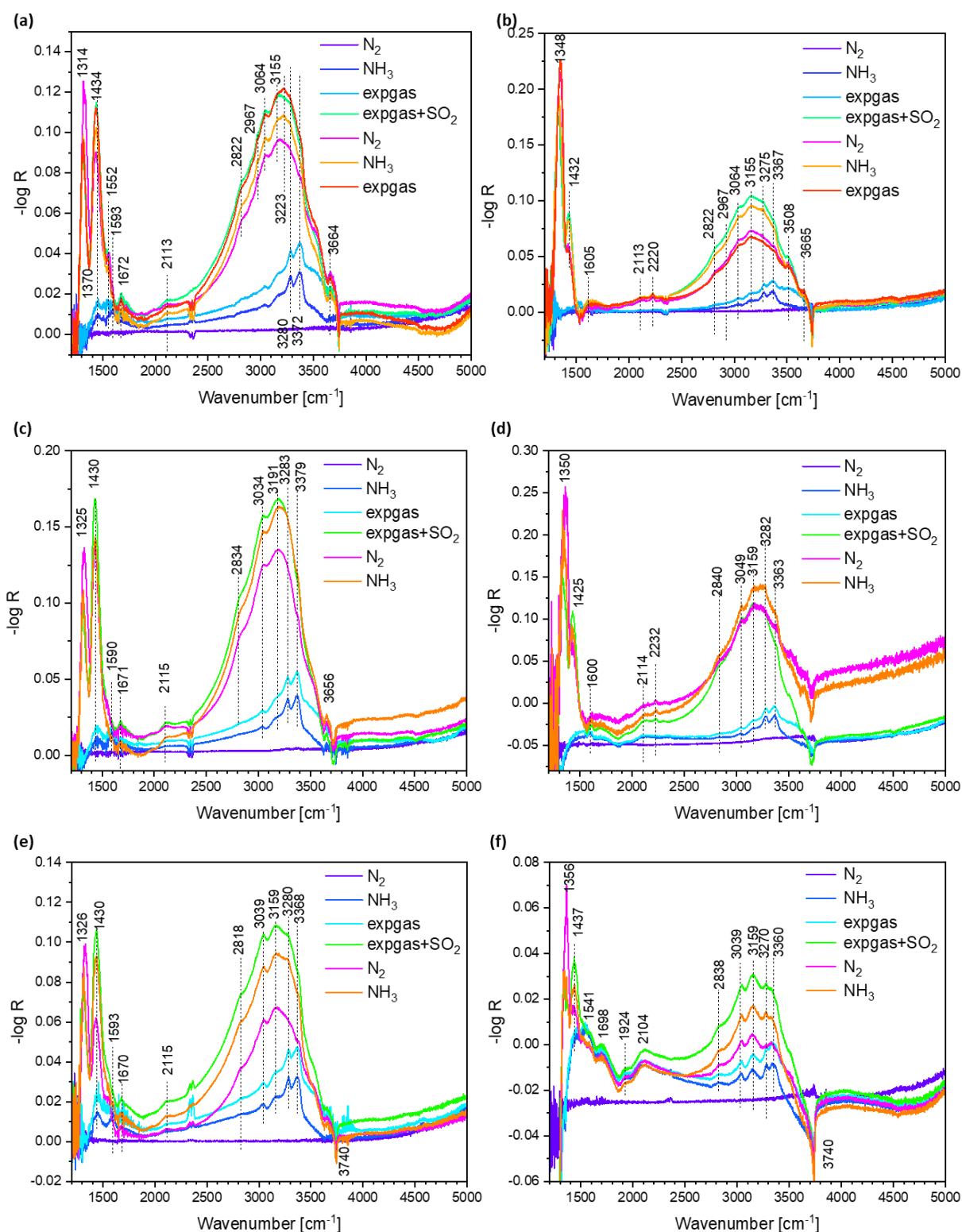
Figure 58. *In situ* DRIFT spectra recorded in different gas atmospheres including NH_3-SCR reaction conditions and the presence of SO_2. (a) 0xSiO_2 at 200 °C, (b) 0xSiO_2 at 300 °C, (c) 5xSiO_2 at 200 °C, (d) 5xSiO_2 at 300 °C, (e) 10xSiO_2 at 200 °C, (f) 10xSiO_2 at 300 °C. Feed gas: 500 ppm NH_3, 500 ppm NO, 5% O_2, 200 ppm SO_2 (if applied), and N_2; GHSV: 60000 h^{-1}. For each series, the sample was first calcined in 500 °C for 1 h and then cooled down to 200 °C for (a)(c)(e) and 300 °C for (b)(d)(f), and the corresponding spectrum was used as reference.

from Ce-O-H-NH$_3$ to Ce-OH with the B-bound NH$_4^+$ desorbing as NH$_3$. The following gas treatments repeats the exposure to NH$_3$ and experimental gas, and show increased B-NH$_4^+$ (1434 cm^{-1}) and decreased -OH (3664 cm^{-1}) signals, while the sulfate peak at 1314 cm^{-1} keeps constant, implying that the SO$_2$ adsorbed on the catalyst surface provides extra B acid sites and is stable at 200 ^{o}C.

As shown in Figure 58(b), increasing the temperature to 300 ^{o}C leads to a shift of the sulfate peak from 1314 to 1348 cm^{-1}. Correspondingly, the shoulder peak at about 1380 cm^{-1} assigned to the asymmetric vibration mode of O=S=O species, indicates the oxidation of SO$_2$ at higher temperature (300 ^{o}C). The peaks at 1432 and 1605 cm^{-1} are attributed to B-NH$_4^+$ and L-NH$_3$, respectively. These two species can also be identified by their N-H vibration vibrations at 2822-3155 cm^{-1} and 3275-3367 cm^{-1}. The peaks at 2113 and 2220 cm^{-1} are typical for the N≡N vibration of N$_2$O or N$_2$-related species. The peak at 3650 cm^{-1} is attributed to the O-H stretching of Ce-OH species, while the band at 3508 cm^{-1} is tentatively assigned to OH-stretching of S-OH and that at 3740 cm-1 to OH stretching of Si-OH. After NH$_3$ adsorption and exposure to the experimental gas, mainly the L-NH$_3$ features appear. After SO$_2$ addition to the experimental gas, a sulfate peak at 1348 cm^{-1} appeared, while the peaks at 1605 and 2822-3665 cm^{-1} increased, indicating formation of NH$_4^+$ on the sulfate sites. After the N$_2$ purge, it is found that the peak at 1432 cm^{-1} decreased while the peak at 1348 cm^{-1} increased, indicating that sulfate-bound NH$_4^+$ desorbed from the sulfate sites exposing the sulfate species. The following exposure to NH$_3$ shows an increase of both L-NH$_3$ and B-NH$_4^+$ species. With further exposure to the experimental gas, the ammonia-related features decrease, implying that the reaction follows the E-R route after SO$_2$ adsorption.

As can be seen in Figure 58(c), with NH$_3$ adsorption, features due to L-NH$_3$ (1590 cm^{-1}) and B-NH$_4^+$ (1430 cm^{-1}) appear and further increase in intensity in the experimental gas. This indicates that the 5×SiO$_2$ coating increases the surface acidity by forming Ce-O-Si species, which is supported by preliminary NH$_3$-TPD results. After adding SO$_2$ to the feed, a strong peak appeared at 1325 cm^{-1} which is assigned to sulfate, and the peaks at 1430, 1671 and 2834-3391 cm^{-1} are enhanced due to the increase of Brønsted acidity. The disappearance of the peak at 1590, 3283 and 3379 cm^{-1} points to a decrease in Lewis acidity, indicating SO$_2$ poisoning of the L acid sites. The following N$_2$ purge decreases the NH$_4^+$ feature at 1430 cm^{-1} and leads to an increased exposure of SO$_x$ species at 1325 cm^{-1}. Finally, the exposure to NH$_3$ recovers the surface ammonia species at 200 ^{o}C.

As shown in Figure 58(d), higher temperature (300 ^{o}C) results in the presence of weak bands at 1590 cm^{-1} for L-NH$_3$ 1435 cm^{-1} for B-NH$_4^+$ species after NH$_3$ adsorption and exposure to the experimental gas. With the addition of SO$_2$, an enhancement of the peak at 1425 cm^{-1} is observed, indicating Brønsted-type acidity. After the N$_2$ purge, the NH$_3$ desorbed, resulting in an increase of the sulfate-related feature at 1350 cm^{-1}, and the -OH features within 3500-3800 cm^{-1} increased. Finally, the

exposure to experimental gas results in an increase of surface ammonia species, L-NH$_3$ and B-NH$_4^+$, and a decrease of -OH groups due to the reaction of ammonia with NO+O$_2$ via the E-R route. Figure 58(e) shows that the thick SiO$_2$ coating (10×SiO$_2$) yields similar spectra as the 5×SiO$_2$ sample (see Figure 57(c)). With the addition of SO$_2$, the peaks at 1430 and 1670 cm^{-1} increase due to enhanced Brønsted acidity. Correspondingly, also the peaks within 2818-3159 cm^{-1} increase, while the bands at 3280/3368 cm^{-1}, assigned to L-NH$_3$ species, show peak features during the whole reaction, compared with the shoulder peaks in Figure 57(c). This indicates that the L-NH$_3$ is more active for the 5×SiO$_2$ than for the 10×SiO$_2$ sample. After the N$_2$ purge, the 1326 cm^{-1} peak increases while the peak at 1430 cm^{-1} decreases, indicating the desorption of NH$_4^+$ as NH$_3$. On the contrary, the shoulder bands at about 1593 cm^{-1}, assigned to L-NH$_3$, do not change in intensity implying that NH$_3$ adsorbed on L acid sites is stable. Finally, upon NH$_3$ exposure the L-NH$_3$- and B-NH$_4^+$-related features are all recovered at 200 ℃.

For the NH$_3$-treated sample (see Figure 58(f)), there are features of L-NH$_3$ (1437 and 1698 cm^{-1}) and B-NH$_4^+$ (1593 cm^{-1}), corresponding to the range of N-H vibrations of 2838-3159 cm^{-1} and 3270-3360 cm^{-1}, respectively. It is found that the relative content of B-NH$_4^+$ is higher for the 10×SiO$_2$ sample than for the bare and 5×SiO$_2$, based on the intensities of the three peaks at 2838/3039/3159 cm^{-1}. The presence of the peaks at 1541, 1924, and 2104 cm^{-1} indicates that there are various N$_x$O$_y$ species formed on the surface. It might be deducted that N$_x$O$_y$ is inactive on the thick SiO$_2$ surface before SO$_2$ feeding. Even upon SO$_2$ exposure, these features exist due to the competitive adsorption between N$_x$O$_y$ and SO$_2$. Interestingly, the N$_2$ purge could decrease the intensity of the N$_x$O$_y$ species by facilitating their desorption at 300 ℃, while a re-feeding of NH$_3$ could not recover these species as before for the reduced catalyst surface.

To sum up, the similarities and differences of the three materials in different gas atmospheres including SO$_2$ were analyzed at low and high temperature. Firstly, at low temperature (200 ℃, see Figure 57(a, c, e)), the adsorption of NH$_3$ is similar for all samples, that is, L-NH$_3$ and B-NH$_4^+$ form on the surface. Similarly, in the experimental gas, the behavior of the samples resembles each other. Note that the small feature at 1552 cm^{-1} (see Figure 57(a)) is assigned to nitrate species, which is attributed to the oxidation effect of bare CeO$_2$ surface. With SO$_2$ poisoning, all three samples show strong B-NH$_4^+$-related peaks. It is concluded that SO$_2$ mainly increases the surface Brønsted acidity. The N$_2$ purge facilitates the desorption of NH$_4^+$ desorbed and exposes the sulfate species (1320 cm^{-1}). It is found that the relative intensity of the 1320 cm^{-1} peak for bare CeO$_2$@SBA-15 is higher than that for the SiO$_2$-coated samples, indicating that the SiO$_2$ coating on CeO$_2$ could prevent the adsorption and oxidation of SO$_2$. With increasing temperature, the sulfate features changes from 1320 cm^{-1} (200 ℃) to 1350 cm^{-1} (300 ℃). The blue-shift is attributed to the stronger S=O bond resulting from the high temperature

oxidation of SO_2.[145] For the same reason, the relative intensity of sulfate (1350 cm^{-1}) to B-NH$_4^+$ (1430 cm^{-1}) features is higher at 300 ºC than that at 200 ºC. It is furthermore found that after N$_2$ purge the 10×SiO$_2$ coated sample shows a low sulfate intensity at 1356 cm^{-1} but a strong Si-OH peak at 3740 cm^{-1}, reflecting that the SiO$_2$-covered part prevents adsorption of SO_2. Please note that the 10×SiO$_2$ sample shows N-H features due to B-NH$_4^+$ and L-NH$_3$ species with equal intensity, while for bare CeO$_2$@SBA-15 the L-NH$_3$ signal is almost covered by that of B-NH$_4^+$.

Thus, the SiO$_2$ coating on the surface improves the SO_2 resistance by weakening the adsorption and oxidation of SO_2. For thick coatings, such as 10×SiO$_2$ leading to a complete coverage the redox properties of ceria are shielded which, consequently, decreases the NH$_3$-SCR catalytic performance.

6.2.5. Conclusion

In this section, CeO$_2$@SBA-15 catalysts were systematically coated with atomic layers of SiO$_2$ using by the ALD technique. The results show that moderate SiO$_2$ coatings (1-5 ALD cycles) enhance the SCR catalytic performance. This is attributed to the presence of Ce-O-Si interaction which improves its acidity and redox properties. On the other hand, a thick SiO$_2$ coating (10 ALD cycles) on CeO$_2$@SBA-15 shows a decreased performance due to the shield effect of SiO$_2$ regarding active CeO$_2$. The SiO$_2$ coating is also beneficial towards SO_2 resistance of the catalysts due to inactivity of SiO$_2$ to oxidize the SO_2 gas and form sulfates poisoning the surface. Importantly, this work proves that a minor atomic layer coating can modify the surface properties significantly, even if the coated material is inert. Moreover, the ALD method allows to quantitatively control the concentration of surface Ce-O-Si species by the number of ALD cycles, which was applied to explore the role of Ce-O-Si on the NH$_3$-SCR and SO_2 resistance.

6.3. VO$_x$ coating on CeO$_2$/SBA-15 for NH$_3$-SCR by site selective ALD (SSALD)

In the past few years, ALD has been rapidly developed for the synthesis of heterogeneous catalysts, including the preparation of highly dispersed metal nanoparticles (even to the extent of single-atom dispersion), such as Ni, Pt, Pd, etc., and the preparation of structurally controlled nanoparticles of metal oxide catalysts, such as TiO$_2$, VO$_x$, CeO$_2$, etc. ALD applications of metal oxides mainly involve substrate coatings to form strong metal-oxide interactions, surface protective layers as physical barriers, and direct deposition of catalytically active metal oxides.[208] So far, ALD techniques for synthesizing metal oxides have generated significant interest in catalyst preparation by controllable design.

To achieve a structurally controlled preparation, area selective ALD (AS-ALD) has been developed to fabricate complex nanostructured materials.[277] For this technique, patterned regions of the substrate are activated or passivated with the assistance of electron/ion beams, self-assembled monolayers (SAMs), or polymer resists. Then during the deposition process, the material is deposited only where it is needed, resulting in an area selective deposition. The catalytic structures prepared by regioselective ALD technology include core-shell structures, discontinuous coating structures, and embedded structures.[277]

However, ALD technology, especially in case of the AS-ALD, was developed mainly to fabricate defect-free 3D patterns and nanostructures for electronic applications in the semi-conductor field. It means that the AS-ALD technique was considered more in the context of structural (e.g. core-shell structure and embedded structure) than chemical catalytic properties. In catalysis, selective ALD is motivated to enable directed and precise tailoring of structural parameters, interfaces, and active sites, which has important implications for advanced catalysis. In the last section, a novel approach of controllably modifying the substrate surface followed by ALD of active metal oxides is proposed to achieve selective deposition. In detail, the bare substrate is pretreated in the NH$_3$-SCR reaction atmosphere to form NH$_x$ and N$_x$O$_y$ species on the surface first, before it is coated with active oxides (MO) by the ALD technique. Due to the different activities among these surface species and the original -OH group, it is proposed that the oxide MO is selectively deposited on the active sites and forms the optimized structure for the NH$_3$-SCR reaction compared with the directly deposited sample. Importantly, the selective deposition is expected to be relevant to the active sites on the surface which is correlated with the pretreatment in the target catalytic reaction (here: NH$_3$-SCR). Considering that the deposition is selective by the chemical active site but not the area, the new method is denoted as site selective ALD (SSALD).

6.3.1. Sample preparation

CeO_2/SBA-15 is prepared by SSI method introduced before. In brief, asSBA-15 and $Ce(NO_3)_3 \cdot 6H_2O$ is ground together and calcined in a furnace to obtain the SBA-15 supported CeO_2 catalyst. VO_x is loaded on the prepared CeO_2/SBA-15 by the ALD method. Vanadium (III) oxychloride ($VOCl_3$) is used as precursor for vanadia and H_2O is sued as oxidant. The temperatures for the feeding system ($VOCl_3$) and the reactor were set as 40 ^{o}C and 60 ^{o}C, respectively. The ALD cycle followed the following order: (1) N_2 purge for 60 s, (2) $VOCl_3$ pulse and reaction in closed reactor for 60 s, (3) N_2 purge for 60 s, (4) H_2O pulse and reaction in closed reactor for 60 s.

For the deposition of VO_x, the sample directly coated with one layer of VO_x will be denoted as CeO_2@SBA-15+ald_VO_x. If, on the other hand, the substrate CeO_2/SBA-15 was pretreated in NH_3-SCR reaction atmosphere at 300 ^{o}C for 1 h, and then coated with one layer of VO_x under the same conditions, the sample will be denoted as CeO_2@SBA-15+aasld_VO_x.

6.3.2. Catalytic test

Figure 59(a) shows the NH_3-SCR catalytic performance of the prepared samples at temperature ranging from 25 to 500 ^{o}C. All three samples show the typical volcano curves for the NO_x conversion as a function of temperature with an optimal operation window at about 300-400 ^{o}C. The VO_x coated samples show an improved NO_x conversion compared to the bare CeO_2@SBA-15 sample within the whole temperature range. Comparing the different ALD techniques, the site selective ALD sample (ssald_VO_x) shows a better NO_x conversion than the sample prepared by conventional ALD (ald_VO_x). The N_2 selectivity follows the order: $0 \times VO_x <$ ald_$VO_x <$ ssald_VO_x at the majority of temperatures except for high temperatures (> 400 ^{o}C) where the ssald_VO_x sample shows a great decrease in N_2 selectivity.

Figure 59(b) depicts the corresponding *in situ* monitoring of the exhaust gases. Interestingly, the results show a very similar behavior of the listed five components as function of temperature. In detail, for the NH_3 curves, the desorption peak appears for all samples at low temperature but the peak intensity followed the order: $0 \times VO_x <$ ald_$VO_x <$ ssald_VO_x, and at temperatures above 250 ^{o}C, the NH_3 desorption peak disappears. This indicates that the three samples possess a similar acid strength but that the ssald_VO_x owns more acid sites to adsorb NH_3. The highest NO_2 emission for the $0 \times VO_x$ sample at high temperature indicates the oxidation by CeO_2, while the highest N_2O emission for ssald_VO_x sample at high temperature is tentatively attributed to Ce-O-V interaction and the surface VO_x structure.
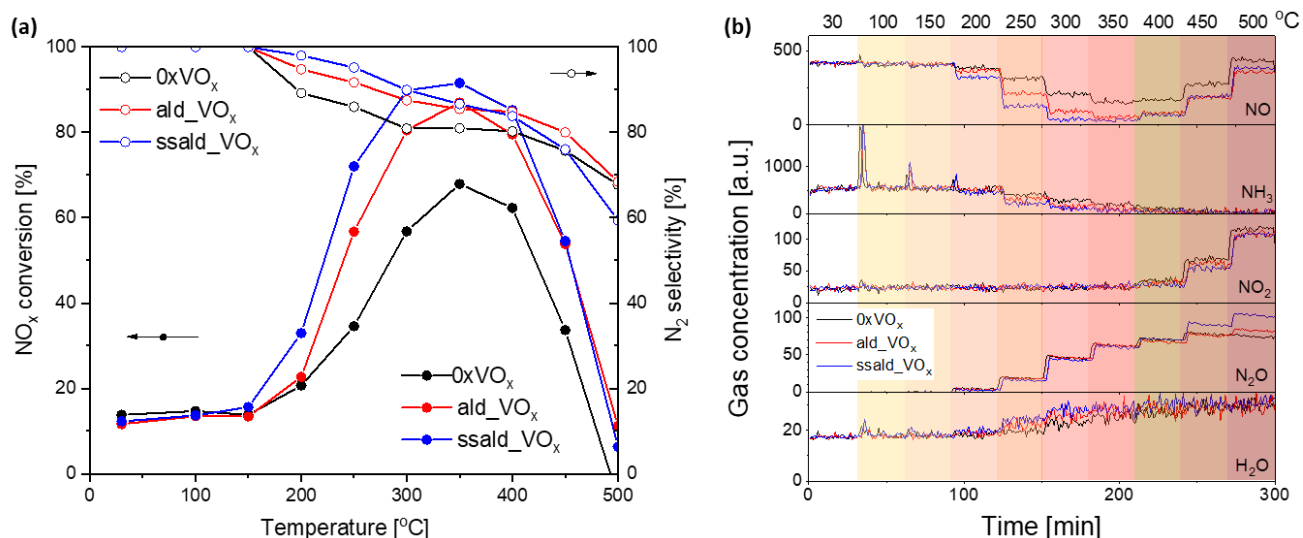
Figure 59. (a) Catalytic performance of NH$_3$-SCR reaction on prepared samples at different temperatures (GHSV=60000 h^{-1}). (b) *In situ* monitoring of the exhaust gas during a step-wise increase of the temperature from 25 to 500 °C.

6.3.3. Characterizations

In order to gain insight into the surface group changes during the NH$_3$-SCR experimental gas (expgas) pre-treatment, *in situ* DRIFT spectroscopy was performed.

As shown in Figure 60(a), starting from the spectrum of the original surface of the prepared CeO$_2$/SBA-15, the sample was heated to 300 °C for 1h to remove surface physiosorbed molecules and cooled down to 25 °C in N$_2$/20 %O$_2$. It is found that the dehydration operation increases the number of surface -OH groups (> 3500 cm^{-1})., which might be attributed to the degradation of surface free water. Afterwards, the sample is exposed to the expgas for 1 h at 300 °C and then cooled down to 25 °C. The features appearing at 1000-2000 and 3500-4000 cm^{-1} are attributed to surface water, which indicates that the NH$_3$-SCR reaction generates water. The increased intensity of the features at 3270 and 3385 cm^{-1} is attributed to L-NH$_3$ species; the intensity increases within 2000-3000 cm^{-1} can be attributed to N$_x$O$_y$ species at room temperature, including NO$^+$ at about 2133 cm^{-1}, N$_2$O at about 2200 cm^{-1}, NO$_3^-$ at about 2400 and 2700 cm^{-1}, NO$_2^-$ at about 2500 cm^{-1}, and NO$_2$ at about 2900 cm^{-1}.[128] Thus, the results prove the presence of a variety of groups on the pretreated CeO$_2$/SBA-15. Figure 60(b), depicts spectra of the pre-treated substrate after purging with N$_2$ gas (200 ml/min; …min), simulating the purge step during the ALD process. The hydroxyl features at 1000-2000 cm^{-1} and 3500-4000 cm^{-1} decrease but still exist. Importantly, the band at 2000-3000 cm^{-1} decreases directly by changing the gas from O$_2$ to N$_2$ and further decreases after the desorption at 120 °C and cooling down to 25 °C, implying the removal of surface

N_xO_y species. The peak at 3744 cm^{-1}, as well as the band at 4000-5000 cm^{-1}, increase after the N_2 purge, indicating an increase in surface -OH groups. The peaks at 3278 and 3369 cm^{-1} assigned to L-NH$_3$ species increase first at N_2/25 °C and then decrease after high temperature (120 °C) desorption. The final purged sample shows a low level of N_xO_y features but a high -OH density, suggesting that the desorbed N_xO_y activates the free water to form -OH group on the surface.
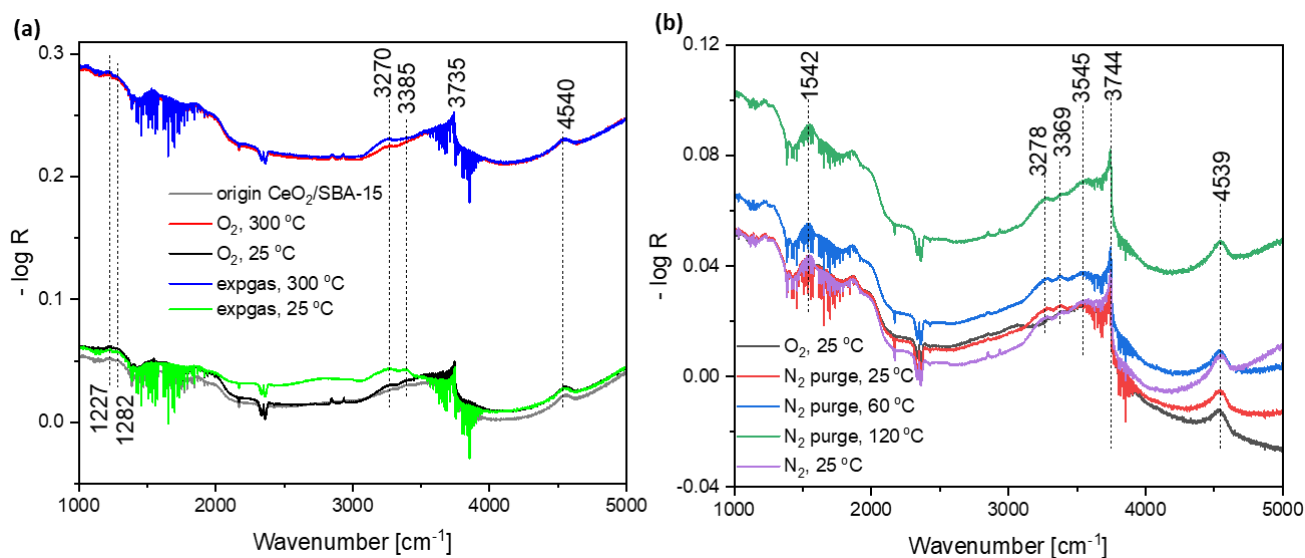
Figure 60. *In situ* DRIFT spectra of original CeO₂/SBA-15 (a) dehydrated at 500 °C for 1h and cooled down to 300 °C and 25 °C in N₂+20% O₂, and then pretreated in NH₃-SCR experimental gas (expgas) at 300 °C for 1h and cooled down to 25 °C, (b) purged by N₂ at increasing temperature to 120 °C and then cooled down to 25 °C after the expgas treatment. KBr was used to record the background spectrum.

Figure 61 shows IR spectra of bare CeO₂/SBA-15 (0×VO$_x$) and after coating of one layer of VO$_x$ (ald_VO$_x$ and ssald_VO$_x$) exposed to ambient atmosphere. Assuming the same number of surface -OH groups for all three samples, the curves were normalized to the peak at 3740 cm^{-1}. Comparing the spectra for the ald_VO$_x$ and ssald_VO$_x$ samples, it is found that the ssald_VO$_x$ sample shows less free water on the surface than the ald_VO$_x$ sample. Although it is difficult to quantify the changes of specific peaks, the spectal profile including the cross point at about 2854 cm^{-1} indicates different surface properties of the two coated samples. The features within 2000-2854 cm^{-1} are attributed to N_xO_y species as discussed above. The lower intensity level of the ssald_VO$_x$ sample compared to that of the ald_VO$_x$ sample might be explained by a transformation of surface N_xO_y species to -OH groups over the pre-treated substrate. The band at 2854-3500 cm^{-1} is assigned to stretching vibrations of O-H or N-H bonds; the higher intensity level in this range for the ssald_VO$_x$ sample suggests that there is adsorbed NH₃ on the pre-treated sample, which is inert towards reaction with the vanadium precursor (VOCl₃).
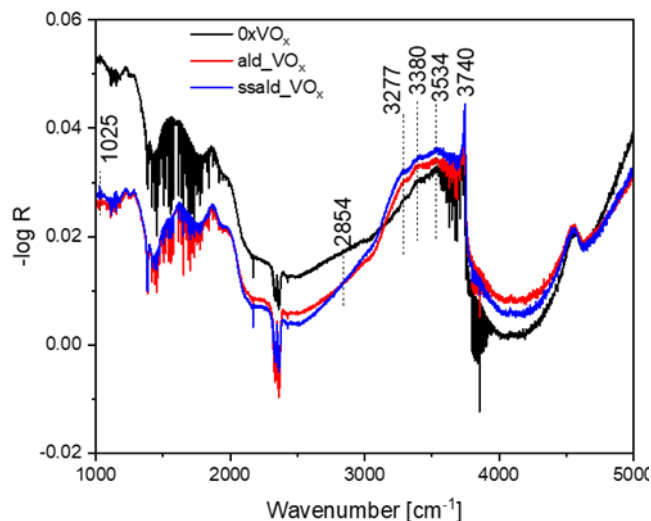
Figure 61. DRIFT spectra of VOx coated and uncoated samples at room temperature under ambient conditions. Standard KBr was used to record a background spectrum in ambient.

From the characterization results above, a preliminary picture for the mechanism of site selective atomic layer deposition (SSALD) is proposed (see Scheme 9). Firstly, it was evidenced that the pre-treated substrate shows different surface terminal groups compared with the non-treated substrate. Secondly, CeO_2/SBA-15 treated with NH_3-SCR experimental gas at 300 $^{\circ}$C shows both NH_3 and N_xO_y adsorbates on the surface. The following N_2 purge at 120 $^{\circ}$C partially desorbs N_xO_y species and transforms free water to hydroxyl groups, while the amount of adsorbed NH_3 stays constant. It is shown that after reaction with the vanadium precursor $VOCl_3$ the adsorbed NH_3 is inert to the oxidation of $VOCl_3$, while the increased density of hydroxyl groups anchored VO_x on the surface even with only one cycle of deposition Previously (see Section 4.2) it was proved that adsorbed NH_3 is the active species while NO_x is partially active or passive for the NH_3-SCR reaction.
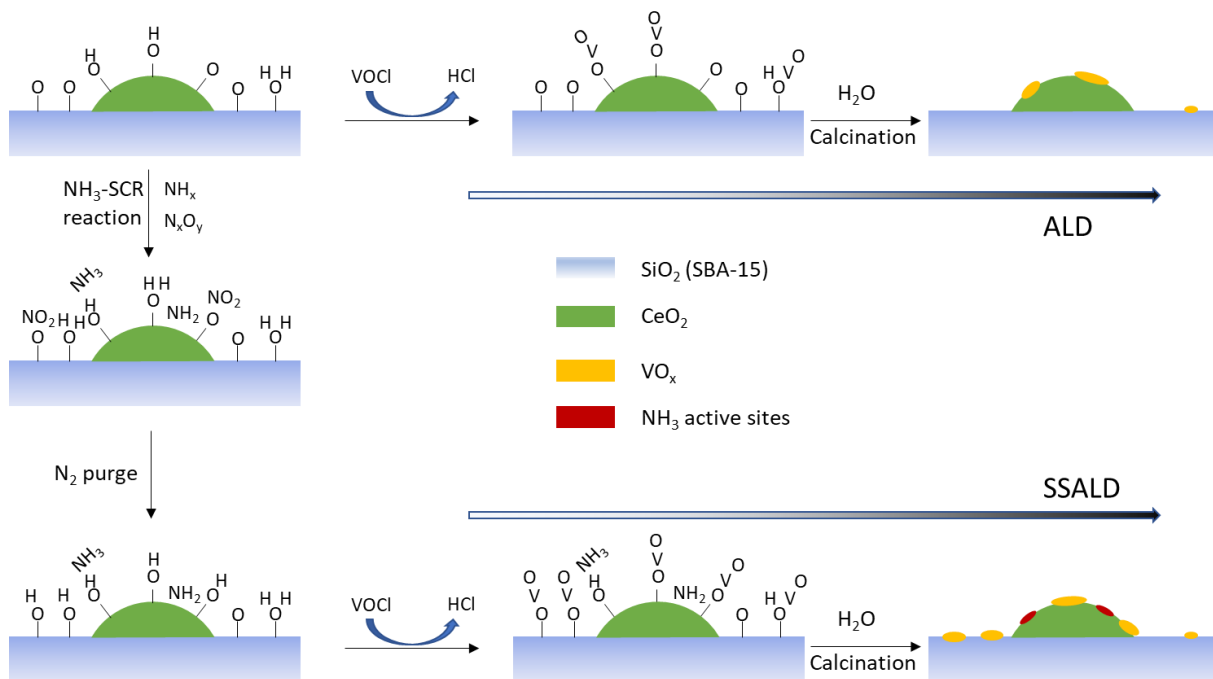
Scheme 9. Schematic diagram illustrating the processes of ALD and SSALD for the deposition of one cycle of VO$_x$ on an CeO$_2$/SBA-15 catalyst.

6.3.4. Conclusion

In this section, a novel synthesis method, referred to as site selective atomic layer deposition (SSALD), is proposed and demonstrated in the context of the NH$_3$-SCR reaction by coating one layer of VO$_x$ on CeO$_2$/SBA-15 by common ALD and by SSALD. The SSALD technique involves the pre-treatment in the target reaction mixture (here: NH$_3$-SCR) and common ALD steps. The results show that the sample prepared by SSALD exhibits the best catalytic performance. Characterizations by DRIFT spectroscopy reveal that during the pre-treatment NH$_x$ and N$_x$O$_y$ species are formed. The NH$_x$ species is inert to react with the VOCl$_3$ precursor and keep its acid sites. And the N$_x$O$_y$ species is desorbed during N$_2$ purge, leading to the formation of active oxygen sites to degrade the free water as -OH groups, which is beneficial for anchoring more active vanadia on the surface. The higher density of active vanadia sites and the reserved NH$_x$ activated sites are proposed to contribute to the improvement in NH$_3$-SCR performance.

7. Correlation between catalytic synthesis and catalytic reaction

7.1. Hypothesis of the catalytically induced growth (CIG)

In the sections above, two types of synthesis routes for ceria-based oxides supported on SBA-15 were discussed and *in situ* characterizations were applied to monitor the catalysts during preparation and NH_3-SCR reaction.

For the solid-state impregnation (SSI) method, one important conclusion was that the synthesis process involves a catalytic reaction, in which cerium species act as a catalyst. It was shown that different synthesis reaction routes can be designed to result in a distinct structure of the final prepared catalysts, which further led to difference in the NH_3-SCR performance (target reaction). On the other hand, when using the ALD method, the pre-treatment of the substrate led to the formation different surface groups which reacted with active precursors. Controlling the pre-treatment allows to obtain various groups to react or not react with the precursor molecule and to achieve site selective deposition of active species, which also influences the performance of the target reaction.

Thus, it can be concluded that the synthesis reaction has a great effect on the target reaction (NH_3-SCR). Considering that both the synthesis reaction and the target reaction include catalytic reactions with the same catalytic species (e.g. Ce^{3+}/Ce^{4+}), especially regarding the redox reaction, it is reasonable to explore the correlation between these two reactions.

Furthermore, considering a coupling effect between these two reactions, one may design the synthesis reaction by including the target reaction. For example, by the SSI method, cerium nitrate is calcined by heating from 25 to 500 ^{o}C in air. the cerium nitrate gradually disappears and ceria forms with Ce^{3+} being oxidized to Ce^{4+}. This process involves the nucleation and growth of CeO_2 accompanied by the oxidation reaction to obtain CeO_{2-x} with a relatively low x value. It was reported that using reduced gas (NH_3) as calcination atmosphere, the prepared CeO_{2-x} owns more oxygen vacancies with a relatively high x value, showing a higher NH_3-SCR reaction performance.[62] It gives rise to the question of how much oxygen vacancies are optimal and how to obtain such an optimized (defect) structure to achieve the highest $DeNO_x$ ability. Herein, the hypothesis is proposed that when using the same atmosphere for calcination as that of the target catalytic reaction ($NH_3/NO/O_2$) the ceria growth will be controlled by the redox properties that apply to the NH_3-SCR reaction. Therefore, the final prepared ceria could be expected to exhibit the same surface state (e.g. regarding oxygen vacancies) as the NH_3-SCR reacted ceria, as shown in Scheme 10.
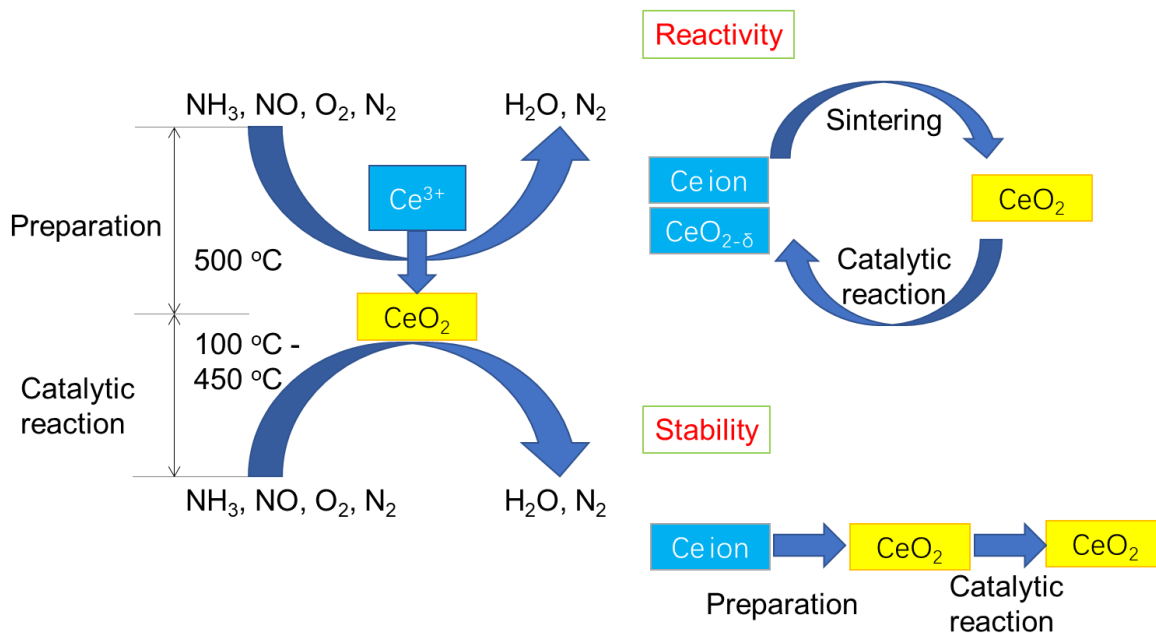
Scheme 10. Schematic diagram illustrating the use of the target reaction gas feed (500 ppm NH_3, 500 ppm NO, 5 vol.% O_2 balanced with N_2) as the calcination atmosphere during the synthesis of the ceria catalyst by the SSI method.

According to the outlined hypothesis, improvements in reactivity and stability for the prepared samples may be expected. Firstly, the CeO_{2-x} forms with low x values as a result of the composition of cerium nitrate and the oxidation from Ce^{3+} to Ce^{4+}. Conversely, the formed CeO_{2-x} acts as a catalyst for the $NH_3/NO/O_2$ gas mixture and x changes based on the redox cycle of the NH_3-SCR-like reaction. When the reaction reaches its equilibrium state, the prepared ceria (CeO_{2-x}) may adopt a stable structure with an x value equal to the optimized number of surface oxygen vacancies for best NH_3-SCR performance. Furthermore, due to the same reaction gases between the preparation process and target catalytic reaction process, there is no structural change from the preparation to the catalytic application, especially when the temperature of the preparation is higher than that of the target reaction, implying the potential of increased stability.

7.2. Experimental results

Figure 62 shows the catalytic performance for the NH_3-SCR reaction using differently prepared CeO_2/SBA-15 catalysts. In detail, cerium nitrate and SBA-15 were mixed in solid state and then calcined in a furnace in different gas atmospheres. The calcination conditions were set as 500 °C for 5 h with a heating rate of 1.5 °C/min. The results in Figure 62(a) show that the sample calcined in NH_3-SCR experimental gas (500 ppm NH_3+500 ppm NO+5% O_2, expgas) exhibits a significant improvement in both NO conversion and N_2 selectivity compared with the sample calcined in simulated air (N_2+20%

O_2). It has been reported that CeO_2 calcined in NH_3, CO, and H_2 shows an enhanced catalytic performance for NH_3-SCR.[28, 29, 125] To this end, Figure 62(b) compares results for samples calcined in NH_3-SCR experimental gas with those obtained for oxidizing and reducing gas atmospheres. The sample calcined in expgas still shows a better NO conversion than in case of the reducing NH_3 and oxidizing $NO+O_2$ gas atmospheres, but the N_2 selectivity of the sample calcined in expgas in is slightly lower.
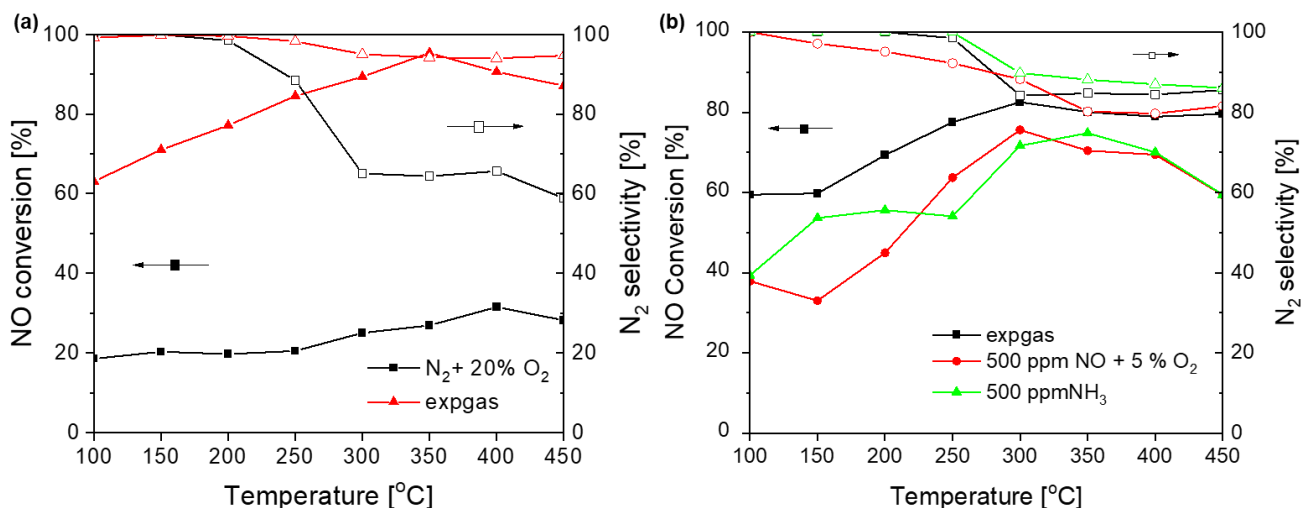
Figure 62. Catalytic performance in NH_3-SCR using CeO_2/SBA-15 samples prepared in different calcination atmospheres (500 °C for 5 h; heating rate: 1.5 °C/min). (a) N_2+O_2 and NH_3-SCR experimental gas, (b) NH_3-SCR experimental gas (expgas), 500 ppm NO + 5% O_2, and 500 ppm NH_3 gas.

Figure 63 depicts the exhaust gases monitored during calcination of the raw sample of tfSBA-CeO_2 in N_2 + 20% O_2 (air) and the NH_3-SCR experimental gas (expgas). The spectra show the decomposition of nitrate salt. Compared with the calcination in air, the decomposition in expgas is characterized by broad NO_2 emission windows at 175-275 °C, attributed to the interaction between the nitrate salt and expgas. Especially NO gas (at 1909 cm^{-1}) is detected and then disappeared starting at 175 °C indicates that the original NO in the expgas is transformed accompanying the decomposition process. Interestingly, in air the release of NO_2 shows the common behavior (see Figure 63(a)) as the NO_2 emission reaches its highest value and then gradually declines at higher temperatures up to about 400 °C , while for the calcination in expgas (see Figure 63(b)), the NO_2 feature disappears after 305 °C but reappears again at about 400 °C, which might be attributed to the oxidation of the expgas (NO or NH_3).
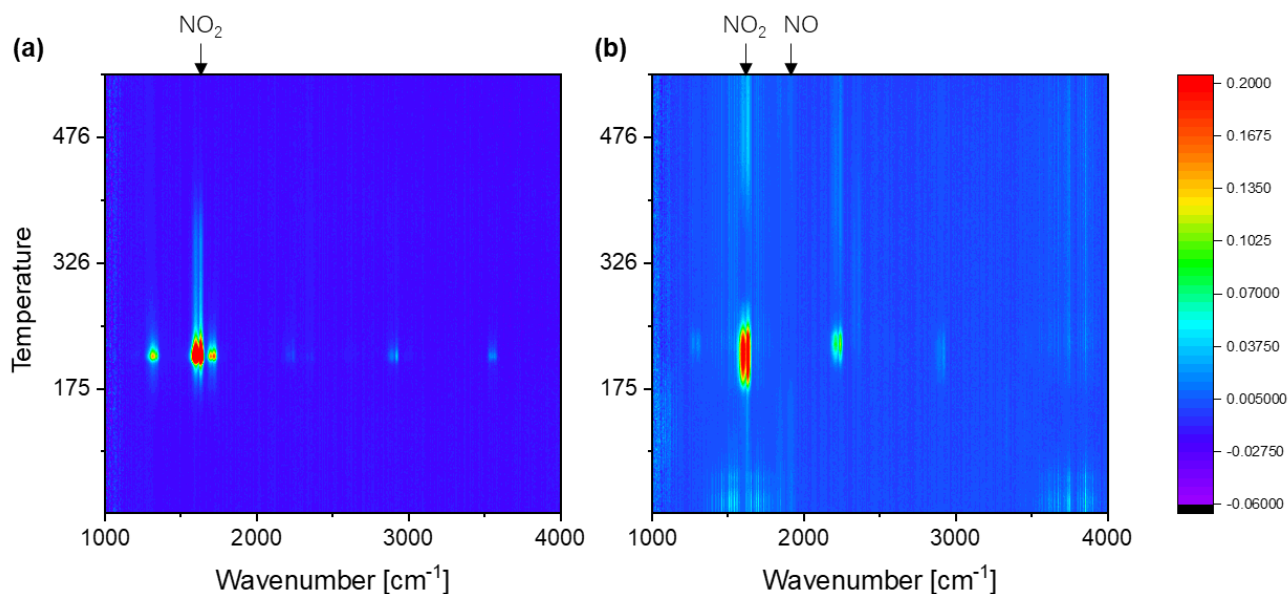
Figure 63. *In situ* FTIR monitoring of the exhaust gases during the calcination of tfSBA-CeO$_2$ at 500 °C for 5h (heating rate: 1.5 °C/min) in (a) N$_2$ + 20% O$_2$ and (b) expgas

Figure 64 depicts *in situ* DR UV-Vis spectra recorded during calcination of raw tfSBA-CeO$_2$ in different gas atmospheres. As discussed above (see section 4.1), the features at 220, 260 and 310 nm of the original samples are attributed to a 4f^1-5d^1 electronic transfer of Ce^{3+}, a charge transfer (CT) of O^{2-} 2p to Ce^{3+} 4f/5d, and a CT of Ce^{3+} 5d to O^{2-} 2p, respectively. With increasing temperature, calcination in air (Figure 64(a)) and NO+O$_2$ (Figure 64(b)) leads to the appearance of a broad band at 320 nm, which is assigned to the charge transfer between O 2p to Ce 4f of ceria, indicating the formation of ceria. It is found that the formation rate of ceria for calcination in NO+O$_2$ is quicker than that in N$_2$+O$_2$, suggesting a catalytic reaction between the gas and cerium nitrate even at low temperature. The intensity decreases of the band ranging from 300-500 nm with the temperature increase to 500 °C (red curve) results in an energy band decrease, originating from the growth of ceria crystals in the oxidative atmosphere. For calcination in NH$_3$+N$_2$ (Figure 64(c)), at low temperatures (<175 °C), the absorbance curves show only small changes, indicating a possible transformation from cerium nitrate to ceric ammonium nitrate. After reaching a temperature of 175 °C, the absorbance strongly increases, whereby the absorbance at 500-800 nm is assigned to d-f transitions of the Ce^{4+}/Ce^{3+} ion pair. The sample calcined in expgas (see Figure 64(d)) shows a similar behavior, but the absorbance changes more gradually at low temperature and the final absorbance level is lower than that for the NH$_3$-calcined sample. This is attributed to the combination of oxidation by NO+O$_2$ and reduction by NH$_3$.
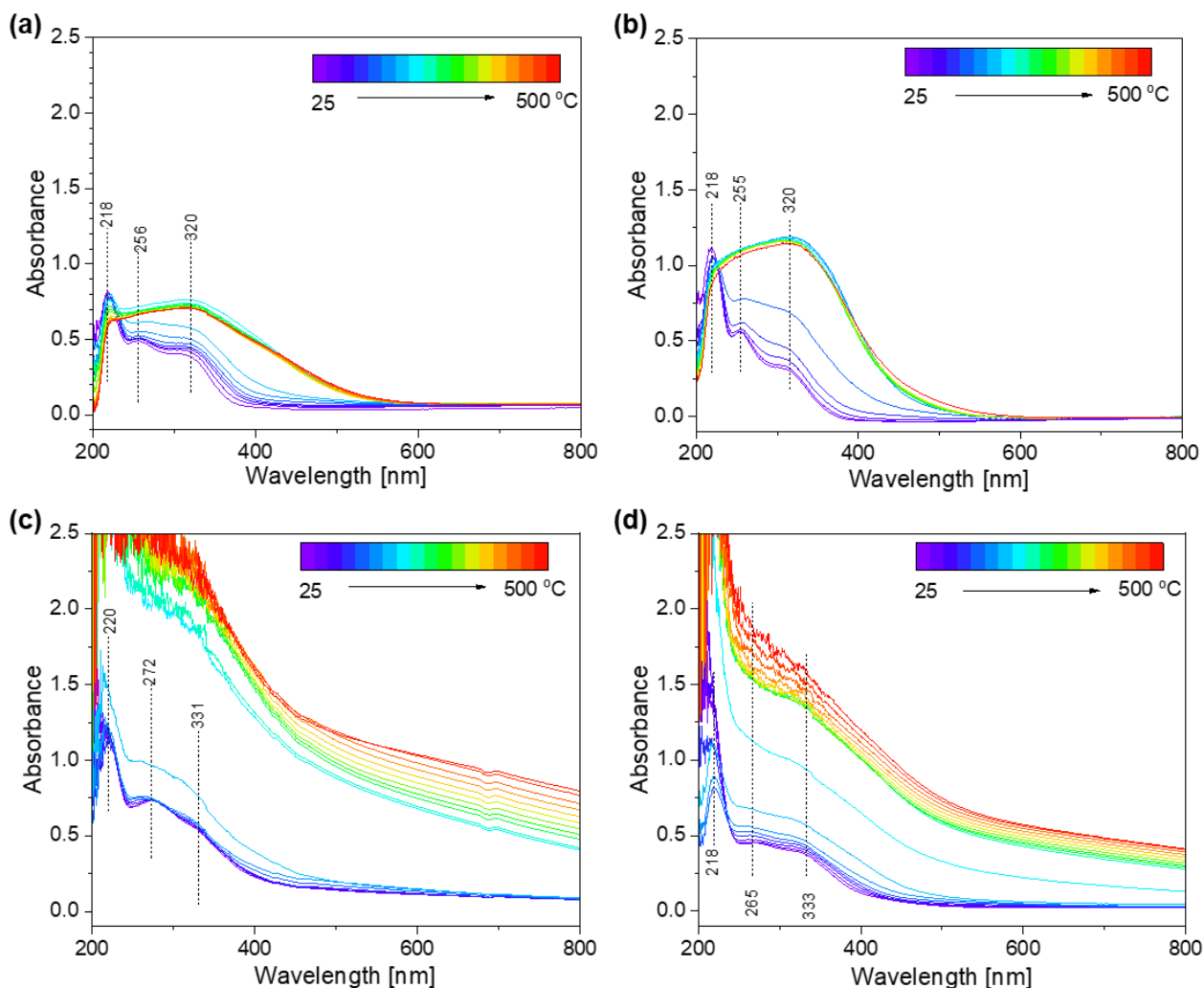
Figure 64. *In situ* DR UV-Vis spectra recorded during the calcination of tfSBA-CeO$_2$ from 25 to 500 °C (heating rate: 1.5 °C/min) in (a) N$_2$+20 % O$_2$, (b) 500 ppm NO + 5% O$_2$ + N$_2$ bal. (c) 500 ppm NH$_3$ + N$_2$ bal. (d) expgas.

Figure 65 shows *in situ* Raman spectra recorded during the calcination of raw tfSBA-CeO$_2$ in air and expgas. For the calcination in air (see Figure 65(a)), with increasing temperature, the intensity of the nitrate-related peaks (1038 and 739 cm^{-1}) decreases and above 200 °C a peak at 450 cm^{-1} appears. In contrast, for the sample calcined in expgas (see Figure 65(b)), the characteristic peak for CeO$_2$ (452 cm^{-1}) appears at relatively low temperature of about 100 °C and disappears after reaching a temperature of 250 °C. This behavior indicates that the expgas can interact with the cerium nitrate to catalytically assist the growth of ceria crystals.
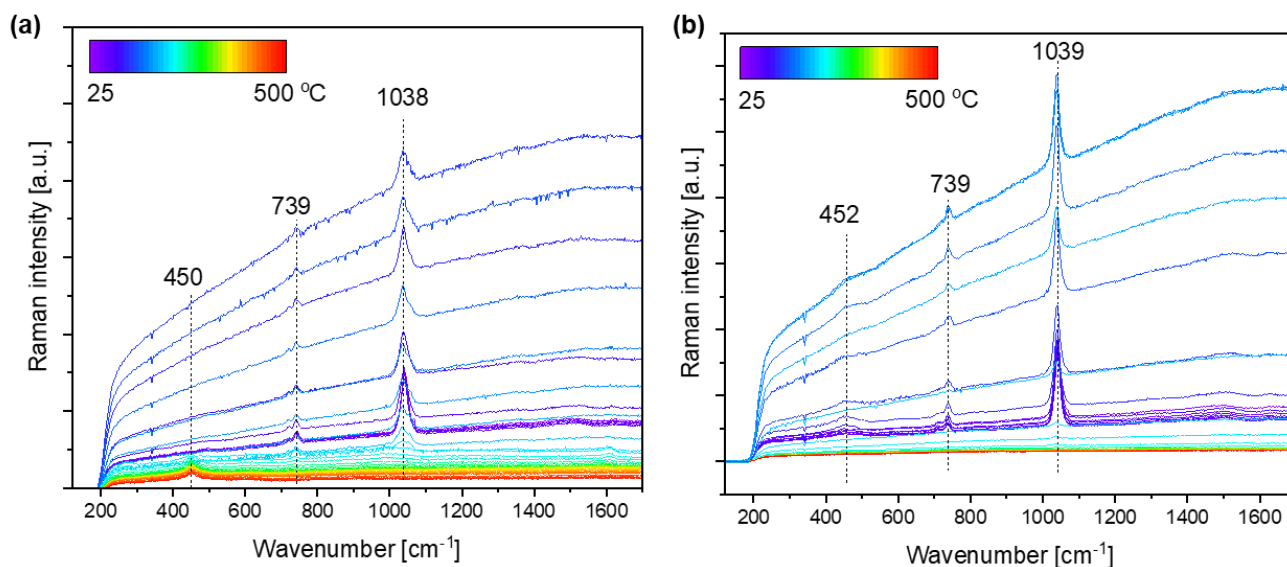
Figure 65. *In situ* Raman spectra (514.5 nm) recorded during calcination of raw tfSBA-CeO$_2$ from 25 to 500 °C (heating rate: 1.5 °C/min).(a) N$_2$ + 20% O$_2$, and (b) expgas.

7.3. Summary

In this part it is demonstrated that the calcination atmosphere influences the catalytic performance. The is illustrated for CeO$_2$/SBA-15 for which an optimized catalytic reactivity for NH$_3$-SCR reaction was found by calcination in the experimental reaction gas mixture (expgas). The preliminary exploration of the calcination process by *in situ* spectroscopy reveals that the cerium decomposition is correlated to the calcination atmosphere and that cerium (III) nitrate acts as a redox catalyst which reversely affects the growth of the ceria particles. Especially, in the NH$_3$-SCR experimental gas, the ceria is assembled accompany with catalyzing the NH$_3$+NO+O$_2$ to produce N$_2$+H$_2$O.

While previous works reported that pretreatment of ceria in NH$_3$, H$_2$, and CO can lead to improved NH$_3$-SCR performance by improving the ceria acidity and redox ability, the interesting finding here is not to achieve improved NH$_3$-SCR performance by gas pretreatment, but to confirm that the treatment with expgas enables an optimal improvement among the various gas atmospheres. Considering the discussion of effect of oxygen vacancy of ceria on the NH$_3$-SCR reaction, and the experimental fact that reductive NH$_3$ and oxidative NO+O$_2$ can improve the NH$_3$-SCR reaction reactivity, it is suggested that the catalytic performance of ceria changes with the number of oxygen vacancies following a "volcano" curve, and that the expgas calcined ceria contains a moderate number of oxygen vacancies needed for optimal reactivity. To confirm this hypothesis, further investigations will be needed.

8. Summary and Outlook

In this work, ceria-based oxides supported on SBA-15 were prepared by solid-state impregnation (SSI) and atomic layer deposition (ALD) methods and applied to the NH_3-SCR reaction of NO. Ex/*in situ* characterizations were performed to explore the mechanisms of both the synthesis and the target catalytic reactions.

In chapters 1-3, the practical and scientific background for this thesis is introduced, including the NH_3-SCR reaction and its mechanism, CeO_2 based catalysts, and mesoporous materials. Besides, the experimental approaches and setups are described, including preparation methods, characterization techniques, and catalytic tests.

In chapter 4, SBA-15 supported ceria (CeO_2/SBA-15) catalysts are addressed. First of all, in order to overcome the low active site exposure of crystalline ceria, mesoporous silica SBA-15 was employed as support material providing a high surface area and stable surface to disperse the nano CeO_2. For catalyst synthesis, the solid-state impregnation (SSI) method was applied due to its environmental friendliness and convenient operation as a solvent-free system. The use of as-made SBA-15 (without removing the template P123 by calcination) to prepare CeO_2/SBA-15 results in a good ceria dispersion and catalytic performance.

To clarify the role of the template (P123) the synthesis mechanism of CeO_2/SBA-15 based on template-free and as-made SBA-15 was studied using TGA and *in situ* Raman, DRIFT, and DR UV-Vis spectroscopies accompanied by gas-phase FTIR analysis, as well as *ex situ* XRD, XPS, and BET measurements. The combined findings from the characterization allow to elucidate the synthesis mechanism and reveal that the good dispersion of as-made SBA-15 supported ceria originates from template P123 playing a physical role by confining the growth of ceria and a chemical role by catalytically reducing ceria.

The prepared CeO_2/SBA-15 catalyst was applied to the NH_3-SCR reaction and further studied to explore the NH_3-SCR reaction mechanism using *in situ* DRIFT spectroscopy. Based on the IR spectra NH_2 and NO- are identified as active species for NH_3 and NO adsorption, respectively., providing evidence for the comproportionation between NH_3 (-3) and NO (+2) to NH_2 (-2) and NO^- (+1), and finally to the product N_2 (0). In addition, distinguishing the vibrational features within 2000-3000 cm^{-1} allowed to understand the nitrogen triple bond related signature at about 2100-2200 cm^{-1}, which was attributed to the over-oxidation of NH_3 and further the generation of N_2O.

In chapter 5, ceria-based bimetallic oxides catalysts supported on SBA-15 were addressed, due to the poor NH_3-SCR reactivity of bare cerium oxide. The secondary metal element was added to form a MO_x-CeO_2 couple, which was expected to improve the catalytic performance. Firstly, several oxides (Cu, Mn, Ni, Mg, and La) were explored towards synergistic effects with ceria. The catalytic test results showed that various valent metals (Cu, Mn, and Ni) coupled with CeO_2 enhanced the catalytic performance in NH_3-SCR compared with a CeO_2 reference sample, while permanent valent metals (Mg and La) coupled with CeO_2 showed a reduced catalytic reactivity. On the one hand, based on this screening, CuO-CeO_2 and MnO_x-CeO_2 catalysts supported on SBA-15 were chosen for further exploration because of their high reactivity. On the other hand, the bimetallic oxides with various valent or permanent valent secondary metal element coupled with ceria showed a distinct reactivity behavior, indicating that redox properties rather than the acidity should contribute to the whole NH_3-SCR reaction process.

Secondly, the CuO-CeO_2 catalyst was explored due to its wide application in various catalytic systems. Although the same SSI method was used to load the ceria and copper oxide onto SBA-15, the synthesis process and the final structure of the prepared samples differed from that of CeO_2/SBA-15 because it involved not only the dispersion of each oxide but also the relative distribution of them. Therefore, the synthesis process of CuO-CeO_2/SBA-15 was monitored again with *in situ* characterizations including Raman, DRIFT, and DR UV-Vis spectroscopy. The template-free SBA-15 and as-made SBA-15 were employed as support precursors leading to two different synthesis routes, the solid thermal decomposition for the template-free SBA-15 prepared sample and a hydrothermal process for the as-made SBA-15 prepared sample. The former route yielded a mixed CuO-CeO_2 phase with strong redox ability, leading to a low optimal temperature window but limited N_2 selectivity, while the latter route led to the formation of separated CuO and CeO_2 phases with moderate redox properties, resulting in a broad and high temperature working window. The above approach showed that catalyst synthesis, catalyst structure, catalyst properties, and catalytic performance are related to each other. To further confirm the generality of the findings, MnO_x-CeO_2 supported on SBA-15 was prepared and *in situ* characterization was employed for mechanistic insight, covering the whole process from the synthesis process to the application in the NH_3-SCR reaction.

In chapter 6, atomic layer deposition (ALD) was adopted to prepare ceria-based mesoporous catalysts. Firstly, by using SBA-15 as a support material to provide a high surface area, VO_x/TiO_2/SBA-15 catalysts were prepared by ALD to explore the feasibility of using mesoporous powder materials as a deposition substrate. The results show that the prepared samples possess a high surface area as expected and the surface-loaded VO_x could be quantitatively controlled by the ALD cycles. The results reveal the

presence of dispersed surface VO_x species on amorphous TiO_2 domains on SBA-15, forming hybrid Si-O-V and Ti-O-V linkages. The high NO_x conversion is attributed to the presence of highly dispersed VO_x species and the moderate acidity of VO_x supported on TiO_2/SBA-15.

Secondly, SiO_2/CeO_2/SBA-15 catalysts were prepared using ALD, by systematically varying the number of SiO_2 layers deposited on CeO_2/SBA-15 to explore the activity of Ce-O-Si species, considering that SiO_2 is an inert support. Due to the sandwich structure of SiO_2/CeO_2/SiO_2 and the controllable amount of Ce-O-Si by ALD, the Ce-O-Si species can be identified as the active site for NH_3-SCR reaction, and the NO_x conversion was found to be proportional to the amount of deposited SiO_2 until full coverage. In addition, experiments exploring the effect of sulfur on the catalytic properties revealed that the presence of SiO_2 coatings provided a better SO_2 resistance than bare CeO_2.

VO_x/CeO_2/SBA-15 was prepared by atomic layer depositing VO_x on CeO_2/SBA-15, which includes the anchoring of VO_x onto CeO_2/SBA-15 by reaction of the $VOCl_3$ precursor with surface hydroxyl groups. Aiming at new strategies towards an improvement of the catalytic properties, the substrate CeO_2/SBA-15 was treated in the NH_3-SCR atmosphere to produce the "target reaction" related surface and then deposited with VO_x. This new deposition route was introduced as "site selective atomic layer deposition (SSALD)". The catalytic results reveal that the sample prepared by the SSALD method shows a better NH_3-SCR performance. Based on DRIFTS results, changes in the surface properties are observed during calcination in NH_3-SCR atmosphere. The pretreated substrate contains adsorbed NH_x species which are inert towards $VOCl_3$ and remain the active acid sites. On the other hand, more -OH groups form on the surface to anchor more active VO_x species. Thus, the SSALD prepared VO_x/CeO_2/SBA-15 represents an optimized surface structure for the target NH_3-SCR reaction.

In chapter 7, the use of the target catalytic reaction to prepare improved ceria-based catalysts is put forward as a hypothesis, based on the correlation between the synthesis reaction and the target catalytic reaction (NH_3-SCR). During the research on the synthesis process by *in situ* characterizations, the synthesis reaction (e.g. the schemes 6 and 7 in section 5.2) is shown to be an important factor, determining the structure of the prepared catalyst, which further results in a distinct catalytic performance. To test this hypothesis, CeO_2/SBA-15 samples were prepared by the SSI method in different gas atmospheres, from reductive NH_3 to oxidative O_2. Most importantly, the expgas for NH_3-SCR reaction (NH_3+NO+O_2 balanced with N_2) was also included. The result proves that the expgas calcined sample owns the best catalytic performance in the NH_3-SCR reaction.

The above studies cover the complete chemistry catalytic triangle (CCT), including the catalyst synthesis (SSI/ALD, with or without P123), catalyst structures (dispersion, distribution, surface species), catalyst properties (redox, acidity), and catalytic performance (NO_x conversion and N_2 selectivity), as

elucidated mainly by *in situ* Raman, DRIFT, and DR UV-Vis spectroscopy as core characterization techniques. Despite the major progress made in this thesis there is still more work necessary to further improve the catalytic reactivity of the present system, and more importantly, to increase the understanding of the catalysts` mode of operation and the correlation between the synthesis and the target catalytic reaction. To this end, the following aspects may be addressed:

(i) For the synthesis of ceria-based oxides on mesoporous SBA-15, *in situ* spectroscopy was applied to understand the reaction during the calcination step of the SSI method. The use of *in situ* DR UV-Vis and Raman spectroscopy provided information about the solid surface and/or sub-surface, *in situ* DRIFT spectroscopy provided information about the adsorbed species, and *in situ* FTIR of the exhaust gas provided information about the gas-phase composition. By combining these spectroscopies, a comprehensive understanding of the chemical reaction was obtained, especially regarding the catalytic effect of the key metal elements during the calcination. However, there is still a gap in understanding the relation between the reaction processes and the finally prepared structures. To this end, for example, *in situ* XRD may be useful to obtain crystal type information and *in situ* TEM may enable monitoring the crystal's growth on a nanometer scale.

(ii) The solid-state impregnation (SSI) method was extensively explored in this thesis, also because of its feasibility for *in situ* characterization. As a main step it involves the decomposition reaction of metal precursors to form active metal oxides. Although the majority of synthesis methods involved a calcination step to obtain stable catalysts, the final structure of the prepared samples is not completely determined in this step. The hydrothermal method has previously been applied to the preparation of metal oxide catalysts for the NH_3-SCR reaction. In particular, it was reported that different conditions in the hydrothermal process of ceria synthesis results in different crystal structures with different catalytic performance.[278] To this end, it would be interesting to apply *in situ* characterization to hydrothermal processes to reveal the effect of condensation reaction on the crystallization.

(iii) ALD was proved to be a promising technique for designing novel catalysts. Several techniques have been developed to achieve an *in situ* monitoring of the ALD process, including mass spectroscopy, spectroscopic ellipsometry, IR spectroscopy, and quartz crystal microbalance. These techniques all require special modifications of the ALD reactor to be applied. Here, a simple adaption was done to achieve the combination of the ALD technique with different kinds of characterizations, as shown in Figure 66. The spectrometer is connected to the ALD system directly. Due to the working principle of ALD, the reactor and the ALD chamber can be exposed to the same atmosphere under the assistance of a vacuum. Considering the small volume of the reactor as part of the spectrometer unit, a larger volume

(empty) bottle is connected to the reactor and during the N_2 purge or precursor pulse steps, there would be enough gas flowing over the sample into the reactor.
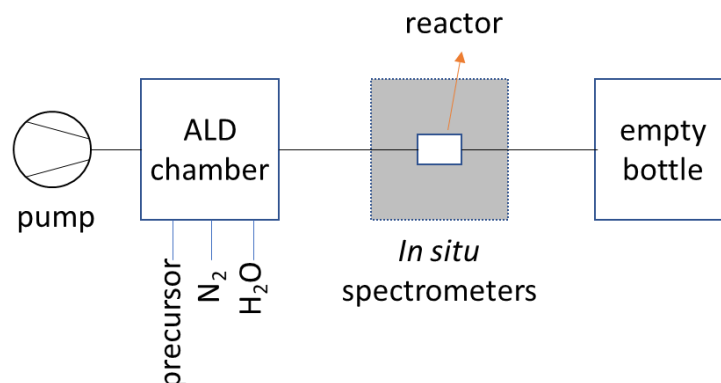

Figure 66. Schematic diagram of the *in situ* spectroscopy linked ALD system.

In this work, site-selective ALD (SSALD) was proposed, by which the substrate was modified by the target NH_3-SCR reaction and then covered by active VO_x species, achieving an enhanced catalytic performance. In Figure 67, the general ideas for the design of a novel catalyst by SSALD are introduced. For the original substrate, there exist three kinds of sites in terms of the target catalytic reaction: active sites such as Lewis site and Bronsted site, inert sites, i.e. sites that do not take part in the reaction, and passive sites, i.e. sites that do not participate directly in the direction. An example may be sites that are blocked by adsorbed species during the reaction. After the pre-treatment by the expgas, the surface species would be changed from original -OH to various species, such as NH_x and N_xO_y species with different structures, which may influence the reactivity. The ALD deposition process would allow depositing different oxides on the surface, such as active oxides like VO_x and TiO_2, or protective oxides like SiO_2 and Al_2O_3. And It is also necessary to consider that some -OH sites modified with stable species would be inert to the precursor and maintain their bare state. An ideal design would keep the active sites bare to retain their inherent activity, to deposit active oxides on the inert sites to increase the activity, and to deposit protective oxides on the passive sites to avoid a decline in performance. Such a design idea was verified in this thesis (see Section 6.3): the active NH_3 sites were inert towards coating and retained their activity for NH_3-SCR and the inactive N_xO_y sites were transformed into a higher concentration of -OH to deposit VO_x achieving improved reactivity. In addition, a protective coating was achieved by deposition of SiO_2 to avoid poisoning by SO_2 (see Section 6.2).
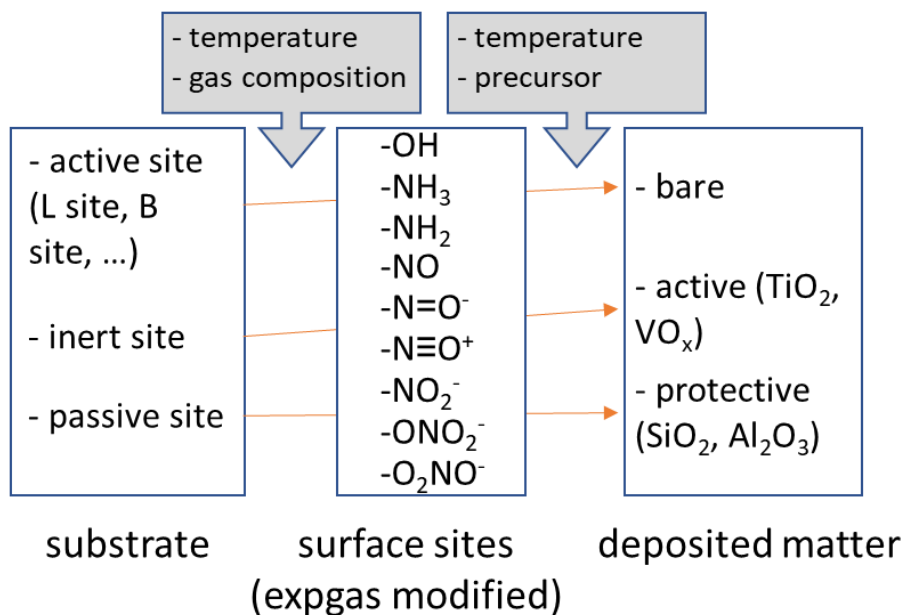
Figure 67. General ideas for the SSALD method to design novel catalysts.

The SSALD method is expected to be a powerful technique to design novel catalysts, as shown in Figure 67. The site selection is achieved in two stages: Firstly, during the surface modification stage. The temperature and the gas composition are adjusted to control the surface anchored species. Secondly, during the ALD deposition stage. The temperature and the precursor are adjusted to control the deposited sites of the metal oxides on the surface. Combining these two operations, site selection could be achieved. To confirm this concept, *in situ* characterization, especially by using *in situ* DRIFT spectroscopy iss crucial to monitor the changes in surface species which would guide the determination of the SSALD parameters.

(iv) The correlation between the synthesis reaction and the target catalytic reaction was emphasized in Section 7, and preliminary results confirm that the catalytically-induced grown (CIG) ceria shows the best catalytic performance. A hypothesis set forward is that the ceria is self-assembled with the assistance of the NH_3-SCR experimental gas and adopts an optimized structure and surface state for the target NH_3-SCR reaction. To this end, preliminary experiments have revealed that for the NH_3-SCR reaction on bare ceria redox properties are rate-determining, and that oxygen vacancies may be of importance. Thus, quantitatively testing the number of oxygen vacancies and determining the volcano shape relationship between oxygen vacancy concentration and the reactivity would be worth further exploration.

9. Appendix

9.1. Quantitative gas phase IR analysis

As noted above, the exhausted gas is detected by the gas phase IR spectrometer. Thus, it is necessary to establish the relationship between the IR signals with the gas compositions. Except for the inactive N_2 and O_2, the other expected gas components are all calibrated below.

NO gas is the object gas to be removed and a series of gas concentrations are adjusted as 5, 20, 50, 100, 200, 400, and 500 ppm by mixing the 2000 ppm NO gas source with pure N_2. The IR spectra are shown in Figure 68(a). For the intensity determination, intensity of single peak at 1909 cm^{-1} and an area ranged by at 1764-1978 cm^{-1} were both tried to establish a linear relationship with the NO concentration. It is found that using the single peak shows an equally good linearization as the area for the dry NO and is even better than the area mode for the NO with moisture, which is because of overlap with moisture peaks in this region. Thus, the peak intensity at 1909 cm^{-1} is chosen for the IR-based analysis of the NO gas. The calibration curve is shown in Figure 68(b)
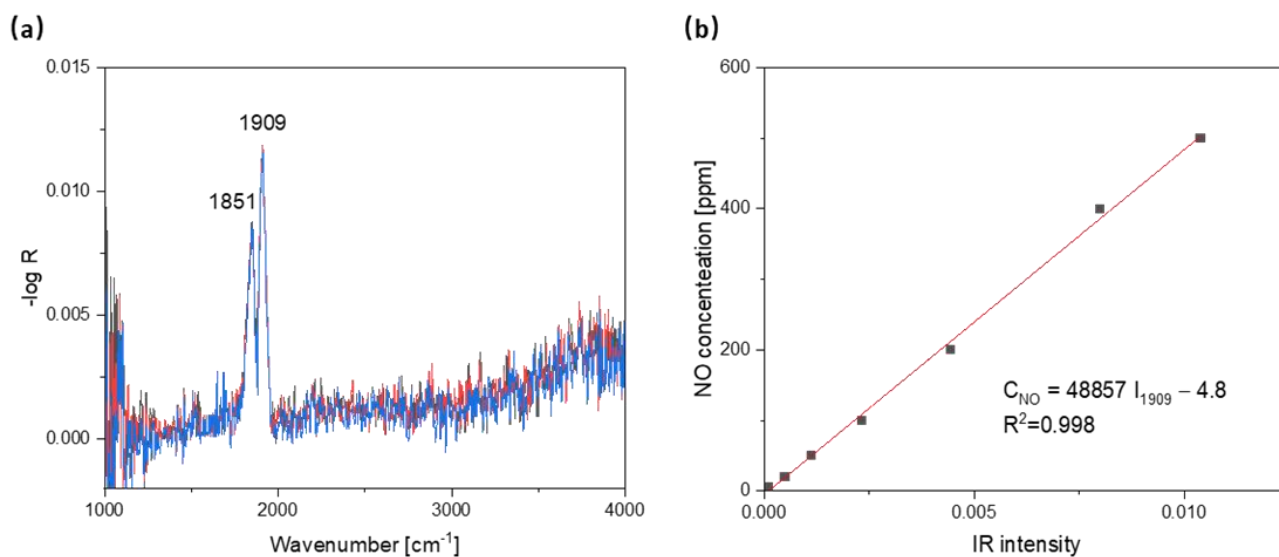

Figure 68. (a) IR spectra of 500 ppm NO balanced with N_2, (b) Calibration of NO concentrations based on the IR intensity at 1909 cm^{-1}.

For the reactant NH_3, the peak at 3334 cm^{-1} is chosen as there is no overlap with other gas signals unlike the other signal at about 1629 cm^{-1}. Similarly, a concentration series of NH_3 is prepared as 5, 10, 50, 100, 200, 400, and 500 ppm by mixing 2000 ppm NH_3/N_2 gas source with pure nitrogen. The IR spectra are shown in Figure 69(a). The linearization between the IR intensity at 3334 cm^{-1} and the concentrations of NH_3 are given in Figure 69(b).
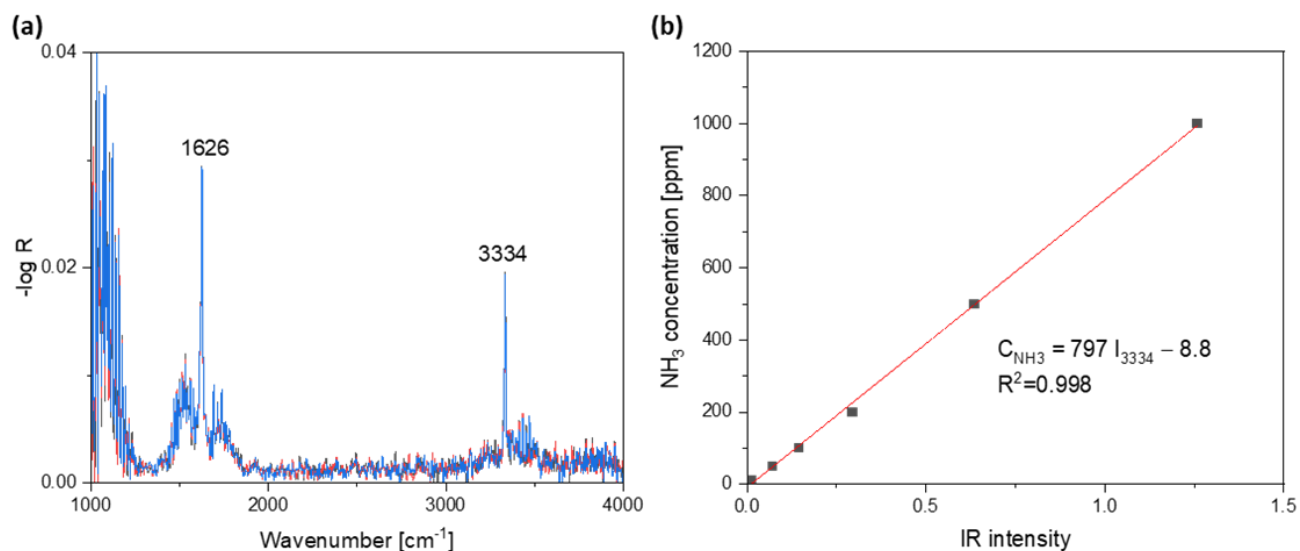
Figure 69. (a) IR spectra of 1000 ppm NH_3 balanced with N_2, (b) Calibration of NH_3 concentrations based on the IR intensity at 3334 cm^{-1}.

For the product gas N_2O, a concentration series is set as 20, 40, 100, 200, 300, and 400 ppm by mixing 2000 ppm N_2O/N_2 gas source with pure nitrogen and the IR spectra are shown in Figure 70(a). A typical IR signal for N_2O is located within the range of 2136-2280 cm^{-1} and the strongest peak at 2237 cm^{-1} is chosen to perform the linearization with the N_2O concentrations as shown in Figure 70(b).
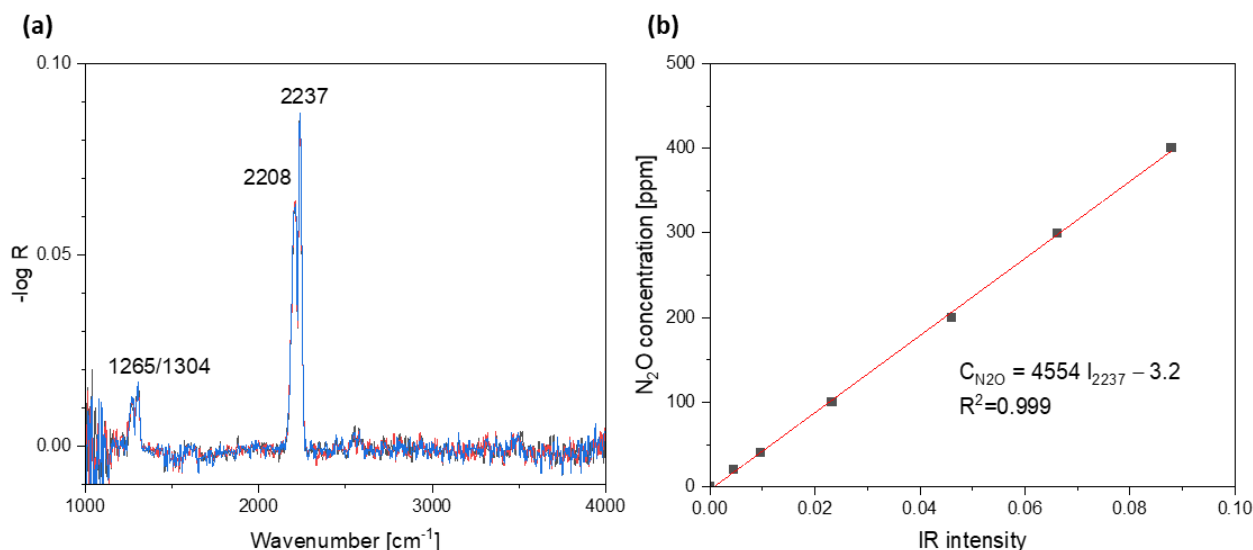

Figure 70. (a) IR spectra of 400 ppm N_2O balanced with N_2, (b) Calibration of N_2O concentrations based on the IR intensity at 2237 cm^{-1}.

NO$_2$ is an important outlet product during the catalytic reaction and directly affects the evaluation of the DeNO$_x$ efficiency. The calibration is done by using a combination of NO and O$_2$ at room temperature, that is, by using known concentrations of NO that are partially oxidized to NO$_2$. From the IR spectra results (Figure 71 (a)), it is confirmed that no other N$_x$O$_y$ products appear except for the NO and NO$_2$ components. and the decomposition of NO to N$_2$ at room temperature is negligible. Thus, the concentration of NO$_2$ can be calculated by subtracting the initial NO concentration by the residual NO concentration. Afterwards, the linearization between the IR signal of NO$_2$ at 1629 cm^{-1} and its concentration is established as shown in Figure 71(b).
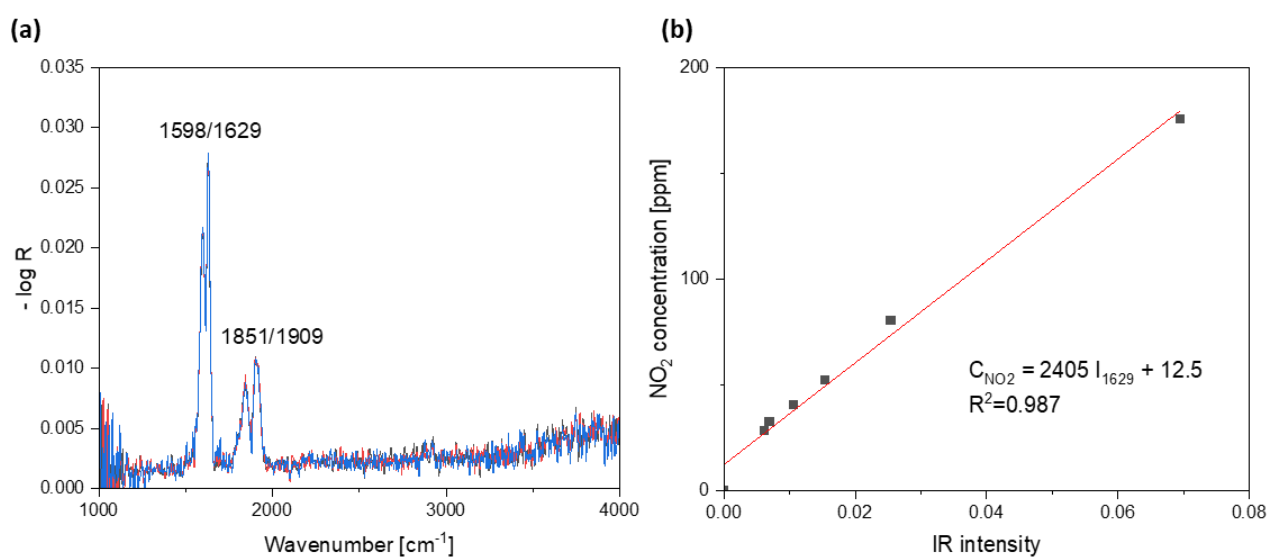

Figure 71. (a) IR spectra of 500 ppm NO$_2$, 5 vol. % O$_2$, balanced with N$_2$ at room temperature, (b) Calibration of NO$_2$ concentrations based on the IR intensity at 1629 cm^{-1}.

For SO$_2$ which is used to evaluate the sulfur effect, the IR spectra of different concentrations of SO$_2$ are shown in Figure 72(a). The strongest feature at 1375 cm^{-1} was chosen and the linearization between the IR intensity and the concentration is shown in Figure 72(b).
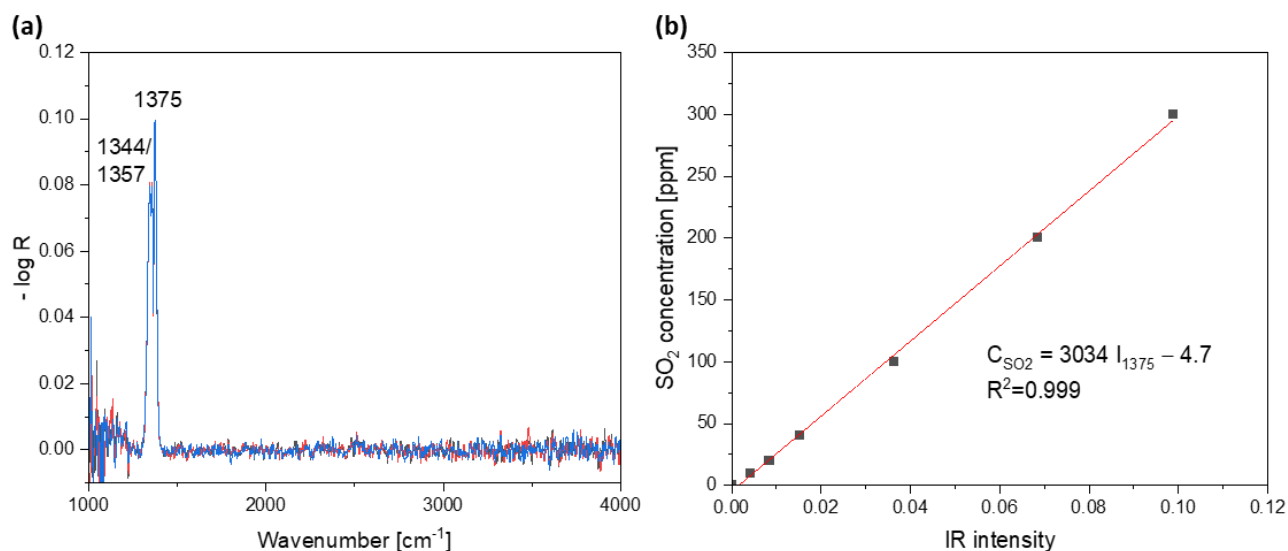
Figure 72. (a) IR spectra of 300 ppm SO_2 balanced with N_2, (b) Calibration of SO_2 concentrations based on the IR intensity at 1375 cm^{-1}.

9.2. Addition and monitoring of water vapor

The effect of water on the NH_3-SCR reaction is one of the key points to evaluate the practical catalytic performance of a certain catalyst. In present experiments, it involves two aspects: water addition to the inlet gas and water detection in the outlet exhaust gas.

Firstly, for the addition of water, the bubbling method was chosen to let the inlet N_2 gas carry the moisture, as shown in Figure 73. The outside water cycle provides a stable temperature atmosphere and the inside part is filled with deionized water. When the inlet N_2 enter the inside bottle through the porous ceramic, a large number of bubbles is produced carrying the vapor by reaching a water-vapor balance, rising up from the bottom and yielding the N_2+H_2O outlet gas.
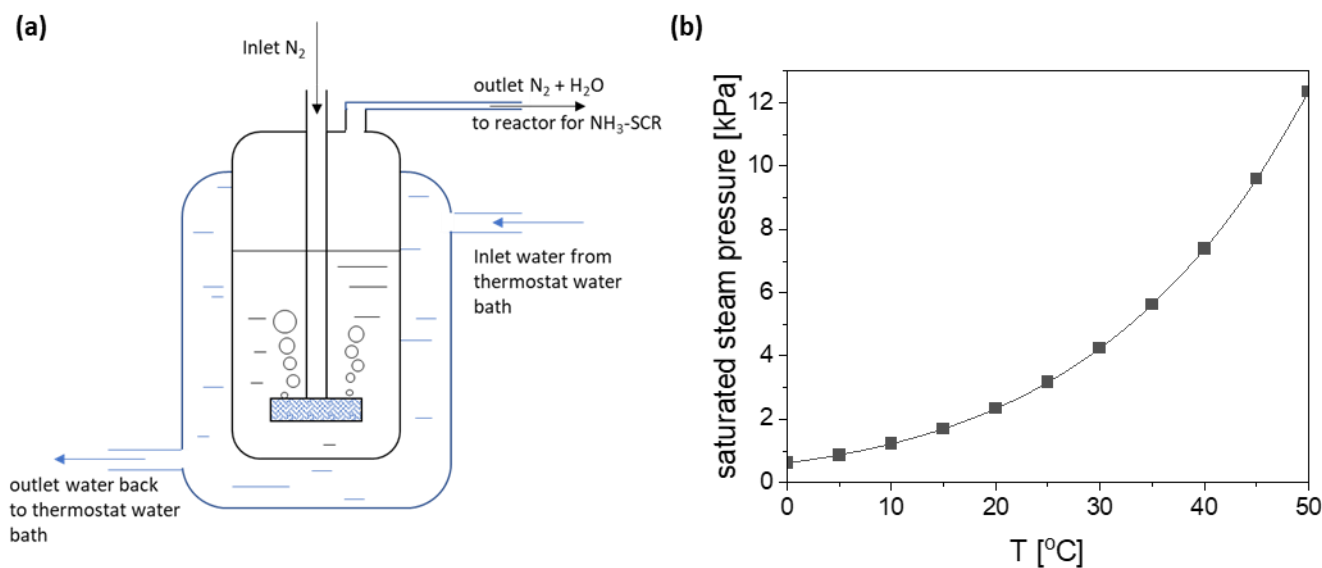
Figure 73. (a) Schematic of the bubbler used to produce the H_2ON_2 feed (b) the saturated vapor pressure at a range of 0-50 °C.

In order to quantify the amount of vapor content, two simplified conditions are included. (i) The inlet N_2 flow is treated as 1 atm pressure. Then the volume percentage of vapor can be simply expressed as the saturated pressure. The inlet N_2 may not be exactly 1 atm and varies depending on various factors. Thus, only if keeping the same treatment for all experiments, the vapor effect should be comparable. (ii) The second simplification is that the addition of water does not change the total gas flow rate (50 mL/min), although the calculated volume of the carried vapor was about 1 mL in all moisture involved experiments.

For the IR detection of the water vapor content, the intensity calibration is performed by using 50 mL/min N_2 to carry the water vapor at temperatures of 21, 25, 30, 35, 40, 45, and 50 °C. The IR spectra are shown in Figure 74(a). For the relationship between IR intensity of water and its content, it is found that a parabolic fitting provides a better description than a linear fit, as shown in Figure 74(b). Considering the overlap of different species (e.g. NH_3, NO, NO_2) in the 1000-2000 cm^{-1} range, the peak at 3676 cm^{-1} is chosen to do the calibration.
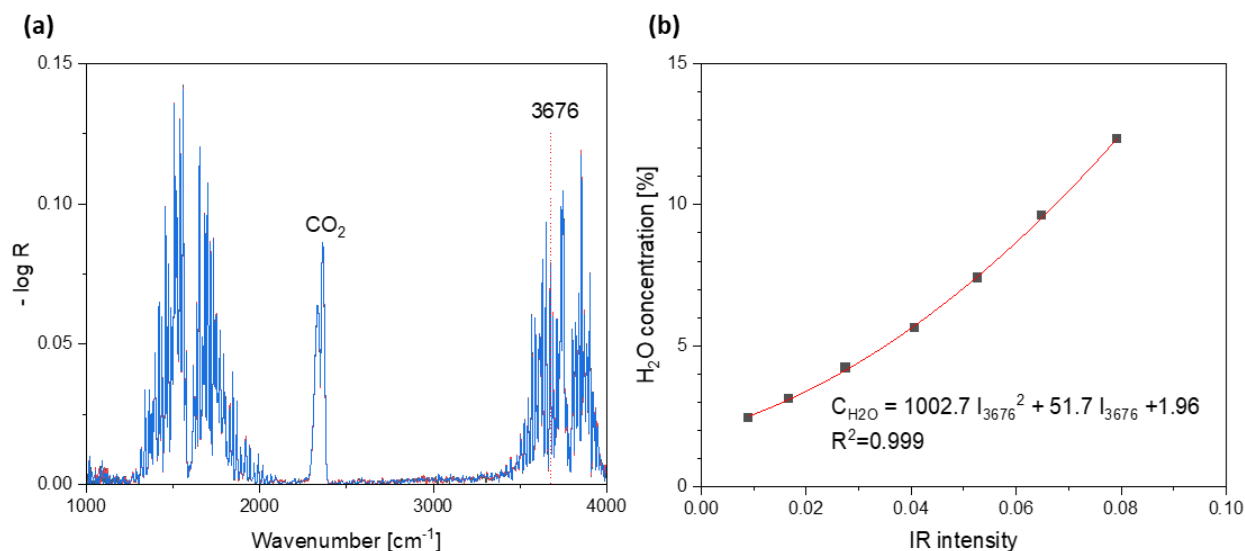
Figure 74. (a) IR spectra of H_2O from a H_2O/N_2 from vapor generation at 50 ºC, (b) Calibration of H_2O concentrations based on the IR intensity at 3676 cm^{-1}.

With the calibration of different gas, IR technique was used to monitor the exhausted gas and calculate the gas components. In detail, it involves several steps:

(i) Considering the baseline drift during the *in situ* monitoring, the blank baseline was necessary to be subtracted. The drift degrees in different wavenumber ranges are different. With time proceeding, the spectrum gradually changes from a horizontal shape to a sloped shape. Regarding the drift, two ranges at 2000-2100 cm^{-1} and 2900-3000 cm^{-1} are chosen as baseline corrections of signals within the range of 1000-2500 cm^{-1} (SO_2, NO, NO_2) and 2500-4000 cm^{-1} (NH_3, H_2O), respectively.

(ii) The concentrations of water and NH_3 can be calculated by the intensity at 3676 and 3334 cm^{-1}, respectively, after subtracting the baseline "2900-3000 cm^{-1}". Similarly, the concentrations of SO_2 and N_2O are calculated by the intensity at 1357 and 2237 cm^{-1}, respectively, after subtracting the baseline "2000-2100 cm^{-1}".

(iii) The NO_2 signal at 1629 cm^{-1} is overlapped with a NH_3 signal, thus, the contribution of NH_3 to the 1629 cm^{-1} intensity is calculated according to the known NH_3 concentration first; then the contribution of NO_2 and further the NO_2 concentration can be calculated.

(iv) For the calculation of the NO concentration, the contribution of water to the intensity at 1909 cm^{-1} needs to be considered.

(v) As N_2 is IR inactive, the concentration can be obtained based on the conservation of mass with respect to N.

tfSBA-L-CeO$_2$-air   asSBA-L-CeO$_2$-air   asSBA-L-CeO$_2$-N$_2$
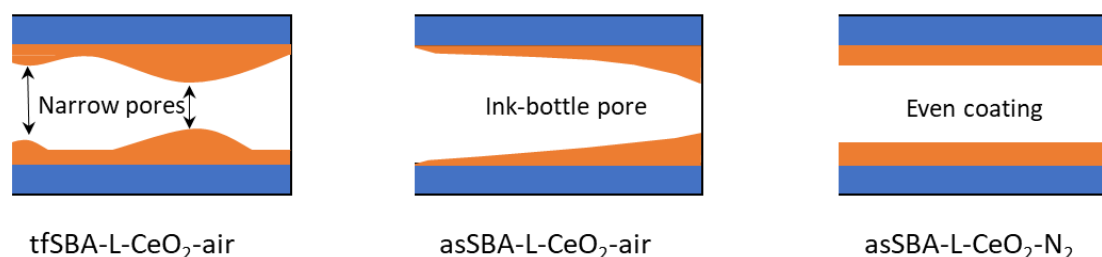
Figure S4-1. Schematic diagrams of pore shapes of the three tested samples.

(a)
(i) Water-acid azeotrope formation:

$$Ce(NO_3)_3 \cdot 6H_2O \rightarrow Ce(OH)_b(NO_3)_{3-b}(H_2O)_{6-b-c} + b\ HNO_3 + c\ H_2O$$

(ii) NO$_3^-$ thermal decomposition:

$$4\ Ce(NO_3)_3 \cdot 6H_2O \rightarrow 4\ Ce(OH)_3 + 12\ NO_x + (15-6x)\ O_2 + 18\ H_2O$$

(iii) Cerium hydroxide condensation:

$$Ce(OH)_4 \rightarrow CeO_2 + 2H_2O$$

(b)
(i) Dehydration:

$$Ce(NO_3)_3 \cdot 6H_2O \rightarrow Ce(NO_3)_3 + 6\ H_2O$$

(ii) Decomposition to CeO$_2$:

$$Ce(NO_3)_3 \rightarrow Ce(NO_3)_2 + NO_2 + \tfrac{1}{2} O_2$$

$$Ce(NO_3)_2 \rightarrow CeNO_3 + NO_2 + \tfrac{1}{2} O_2$$
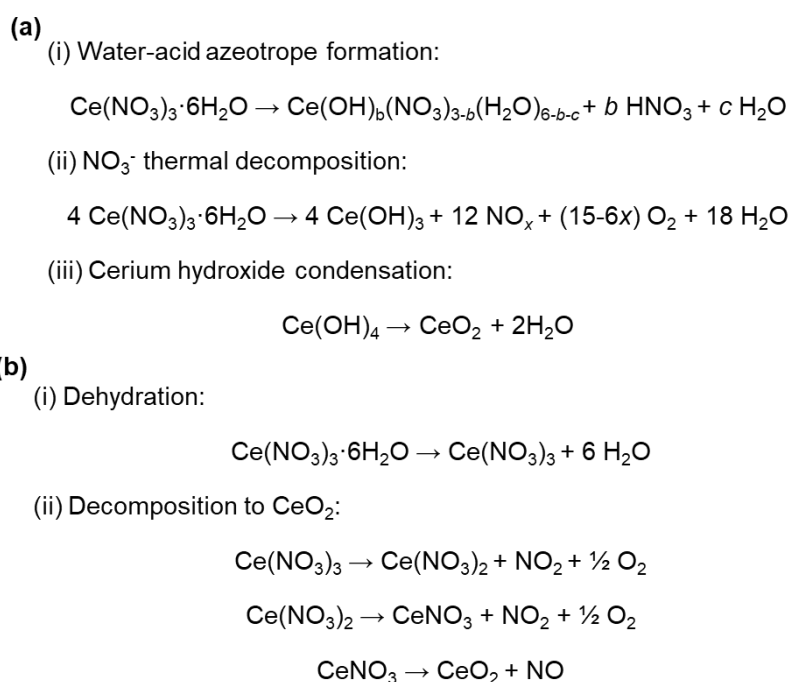
$$CeNO_3 \rightarrow CeO_2 + NO$$

Figure S4-2. According to Cochran et al.((a)),[100] the weight loss can be subdivided into three stages: (i) prior to decomposition, the salt melts and releases loosely bound water (<100 °C), or evaporates as aqueous acid azeotrope at a boiling point of about 120 °C; (ii) at higher temperature (>266 °C), residual nitrate thermally decomposes into NO$_x$ gas and forms a solid metal hydroxide product; (iii) the resulting cerium hydroxide condenses to form ceria. Kang et al. have proposed a more detailed mechanism for the decomposition of Ce(NO₃)₃ ((b)) according to which Ce(NO₃)₃ transforms first to Ce(NO₃)₂ at about 245 °C, then to Ce(NO₃) at about 270 °C, and finally to CeO₂ at about 295 °C.[101]
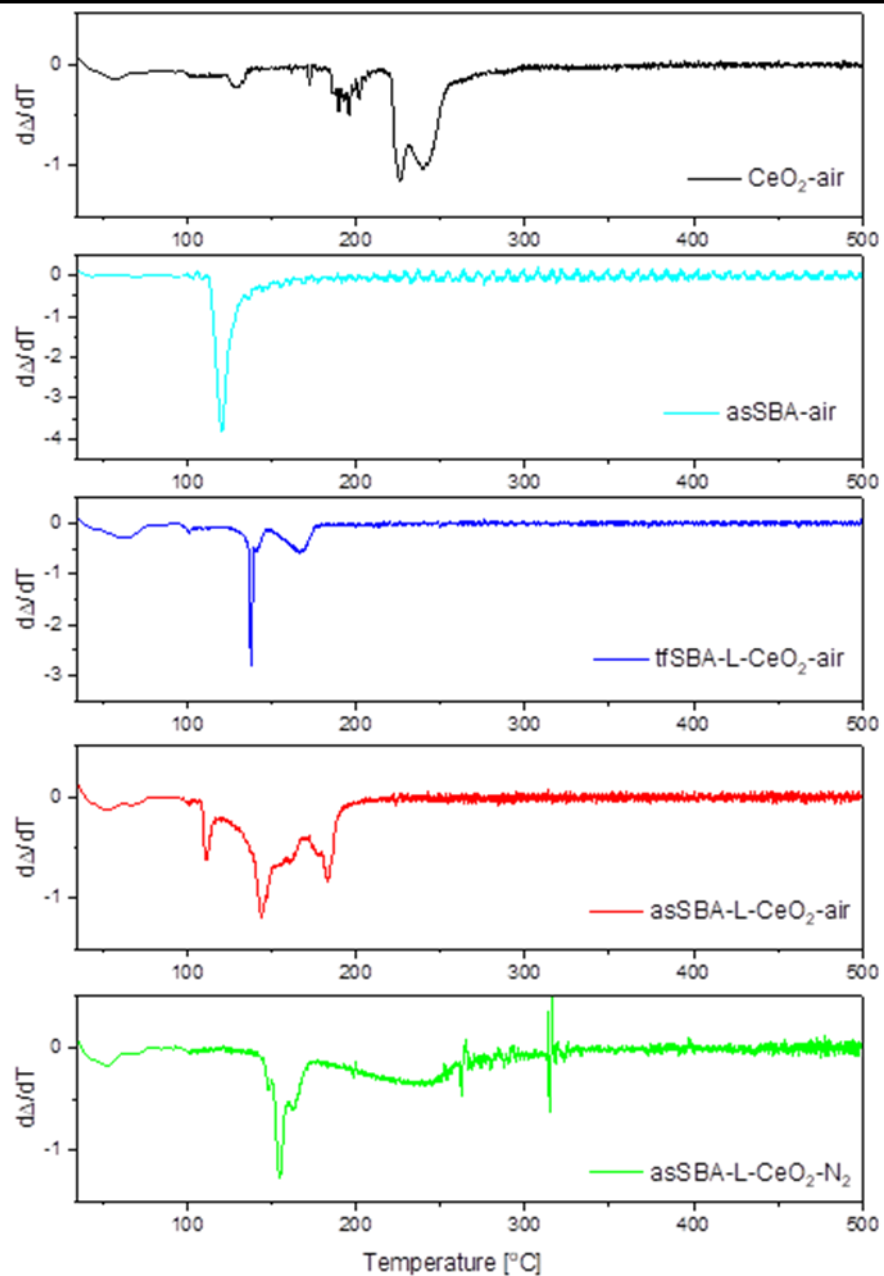
Figure S4-3. DTG profiles of bare cerium nitrate, asSBA-15, and mixtures of SBA-15 and cerium nitrate during heating to 500 °C in air or inert N_2 (heating rate: 1.5 °C/min).
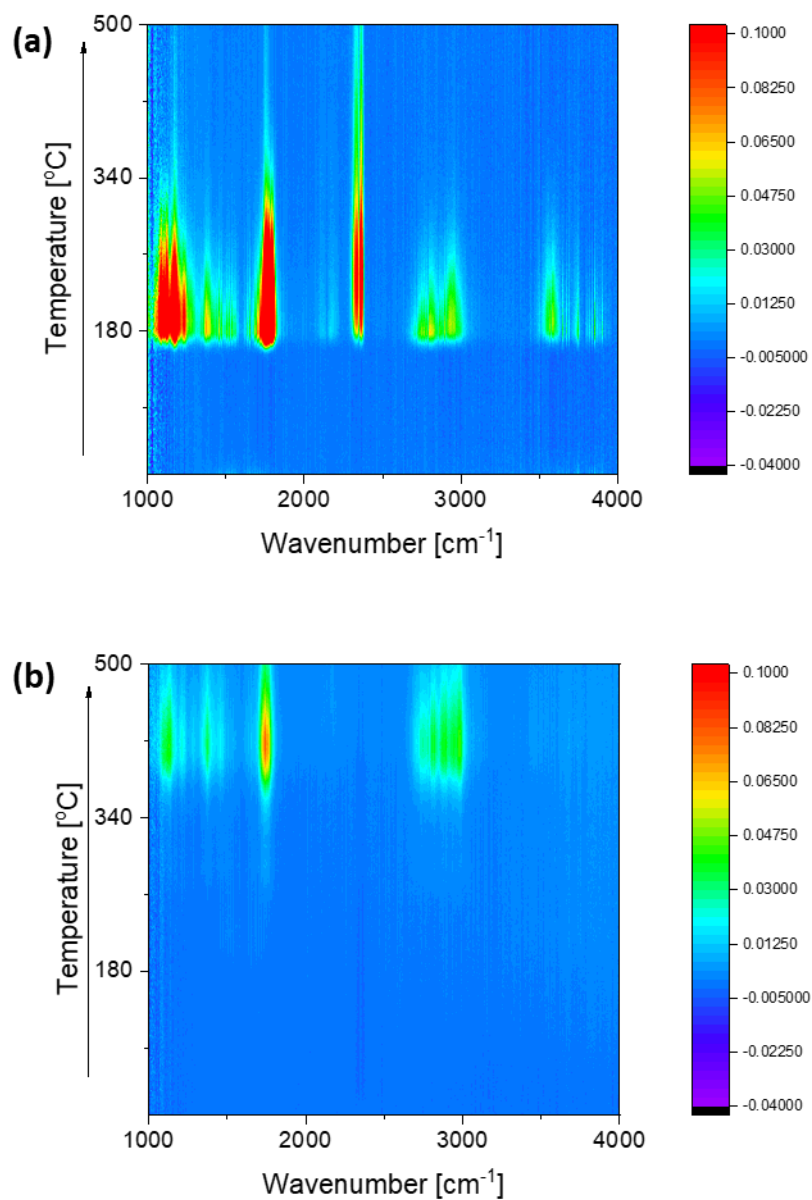
Figure S4-4. *In situ* detection of exhaust during calcination of samples (a) asSBA15-air, (b) asSBA15-N$_2$.
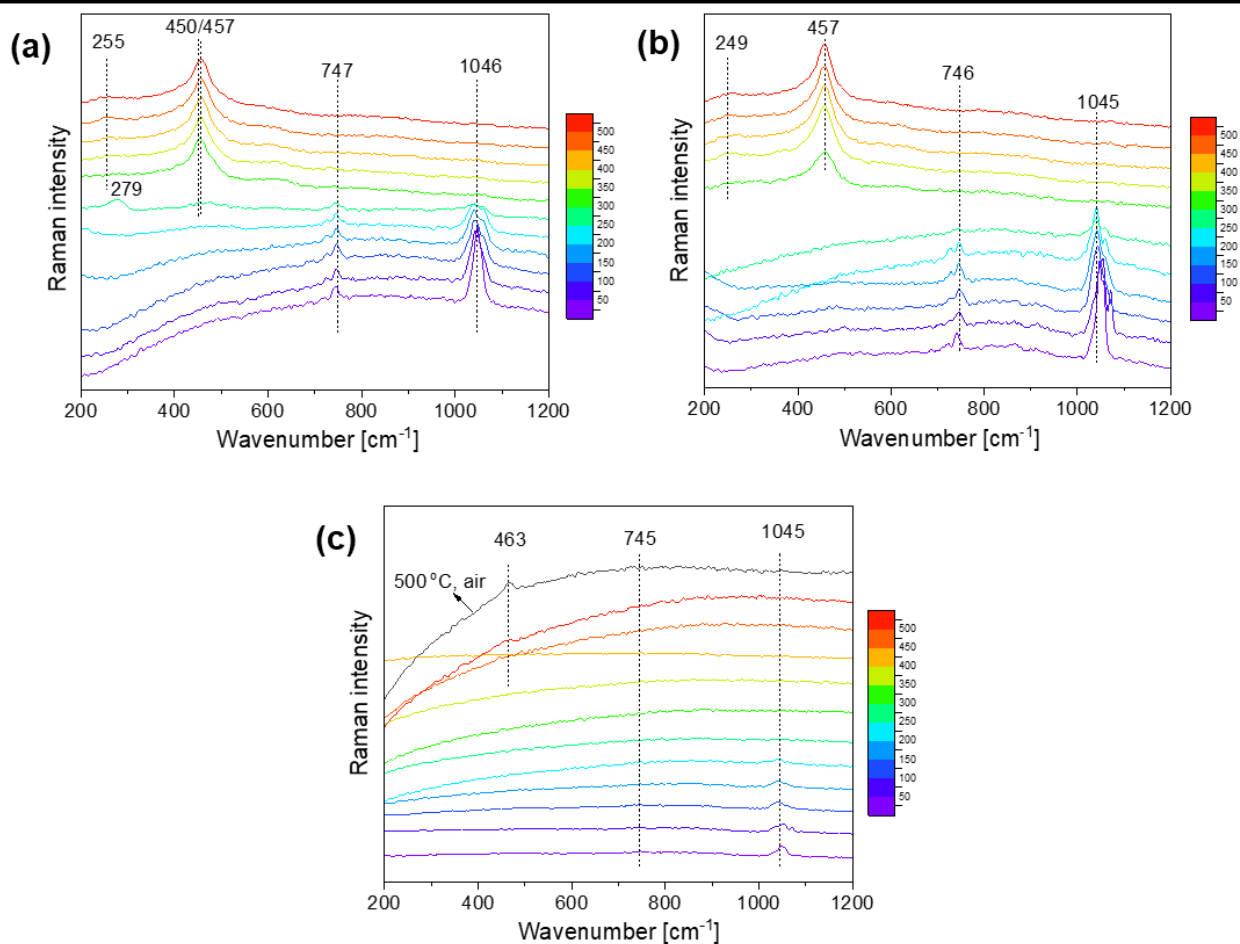
Figure S4-5. *In situ* Raman spectra (514.5 nm) during the calcination of (a) tfSBA-L-CeO₂-air, (b) asSBA-L-CeO₂-air, and (c) asSBA-L-CeO₂-N₂, following the protocol given in Fig. 4-1a. Spectra are offset for clarity. The feature at about 250 cm⁻¹ has been shown to originate from the longitudinal stretching mode of surface oxygen against cerium ions (Ce-O) as well as a contribution of the 2TA phonon,[3, 4] whereas the additional feature at about 279 cm⁻¹ is tentatively assigned to a nitro species formed during the transformation from cerium nitrate to crystalline ceria.[5]
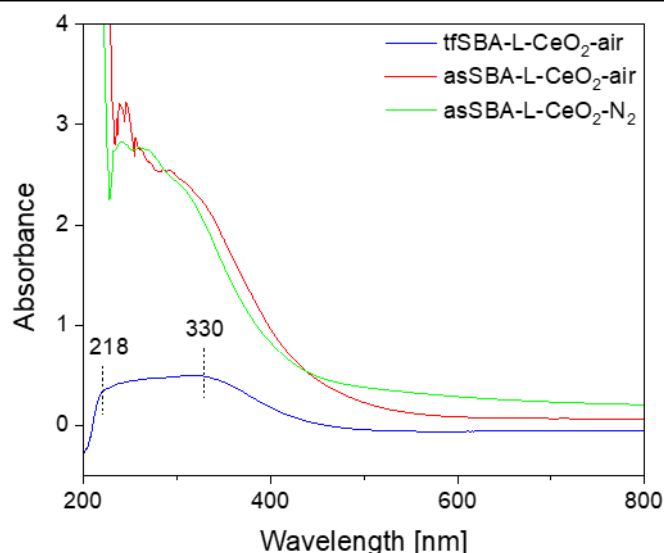
Figure S4-6. DR UV-Vis spectra of the samples tfSBA-L-CeO$_2$-air, asSBA-L-CeO$_2$-air, and asSBA-L-CeO$_2$-N$_2$, recorded at room temperature after cooling from high temperature calcination in synthetic air.
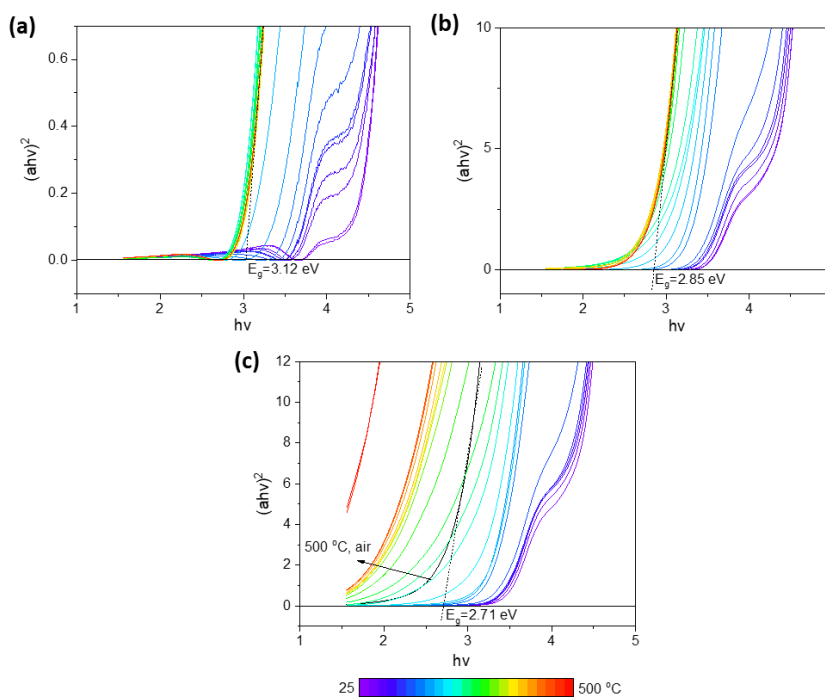

Figure S4-7. Calculation of band gap energies according to the *in situ* DR UV-Vis spectra by applying Tauc's method. (a) tfSBA-L-CeO$_2$-air, (b) asSBA-L-CeO$_2$-air, and (c) asSBA-L-CeO$_2$-N$_2$. In (c) the black curve represents the sample calcined in N$_2$, followed by calcination in air at 500 °C for 2 hours.

Table S4-1. Assignment of the IR features observed by *in situ* DRIFT spectroscopy.

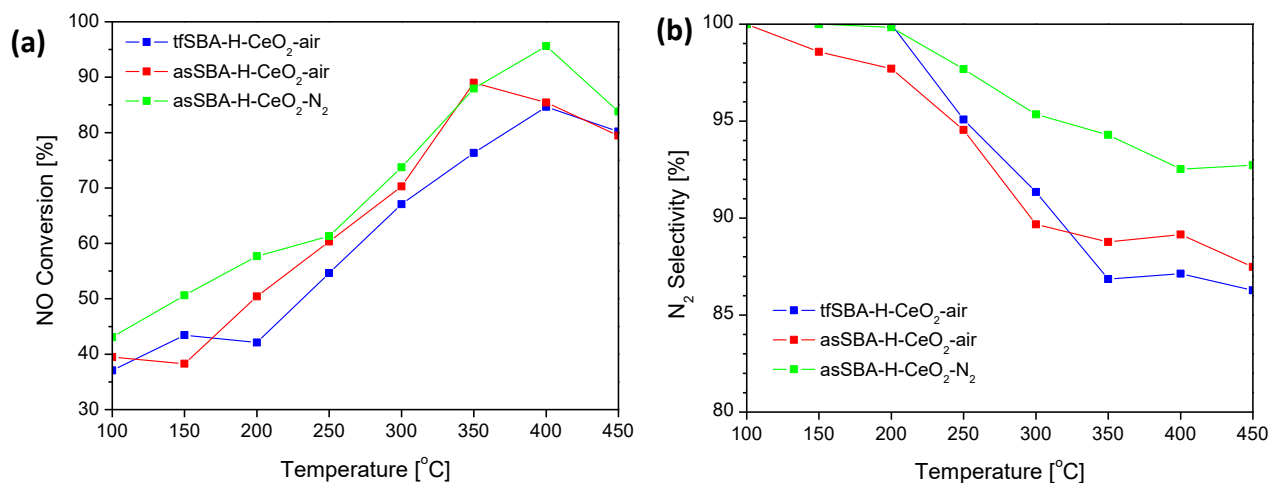| Wavenumber, cm^{-1}	tfSBA-CeO$_2$-air	asSBA-CeO$_2$-air	asSBA-CeO$_2$-N$_2$	Ref.
1225-1237		Hydrogen carbonates	Hydrogen carbonates	[279]
1253	Chelate NO$_2^-$			[280]
1303	Monodentate nitrates			[133]
1345-1357	Free nitrate ions		Free nitrate ions	[133]
1458			C-H deformation	[281]
1539-1543	Bidentate nitrates	Bidentate nitrates		[110]
1613	Bridging nitrates			[110]
1625-1636	Adsorbed NO$_2$	Adsorbed NO$_2$	Adsorbed NO$_2$	[133]
1663	Adsorbed N$_2$O$_4$			[133]
1729-1732		C=O	C=O	[280]
1764-1767	Adsorbed NO	Adsorbed NO	Adsorbed NO	[280]
1849-1981	Silica framework	Silica framework	Silica framework	[133]
2290/2341		Adsorbed CO$_2$		[280]
2356-2360	CO$_2$	CO$_2$	CO$_2$	[282]
2484-2491	C-H	C-H	C-H	[283]
2809	C-H$_2$			[284]
2867/2933/2976		C-H	C-H	[282]
2941	CH$_2$			[281]
3176	-OH			[285]
3266	-OH			[284]
3200-3500	-OH			[284]
3700			Ce-OH	[286]
3740	Si-OH	Si-OH		[284]

Figure S4-8. (a) NO conversion and (b) N_2 selectivity of the indicated samples in NH_3-SCR of NO, using a feed gas consisting of 500 ppm NH_3, 500 ppm NO, and 5% O_2 (balanced with N_2) and a total gas flow of 50 ml·min^{-1} (GHSV=30000 h^{-1}).
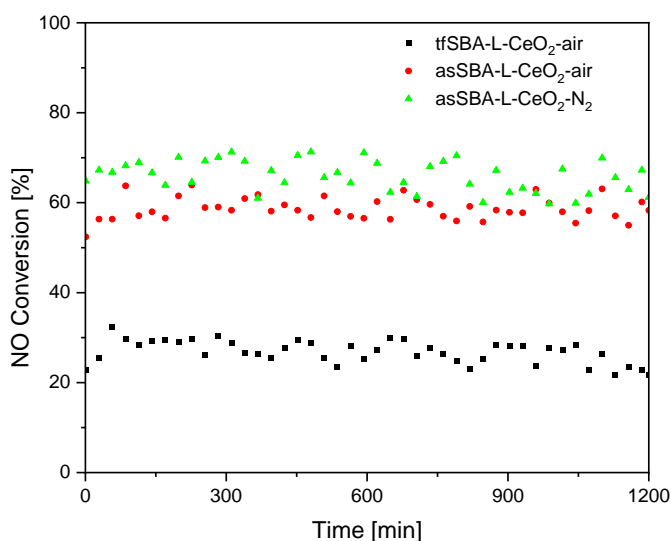

Figure S4-9. Stability at 300 °C over the indicated samples in NH_3-SCR of NO, using a feed gas consisting of 500 ppm NH_3, 500 ppm NO, and 5% O_2 (balanced with N_2) and a total gas flow of 50 ml·min^{-1} (GHSV=30000 h^{-1}).

Table S4-2. Catalytic temperature ranges and catalytic activities of cerium-based deNOx catalysts synthesized by different methods.

| Catalysts	Preparation methods	Reaction conditions	NO$_x$ conversion (temperature range)	GHSV or GWSV	Sources
CeO$_2$	precipitation method	NO =600 ppm, NH$_3$=600 ppm, O$_2$ =5%	45-60% (225-350 ^{o}C)	108000 h^{-1}	[287]
CeO$_2$	hydrothermal method	NH$_3$ = NO = 500 ppm, O$_2$ = 3.%,	50% (300 ^{o}C)	120000 ml g^{-1} h^{-1}	[288]
CeO$_2$	thermal decomposition	NO=736 mg/m^3, NH3=417 mg/m^3, O2 = 5%	60-65% (300-400 ºC)	108000 h^{-1}	[28]
CeO$_2$	impregnation	NH$_3$ = NO = 500 ppm, O$_2$ = 5%,	15-20 % (350-450 ºC)	120000 ml g^{-1}h^{-1}	[289]
CeO$_2$	thermal decomposition	NH$_3$ = NO = 600 ppm, O$_2$ = 5%,	40-50% (250-325 ºC)	108000 h^{-1}	[29]
CeO$_2$	one-pot	NH$_3$ = NO = 500 ppm, O$_2$ = 3%,	50-60% (300-400 ºC)	45000 h^{-1}	[290]
CeO$_2$	spread self-combustion	NH$_3$ = NO = 500 ppm, O$_2$ = 5%,	15 % (300-500 ºC)	200000 ml g^{-1}h^{-1}	[113]
CeO$_2$/SiO$_2$	wet impregnation	NH$_3$ = NO = 500 ppm, O$_2$ = 5%,	70-80% (275-325 ºC)	48000 ml g^{-1}h^{-1}	[66]
CeO$_2$/SBA-15	wet impregnation	NH$_3$ = 1100 ppm, NO = 1000 ppm, O$_2$ = 5%,	60-70% (200-300 ºC)	10000 h^{-1}	[291]
tfSBA-CeO$_2$-air			30% (300-400 ºC)		
asSBA-CeO$_2$-air	Solid state impregnation	NH$_3$ = NO = 500 ppm, O$_2$ = 5%,	50-60% (250-400ºC)	30000 h^{-1} (150000 ml g^{-1}h^{-1})	This work
asSBA-CeO$_2$-N$_2$			55-65% (200-450 ºC)		
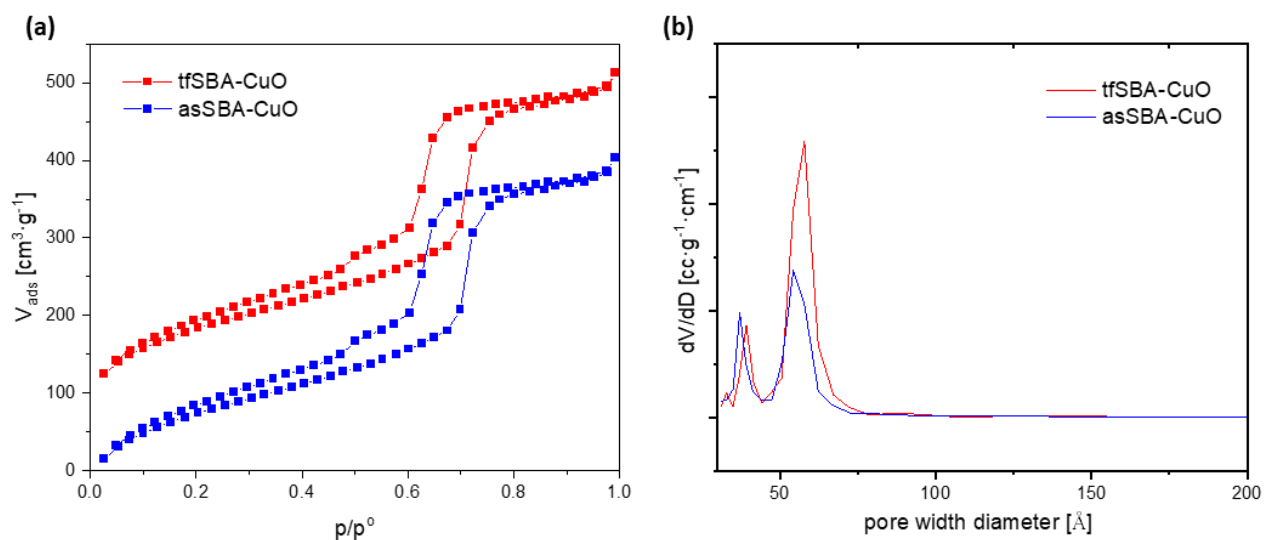
Figure S5-1. (a) N_2 adsorption/desorption isotherms, and (b) NLDFT pore size distributions of tfSBA-CuO and asSBA-CuO. The N_2 adsorption/desorption experiments were carried out at 77 K using on an Autosorb-3B (Quantachrome Instruments, USA) device.
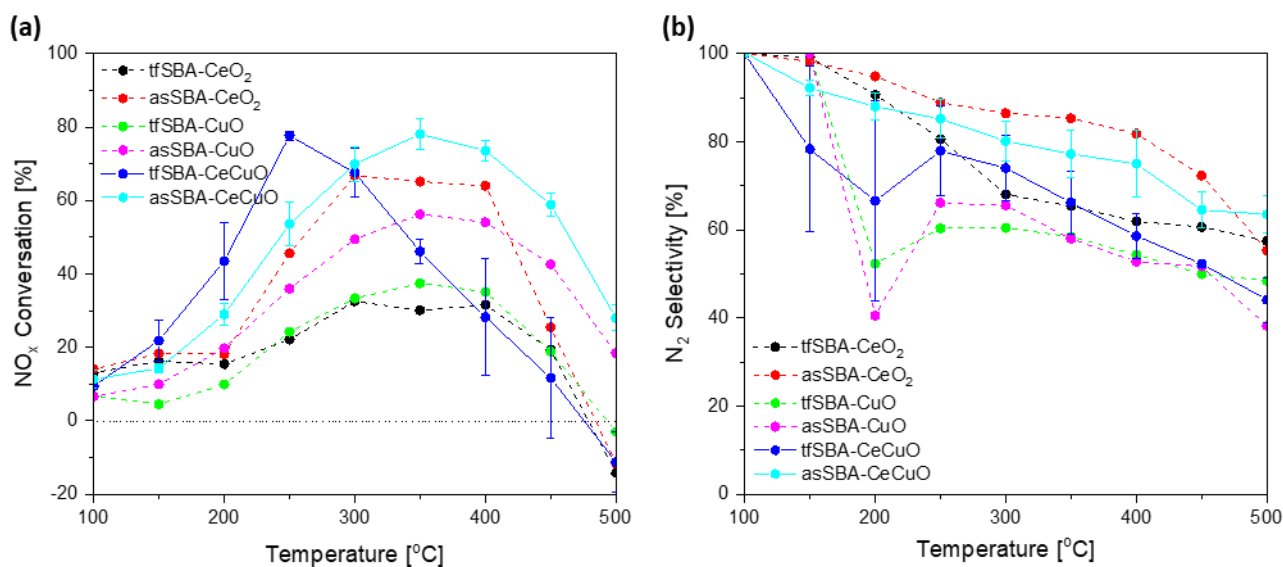

Figure S5-2. Temperature-dependent NH_3-SCR performance for the synthesized samples: (a) NO_x conversion, (b) N_2 selectivity.
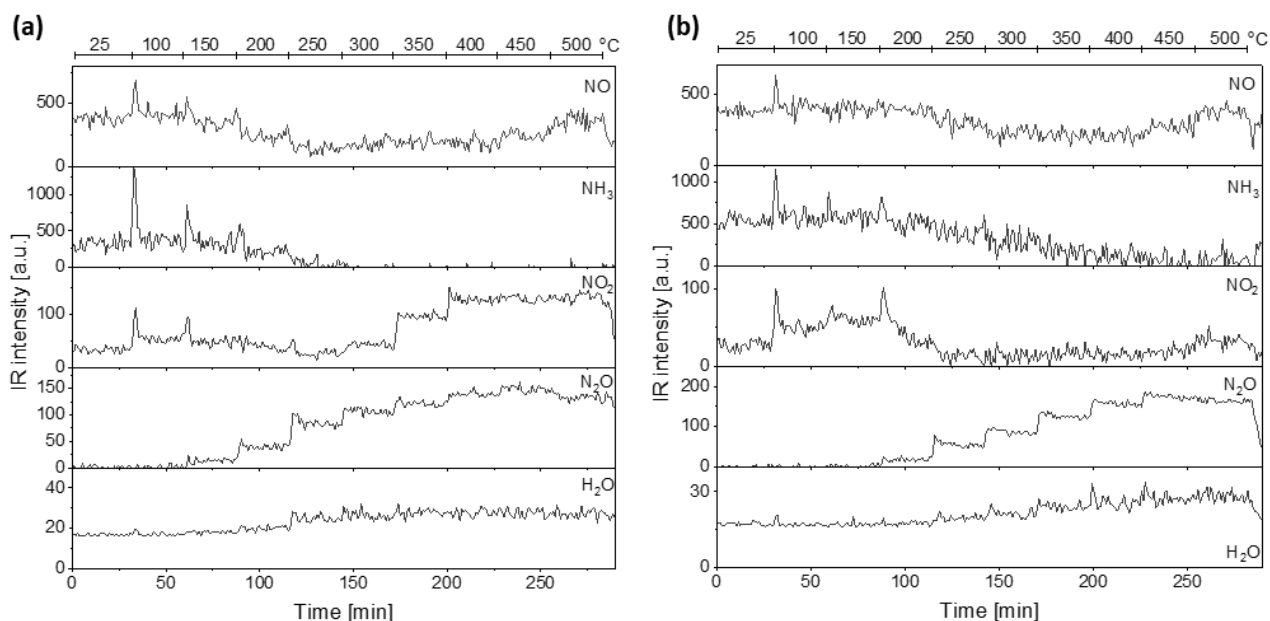
Figure S5-3. *In situ* detection of the exhaust gas during NH₃-SCR reaction of (a) tfSBA-CeCuO, (b) asSBA-CeCuO. The temperature was increased stepwise from 25°C to 500°C. The feed consisted of 500 ppm NH₃, 500 ppm NO, and 5% O₂ (balanced with N₂) at a total flow rate of 50 NmL/min (GHSV = 60,000 h⁻¹).
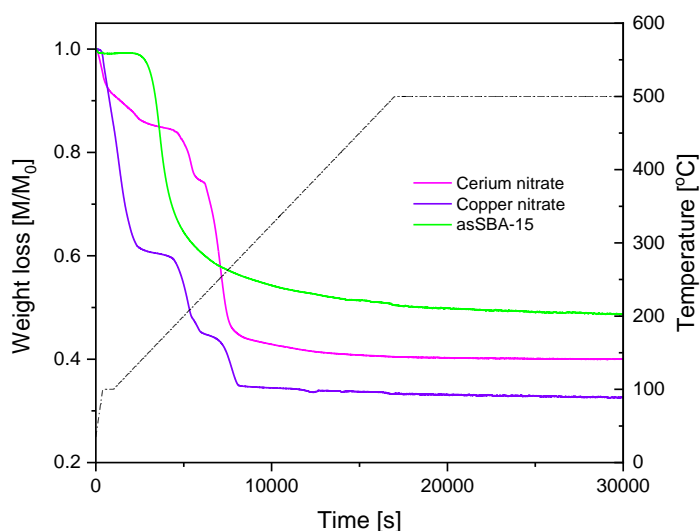
Figure S5-4. TGA profiles of asSBA-15, bare cerium nitrate and bare copper nitrate during heating to 500 °C in air (heating rate: 1.5 °C/min).
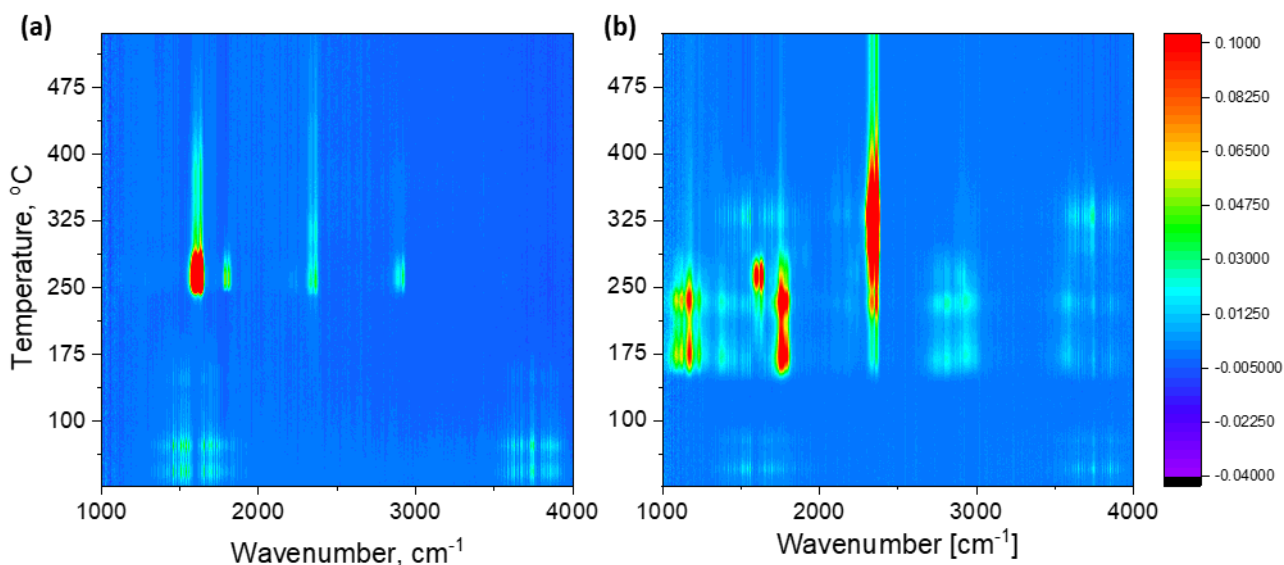
Figure S5-5. Online IR detection of the exhaust gases during air calcination of the precursor samples (a) tfSBA-CeO₂, (b) asSBA-CeO₂. The temperature was raised from 25 °C to 500 °C at a heating rate of 1.5 °C/min.
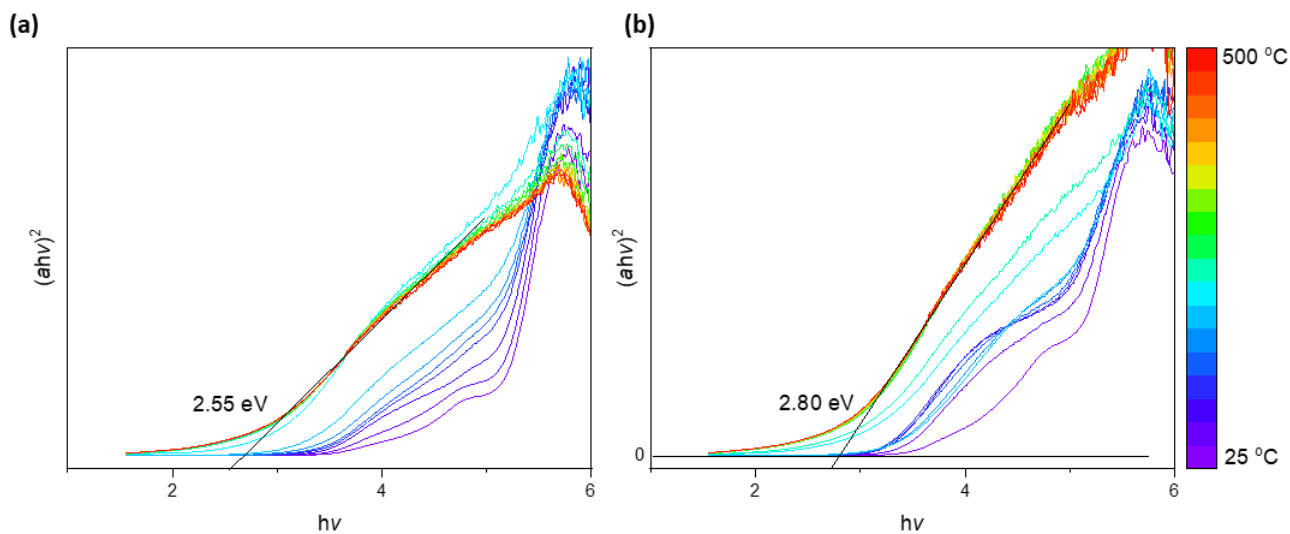
Figure S5-6. Calculation of band gap energies based on the *in situ* DR UV-Vis spectra shown in Fig. 5-8 by applying Tauc's method. (a) tfSBA-CeCuO and (b) asSBA-CeCuO.
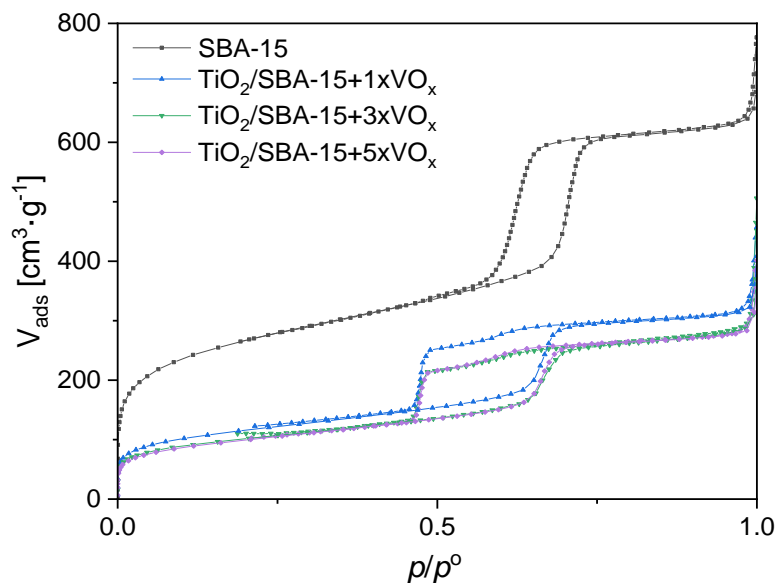
Figure S6-1. N$_2$ adsorption-desorption isotherms of TiO$_2$ / SBA-15+nVO$_x$ (n = 1, 3, and 5) materials and SBA-15.
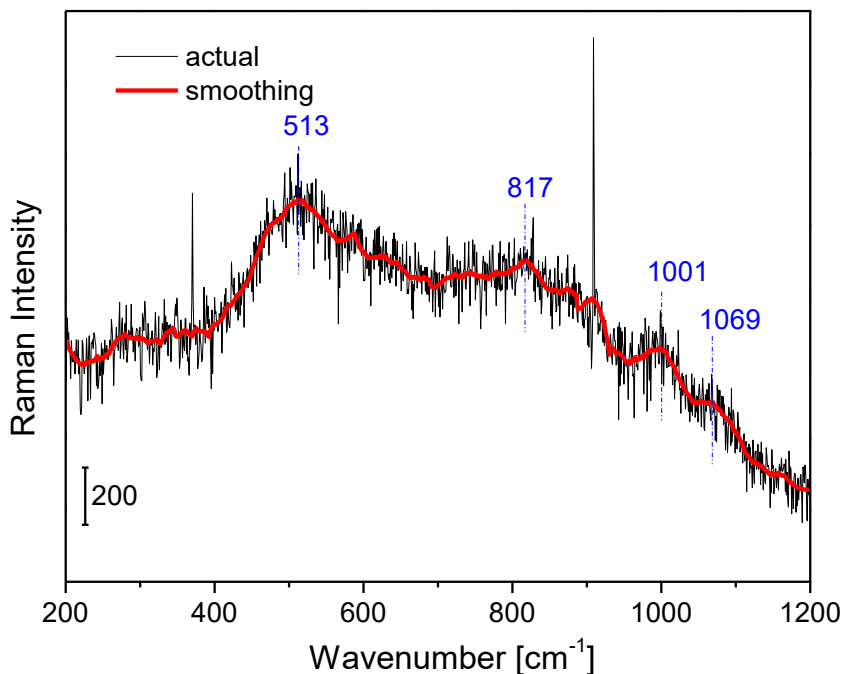
Figure S6-2. UV-Raman (256.7 nm) of the TiO$_2$ /SBA-15+3xVO$_x$ sample. Prior to VO$_x$ deposition the TiO$_2$/SBA-15 sample was calcined at 500°C for 2h.

Table S6-1. Results of the XPS analysis of TiO_2/SBA-15+3xVO$_x$.

Elements	Position (eV)	FWHM (eV)	% Area	% Area in total
Si	103.8	2.6		23.5
C				5.5
O	532.9	3.4		65.8
V				2.4
V^{4+}	517.6	3.2	66.5	
V^{5+}	516.3	3.2	33.5	
Ti				2.8
Ti-O-Ti	458.7	2.0	51.7	
Ti-O-Si	459.9	2.4	48.3	
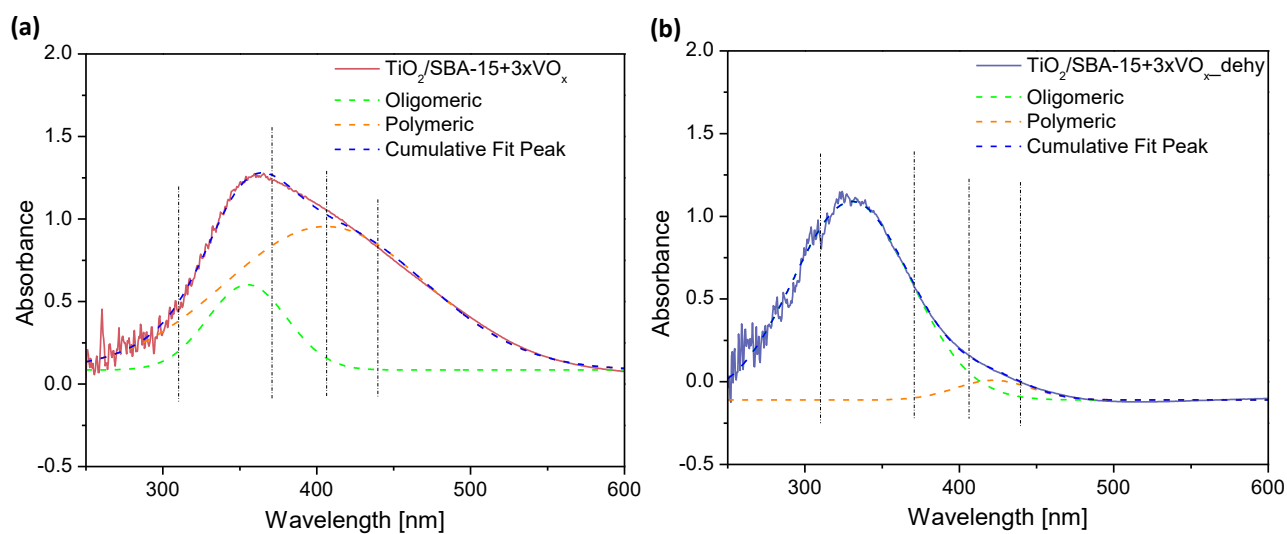
Figure S6-3. UV-Vis DRS of TiO_2/SBA-15+3xVO$_x$ sample using TiO_2/SBA-15 as the reference background. (a) hydrated, (b) dehydrated.
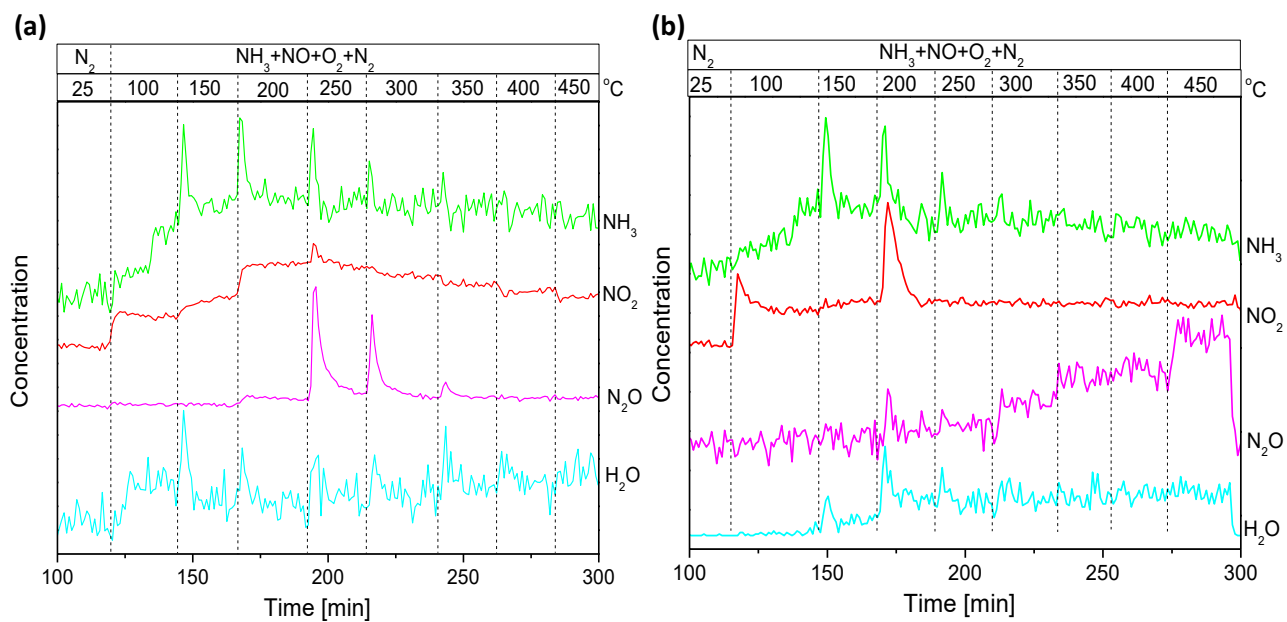
Figure S6-4. *In situ* detection of the exhaust gas during NH_3-SCR reaction of (a) TiO_2/SBA-15+1xVO_x and (b) TiO_2/SBA-15+5xVO_x at 100-450°C. The feed consisted of 500 ppm NH_3, 500 ppm NO, and 5% O_2 (balanced with N_2) at a total flow rate of 50 Nml/min (GHSV = 40000 h^{-1}).

References

[1]   L. P. Han, S. X. Cai, M. Gao, J. Hasegawa, P. L. Wang, J. P. Zhang, L. Y. Shi, D. S. Zhang. Selective Catalytic Reduction of NO_x with NH_3 by Using Novel Catalysts: State of the Art and Future Prospects. Chem. Rev., 119: 10916-10976, 2019.

[2]   World Health Organization. Ambient (outdoor) air pollution, https://www.who.int/news-room/fact-sheets/detail/ambient-(outdoor)-air-quality-and-health. Accessed: 02. Nov 2022.

[3]   Z. M. Liu, S. I. Woo. Recent Advances in Catalytic $DeNO_x$ Science and Technology. Catal. Rev., 48: 43-89, 2006.

[4]   V. Franco J. Miller. Impact of Improved Regulation of Real-World NO_x Emissions from Diesel Passanger Cars in the EU, ICCT http://www.theicct.org/sites/default/files/publications/ICCT_real-world-NOX-RDE-2015-2030_dec2016.pdf. accessed: 02. Nov 2022.

[5]   R. K. Srivastava, W. Nueffer, D. Grano, S. Khan, J. E. Staudt, W. Jozewicz. Controlling NO_x Emission from Industrial Sources. Environ. Prog., 24: 181-197, 2005.

[6]   B. Choi, K. Lee, G. Son. Review of Recent After-Treatment Technologies for $DeNO_x$ Process in Diesel Engines. Int. J. Auto. Tech.-Kor., 21: 1597-1618, 2020.

[7]   G. Sun, X. Duan, B. Hao, A. Davarpanah. Modeling of a Dry Low Nitrogen Oxides Burner Using a Three-dimensional Computational Fluid Dynamics Simulation. P. I. Mech. Eng. E - J. Pro., 235: 2209-2220, 2021.

[8]   F. Martinovic, L. Castoldi, F. A. Deorsola. Aftertreatment Technologies for Diesel Engines: An Overview of the Combined Systems. Catalysts, 11: 653, 2021.

[9]   M. T. Javed, N. Irfan, B. M. Gibbs. Control of Combustion-generated Nitrogen Oxides by Selective Non-catalytic Reduction. J. Environ. Manage., 83: 251-289, 2007.

[10] X. J. Yao, Z. Wang, S. H. Yu, F. M. Yang, L. Dong. Acid Pretreatment Effect on the Physicochemical Property and Catalytic Performance of CeO_2 for NH_3-SCR. Appl. Catal. A-Gen., 542: 282-288, 2017.

[11] Y. Jia, J. Jiang, R. Z. Zheng, L. N. Guo, J. Yuan, S. L. Zhang, M. Y. Gu. Insight into the Reaction Mechanism over PMoA for Low Temperature NH_3-SCR: A Combined In-situ DRIFTs and DFT Transition State Calculations. J. Hazard. Mater., 412: 125258, 2021.

[12] R. J. G. Nuguid, D. Ferri, A. Marberger, M. Nachtegaal, O. Krocher. Modulated Excitation Raman Spectroscopy of V_2O_5/TiO_2: Mechanistic Insights into the Selective Catalytic Reduction of NO with NH_3. ACS Catal., 9: 6814-6820, 2019.

[13] Q. X. Wu, L. D. L. Duchstein, G. L. Chiarello, J. M. Christensen, C. D. Damsgaard, C. F. Elkjaer, J. B. Wagner, B. Temel, J. D. Grunwaldt, A. D. Jensen. In Situ Observation of Cu-Ni Alloy Nanoparticle Formation by X-Ray Diffraction, X-Ray Absorption Spectroscopy, and Transmission Electron Microscopy: Influence of Cu/Ni Ratio. ChemCatChem, 6: 301-310, 2014.

[14] F. Golks, Y. Grunder, J. Stettner, K. Krug, J. Zegenhagen, O. M. Magnussen. In situ Surface X-ray Diffraction Studies of Homoepitaxial Growth on Cu(001) from Aqueous Acidic Electrolyte. Surf. Sci., 631: 112-122, 2015.

[15] T. Rojac, B. Malic, M. Kosec, M. Polomska, B. Hilczer, B. Zupancic, B. Zalar. Mechanochemical Synthesis of $NaNbO_3$: A Complementary Study of Reaction Mechanism Using Raman

Spectroscopy and Quadrupole Perturbed Na^{23} Nuclear Magnetic Resonance. <u>Solid State Ionics</u>, 215: 1-6, 2012.

[16] D. Gracin, V. Strukil, T. Friscic, I. Halasz, K. Uzarevic. Laboratory Real-Time and In Situ Monitoring of Mechanochemical Milling Reactions by Raman Spectroscopy. <u>Angew. Chem.-Int. Ed.</u>, 53: 6193-6197, 2014.

[17] Y. Du, X. Du, S. M. George. SiO_2 Film Growth at Low Temperatures by Catalyzed Atomic Layer Deposition in a Viscous Flow Reactor. <u>Thin Solid Films</u>, 491: 43-53, 2005.

[18] C. J. Tang, H. L. Zhang, L. Dong. Ceria-based Catalysts for Low-temperature Selective Catalytic Reduction of NO with NH_3. <u>Catal. Sci. Technol.</u>, 6: 1248-1264, 2016.

[19] V. I. Parvulescu, P. Grange, B. Delmon. Catalytic Removal of NO. <u>Catal. Today</u>, 46: 233-316, 1998.

[20] Y. Guan, Y. H. Liu, Q. Lv, B. Wang, D. F. Che. Review on the Selective Catalytic Reduction of NO_x with H_2 by Using Novel Catalysts. <u>J. Environ. Chem. Eng.</u>, 9: 106770, 2021.

[21] Y. Q. Zeng, K. G. Haw, Y. A. Wang, S. L. Zhang, Z. G. Wang, Q. Zhong, S. Kawi. Recent Progress of CeO_2-TiO_2 Based Catalysts for Selective Catalytic Reduction of NO_x by NH_3. <u>ChemCatChem</u>, 13: 491-505, 2021.

[22] R. T. Guo, W. L. Zhen, W. G. Pan, Y. Zhou, H. Jie-Nan, H. J. Xu, Q. Jin, C. G. Ding, S. Y. Guo. Effect of Cu Doping on the SCR Activity of CeO_2 Catalyst Prepared by Citric Acid Method. <u>J. Ind. Eng. Chem.</u>, 20: 1577-1580, 2014.

[23] W. M. Meier. Zeolites and Zeolite-like Materials. <u>Pure Appl. Chem.</u>, 58: 1323-1328, 1986.

[24] M. E. Davis. Zeolites and Molecular-sieves – not just Ordinary Catalysts. <u>Ind. Eng. Chem. Res.</u>, 30: 1675-1683, 1991.

[25] W. M. Meier. Molecular-sieves and Zeolite Catalysts. <u>ACTA Crystallograp. A</u>, 40: C180, 1984.

[26] A. Boubnov, H. W. P. Carvalho, D. E. Doronkin, T. Gunter, E. Gallo, A. J. Atkins, C. R. Jacob, J. D. Grunwaldt. Selective Catalytic Reduction of NO Over Fe-ZSM-5: Mechanistic Insights by Operando HERFD-XANES and Valence-to-Core X-ray Emission Spectroscopy. <u>J. Am. Chem. Soc.</u>, 136: 13006-13015, 2014.

[27] J. Q. Xu, H. J. Yu, C. Zhang, F. Guo, J. Q. Xie. Development of Cerium-based Catalysts for Selective Catalytic Reduction of Nitrogen Oxides: A Review. <u>New J. Chem.</u>, 43: 3996-4007, 2019.

[28] H. Lv, X. Hua, W. Xie, Q. Hu, J. Wu, R. Guo. Promotion Effect of H_2 Pretreatment on CeO_2 Catalyst for NH_3-SCR Reaction. <u>J. Rare Earth.</u>, 36: 708-714, 2018.

[29] X. Sun, R.T. Guo, S.W. Liu, J. Liu, W.G. Pan, X. Shi, H. Qin, Z.Y. Wang, Z.Z. Qiu, X.Y. Liu. The Promoted Performance of CeO_2 Catalyst for NH_3-SCR Reaction by NH_3 treatment. <u>Appl. Surf. Sci.</u>, 462: 187-193, 2018.

[30] J. X. Chen, Y. X. Chen, M. J. Zhou, Z. W. Huang, J. Y. Gao, Z. Ma, J. M. Chen, X. F. Tang. Enhanced Performance of Ceria-Based NO_x Reduction Catalysts by Optimal Support Effect. <u>Environ. Sci. Technol.</u>, 51: 473-478, 2017.

[31] B. Chi, H. X. Qu, X. Xing, Q. Zhong. Assembly of Hollow CeO_2@Fe-ZSM-5 and SCR Performance. <u>J. Alloy Compd.</u>, 726: 906-912, 2017.

[32] H. Z. Chang, L. Ma, S. J. Yang, J. H. Li, L. Chen, W. Wang, J. M. Hao. Comparison of Preparation Methods for Ceria Catalyst and the Effect of Surface and Bulk Sulfates on its Activity toward NH_3-SCR. J. Hazard. Mater., 262: 782-788, 2013.

[33] F. Li, Y. B. Zhang, D. H. Xiao, D. Q. Wang, X. Q. Pan, X. G. Yang. Hydrothermal Method Prepared Ce-P-O Catalyst for the Selective Catalytic Reduction of NO with NH_3 in a Broad Temperature Range. ChemCatChem, 2: 1416-1419, 2010.

[34] J. Fan, X. Jiang, H. Min, D. Li, X. Ran, L. Zou, Y. Sun, W. Li, J. Yang, W. Teng, G. Li, D. Zhao. Facile Preparation of Cu–Mn/CeO_2/SBA-15 Catalysts Using Ceria as an Auxiliary for Advanced Oxidation Processes. J. Mater. Chem. A, 2: 10654, 2014.

[35] L. Xu, X. S. Li, M. Crocker, Z. S. Zhang, A. M. Zhu, C. Shi. A Study of the Mechanism of Low-temperature SCR of NO with NH_3 on MnO_x/CeO2. J. Mol. Catal. A-Chem., 378: 82-90, 2013.

[36] Z. Ma, D. Weng, X. Wu, Z. J. J. o. E. S. Si. Effects of WO_x Modification on the Activity, Adsorption and Redox Properties of CeO_2 catalyst for NO_x Reduction with Ammonia. J. Environ. Sci., 24: 1305-1316, 2012.

[37] P. Maitarad, J. Han, D. Zhang, L. Shi, S. Namuangruk, T. Rungrotmongkol. Structure-activity Relationships of NiO on CeO_2 Nanorods for the Selective Catalytic Reduction of NO with NH_3: Experimental and DFT Studies. J. Phys. Chem. C,118: 9612-9620, 2014.

[38] J. Zhu, F. Gao, L. Dong, W. Yu, L. Qi, Z. Wang, L. Dong, Y. Chen. Studies on Surface Structure of M_xO_y/MoO_3/CeO_2 system (M= Ni, Cu, Fe) and its influence on SCR of NO by NH_3. Appl. Catal. B-Environ., 95: 144-152, 2010.

[39] P. Li, Y. Xin, Q. Li, Z. Wang, Z. Zhang, L. Zheng. Ce–Ti Amorphous Oxides for Selective Catalytic Reduction of NO with NH_3: Confirmation of Ce–O–Ti Active Sites. Environ. Sci. Technol., 46: 9600-9605, 2012.

[40] D. Y. Zhao, J. L. Feng, Q. S. Huo, N. Melosh, G. H. Fredrickson, B. F. Chmelka, G. D. Stucky. Triblock Copolymer Syntheses of Mesoporous Silica with Periodic 50 to 300 Angstrom Pores. Science, 279: 548-552, 1998.

[41] J. Shen, C. Hess. Controlling the dispersion of ceria using nanoconfinement: application to CeO_2/SBA-15 catalysts for NH_3-SCR. Mater. Adv., 2: 7400-7412, 2021.

[42] W. Li, J. Liu, D. Y. Zhao. Mesoporous materials for energy conversion and storage devices. Nat. Rev. Mater., 1: 16023, 2016.

[43] R. Huirache-Acuna, R. Nava, C. L. Peza-Ledesma, J. Lara-Romero, G. Alonso-Nunez, B. Pawelec, E. M. Rivera-Munoz. SBA-15 Mesoporous Silica as Catalytic Support for Hydrodesulfurization Catalysts-Review. Materials, 6: 4139-4167, 2013.

[44] D. Zhao, P. Yang, N. Melosh, J. Feng, B. F. Chmelka, G. D. Stucky. Continuous Mesoporous Silica Films with Highly Ordered Large Pore Structures. Adv. Mater., 10: 1380, 1998.

[45] V. Chaudhary, S. Sharma. An Overview of Ordered Mesoporous Material SBA-15: Synthesis, Functionalization and Application in Oxidation Reactions. J. Porous Mat., 24: 741-749, 2017.

[46] N. Y. Topsoe, J. A. Dumesic, H. Topsoe. Vanadia-titania Catalysts for Selective Catalytic Nitric-oxide by Ammonia 2. Studies of Active-sites and Formulation of Catalytic Cycles. J. Catal., 151: 241-252, 1995.

[47] N. Y. Topsoe, H. Topsoe, J. A. Dumesic. Vanadia-titania Catalysts for Selective Catalytic Reduction (SCR) of Nitric-oxides by Ammonia 1. Combined Temperature-programmed In Situ FTIR and Online Mass-spectroscopy Studies. <u>J. Catal.</u>, 151: 226-240, 1995.

[48] N. Y. Topsoe, M. Anstrom, J. A. Dumesic. Raman, FTIR and Theoretical Evidence for Dynamic Structural Rearrangements of Vanadia/Titania DeNO$_x$ Catalysts. <u>Catal. Lett.</u>, 76: 11-20, 2001.

[49] G. Ramis, L. Yi, G. Busca. Ammonia Activation over Catalysts for the Selective Catalytic Reduction of NO$_x$ and the Selective Catalytic Oxidation of NH$_3$. An FTIR study. <u>Catal. Today</u>, 28: 373-380, 1996.

[50] A. Marberger, D. Ferri, M. Elsener, O. Krocher. The Significance of Lewis Acid Sites for the Selective Catalytic Reduction of Nitric Oxide on Vanadium-Based Catalysts. <u>Angew. Chem.-Int. Ed.</u>, 55: 11989-11994, 2016.

[51] A. Marberger, D. Ferri, M. Elsener, A. Sagar, C. Artner, K. Schermanz, O. Krocher. Relationship between Structures and Activities of Supported Metal Vanadates for the Selective Catalytic Reduction of NO by NH$_3$. <u>Appl. Catal. B-Environ.</u>, 218: 731-742, 2017.

[52] M. H. Zhu, J. K. Lai, U. Tumuluri, Z. L. Wu, I. E. Wachs. Nature of Active Sites and Surface Intermediates during SCR of NO with NH$_3$ by Supported V$_2$O$_5$-WO$_3$/TiO$_2$ Catalysts. <u>J. Am. Chem. Soc.</u>, 139: 15624-15627, 2017.

[53] G. Silversmit, H. Poelman, I. Sack, G. Buyle, G. B. Marin, R. De Gryse. An In-situ Reduction/Oxidation XAS Study on the EL10V8 VO$_x$/TiO$_2$(Anatase) Powder Catalyst. <u>Catal. Lett.</u>, 107: 61-71, 2006.

[54] G. Silversmit, J. A. van Bokhoven, H. Poelman, A. M. J. van der Eerden, G. B. Marin, M. F. Reyniers, R. De Gryse. The Structure of Supported and Unsupported Vanadium Oxide Under Calcination, Reduction and Oxidation Determined with XAS. <u>Appl. Catal. A- Gen.</u>, 285: 151-162, 2005.

[55] H. Feng, J. W. Elam, J. A. Libera, M. J. Pellin, P. C. Stair. Oxidative Dehydrogenation of Cyclohexane over Alumina-Supported Vanadium Oxide Nanoliths. <u>J. Catal.</u>, 269: 421-431, 2010.

[56] Z. X. Feng, J. L. Lu, H. Feng, P. C. Stair, J. W. Elam, M. J. Bedzyk. Catalysts Transform While Molecules React: An Atomic-Scale View. <u>J. Phys. Chem. Lett.</u>, 4: 285-291, 2013.

[57] L. Arnarson, S. B. Rasmussen, H. Falsig, J. V. Lauritsen, P. G. Moses. Coexistence of Square Pyramidal Structures of Oxo Vanadium (+5) and (+4) Species Over Low-Coverage VO$_x$/TiO$_2$ (101) and (001) Anatase Catalysts. <u>J. Phys. Chem. C</u>, 119: 23445-23452, 2015.

[58] V. I. Avdeev, A. F. Bedilo. Molecular Mechanism of Oxygen Isotopic Exchange over Supported Vanadium Oxide Catalyst VO$_x$/TiO$_2$. <u>J. Phys. Chem. C</u>, 117: 2879-2887, 2013.

[59] V. I. Avdeev, V. M. Tapilin. Water Effect on the Electronic Structure of Active Sites of Supported Vanadium Oxide Catalyst VO$_x$/TiO$_2$(001). <u>J. Phys. Chem. C</u>, 114: 3609-3613, 2010.

[60] J. M. Jehng, G. Deo, B. M. Weckhuysen, I. E. Wachs. Effect of Water Vapor on the Molecular Structures of Supported Vanadium Oxide Catalysts at Elevated Temperatures. <u>J. Mol. Catal. A-Chem.</u>, 110: 41-54, 1996.

[61] W. G. Pan, Y. Zhou, R. T. Guo, Q. Jin, C. G. Ding, S. Y. Guo. Effect of Cerium Precursor on the Performance of Pure CeO_2 Catalysts for Selective Catalytic Reduction of NO with NH_3. Asian J. Chem., 25: 9079-9082, 2013.

[62] B. L. Zhang, S. G. Zhang, B. Liu. Effect of Oxygen Vacancies on Ceria Catalyst for Selective Catalytic Reduction of NO with NH_3. Appl. Surf. Sci., 529: 147068, 2020.

[63] L. Chen, D. Weng, Z. C. Si, X. Wu. Synergistic Effect between Ceria and Tungsten Oxide on WO_3-CeO_2-TiO_2 Catalysts for NH_3-SCR Reaction. Prog. Nat. Sci., 22: 265-272, 2012.

[64] W. Tan, J. M. Wang, L. L. Li, A. N. Liu, G. Song, K. Gun, Y. D. Luo, F. D. Liu, F. Gao, L. Dong. Gas Phase Sulfation of Ceria-zirconia Solid Solutions for Generating Highly Efficient and SO_2 resistant NH_3-SCR Catalysts for NO Removal. J. Hazard. Mater., 388:121729, 2020.

[65] N. Huang, Y. Geng, S. C. Xiong, X. Huang, L. N. Kong, S. J. Yang, Y. Peng, J. J. Chen, J. H. Li. The Promotion Effect of Ceria on High Vanadia Loading NH_3-SCR Catalysts. Catal. Commun., 121: 84-88, 2019.

[66] W. Tan, A. N. Liu, S. H. Xie, Y. Yan, T. E. Shaw, Y. Pu, K. Guo, L. L. Li, S. H. Yu, F. Gao, F. D. Liu, L. Dong. Ce-Si Mixed Oxide: A High Sulfur Resistant Catalyst in the NH_3-SCR Reaction through the Mechanism-Enhanced Process. Environ. Sci. Technol., 55: 4017-4026, 2021.

[67] L. Ma, C. Y. Seo, M. Nahata, X. Y. Chen, J. H. Li, J. W. Schwank. Shape Dependence and Sulfate Promotion of CeO_2 for Selective Catalytic Reduction of NO_x with NH_3. Appl. Catal. B-Environ., 232: 246-259, 2018.

[68] Y. Geng, K. Jin, J. Mei, G. Y. Su, L. Ma, S. J. Yang. CeO_2 Grafted with Different Heteropoly Acids for Selective Catalytic Reduction of NO_x with NH_3. J. Hazard. Mater., 382: 121032, 2020.

[69] S. J. Yang, Y. F. Guo, H. Z. Chang, L. Ma, Y. Peng, Z. Qu, N. Q. Yan, C. Z. Wang, J. H. Li. Novel Effect of SO_2 on the SCR Reaction over CeO_2: Mechanism and Significance. Appl. Catal. B-Environ., 136: 19-28, 2013.

[70] S. Li, Z. Q. Zheng, Z. C. Zhao, Y. L. Wang, Y. Yao, Y. Liu, J. M. Zhang, Z. T. Zhang. CeO_2 Nanoparticle-Loaded MnO_2 Nanoflowers for Selective Catalytic Reduction of NO_x with NH_3 at Low Temperatures. Molecules, 27: 4863, 2022.

[71] T. Zhang, H. Z. Chang, K. Z. Li, Y. Peng, X. Li, J. H. Li. Different Exposed Facets VO_x/CeO_2 Catalysts for the Selective Catalytic Reduction of NO with NH_3. Chem. Eng. J., 349: 184-191, 2018.

[72] J. P. Wang, Z. Yan, L. L. Liu, Y. Y. Zhang, Z. T. Zhang, X. D. Wang. Low-temperature SCR of NO with NH_3 over Activated Semi-coke Composite-supported Rare Earth Oxides. Appl. Surf. Sci., 309: 1-10, 2014.

[73] J. Fan, P. Ning, Z. X. Song, X. Liu, L. Y. Wang, J. Wang, H. M. Wang, K. X. Long, Q. L. Zhang. Mechanistic Aspects of NH_3-SCR Reaction over CeO_2/TiO_2-ZrO_2-SO_4^{2-} Catalyst: In Situ DRIFTS Investigation. Chem. Eng. J., 334: 855-863, 2018.

[74] K. Zhang, J. J. Wang, P. F. Guan, N. Li, Z. J. Gong, R. Zhao, H. J. Luo, W. F. Wu. Low-temperature NH_3-SCR Catalytic Characteristic of Ce-Fe Solid Solutions based on Rare Earth Concentrate. Mater. Res. Bull., 128: 110871, 2020.

[75] Y. Ke, W. J. Huang, S. C. Li, Y. Liao, J. X. Li, Z. Qu, N. Q. Yan. Surface Acidity Enhancement of CeO_2 Catalysts via Modification with a Heteropoly Acid for the Selective Catalytic Reduction of NO with ammonia. Catal. Sci. Technol., 9: 5774-5785, 2019.

[76] J. Yang, S. Ren, M. Wang, Z. Chen, L. Chen, L. Liu. Time-resolved In Situ DRIFTS Study on NH_3-SCR of NO on a CeO_2/TiO_2 Catalyst. Catal. Sci. Technol., 12: 1245-1256, 2022.

[77] J. Yu, Z. C. Si, X. K. Li, L. Chen, X. D. Wu, D. Weng. Effect of Lean-oxygen Treatment on the Adsorption and Activity of Zirconium Phosphate @ $Ce_{0.75}Z_{0.25}O_2$ for NH_3-SCR $deNO_x$. Catal. Today, 267: 47-55, 2016.

[78] Y. H. Zhou, S. Ren, J. Yang, W. Z. Liu, Z. H. Su, Z. C. Chen, M. M. Wang, L. Chen. Effect of Oxygen Vacancies on Improving NO Oxidation over CeO_2 {111} and {100} Facets for Fast SCR Reaction. J. Environ. Chem. Eng., 9: 106218, 2021.

[79] R. L. Puurunen. Learnings from an Open Science Effort: Virtual Project on the History of ALD. ECS Trans., 86: 3-17, 2018.

[80] P. Hongmanorom, J. Ashok, S. Das, N. Dewangan, Z. Bian, G. Mitchell, S. Xi, A. Borgna, S. Kawi. Zr-Ce-incorporated Ni/SBA-15 catalyst for High-temperature Water Gas Shift Reaction: Methane Suppression by Incorporated Zr and Ce. J. Catal., 387: 47-61, 2020.

[81] O. Daoura, G. Fornasieri, M. Boutros, N. El Hassan, P. Beaunier, C. Thomas, M. Selmane, A. Miche, C. Sassoye, O. Ersen, W. Baaziz, P. Massiani, A. Bleuzen, F. Launay. One-pot Prepared Mesoporous Silica SBA-15-like Monoliths with Embedded Ni Particles as Selective and Stable Catalysts for Methane Dry Reforming. Appl. Catal. B-Environ., 280: 119417, 2021.

[82] J. W. Fan, X. F. Niu, W. Teng, P. Zhang, W. X. Zhang, D. Y. Zhao. Highly Dispersed Fe-Ce Mixed Oxide Catalysts Confined in Mesochannels toward Low-temperature Oxidation of Formaldehyde. J. Mater. Chem. A, 8: 17174-17184, 2020.

[83] A. Trovarelli. Catalytic Properties of Ceria and CeO_2-containing Materials. Catal. Rev., 38: 439-520, 1996.

[84] J. Strunk, W. C. Vining, A. T. Bell. Synthesis of Different CeO_2 Structures on Mesoporous Silica and Characterization of Their Reduction Properties. J. Phys Chem C, 115: 4114-4126, 2011.

[85] J. Shen, C. Hess. High Surface Area $VO_x/TiO_2/SBA$-15 Model Catalysts for Ammonia SCR Prepared by Atomic Layer Deposition. Catalysts, 10: 1386, 2020.

[86] N. N. Mikheeva, V. I. Zaikovskii, G. V. Mamontov. Synthesis of Ceria Nanoparticles in Pores of SBA-15: Pore Size Effect and Influence of Citric Acid Addition. Micropor. Mesopor. Mat., 277: 10-16, 2019.

[87] C. Chong, A. H. K. Owgi, N. Ainirazali, S. Y. Chin, H. D. Setiabudi. CO_2 Reforming of CH_4 over Ni/SBA-15 Prepared by Surfactant-assisted Impregnation Method: Comparative Study of Surfactant Types. Mater. Today-Proc., 5: 21644-21651, 2018.

[88] W. W. Yang, H. M. Liu, Y. M. Li, D. H. He. Interaction Mechanism of $Ni(NO_3)_2 \cdot 6H_2O$ and P123 in preparing highly-dispersed Ni/SBA-15 catalytic materials. Micropor. Mesopor. Mat., 228: 174-181, 2016.

[89] W. W. Yang, H. M. Liu, Y. M. Li, H. Wu, D. H. He. CO_2 Reforming of Methane to Syngas over Highly-stable Ni/SBA-15 Catalysts Prepared by P123-assisted Method. Int. J. Hydrogen Energ., 41: 1513-1523, 2016.

[90]   B. Dragoi, I. Mazilu, A. Chirieac, C. Ciotonea, A. Ungureanu, E. Marceau, E. Dumitriu, S. Royer. Highly Dispersed Copper (Oxide) Nanoparticles Prepared on SBA-15 Partially Occluded with the P123 Surfactant: toward the Design of Active Hydrogenation Catalysts. Catal. Sci. Technol., 7: 5376-5385, 2017.

[91]   Y. Yin, P. Tan, X. Q. Liu, J. Zhu, L. B. Sun. Constructing a Confined Space in Silica Nanopores: an Ideal Platform for the Formation and Dispersion of Cuprous Sites. J. Mater. Chem. A, 2: 3399-3406, 2014.

[92]   Y. Yin, Z. H. Wen, X. Q. Liu, A. H. Yuan, L. Shi. Functionalization of SBA-15 with CeO_2 Nanoparticles for Adsorptive Desulfurization: Matters of Template P123. Adsorpt. Sci. Technol., 36: 953-966, 2018.

[93]   Y. Yin, Z. F. Yang, Z. H. Wen, A. H. Yuan, X. Q. Liu, Z. Z. Zhang, H. Zhou. Modification of as Synthesized SBA-15 with Pt nanoparticles: Nanoconfinement Effects Give a Boost for Hydrogen Storage at Room Temperature. Sci. Rep., 7: 4509, 2017.

[94]   Y. Yin, H. Wu, L. Shi, J. Q. Zhang, X. Y. Xu, H. Y. Zhang, S. B. Wang, M. Sillanpaad, H. Q. Sun. Quasi Single Cobalt Sites in Nanopores for Superior Catalytic Oxidation of Organic Pollutants. Environ. Sci.-Nano, 5: 2842-2852, 2018.

[95]   Y. Yin, L. Shi, W. L. Li, X. N. Li, H. Wu, Z. M. Ao, W. J. Tian, S. M. Liu, S. B. Wang, H. Q. Sun. Boosting Fenton-Like Reactions via Single Atom Fe Catalysis. Environ. Sci. Technol., 53: 11391-11400, 2019.

[96]   A. Taratayko, Y. Larichev, V. Zaikovskii, N. Mikheeva, G. Mamontov. Ag–CeO_2/SBA-15 Composite Prepared from Pluronic P123@SBA-15 Hybrid as Catalyst for Room-temperature Reduction of 4-nitrophenol. Catal. Today, 375: 576-584, 2020.

[97]   M. T. Weller. Inorganic materials chemistry, Oxford University Press: Oxford, New York, 1994.

[98]   J. P. Thielemann, F. Girgsdies, R. Schlogl, C. Hess. Pore Structure and Surface Area of Silica SBA-15: Influence of Washing and Scale-up. Beilstein J. Nanotech., 2: 110-118, 2011.

[99]   S. Y. Chen, T. Mochizuki, Y. Abe, M. Toba, Y. Yoshimura, P. Somwongsa, S. Lao-ubol. Carbonaceous Ti-incorporated SBA-15 with Enhanced Activity and Durability for High-quality Biodiesel Production: Synthesis and Utilization of the P123 Template as Carbon Source. Appl. Catal. B-Environ., 181: 800-809, 2016.

[100]   E. A. Cochran, K. N. Woods, D. W. Johnson, C. J. Page, S. W. Boettcher. Unique Chemistries of Metal-nitrate Precursors to Form Metal-Oxide Thin Films from Solution: Materials for Electronic and Energy Applications. J. Mater. Chem. A, 7: 24124-24149, 2019.

[101]   W. Kang, D. O. Ozgur, A. Varma. Solution Combustion Synthesis of High Surface Area CeO_2 Nanopowders for Catalytic Applications: Reaction Mechanism and Properties. ACS Appl. Nano Mater., 1: 675-685, 2018.

[102]   A. M. Rijs, J. Oomens. Gas-Phase IR Spectroscopy and Structure of Biological Molecules. In Topics in Current Chemistry, Springer Cham, Switzerland, 2015.

[103]   Y. L. Liu, H. J. Kim. Fourier Transform Infrared Spectroscopy (FT-IR) and Simple Algorithm Analysis for Rapid and Non-Destructive Assessment of Developmental Cotton Fibers. Sensors, 17: 1469, 2017.

[104] A. Filtschew, K. Hofmann, C. Hess. Ceria and Its Defect Structure: New Insights from a Combined Spectroscopic Approach. J. Phys. Chem. C, 120: 6694-6703, 2016.

[105] A. Filtschew, D. Stranz, C. Hess. Mechanism of NO_2 Storage in Ceria Studied Using Combined In Situ Raman/FT-IR Spectroscopy. Phys. Chem. Chem. Phys., 15: 9066-9069, 2013.

[106] J. Seo, J. W. Lee, J. Moon, W. Sigmund, U. Paik. Role of the Surface Chemistry of Ceria Surfaces on Silicate Adsorption. ACS Appl. Mater. Interfaces, 6: 7388-7394, 2014.

[107] V. Nicolini, E. Varini, G. Malavasi, L. Menabue, M. C. Menziani, G. Lusvardi, A. Pedone, F. Benedetti, P. Luches. The Effect of Composition on Structural, Thermal, Redox and Bioactive Properties of Ce-containing Glasses. Materials & Design, 97: 73-85, 2016.

[108] C. M. Aiube, K. V. de Oliveira, J. L. de Macedo. Effect of Cerium Precursor in the Synthesis of Ce-MCM-41 and in the Efficiency for Liquid-Phase Oxidation of Benzyl Alcohol. Catalysts, 9: 377, 2019.

[109] S. Phokha, S. Pinitsoontorn, P. Chirawatkul, Y. Poo-arporn, S. Maensiri. Synthesis, Characterization, and Magnetic Properties of Monodisperse CeO_2 Nanospheres Prepared by PVP-assisted Hydrothermal Method. Nanoscale Res. Lett., 7: 425, 2012.

[110] C. X. Wang, D. Z. Ren, J. C. Du, Q. G. Qin, A. M. Zhang, L. Chen, H. Cui, J. L. Chen, Y. K. Zhao. In Situ Investigations on the Facile Synthesis and Catalytic Performance of CeO_2-Pt/Al_2O_3 Catalyst. Catalysts, 10: 143, 2020.

[111] J. Shen, S. Lauterbach, C. Hess. Rational Design of Mesoporous CuO–CeO_2 Catalysts for NH_3-SCR Applications Guided by Multiple In Situ Spectroscopies. ACS Appl. Mater. Interfaces, 14: 43407-43420, 2022.

[112] X. Sun, R. T. Guo, S. W. Liu, J. Liu, W. G. Pan, X. Shi, H. Qin, Z. Y. Wang, Z. Z. Qiu, X. Y. Liu. The Promoted Performance of CeO_2 Catalyst for NH_3-SCR Reaction by NH_3 Treatment. Appl. Surf. Sci., 462: 187-193, 2018.

[113] Z.-b. Xiong, Z.-z. Li, C.-x. Li, W. Wang, W. Lu, Y.-p. Du, S.-l. Tian. Green Synthesis of Tungsten-doped CeO_2 Catalyst for Selective Catalytic Reduction of NO_x with NH_3 Using Starch Bio-template. Appl. Surf. Sci., 536: 147719, 2021.

[114] X. Li, X. S. Li, J. H. Li, J. M. Hao. High Calcium Resistance of CeO_2-WO_3 SCR Catalysts: Structure Investigation and Deactivation Analysis. Chem. Eng. J., 317: 70-79, 2017.

[115] X. Li, J. H. Li, Y. Peng, X. S. Li, K. Z. Li, J. M. Hao. Comparison of the Structures and Mechanism of Arsenic Deactivation of CeO_2-MoO_3 and CeO_2-WO_3 SCR Catalysts. J. Phys. Chem. C, 120: 18005-18014, 2016.

[116] S. S. Liu, H. Wang, Y. Wei, R. D. Zhang. Core-shell Structure Effect on CeO_2 and TiO_2 Supported WO_3 for the NH_3-SCR Process. Mol. Catal., 485: 110822, 2020.

[117] T. R. Zhang, S. B. Ma, L. Q. Chen, R. Li, X. S. Leng, Y. S. Li, F. L. Yuan, X. Y. Niu, Y. J. Zhu. Effect of Cu Doping on the SCR Activity over the $Cu_mCe_{0.1-m}TiO_x$ (m=0.01, 0.02 and 0.03) catalysts. Appl. Catal. A-Gen., 570: 251-261, 2019.

[118] L. Chen, Z. C. Si, X. D. Wu, D. Weng, Z. W. Wu. Effect of Water Vapor on NH_3-NO/NO_2 SCR Performance of Fresh and Aged MnO_x-NbO_x-CeO_2 Catalysts. J. Environ. Sci., 31: 240-247, 2015.

[119] B. H. Zhao, R. Ran, X. G. Guo, L. Cao, T. F. Xu, Z. Chen, X. D. Wu, Z. C. Si, D. Weng. Nb-Modified Mn/Ce/Ti Catalyst for the Selective Catalytic Reduction of NO with NH_3 at Low Temperature. Appl. Catal. A-Gen., 545: 64-71, 2017.

[120] G. S. Qi, R. T. Yang, R. Chang. MnO_x-CeO_2 Mixed Oxides Prepared by Co-precipitation for Selective Catalytic Reduction of NO with NH_3 at Low Temperatures. Appl. Catal. B-Environ., 51: 93-106, 2004.

[121] Y. Peng, K. H. Li, J. H. Li. Identification of the Active Sites on CeO_2-WO_3 Catalysts for SCR of NO_x with NH_3: An In Situ IR and Raman Spectroscopy Study. Appl. Catal. B-Environ., 140: 483-492, 2013.

[122] X. B. Huang, P. Wang, J. Z. Tao, Z. S. Xi. CeO_2 Modified Mn-Fe-O Composites and Their Catalytic Performance for NH_3-SCR of NO. J. Inorg. Mater., 35: 573-580, 2020.

[123] N. Z. Yang, R. T. Guo, Y. Tian, W. G. Pan, Q. L. Chen, Q. S. Wang, C. Z. Lu, S. X. Wang. The Enhanced Performance of Ceria by HF Treatment for Selective Catalytic Reduction of NO with NH_3. Fuel, 179: 305-311, 2016.

[124] G. Ramis, G. Busca, F. Bregani, P. Forzatti. Fourier Transform-Infrared Study of the Adsorption and Coadsorption of Nitric-Oxide, Nitrogen-Dioxide and Ammonia on Vanadia Titania and Mechanism of Selective Catalytic Reduction. Appl. Catal., 64: 259-278, 1990.

[125] P. Zhang, R. T. Guo, L. J. Wu, W. G. Pan. The Enhancement of NH_3-SCR Performance for CeO_2 Catalyst by CO Pretreatment. Environ. Sci. Pollut. Res., 27: 13617-13636, 2020.

[126] J. Zhang, X. Q. Gong, G. Z. Lu. A DFT+U Study of NO Evolution at Reduced CeO_2(110). Phys. Chem. Chem. Phys., 16: 16904-16908, 2014.

[127] A. Filtschew, C. Hess. Unravelling the Mechanism of NO and NO_2 Storage in Ceria: The Role of Defects and Ce-O Surface Sites. Appl. Catal. B-Environ., 237: 1066-1081, 2018.

[128] K. I. Hadjiivanov. Identification of Neutral and Charged N_xO_y Surface Species by IR Spectroscopy. Catal. Rev., 42: 71-144, 2000.

[129] A. Joshi, A. Rammohan, Y. Jiang, S. Ogunwumi. Density Functional Theory (DFT) Study of the Interaction of Ammonia with Pure and Tungsten-doped Ceria. J. Mol. Struc.-Theochem., 912: 73-81, 2009.

[130] Z. L. Wu, A. K. P. Mann, M. J. Li, S. H. Overbury. Spectroscopic Investigation of Surface-Dependent Acid Base Property of Ceria Nanoshapes. J. Phys. Chem. C, 119: 7340-7350, 2015.

[131] M. G. Cutrufello, I. Ferino, V. Solinas, A. Primavera, A. Trovarelli, A. Auroux, C. Picciau. Acid-base Properties and Catalytic Activity of Nanophase Ceria-zirconia Catalysts for 4-methylpentan-2-ol dehydration. Phys. Chem. Chem. Phys., 1: 3369-3375, 1999.

[132] K. Liu, F. D. Liu, L. J. Xie, W. P. Shan, H. He. DRIFTS Study of a Ce-W Mixed Oxide Catalyst for the Selective Catalytic Reduction of NO_x with NH_3. Catal. Sci. Technol., 5: 2290-2299, 2015.

[133] R. Wu, N. Q. Zhang, L. C. Li, H. He, L. Y. Song, W. G. Qiu. DRIFT Study on Promotion Effect of the Keggin Structure over V_2O_5-MoO_3/TiO_2 Catalysts for Low Temperature NH_3-SCR Reaction. Catalysts, 8: 143, 2018.

[134] J. M. G. Amores, V. S. Escribano, G. Ramis, G. Busca. An FT-IR Study of Ammonia Adsorption and Oxidation over Anatase-supported Metal Oxides. Appl. Catal. B-Environ., 13: 45-58, 1997.

[135] S. X. Wang, Z. W. Chen, B. N. He, Z. Yan, H. Wang, L. L. Liu, X. D. Wang. In Situ DRIFTS Investigation on CeO_x Catalyst Supported by Fly-Ash-Made Porous Cordierite Ceramics for Low-Temperature NH_3-SCR of NO_x. Catalysts, 9: 496, 2019.

[136] P. Wang, H. M. Zhao, H. Sun, H. T. Yu, S. Chen, X. Quan. Porous Metal-organic Framework MIL-100(Fe) as an Efficient Catalyst for the Selective Catalytic Reduction of NO_x with NH_3. RSC Adv., 4: 48912-48919, 2014.

[137] L. A. Chen, J. H. Li, M. F. Ge. DRIFT Study on Cerium-Tungsten/Titiania Catalyst for Selective Catalytic Reduction of NO_x with NH_3. Environ. Sci. Technol., 44: 9590-9596, 2010.

[138] K. Hadjiivanov, D. Klissurski, G. Ramis, G. Busca. Fourier Transform IR Study of NO_x Adsorption on a Cu-ZSM-5 $DeNO_x$ catalyst. Appl. Catal. B-Environ., 7: 251-267, 1996.

[139] G. Ramis, L. Yi, G. Busca, M. Turco, E. Kotur, R. J. Willey. Adsorption, Activation, and Oxidation of Ammonia over SCR Catalysts. J. Catal., 157: 523-535, 1995.

[140] G. Martra, E. Borello, E. Giamello, S. Coluccia. Acid-Base Catalysis II. Elsevier, Amsterdam, 1994.

[141] V. A. Matyshak, O. V. Krylov. In situ IR Spectroscopy of Intermediates in Heterogeneous Oxidative Catalysis. Catal. Today, 25: 1-87, 1995.

[142] M. E. C. Villalba, C. A. Franca, J. A. Guida. Photo Release of Nitrous Oxide from the Hyponitrite Ion Studied by Infrared Spectroscopy. Evidence for the Generation of a Cobalt-N_2O Complex. Experimental and DFT calculations. Spectrochimi. ACTA A, 176: 189-196, 2017.

[143] H. A. Ghouti, A. Zegaoui, M. Derradji, W. A. Cai, J. Wang, W. B. Liu, A. Q. Dayo. Multifunctional Hybrid Composites with Enhanced Mechanical and Thermal Properties Based on Polybenzoxazine and Chopped Kevlar/Carbon Hybrid Fibers. Polymers-Basel, 10: 1308 2018.

[144] G. E. Moore. The Spectrum of Nitrogen Dioxide in the 1.4-3.4μ Region and the Vibrational and Rotational Constants of the NO_2 Molecule. J. Opt. Soc. Am., 43: 1045-1050, 1953.

[145] B. Q. Jiang, Z. B. Wu, Y. Liu, S. C. Lee, W. K. Ho. DRIFT Study of the SO_2 Effect on Low-Temperature SCR Reaction over Fe-Mn/TiO_2. J. Phys. Chem. C, 114: 4961-4965, 2010.

[146] L. Zhang, J. Pierce, V. L. Leung, D. Wang, W. S. Epling. Characterization of Ceria's Interaction with NO_x and NH_3. J. Phys. Chem. C, 117: 8282-8289, 2013.

[147] H. Y. Zhu, Y. J. Li, X. L. Zheng. In-situ DRIFTS Study of CeO_2 Supported Rh Catalysts for N_2O Decomposition. Appl. Catal. A-Gen., 571: 89-95, 2019.

[148] K. Hadjiivanov, J. Saussey, J. L. Freysz, J. C. Lavalley. FT-IR Study of $NO+O_2$ Co-adsorption on H-ZSM-5: Re-assignment of the 2133 cm^{-1} band to NO^+ species. Catal. Lett., 52: 103-108, 1998.

[149] R. Kato, J. Rolfe. Vibration Frequencies of NO_2^- and NO_3^- Ions in Kbr Crystals. J. Chem. Phys., 47: 1901, 1967.

[150] J. M. Dorhout, A. S. Anderson, E. Batista, R. K. Carlson, R. P. Currier, R. K. Martinez, S. M. Clegg, M. P. Wilkerson, K. Nowak-Lovato. NO_x Speciation from Copper Dissolution in Nitric Acid/Water Solutions Using FTIR Spectroscopy. J. Mol. Spectrosc., 372: 111334, 2020.

[151] M. J. Pavlovich, T. Ono, C. Galleher, B. Curtis, D. S. Clark, Z. Machala, D. B. Graves. Air spark-like Plasma Source for Antimicrobial NO_x Generation. J. Phys. D-Appl. Phys., 47: 505202, 2014.

[152] P. C. Gomez, O. Galvez, R. G. Mosteo, C. Puzzarini, R. Escribano. Clusters of Atmospheric Relevance: H_2O/HCl/HNO_3. Prediction of IR & MW Spectra. Phys. Chem. Chem. Phys., 12: 4617-4624, 2010.

[153] R. M. Escribano, D. Fernandez-Torre, V. J. Herrero, B. Martin-Llorente, B. Mate, I. K. Ortega, H. Grothe. The Low-frequency Raman and IR Spectra of Nitric Acid Hydrates. Vib. Spectrosc., 43: 254-259, 2007.

[154] V. I. Parvulescu, P. Grange, B. Delmon. Effect of Coexchanging with a Second Metal upon the Interaction of Nitric Oxide with Cu-ZSM-5. J. Phys. Chem. B, 101: 6933-6942, 1997.

[155] A. Zecchina, C. O. Arean, G. T. Palomino, F. Geobaldo, C. Lamberti, G. Spoto, S. Bordiga. The Vibrational Spectroscopy of H_2, N_2, CO and NO Adsorbed on the Titanosilicate Molecular Sieve ETS-10. Phys. Chem. Chem. Phys., 1: 1649-1657, 1999.

[156] T. Wang, C. T. Li, L. K. Zhao, J. Y. Zhang, S. H. Li, G. M. Zeng. The Catalytic Performance and Characterization of ZrO_2 Support Modification on CuO-CeO_2/TiO_2 Catalyst for the Simultaneous Removal of Hg^0 and NO. Appl. Surf. Sci., 400: 227-237, 2017.

[157] L. Wang, Z. Sofer, M. Pumera. Will Any Crap We Put into Graphene Increase Its Electrocatalytic Effect? ACS Nano, 14: 21-25, 2020.

[158] D. Y. Zhao, J. Y. Sun, Q. Z. Li, G. D. Stucky. Morphological Control of Highly Ordered Mesoporous Silica SBA-15. Chem. Mater., 12: 275, 2000.

[159] S. Weber, A. Diaz, M. Holler, A. Schropp, M. Lyubomirskiy, K. L. Abel, M. Kahnt, A. Jeromin, S. Kulkarni, T. F. Keller, R. Glaser, T. L. Sheppard. Evolution of Hierarchically Porous Nickel Alumina Catalysts Studied by X-Ray Ptychography. Adv. Sci., 9: 2105432, 2022.

[160] A. I. Frenkel, Q. Wang, N. Marinkovic, J. G. Chen, L. Barrio, R. Si, A. L. Camara, A. M. Estrella, J. A. Rodriguez, J. C. Hanson. Combining X-ray Absorption and X-ray Diffraction Techniques for In Situ Studies of Chemical Transformations in Heterogeneous Catalysis: Advantages and Limitations. J. Phys. Chem. C, 115: 17884-17890, 2011.

[161] S. H. Zeng, W. L. Zhang, M. Sliwa, H. Q. Su. Comparative Study of CeO_2/CuO and CuO/CeO_2 Catalysts on Catalytic Performance for Preferential CO Oxidation. Int. J. Hydrogen Energ., 38: 3597-3605, 2013.

[162] Z. X. Yang, L. G. Xie, D. W. Ma, G. T. Wang. Origin of the High Activity of the Ceria-Supported Copper Catalyst for H_2O Dissociation. J. Phys. Chem. C, 115: 6730-6740, 2011.

[163] C. T. Nottbohm, C. Hess. Investigation of Ceria by Combined Raman, UV-Vis and X-ray Photoelectron Spectroscopy. Catal. Commun., 22: 39-42, 2012.

[164] D. Q. Gao, J. Zhang, J. Y. Zhu, J. Qi, Z. H. Zhang, W. B. Sui, H. G. Shi, D. S. Xue. Vacancy-Mediated Magnetism in Pure Copper Oxide Nanoparticles. Nanoscale Res. Lett., 5: 769-772, 2010.

[165] C. Q. Zhu, A. Osherov, M. J. Panzer. Surface Chemistry of Electrodeposited Cu_2O Films Studied by XPS. Electrochim. ACTA, 111: 771-778, 2013.

[166] J. R. A. Sietsma, J. D. Meeldijk, J. P. den Breejen, M. Versluijs-Helder, A. J. van Dillen, P. E. de Jong, K. P. de Jong. The Preparation of Supported NiO and Co_3O_4 Nanoparticles by the

Nitric Oxide Controlled Thermal Decomposition of Nitrates. Angew. Chem.-Int. Ed., 46: 4547-4549, 2007.

[167] I. V. Morozov, K. O. Znamenkov, Y. M. Korenev, O. A. Shlyakhtin. Thermal Decomposition of $Cu(NO_3)_2 \cdot 3H_2O$ at Reduced Pressures. Thermochim. ACTA, 403: 173-179, 2003.

[168] S. Yuvaraj, L. Fan-Yuan, C. Tsong-Huei, Y. Chuin-Tih. Thermal Decomposition of Metal Nitrates in Air and Hydrogen Environments. J. Phys. Chem. B, 107: 1044-1047, 2003.

[169] B. A. Morrow, A. J. Mcfarlan. Surface Vibrational-Modes of Silanol Groups on Silica. J. Phys. Chem.-Us, 96: 1395-1400, 1992.

[170] A. Sakthivel, F. M. Pedro, A. S. T. Chiang, F. E. Kuhn. Grafting of Cyclopentadienyl Ruthenium Complexes on Aminosilane Linker Modified Mesoporous SBA-15 Silicates. Dalton Trans., 3: 320-326, 2007.

[171] K. Hadjiivanov. Identification and Characterization of Surface Hydroxyl Groups by Infrared Spectroscopy. Adv. Catal., 57: 99-318, 2014.

[172] W. W. Wendlandt, J. L. Bear. Thermal Decomposition of the Heavier Rare-Earth Metal Nitrate Hydrates - Thermobalance and Differential Thermal Analysis Studies. J. Inorg. Nucl. Chem., 12: 276-280, 1960.

[173] M. M. Sabzehmeidani, H. Karimi, M. Ghaedi. Enhanced Visible Light-Active $CeO_2/CuO/Ag_2CrO_4$ Ternary Heterostructures Based on CeO_2/CuO Nanofiber Heterojunctions for the Simultaneous Degradation of a Binary Mixture of Dyes. New J. Chem., 44: 5033-5048, 2020.

[174] J. J. Guo, Y. Peng, Y. N. Zhang, W. N. Yang, L. N. Gan, K. Z. Li, J. J. Chen, J. H. Li. Comparison of NH_3-SCO Performance over CuO_x/H-SSZ-13 and CuO_x/H-SAPO-34 Catalysts. Appl. Catal. A-Gen., 585: 117119, 2019.

[175] S. Pande, M. G. Weir, B. A. Zaccheo, R. M. Crooks. Synthesis, Characterization, and Electrocatalysis Using Pt and Pd Dendrimer-encapsulated Nanoparticles Prepared by Galvanic Exchange. New J. Chem., 35: 2054-2060, 2011.

[176] T. F. Pascher, M. Oncak, C. van der Linde, M. K. Beyer. Spectroscopy and Photochemistry of Copper Nitrate Clusters. Phys. Chem. Chem. Phys., 23: 9911-9920, 2021.

[177] R. Bosigo, L. M. Lepodise, A. Kuvarega, C. Muiva. Hydrothermal synthesis of CuO and CeO_2/CuO Nanostructures: Spectroscopic and Temperature Dependent Electrical Properties. J Mater. Sci.-Mater. El., 32: 7136-7152, 2021.

[178] M. Y. Mihaylov, V. R. Zdravkova, E. Z. Ivanova, H. A. Aleksandrov, P. St Petkov, G. N. Vayssilov, K. I. Hadjiivanov. Infrared Spectra of Surface Nitrates: Revision of the Current Opinions Based on the Case Study of Ceria. J. Catal., 394: 245-258, 2021.

[179] M. Xu, J. P. Larentzos, M. Roshdy, L. J. Criscenti, H. C. Allen. Aqueous Divalent Metal-Nitrate Interactions: Hydration Versus Ion Pairing. Phys. Chem. Chem. Phys., 10: 4793-4801, 2008.

[180] M. N. Jackson, M. K. Kamunde-Devonish, B. A. Hammann, L. A. Wills, L. B. Fullmer, S. E. Hayes, P. H. Y. Cheong, W. H. Casey, M. Nyman, D. W. Johnson. An Overview of Selected Current Approaches to the Characterization of Aqueous Inorganic Clusters. Dalton Trans., 44: 16982-17006, 2015.

[181] W. W. Rudolph, C. C. Pye. Gallium(III) Hydration in Aqueous Solution of Perchlorate, Nitrate and Sulfate. Raman and [71]Ga NMR Spectroscopic Studies and ab initio Molecular Orbital Calculations of Gallium(III) Water Clusters. Phys. Chem. Chem. Phys., 4: 4319-4327, 2002.

[182] S. Chen, C. Hu, W. Zhang, J. Chen. A Self-Assembling Octahedral Aggregate of Poly(methyl methacrylate) Nanospheres on a Silver Substrate. Chempluschem, 81: 161-165, 2016.

[183] V. Hayez, V. Costa, J. Guillaume, H. Terryn, A. Hubin. Micro Raman Spectroscopy Used for the Study of Corrosion Products on Copper Alloys: Study of the Chemical Composition of Artificial Patinas Used for Restoration Purposes. Analyst, 130: 550-556, 2005.

[184] W. W. Wang, P. P. Du, S. H. Zou, H. Y. He, R. X. Wang, Z. Jin, S. Shi, Y. Y. Huang, R. Si, Q. S. Song, C. J. Jia, C. H. Yan. Highly Dispersed Copper Oxide Clusters as Active Species in Copper-Ceria Catalyst for Preferential Oxidation of Carbon Monoxide. ACS Catal., 5: 2088-2099, 2015.

[185] R. Si, J. Raitano, N. Yi, L. H. Zhang, S. W. Chan, M. Flytzani-Stephanopoulos. Structure Sensitivity of the Low-temperature Water-gas Shift Reaction on $Cu-CeO_2$ Catalysts. Catal. Today, 180: 68-80, 2012.

[186] J. F. Chen, Y. Y. Zhan, J. J. Zhu, C. Q. Chen, X. Y. Lin, Q. Zheng. The Synergetic Mechanism between Copper Species and Ceria in NO Abatement over Cu/CeO_2 Catalysts. Appl. Catal. A-Gen., 377: 121-127, 2010.

[187] M. Konsolakis. The Role of Copper-Ceria Interactions in Catalysis Science: Recent Theoretical and Experimental Advances. Appl. Catal. B-Environ., 198: 49-66, 2016.

[188] C. T. Campbell. Catalyst-support Interactions Electronic Perturbations. Nat. Chem., 4: 597-598, 2012.

[189] L. Ma, M. F. Luo, S. Y. Chen. Redox Behavior and Catalytic Properties of $CuO/Ce_{0.8}Zr_{0.2}O_2$ Catalysts. Appl. Catal. A-Gen., 242: 151-159, 2003.

[190] S. Andreoli, F. A. Deorsola, R. Pirone. MnO_x-CeO_2 Catalysts Synthesized by Solution Combustion Synthesis for the Low-temperature NH_3-SCR. Catal. Today, 253: 199-206, 2015.

[191] J. Shen, C. Hess. Controlling the Dispersion of Ceria Using Nanoconfinement: Application to CeO_2/SBA-15 Catalysts for NH_3-SCR. Mater. Adv., 2: 7400-7412, 2021.

[192] D. Mukherjee, P. Venkataswamy, D. Devaiah, A. Rangaswamy, B. M. Reddy. Crucial Role of Titanium Dioxide Support in Soot Oxidation Catalysis of Manganese Doped Ceria. Catal. Sci. Technol., 7: 3045-3055, 2017.

[193] Q. Zhang, Y. Jiang, J. Gao, M. Fu, S. Zou, Y. Li, D. Ye. Interfaces in MOF-Derived CeO_2-MnO_x Composites as High-Activity Catalysts for Toluene Oxidation: Monolayer Dispersion Threshold. Catalysts, 10: 681, 2020.

[194] H. B. Wang, Y. Chen, N. Li, Y. M. Liu. A Fluorescent Glucose Bioassay Based on the Hydrogen Peroxide-induced Decomposition of a Quencher System Composed of MnO_2 Nanosheets and Copper Nanoclusters. Microchim. ACTA, 184: 515-523, 2017.

[195] J. Hernandez-Paredes, D. Glossman-Mitnik, H. E. Esparza-Ponce, M. E. Alvarez-Ramos, A. Duarte-Moller. Band Structure, Optical Properties and Infrared Spectrum of Glycine-Sodium Nitrate Crystal. J. Mol. Struct., 875: 295-301, 2008.

[196] V. Tsaryuk, V. Savchenko, V. J. J. o. A. S. Kudryashova. Influence of the Effective Ligand Charge on the Intensity Distribution in Vibronic Spectra of Europium Nitrates. J. Appl. Spectrosc., 60: 373-380, 1994.

[197] D. Meng, W. Zhan, Y. Guo, Y. Guo, L. Wang, G. Lu. A Highly Effective Catalyst of Sm-MnO$_x$ for the NH$_3$-SCR of NO$_x$ at Low Temperature: Promotional Role of Sm and Its Catalytic Performance. ACS Catal., 5: 5973-5983, 2015.

[198] Y. Z. Liu, Q. Y. Xu, R. T. Guo, C. P. Duan, G. L. Wu, Y. F. Miao, J. W. Gu. Enhancement of the Activity of Cu/TiO$_2$ Catalyst by Eu Modification for Selective Catalytic Reduction of NO$_x$ with NH$_3$. Environ. Sci. Pollut. Res., 27: 27663-27673, 2020.

[199] B. J. O'Neill, D. H. K. Jackson, J. Lee, C. Canlas, P. C. Stair, C. L. Marshall, J. W. Elam, T. F. Kuech, J. A. Dumesic, G. W. Huber. Catalyst Design with Atomic Layer Deposition. ACS Catal., 5: 1804-1825, 2015.

[200] S. S. R. Putluru, L. Schill, A. Godiksen, R. Poreddy, S. Mossin, A. D. Jensen, R. Fehrmann. Promoted V$_2$O$_5$/TiO$_2$ Catalysts for Selective Catalytic Reduction of NO with NH$_3$ at Low Temperatures. Appl. Catal. B-Environ., 183: 282-290, 2016.

[201] M. A. Reiche, E. Ortelli, A. Baiker. Vanadia Grafted on TiO$_2$-SiO$_2$, TiO$_2$ and SiO$_2$ aerogels - Structural Properties and Catalytic Behaviour in Selective Reduction of NO by NH$_3$. Appl. Catal. B-Environ., 23: 187-203, 1999.

[202] G. Z. He, Z. H. Lian, Y. B. Yu, Y. Yang, K. Liu, X. Y. Shi, Z. D. Yan, W. P. Shan, H. He. Polymeric Vanadyl Species Determine the Low-temperature Activity of V-based Catalysts for the SCR of NO$_x$ with NH$_3$. Sci. Adv., 4: 4637, 2018.

[203] I. Song, S. Youn, H. Lee, S. G. Lee, S. J. Cho, D. H. Kim. Effects of Microporous TiO$_2$ Support on the Catalytic and Structural Properties of V$_2$O$_5$/Microporous TiO$_2$ for the Selective Catalytic Reduction of NO by NH$_3$. Appl. Catal. B-Environ., 210: 421-431, 2017.

[204] P. Ruff, L. Schumacher, S. Rogg, C. Hess. Atomic Layer Deposition-Assisted Synthesis of Embedded Vanadia Catalysts. ACS Catal., 9: 6349-6361, 2019.

[205] C. Hess. Direct Correlation of the Dispersion and Structure in Vanadium Oxide Supported on Silica SBA-15. J. Catal., 248: 120-123, 2007.

[206] C. Hess, P. Waleska, M. Ratzka, T. V. W. Janssens, S. B. Rasmussen, P. Beato. Hierarchical Vanadia Model Catalysts for Ammonia Selective Catalytic Reduction. Top. Catal., 60: 1631-1640, 2017.

[207] Y. Segura, L. Chmielarz, P. Kustrowski, P. Cool, R. Dziembaj, E. F. Vansant. Characterisation and Reactivity of Vanadia-titania Supported SBA-15 in the SCR of NO with Ammonia. Appl. Catal. B-Environ., 61: 69-78, 2005.

[208] J. L. Lu, J. W. Elam, P. C. Stair. Atomic Layer Deposition-Sequential Self-limiting Surface Reactions for Advanced Catalyst "Bottom-up" Synthesis. Surf. Sci. Rep., 71: 410-472, 2016.

[209] S. Z. Li, J. H. Xu, L. X. Wang, N. Yang, X. J. Ye, X. Yuan, H. T. Xiang, C. Liu, H. B. Li. Effect of Post-deposition Annealing on Atomic Layer Deposited SiO$_2$ Film for Silicon Surface Passivation. Mat. Sci. Semicon. Proc., 106: 104777, 2020.

[210] S. Fengler, H. Kriegl, M. Schieda, H. Gutzmann, T. Klassen, M. Wollgarten, T. Dittrich. Charge Transfer in c-Si(n^{++})/TiO$_2$(ALD) at the Amorphous/Anatase Transition: A Transient Surface Photovoltage Spectroscopy Study. <u>ACS Appl. Mater. Interfaces</u>, 12: 3140-3149, 2020.

[211] I. A. Samek, N. S. Bobbitt, R. Q. Snurr, P. C. Stair. Interactions of VO$_x$ Species with Amorphous TiO$_2$ Domains on ALD-Derived Alumina-Supported Materials. <u>J Phys. Chem. C</u>, 123: 7988-7999, 2019.

[212] J. Keranen, C. Guimon, A. Auroux, E. I. Iiskola, L. Niinisto. Gas-phase Synthesis, Structure and Surface Acid-base Properties of Highly Dispersed Vanadia/Titania/Silica Catalysts. <u>Phys. Chem. Chem. Phys.</u>, 5: 5333-5342, 2003.

[213] J. Keranen, C. Guimon, E. Liskola, A. Auroux, L. Niinisto. Atomic Layer Deposition and Surface Characterization of Highly Dispersed Titania/Silica-supported Vanadia Catalysts. <u>Catal. Today</u>, 78: 149-157, 2003.

[214] P. Ruff, S. Lauterbach, H. J. Kleebe, C. Hess. Surface Structuring of Mesoporous Materials by Controlled Synthesis of Nanocavities. <u>Micropor. Mesopor. Mat.</u>, 235: 160-169, 2016.

[215] Y. Huang, D. M. Gao, Z. Q. Tong, J. F. Zhang, H. Luo. Oxidation of NO over Cobalt Oxide Supported on Mesoporous Silica. <u>J. Nat. Gas Chem.</u>, 18: 421-428, 2009.

[216] Q. Zhang, L. S. Ma, M. H. Shao, J. Z. Huang, M. Ding, X. L. Deng, X. Q. Wei, X. J. Xu. Anodic Oxidation Synthesis of One-Dimensional TiO$_2$ Nanostructures for Photocatalytic and Field Emission Properties. <u>J. Nanomater.</u>, 2014: 831752, 2014.

[217] P. Waleska, S. Rupp, C. Hess. Operando Multiwavelength and Time-Resolved Raman Spectroscopy: Structural Dynamics of a Supported Vanadia Catalyst at Work. <u>J. Phys. Chem. C</u>, 122: 3386-3400, 2018.

[218] C. K. P. Neeli, V. S. P. Ganjala, V. Vakati, K. S. R. Rao, D. R. Burri. V$_2$O$_5$/SBA-15 Nanocatalysts for the Selective Synthesis of 2,3,5-trimethyl-1,4-benzoquinone at Room Temperature. <u>New J. Chem.</u>, 40: 679-686, 2016.

[219] M. Chligui, G. Guimbretiere, A. Canizares, G. Matzen, Y. Vaills, P. Simon. New Features in the Raman Spectrum of Silica: Key-points in the Improvement on Structure Knowledge. <u>hal-00520823</u>, 2010.

[220] T. Huang, Z. G. Hu, G. S. Xu, X. L. Zhang, J. Z. Zhang, J. H. Chu. Inherent Optical Behavior and Structural Variation in Na$_{0.5}$Bi$_{0.5}$TiO$_3$-6% BaTiO$_3$ Revealed by Temperature Dependent Raman Scattering and Ultraviolet-visible Transmittance. <u>Appl. Phys. Lett.</u>, 104: 111908, 2014.

[221] G. E. Walrafen, Y. C. Chu, M. S. Hokmabadi. Raman Spectroscopic Investigation of Irreversibly Compacted Vitreous Silica. <u>J. Chem. Phys.</u>, 92: 6987-7002, 1990.

[222] C. Li, G. Xiong, J. Liu, P. Ying, Q. Xin, Z. Feng. Identifying Framework Titanium in TS-1 Zeolite by UV Resonance Raman Spectroscopy. <u>J. Phys. Chem. B</u>, 105: 2993-2997, 2001.

[223] C. Hess, G. Tzolova-Muller, R. Herbert. The Influence of Water on the Dispersion of Vanadia Supported on Silica SBA-15: A Combined XPS and Raman Study. <u>J. Phys. Chem. C</u>, 111: 9471-9479, 2007.

[224] M. A. Eberhardt, A. Proctor, M. Houalla, D. M. Hercules. Investigation of V Oxidation States in Reduced V/Al$_2$O$_3$ Catalysts by XPS. <u>J. Catal.</u>, 162: 368, 1996.

[225] Y. X. Pan, W. Zhao, Q. Zhong, W. Cai, H. Y. Li. Promotional Effect of Si-doped V_2O_5/TiO_2 for Selective Catalytic Reduction of NO_x by NH_3. J. Environ. Sci., 25: 1703-1711, 2013.

[226] D. Nitsche, C. Hess. Structure of Isolated Vanadia and Titania: A Deep UV Raman, UV-Vis, and IR Spectroscopic Study. J. Phys. Chem. C, 120: 1025-1037, 2016.

[227] P. Waleska, C. Hess. Structural Dynamics of Dispersed Titania During Dehydration and Oxidative Dehydrogenation Studied by In Situ UV Raman Spectroscopy. Catal. Lett., 148: 2537-2547, 2018.

[228] X. T. Gao, S. R. Bare, J. L. G. Fierro, M. A. Banares, I. E. Wachs. Preparation and In-situ Spectroscopic Characterization of Molecularly Dispersed Titanium Oxide on Silica. J. Phys. Chem. B, 102: 5653-5666, 1998.

[229] B. Beck, M. Harth, N. G. Hamilton, C. Carrero, J. J. Uhlrich, A. Trunschke, S. Shaikhutdinov, H. Schubert, H. J. Freund, R. Schlogl, J. Sauer, R. Schomacker. Partial Oxidation of Ethanol on Vanadia Catalysts on Supporting Oxides with Different Redox Properties Compared to Propane. J. Catal., 296: 120-131, 2012.

[230] M. Schramlmarth, A. Wokaun, M. Pohl, H. L. Krauss. Spectroscopic Investigation of the Structue of Silica-supported Vanadium-Oxide Catalysts at Submonolayer Coverages. J. Chem. Soc.-Faraday Trans., 87: 2635-2646, 1991.

[231] F. Arena, F. Frusteri, G. Martra, S. Coluccia, A. Parmaliana. Surface Structures, Reduction Pattern and Oxygen Chemisorption of V_2O_5/SiO_2 Catalysts. J. Chem. Soc.-Faraday Trans., 93: 3849-3854, 1997.

[232] D. W. Kwon, K. H. Park, S. C. Hong. Influence of VO_x, Surface Density and Vanadyl Species on the Selective Catalytic Reduction of NO by NH_3 over VO_x/TiO_2 for Superior Catalytic Activity. Appl. Catal. A-Gen., 499: 1-12, 2015.

[233] L. J. Burcham, G. Deo, X. T. Gao, I. E. Wachs. In situ IR, Raman, and UV-Vis DRS Spectroscopy of Supported Vanadium Oxide Catalysts during Methanol Oxidation. Top. Catal., 11: 85-100, 2000.

[234] X. T. Gao, I. E. Wachs. Investigation of Surface Structures of Supported Vanadium Oxide Catalysts by UV-Vis-NIR Diffuse Reflectance Spectroscopy. J. Phys. Chem. B, 104: 1261-1268, 2000.

[235] D. Srinivas, W. F. Holderich, S. Kujath, M. H. Valkenberg, T. Raja, L. Saikia, R. Hinze, V. Ramaswamy. Active Sites in Vanadia/Titania Catalysts for Selective Aerial Oxidation of Beta-picoline to Nicotinic Acid. J. Catal., 259: 165-173, 2008.

[236] E. A. Davis, N. F. Mott. Conduction in Non-crystalline Systems 5. Conductivity, Optical Absorption and Photoconductivity in Amophous Semiconductors. Philos. Mag., 22: 903, 1970.

[237] J. Tauc. Absorption Edge and Internal Eletric Fields in Amophous Semiconductors. Mat. Res. Bull., 5: 721, 1970.

[238] P. S. Waleska, C. Hess. Oligomerization of Supported Vanadia: Structural Insight Using Surface-Science Models with Chemical Complexity. J. Phys. Chem. C, 120: 18510-18519, 2016.

[239] H. Kamata, K. Takahashi, C. U. I. Odenbrand. The Role of K_2O in the Selective Reduction of NO with NH_3 over a $V_2O_5(WO_3)$/TiO_2 Commercial Selective Catalytic Reduction Catalyst. J. Mol. Catal. A-Chem., 139: 189-198, 1999.

[240] J. L. Lu, K. M. Kosuda, R. P. Van Duyne, P. C. Stair. Surface Acidity and Properties of TiO_2/SiO_2 Catalysts Prepared by Atomic Layer Deposition: UV-visible Diffuse Reflectance, DRIFTS, and Visible Raman Spectroscopy Studies. J. Phys. Chem. C, 113: 12412-12418, 2009.

[241] K. Cheng, J. Liu, Z. Zhao, Y. C. Wei, G. Y. Jiang, A. J. Duan. Direct synthesis of V-W-Ti Nanoparticle Catalysts for Selective Catalytic Reduction of NO with NH_3. RSC Adv., 5: 45172-45183, 2015.

[242] M. Anstrom, N. Y. Topsoe, J. A. Dumesic. Density Functional Theory Studies of Mechanistic Aspects of the SCR Reaction on Vanadium Oxide Catalysts. J. Catal., 213: 115-125, 2003.

[243] M. Farber, S. P. Harris. Kinetics of NH_3-NO Reactions on Vanadium-oxide Catalysts. J. Phys. Chem.-Us, 88: 680-682, 1984.

[244] H. C. Yao, Y. Chen, Z. Zhao, Y. C. Wei, Z. C. Liu, D. Zhai, B. J. Liu, C. M. Xu. Periodic DFT Study on Mechanism of Selective Catalytic Reduction of NO via NH_3 and O_2 over the V_2O_5 (001) Surface: Competitive Sites and Pathways. J. Catal., 305: 67-75, 2013.

[245] S. J. Yang, C. Z. Wang, L. Ma, Y. Peng, Z. Qu, N. Q. Yan, J. H. Chen, H. Z. Chang, J. H. Li. Substitution of WO_3 in V_2O_5/WO_3-TiO_2 by Fe_2O_3 for Selective Catalytic Reduction of NO with NH_3. Catal. Sci. Technol., 3: 161-168, 2013.

[246] L. G. Pinaeva, A. P. Suknev, A. A. Budneva, E. A. Paukshtis, B. S. Balzhinimaev. On the Role of Oxygen in the Reaction of NO Reduction by NH_3 over Monolayer V_2O_5-TiO_2 Catalyst. J. Mol. Catal. A-Chem., 112: 115-124, 1996.

[247] O. Mihai, D. Creaser, L. Olsson. Adsorption and Oxidation Investigations over Pt/Al_2O_3 Catalyst: A Microcalorimetric Study. Catalysts, 6: 73, 2016.

[248] A. Klyushina, K. Pacultova, K. Karaskova, K. Jiratova, M. Ritz, D. Fridrichova, A. Volodarskaja, L. Obalova. Effect of Preparation Method on Catalytic Properties of Co-Mn-Al Mixed Oxides for N_2O Decomposition. J. Mol. Catal. A-Chem., 425: 237-247, 2016.

[249] N. Hamilton, T. Wolfram, G. T. Muller, M. Havecker, J. Krohnert, C. Carrero, R. Schomacker, A. Trunschke, R. Schlogl. Topology of Silica Supported Vanadium-titanium Oxide Catalysts for Oxidative Dehydrogenation of Propane. Catal. Sci. Technol., 2: 1346-1359, 2012.

[250] J. M. Jehng, I. E. Wachs. The Molecular Structures and Reactivity of $V_2O_5/TiO_2/SiO_2$ Catalysts. Catal. Lett., 13: 9-19, 1992.

[251] F. Rouquerol, J. Rouquerol, K. Sing, P. L. Llewellyn, G. Maurin, Adsorption by Powders and Porous Solids : Principles, Methodology and Applications. 2nd edition, Elsevier/AP, Amsterdam, 2014.

[252] C. B. Wang, Y. P. Cai, I. E. Wachs. Reaction-induced Spreading of Metal Oxides onto Surfaces of Oxide Supports during Alcohol Oxidation: Phenomenon, Nature, and Mechanisms. Langmuir, 15: 1223-1235, 1999.

[253] H. B. Zhu, S. Ould-Chikh, H. L. Dong, I. Llorens, Y. Saih, D. H. Anjum, J. L. Hazemann, J. M. Basset. VO_x/SiO_2 Catalyst Prepared by Grafting $VOCl_3$ on Silica for Oxidative Dehydrogenation of Propane. ChemCatChem, 7: 3332-3339, 2015.

[254] L. Arnarson, H. Falsig, S. B. Rasmussen, J. V. Lauritsen, P. G. Moses. A Complete Reaction Mechanism for Standard and Fast Selective Catalytic Reduction of Nitrogen Oxides on Low Coverage VO_x/TiO_2(001) Catalysts. J. Catal., 346: 188-197, 2017.

[255] I. Giakoumelou, C. Fountzoula, C. Kordulis, S. Boghosian. Molecular Structure and Catalytic Activity of V_2O_5/TiO_2 Catalysts for the SCR of NO by NH_3: In situ Raman Spectra in the Presence of O_2, NH_3, NO, H_2, H_2O, and SO_2. J. Catal., 239: 1-12, 2006.

[256] S. L. Zhang, Q. Zhong. Promotional effect of WO_3 on O_2^- over V_2O_5/TiO_2 Catalyst for Selective Catalytic Reduction of NO with NH_3. J. Mol. Catal. A-Chem., 373: 108-113, 2013.

[257] M. Kobayashi, R. Kuma, S. Masaki, N. Sugishima. TiO_2-SiO_2 and V_2O_5/TiO_2-SiO_2 Catalyst: Physico-chemical Characteristics and Catalytic Behavior in Selective Catalytic Reduction of NO by NH_3. Appl. Catal. B-Environ., 60: 173-179, 2005.

[258] J. M. Won, M. S. Kim, S. C. Hong. Effect of Vanadium Surface Density and Structure in VO_x/TiO_2 on Selective Catalytic Reduction by NH_3. Korean J. Chem. Eng., 35: 2365-2378, 2018.

[259] D. C. M. Dutoit, M. A. Reiche, A. Baiker. Vanadia-silica Aerogels - Structure and Catalytic Properties in Selective Reduction of NO by NH_3. Appl. Catal. B-Environ., 13: 275-288, 1997.

[260] S. Soyer, A. Uzun, S. Senkan, I. Onal. A Quantum Chemical Study of Nitric Oxide Reduction by Ammonia (SCR reaction) on V_2O_5 Catalyst Surface. Catal. Today, 118: 268-278, 2006.

[261] H. X. Dai, A. T. Bell, E. Iglesia. Effects of Molybdena on the Catalytic Properties of Vanadia Domains Supported on Alumina for Oxidative Dehydrogenation of Propane. J. Catal., 221: 491-499, 2004.

[262] Y. Li, Z. H. Wei, F. Gao, L. Kovarik, R. A. L. Baylon, C. H. F. Peden, Y. Wang. Effect of Oxygen Defects on the Catalytic Performance of VO_x/CeO_2 Catalysts for Oxidative Dehydrogenation of Methanol. ACS Catal., 5: 3006-3012, 2015.

[263] F. Y. Gao, X. L. Tang, H. H. Yi, J. Y. Li, S. Z. Zhao, J. G. Wang, C. Chu, C. L. Li. Promotional Mechanisms of Activity and SO_2 Tolerance of Co- or Ni-doped MnO_x-CeO_2 Catalysts for SCR of NO_x with NH_3 at Low Temperature. Chem. Eng. J., 317: 20-31, 2017.

[264] A. Trovarelli, M. Boaro, E. Rocchini, C. de Leitenburg, G. Dolcetti. Some Recent Developments in the Characterization of Ceria-based Catalysts. J. Alloy. Compd., 323-324: 584-591, 2001.

[265] R. Craciun. Characterization of Mixed Amorphous/Crystalline Cerium Oxide Supported on SiO_2. Solid State Ionics, 110: 83-93, 1998.

[266] B. M. Reddy, A. Khan, P. Lakshmanan, M. Aouine, S. Loridant, J.-C. Volta. Structural Characterization of Nanosized CeO_2−SiO_2, CeO_2−TiO_2, and CeO_2−ZrO_2 Catalysts by XRD, Raman, and HREM Techniques. J. Phys. Chem. B, 109: 3355-3363, 2005.

[267] N. Fang, Y. Y. Ding, C. B. Liu, Z. G. Chen. Role of SiO_2 in synthesis of SiO_2-supported CeO_2 Composites. Ceram. Int., 44: 12363-12369, 2018.

[268] H. T. T. Nguyen, M. Ohtani, K. Kobiro. One-pot Synthesis of SiO_2-CeO_2 Nanoparticle Composites with Enhanced Heat Tolerance. Micropor. Mesopor. Mat., 273: 35-40, 2019.

[269] B. A. Reddy, A. Khan, Y. Yamada, T. Kobayashi, S. Loridant, J. C. Volta. Surface Characterization of CeO_2/SiO_2 and $V_2O_5/CeO_2/SiO_2$ Catalysts by Raman, XPS, and Other Techniques. J. Phys. Chem. B, 106: 10964-10972, 2002.

[270] Y. Peng, C. X. Liu, X. Y. Zhang, J. H. Li. The Effect of SiO_2 on a Novel CeO_2-WO_3/TiO_2 Catalyst for the Selective Catalytic Reduction of NO with NH_3. Appl. Catal. B-Environ., 140: 276-282, 2013.

[271] R. R. Fan, Z. Q. Li, Y. Wang, C. Zhang, Y. Wang, Z. Y. Ding, X. Guo, R. Wang. Effects of WO_3 and SiO_2 Doping on CeO_2-TiO_2 Catalysts for Selective Catalytic Reduction of NO with Ammonia. RSC Adv., 10: 5845-5852, 2020.

[272] C. X. Liu, L. Chen, J. H. Li, L. Ma, H. Arandiyan, Y. Du, J. Y. Xu, J. M. Hao. Enhancement of Activity and Sulfur Resistance of CeO_2 Supported on TiO_2-SiO_2 for the Selective Catalytic Reduction of NO by NH_3. Environ. Sci. Technol., 46: 6182-6189, 2012.

[273] H. T. Xu, Y. S. Shen, C. H. Shao, F. W. Lin, S. M. Zhu, T. Qiu. A Novel Catalyst of Silicon Cerium Complex Oxides for Selective Catalytic Reduction of NO by NH_3. J. Rare Earths, 28: 721-726, 2010.

[274] Z. Q. Chen, L. Liu, H. X. Qu, Q. Zhong, Z. Liu. The Effect of CeO_2 Dispersity and Active Oxygen Species on the SCR Reaction Over Fe-ZSM-5@Ce/meso-SiO_2. Catal. Lett., 150: 514-523, 2020.

[275] W. W. Shen, D. S. Mao, Z. M. Luo, J. Yu. CO oxidation on mesoporous SBA-15 supported CuO-CeO_2 Catalyst Prepared by a Surfactant-assisted Impregnation Method. RSC Adv., 7: 27689-27698, 2017.

[276] S. Han, Q. Ye, Q. Gao, H. Dai. Improved SO_2 Tolerance of Cu-SAPO-18 by Ce-Doping in the Selective Catalytic Reduction of NO with NH_3. Catalysts, 10: 783, 2020.

[277] K. Cao, J. M. Cai, X. Liu, R. Chen. Review Article: Catalysts Design and Synthesis via Selective Atomic Layer Deposition. J. Vac. Sci. Technol. A, 36: 010801, 2018.

[278] M. Ziemba, C. Schilling, M. V. Ganduglia-Pirovano, C. Hess. Toward an Atomic-Level Understanding of Ceria-Based Catalysts: When Experiment and Theory Go Hand in Hand. Accounts Chem. Res., 54: 2884-2893, 2021.

[279] S. M. Lee, Y. H. Lee, D. H. Moon, J. Y. Ahn, D. D. Nguyen, S. W. Chang, S. S. Kim. Reaction Mechanism and Catalytic Impact of Ni/CeO_{2-x} Catalyst for Low-Temperature CO_2 Methanation. Ind. Eng. Chem. Res., 58: 8656-8662, 2019.

[280] L. Y. Wang, Z. Q. Wang, X. X. Cheng, M. Z. Zhang, Y. K. Qin, C. Y. Ma. In situ DRIFTS Study of the NO+CO Reaction on Fe-Co Binary Metal Oxides over Activated Semi-coke Supports. RSC Adv., 7: 7695-7710, 2017.

[281] D. Parimi, V. Sundararajan, O. Sadak, S. Gunasekaran, S. S. Mohideen, A. Sundaramurthy. Synthesis of Positively and Negatively Charged CeO_2 Nanoparticles: Investigation of the Role of Surface Charge on Growth and Development of Drosophila melanogaster. ACS Omega, 4: 104-113, 2019.

[282] H. Song, B. Mirkelamoglu, U. S. Ozkan. Effect of Cobalt Precursor on the Performance of Ceria-supported Cobalt Catalysts for Ethanol Steam Reforming. Appl. Catal. A-Gen., 382: 58-64, 2010.

[283] N. Bourenane, Y. Hamlaoui, C. Remazeilles, F. Pedraza. Effect of the pH of the Electrolyte on the Formation and on the Corrosion Properties of Ceria Based Coating on Carbon Steel. Mater. and Corros., 70: 110-119, 2019.

[284] C. Vittoni, G. Gatti, G. Paul, E. Mangano, S. Brandani, C. Bisio, L. Marchese. Non-Porous versus Mesoporous Siliceous Materials for CO_2 Capture. Chemistryopen, 8: 719-727, 2019.

[285] B. Xu, Y. W. Liu, Y. Li, L. L. Wang, N. N. Li, M. Fu, P. Wang, Q. Wang. High Strength and Anti-fatigue Nanocomposite Hydrogels Prepared via Self-initiated Free Radical Polymerization Triggered by Daylight. New J. Chem., 42: 11796-11803, 2018.

[286] Z. L. Wu, Y. Q. Cheng, F. Tao, L. Daemen, G. S. Foo, L. Nguyen, X. Y. Zhang, A. Beste, A. J. Ramirez-Cuesta. Direct Neutron Spectroscopy Observation of Cerium Hydride Species on a Cerium Oxide Catalyst. J. Am. Chem. Soc., 139: 9721-9727, 2017.

[287] F. D. Liu, W. P. Shan, X. Y. Shi, C. B. Zhang, H. He. Research Progress in Vanadium-Free Catalysts for the Selective Catalytic Reduction of NO with NH_3. Chinese J. Catal., 32: 1113-1128, 2011.

[288] X. L. Hu, J. X. Chen, W. Y. Qu, R. Liu, D. R. Xu, Z. Ma, X. F. Tang. Sulfur-Resistant Ceria-Based Low-Temperature SCR Catalysts with the Non-bulk Electronic States of Ceria. Environ. Sci. Technol., 55: 5435-5441, 2021.

[289] H. L. Zhang, L. Ding, H. M. Long, J. X. Li, W. Tan, J. W. Ji, J. F. Sun, C. J. Tang, L. Dong. Influence of CeO_2 Loading on Structure and Catalytic Activity for NH_3-SCR over TiO_2-Supported CeO_2. J. Rare Earths, 38: 883-890, 2020.

[290] Y. Q. Zeng, Y. N. Wang, S. L. Zhang, Q. Zhong, W. L. Rong, X. H. Li. One-pot Synthesis of Ceria and Cerium Phosphate (CeO_2-$CePO_4$) Nanorod Composites for Selective Catalytic Reduction of NO with NH_3: Active Sites and Reaction Mechanism. J. Colloid Interface Sci., 524: 8-15, 2018.

[291] X. Q. Ran, M. H. Li, K. Wang, X. Y. Qian, J. W. Fan, Y. Sun, W. Luo, W. Teng, W. X. Zhang, J. P. Yang. Spatially Confined Tuning the Interfacial Synergistic Catalysis in Mesochannels toward Selective Catalytic Reduction. ACS Appl. Mater. Interfaces, 11: 19242-19251, 2019.